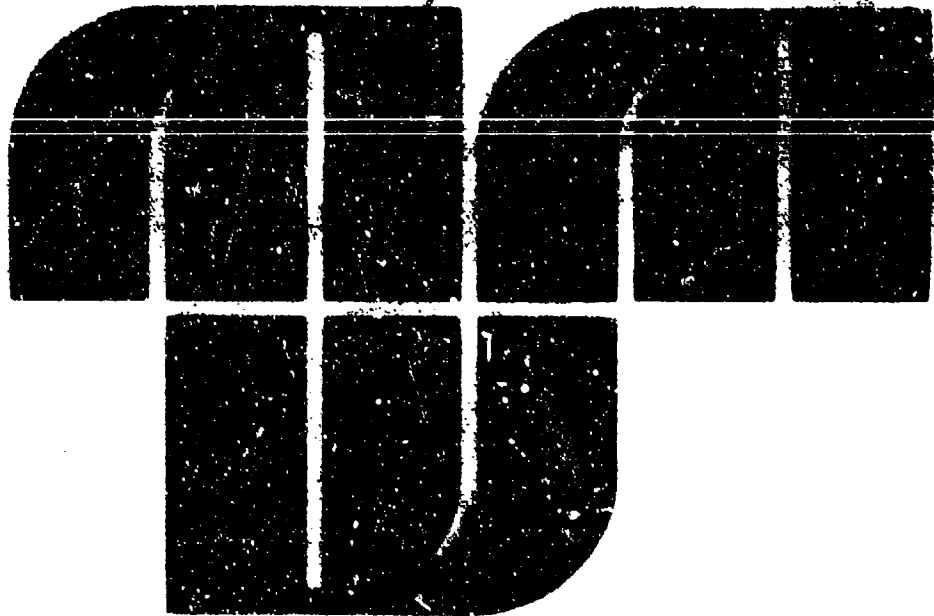042060

B. S.

Volume 2

1974 MILLIMETER WAVES TECHNIQUES CONFERENCE

26-28 MARCH

Sponsored by

NAVAL ELECTRONICS LABORATORY CENTER
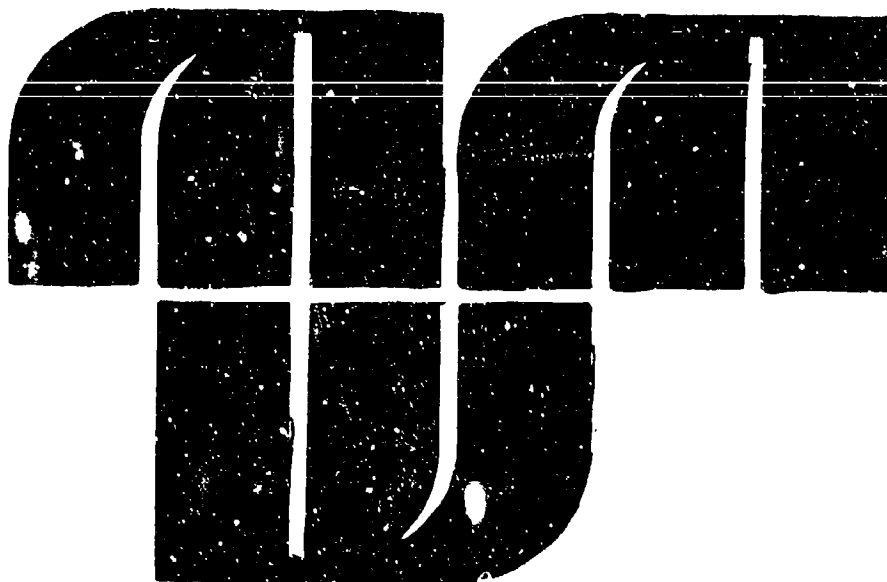San Diego, California 92152

PRICES SUBJECT TO CHANGE

NELC/TD 398

Volume 2

1974 MILLIMETER WAVES TECHNIQUES CONFERENCE

26-28 MARCH

PAPERS PRESENTED

SESSION E

STANDARDS AND MEASUREMENTS: TUBES, RADOMES

SESSION F

EHF SYSTEMS

SUPPLEMENTARY PAPERS

SESSION D
MIC; Components
and Circuits

DEVELOPMENT OF ANALYSES FOR INVESTIGATION OF MILLIMETER WAVE INTEGRATED CIRCUITS

by

Barry E. Spielman
Naval Research Laboratory
Washington, D.C.   20375

INTRODUCTION

Microwave integrated circuit (MIC) techniques have developed
rapidly in recent years in the frequency range from D-band up into J-band.
The benefits resulting from MIC technology--savings in component cost,
size, and weight--are also desirable for system applications at fre-
quencies in J-band and above. Attempts to apply circuit integration
techniques at millimeter wave frequencies have encountered several
problems. Some of these problems are: (1) high transmission line loss,
(2) high cost, (3) a need for broader bandwidth capability, (4) a lack
of design data, and (5) a need for transmission lines with greater
suitability for component implementation.

This paper describes a research effort which is oriented to develop
computer-aided analysis methods which will not only enable the in-
vestigator to inexpensively and systematically evaluate new transmission
media, but will also furnish design information for components employing
isolated and coupled parallel transmission lines. An in-house, computer-
aided, quasi-TEM analysis, suitable for characterizing a variety of
lossless isolated and coupled transmission lines below 40 GHz, has been
extended to compute conductor and dielectric losses in these media. A
discussion of this extension is presented. Illustrative computations of
conductor and dielectric loss coefficients are presented for both micro-
strip and coplanar waveguide. Plans are discussed related to a recently
initiated effort to develop a method of moments analysis which adequately
treats nonmagnetic, dispersive media and determines higher order modes
for propagation at frequencies through and above 40 GHz.

QUASI-TEM ANALYSIS DEVELOPMENT

Lossless Media

The investigation described here was initiated as a logical extension of previous in-house research relating to the development of directional couplers for broadband MIC applications. During this previous effort the primary problem was to reduce the degradation of coupler directivity resulting from different even and odd mode phase velocities in commonly employed configurations of coupled transmission lines. For the purpose of solving this problem a computer-aided, method of moments, quasi-TEM analysis was developed, with suitability for determining propagation characteristics in a variety of lossless, isolated, and coupled transmission lines for applications below 40 GHz. The accuracy of this analysis has been demonstrated for computations of isolated microstrip line characteristics [1,2] and via microwave measurements of computer designed directional couplers employing: (1) microstrip with a slotted ground plane [2], (2) coupled microstrip with a ground plane of reduced extent [2], and (3) edge-coupled microstrip with dielectric overlays.[3]

In order to assess the higher transmission line losses encountered at millimeter wave frequencies this analysis has been extended to determine conductor and dielectric losses as described in the next two sections.

Conductor Losses

The method used to compute propagation losses due to imperfect conductors in either isolated or coupled transmission lines is described as follows. The loss coefficient due to conductor losses, α_c, for an isolated transmission line or the even or odd mode transmission line for a coupled line pair can be expressed as

$$\alpha_c = \frac{\overline{P}_d}{2\,\overline{P}_f} \tag{1}$$

Here, $\overline{P}_d$ is the time average power dissipated per unit length due to conductor losses and $\overline{P}_f$ is the time average power flow along the line.

$\bar{P}_f$ is expressed approximately as

$$\bar{P}_f = \frac{|V|^2}{Z_0} \qquad (2)$$

where $|V|$ is the amplitude of static voltage impressed across the conductors of this system, while Z_0 is the value of impedance determined by the lossless analysis referred to in the previous section. $\bar{P}_d$ is described initially by

$$\bar{P}_d = \int_{cond} |H|^2 R \, d\ell \qquad (3)$$

In equation (3), $|H|$ is the amplitude of magnetic field at the boundaries of conductors in the system, R is the surface resistance of the conductors (all taken to be the same material here). The integration in equation (3) is taken over the surfaces of all conductors in the transmission line under consideration. The magnetic field in the lossy problem is approximated by that in the lossless problem, which in turn can be represented in terms of an equivalent charge distribution [4], q, determined in the solution of the lossless problem. Hence,

$$\bar{P}_d \approx \frac{4\pi^2 \, \mu_0 \, R}{(\epsilon_r)_{eff} \, \epsilon_0} \int_{cond} |q|^2 \, d\ell \qquad (4)$$

The integral in equation (4) is numerically approximated by a summation and the effective relative permittivity, $(\epsilon_r)_{eff}$, is determined consistent with the lossless analysis formulation set down previously [2]. The surface resistance R is determined by

$$R = \sqrt{\frac{\pi \mu_0 f}{\sigma}} \qquad (5)$$

where f is the operating frequency and σ is the d.c. conductivity of the metal. Using equations (2), (4), and (5) together with equation (1), the

conductor loss coefficient can be approximated as

$$\alpha_c \ (dB/in) \approx \frac{4.35 \ Z_0 \ \mu_0}{|V|^2 \ (\epsilon_r)_{eff} \ \epsilon_0} \ \sqrt{\frac{\pi \mu_0}{\sigma}} \ \int_{cond} |q|^2 \ d\ell \tag{6}$$

As an illustrative example, the conductor loss coefficient was computed for a microstrip line with an impedance of $50\,\Omega$ (nominally). The linewidth was 0.024 inch, the substrate thickness was 0.025 inch, the substrate dielectric constant was 10.0, and the metalization was taken to 0.00025 inch thick. The d.c. conductivity, σ, was taken to be $9.61 \times 10^{-7} \Omega$-inch. The computed values of α_c are represented in Figure 1 by the solid curve. The reference values, represented by a broken curve, are due to a computer program version of Schneider's results. [5]

As another illustrative example, the conductor loss coefficient was computed by the method developed here for a $50\,\Omega$ coplanar waveguide. The linewidth of the strip was 0.025 inch, the gaps in the conductor were 0.01065 inch, the substrate thickness was 0.025 inch, the substrate dielectric constant was taken to be 10.4. Again, the metalization thickness was 0.00025 inch with $\sigma = 9.61 \times 10^{-7} \Omega$-inch. Figure 2 shows the computed α_c versus frequency for this case. For reference the computed α_c for microstrip is replotted in Figure 2.

Dielectric Losses

Consistent with the quasi-TEM approach set down in previous sections and using an approach similar to one due to Schneider [6], for isolated, even mode, or odd mode transmission lines the dielectric loss coefficient, α_d, can be expressed as

$$\alpha_d = \frac{27.3}{c} \ \sqrt{(\epsilon_r)_{eff}} \ (\tan \delta)_{eff} \tag{7}$$

where $(\epsilon_r)_{eff}$ is determined by the method discussed for equation (4), c is the speed of light in free space, and $(\tan \delta)_{eff}$ can be expressed as

$$(\tan \delta)_{eff} = \frac{1}{(\epsilon_r)_{eff}} \sum_{n=1}^{N} (\epsilon_r)_n \frac{\partial(\epsilon_r)_{eff}}{\partial(\epsilon_r)_n} \tan \delta_n \qquad (8)$$

In equation (8), N is the number of different homogeneous dielectric regions in the transmission line cross section, $\tan \delta_n$ and $(\epsilon_r)_n$ are the loss tangent and relative permittivity of the nth dielectric region, respectively. The partial derivative in equation (8) is approximated by a finite difference quotient.

Using equations (7) and (8), α_d was computed for the same microstrip example described in the previous section. The results are represented by the solid curve in Figure 3. These are compared with reference values due to Pucel, et. al. [7] for reference.

For the coplanar waveguide described in the previous section, α_d was computed and is plotted in Figure 4.

DISPERSIVE ANALYSIS

Due to dispersion and higher order moding, the quasi-TEM analysis approach has limited validity for applications above 40 GHz. Effort is currently underway on the development of a method of moments, computer-aided analysis which adequately treats nonmagnetic, dispersive media and determines higher order modes. This analysis will be useful for applications above 40 GHz. The successful development of this analysis will furnish a means for generating accurate design data for both conductor oriented transmission media (e.g.,microstrip, microguide, trapped inverted microstrip) and dielectric oriented transmission media (e.g., image line and insular waveguide). Such data would lead to substantial reductions in engineering and fabrication expenditures in investigations which could lead to improved passive components (e.g., coupler, hybrids, filters). Furthermore, the capability, furnished by this analysis, of studying higher order modes in a variety of media could lead to the isolation of a mode with more desirable loss characteristics.

SUMMARY

The effort described in this presentation is unique in its capability for inexpensively and systematically investigating a wide variety of transmission line media, reducing costly engineering and fabrication costs by exploiting versatile, computer-aided analysis methods. The investigative approach underway can: (1) furnish design curves for development efforts, (2) allow for comparative and feasibility evaluations and (3) should lead to components with improved characteristics.

REFERENCES

[1]   Spielman, B.E., "The Development of Microwave Couplers and Filters Using a New Computer-Aided Technique," Late Paper, 1972 IEEE-GMTT International Microwave Symposium, Arlington Heights, Ill., May 22-24, 1972

[2]   Spielman, B.E.. "A Computer-Aided Method for the Design of Wide Class of Microwave Couplers and Filters," GOMAC Digest, San Diego, CA, October 10-12, 1972, pp.361-73

[3]   Spielman, B.E., "The Development of 20 dB Multi-Octave Directional Coupler for MIC Applications," Late Paper, 1973 IEEE-GMTT International Microwave Symposium, Boulder, CO, June 4-6, 1973

[4]   Harrington, R.F., et. al., "Computation of Laplacion Potentials by an Equivalent-Source Method," Proc.IEE, Vol.116, October 1969, pp.1715-20

[5]   Schneider, M.V., "Microstrip Lines for Microwave Integrated Circuits," BSTJ, Vol.48, May-June 1969, pp.1421-44

[6]   Schneider, M.V., "Dielectric Loss in Microwave Integrated Circuits," BSTJ, Vol.48, September 1969, pp.2325-32

[7]   Pucel, R.A., "Losses in Microstrip," IEEE Trans.Micr.Th.Techs., Vol.MTT-16, June 1968, pp.342-50
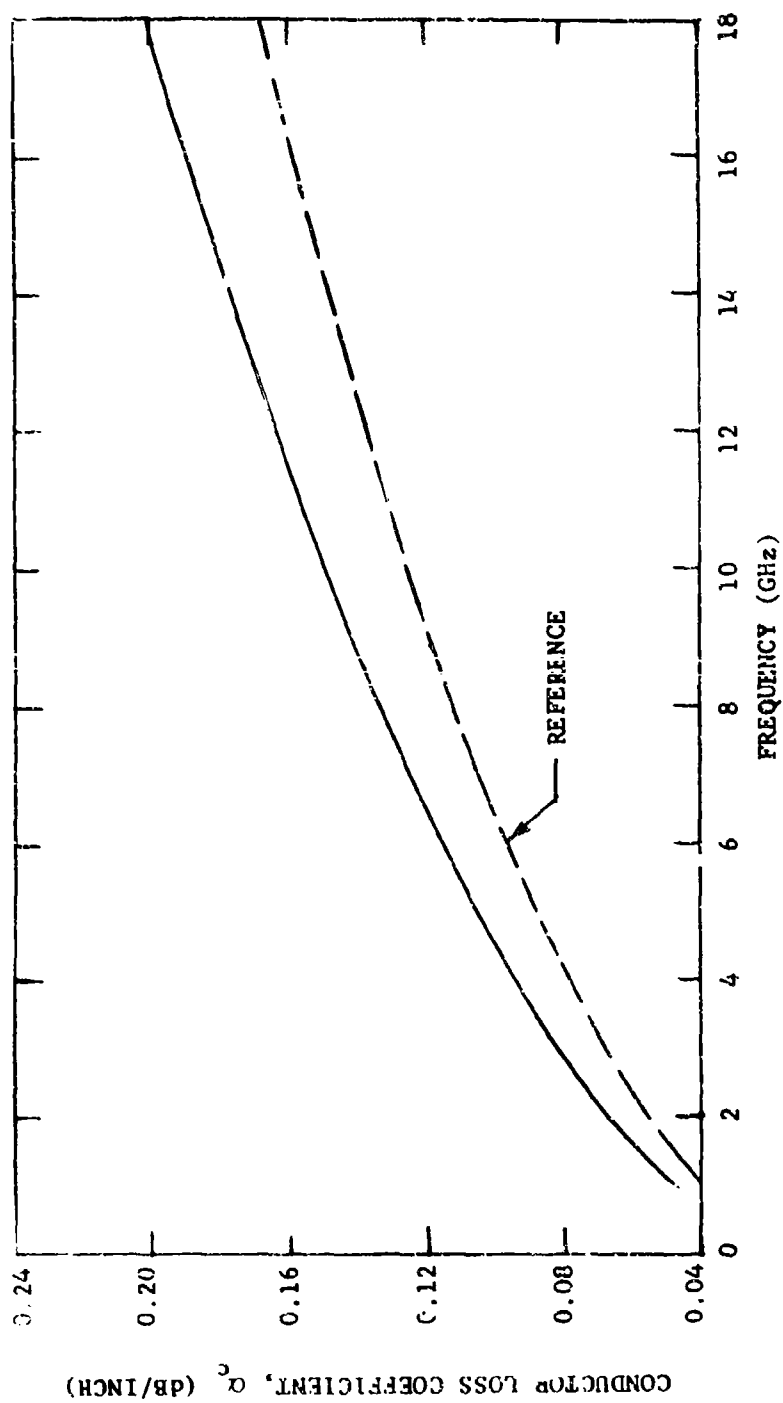
FIGURE 1 CONDUCTOR ATTENUATION COEFFICIENT FOR MICROSTRIP ($Z_o = 50 \, \Omega$)
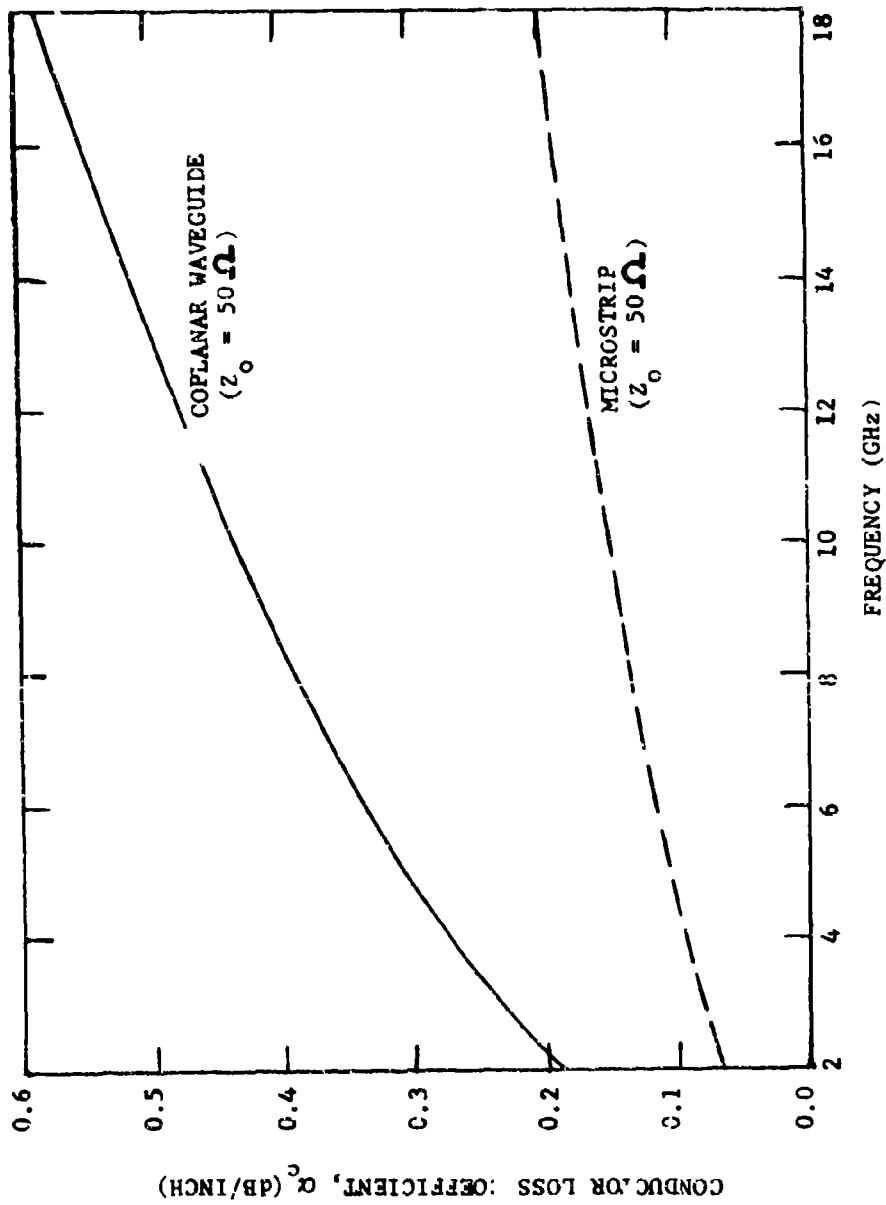
FIGURE 2. CONDUCTOR LOSS COEFFICIENT FOR COPLANAR WAVEGUIDE AND MICROSTRIP
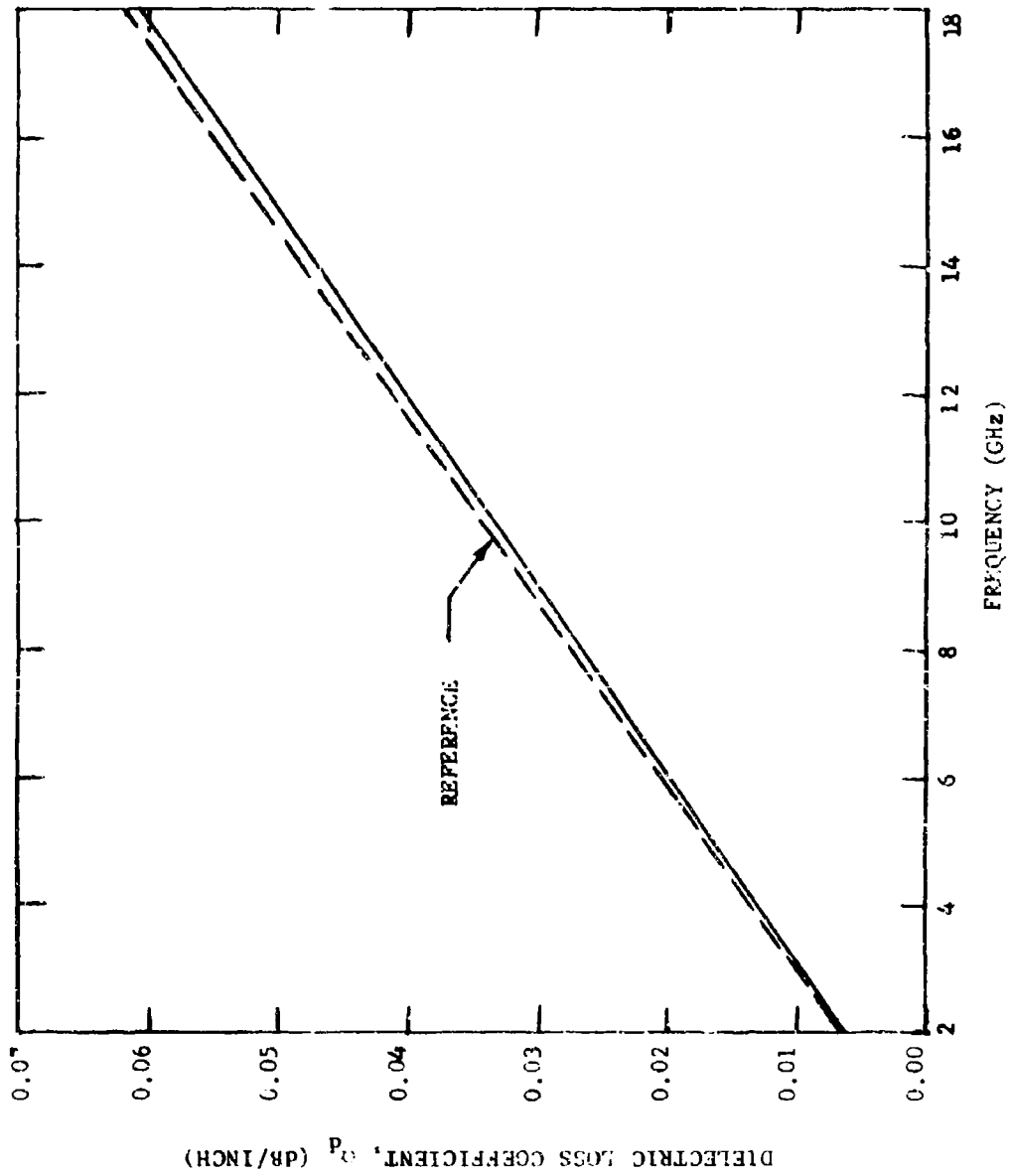
FIGURE 3. DIELECTRIC LOSS COEFFICIENT FOR MICROSTRIP(Z_o = 50 Ω)
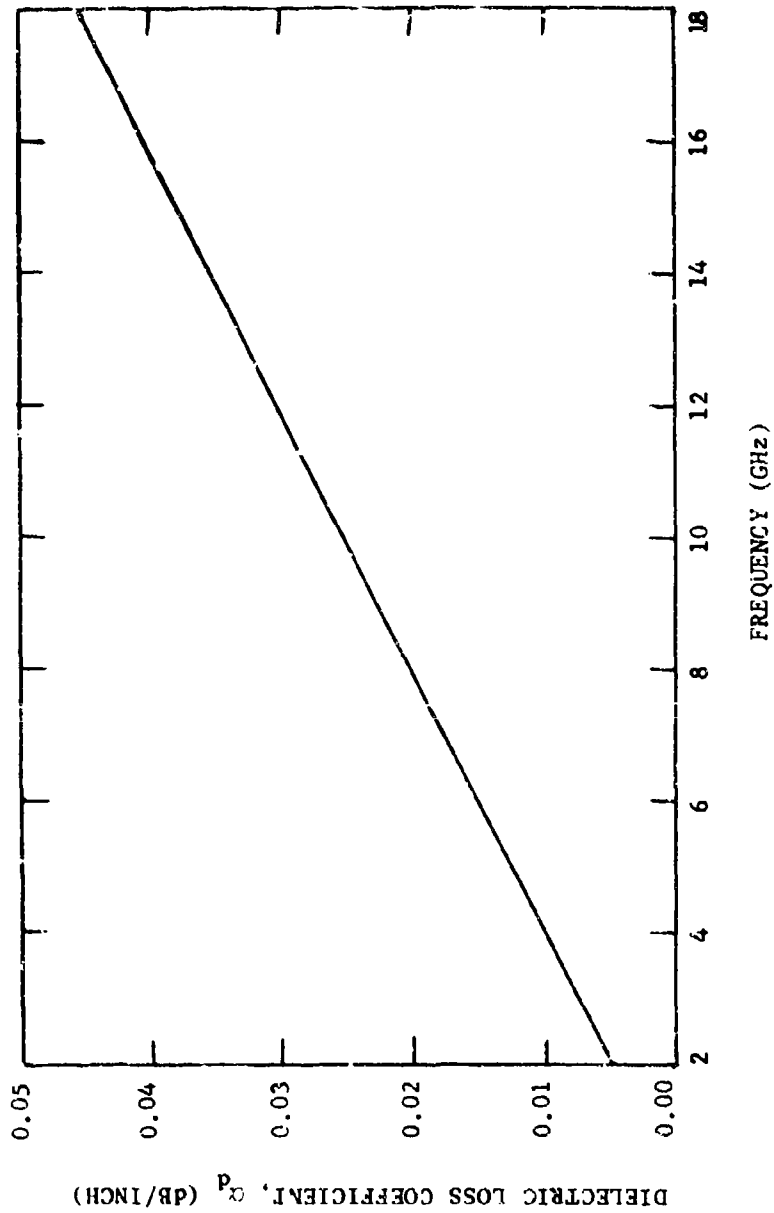
FIGURE 4. DIELECTRIC LOSS COEFFICIENT FOR COPLANAR WAVEGUIDE (Z_o = 50 Ω)

LOW-COST HIGH-PERFORMANCE MILLIMETER INTEGRATED CIRCUITS CONSTRUCTED BY FIN-LINE TECHNIQUES

by

Paul J. Meier

Applied Electronics Division
AIL, a division of CUTLER-HAMMER
Melville, New York 11746

Integrated fin-line techniques have been proposed as a superior method for constructing millimeter integrated circuits (references 1 and 2). The advantages of integrated fin-line over microstrip at millimeter wavelengths include lower loss, less stringent tolerances, better compatibility with hybrid devices, and simple waveguide interfaces. This paper will describe low-cost, high-performance millimeter components which have been developed to demonstrate the capability of integrated fin-line. The components include a PIN attenuator and several band-pass filters.

Figure 1 shows the cross-section of a fin-line structure which is suitable for mounting semiconductor devices. Metal fins are printed on a dielectric substrate which bridges the broad walls of a rectangular waveguide. The substrate material can have a low dielectric constant, which eases tolerance problems at millimeter wavelengths. In the structure shown, the upper fin is insulated from the housing at dc by a dielectric gasket, but is grounded at RF by choosing the thickness of the broad walls to be a quarter wavelength in the dielectric medium. Bias may be applied to a semiconductor device mounted between the insulated fin and lower fin, which is directly grounded by a metal gasket.

Figure 2 shows a test fixture which mates directly with two standard WR28 waveguides and has identical inner dimensions (0.140 × 0.280 inch). The substrate is cut from 0.010-inch Duroid and includes six

mounting holes and two stepped edges. The latter protrude into the abutting WR28 waveguides and serve as quarterwave transformers. After establishing a low-reflection transition between WR28 waveguide and a slotted waveguide loaded by a dielectric slab (d b 1.0), the substrate metallization is tapered until the desired gap between the fins is obtained. The measured VSWR of each transition is 1.2 or better across the 26.5 to 40 GHz band. The substrate metallization also includes an RF-blocking network connected to the upper fin.

To demonstrate the compatibility of integrated fin-line with semiconductor devices, two beam-lead PIN diodes (Alpha D5840B) were mounted across the fins near the center of the previously discussed substrate (d b - 0.1). The diodes were spaced a quarter wavelength apart at a frequency near the lower end of the instrumentation band. The measured insertion loss of the PIN fin-line attenuator is plotted in Figure 3 as a function of bias, with frequency as a parameter. At the lower end of the band, where the diode spacing is optimum, the reversed-bias insertion loss of the attenuator is only C.3 dB, thereby demonstrating the capability of constructing low-loss semiconductor mounts in fin-line. As the bias is varied in the forward direction, the attenuation varies smoothly over a 14-dB range throughout a 20-percent band. This level of performance clearly shows that more complex circuits such as phase shifters, amplifiers, mixers, and local oscillators can be successfully constructed in fin-line by low-cost batch techniques.

In fin-line circuits where semiconductors are not required, lower loss can be obtained by printing the fins on both sides of the dielectric substrate and grounding these directly to the housing (reference 2).

To demonstrate the capability of constructing low-cost passive millimeter components in integrated fin-line, various filter components were printed on 0.020-inch Duroid, as shown in Figure 4. One- and four-pole inductively coupled filters are shown at the center of the photograph.

surrounded by four substrates, each printed with a single inductive element. By measuring the insertion loss of these elements across the 26.5 to 40 GHz band, families of design curves were generated to present the shunt susceptance as a function of strip width, with free-space wavelength as a parameter.

Based upon the characterization of fin-line filter elements and published design curves (reference 3), a four-pole equal-element filter has been constructed and tested. Figure 5 compares the calculated response with some preliminary measurements. The calculation was performed by a computer-aided technique which solves for the overall ABCD matrix of the entire filter network. The good agreement that has been obtained between the four-pole measurements and theory demonstrates that integrated fin-line is an excellent medium for constructing low-cost millimeter filters, particularly for those applications where the unloaded Q can be less than 400, or where close integration is desired with hybrid circuits.

In summary, this paper has described some examples of low-cost high-performance millimeter components constructed in integrated fin-line. The high level of performance obtained during this preliminary program clearly shows that fin-line construction techniques may be profitably employed in a wide range of millimeter components and systems. Integrated fin-line is markedly superior to microstrip at millimeter wavelengths, where the former offers lower loss, less stringent tolerances, simple waveguide interfaces, and better compatibility with hybrid devices.

REFERENCES

1. P. J. Meier, "Two New Integrated-Circuit Media with Special Advantages at Millimeter Wavelengths.' Digest of IEEE 1972 G-MTT Symposium, p 221-223. May 1972.

2. P. J. Meier, "Equivalent Relative Permittivity and Unloaded Q Factor of Integrated Fin-Line," Electronics Letters. Vol 9, No. 7, p 162-163. 5 April 1973.

3. J. J. Taub. "Design of Minimum Loss Band-Pass Filters," Microwave Journal, November 1963.
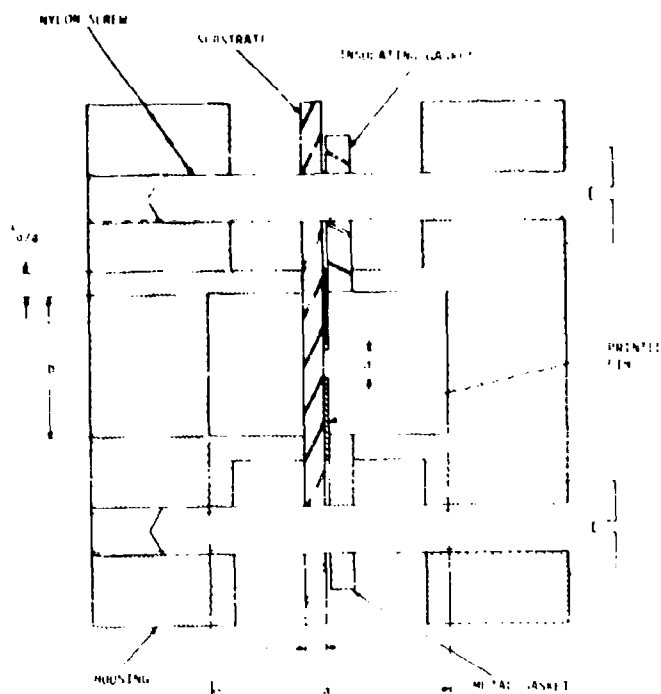
Figure 1. Integrated Fin-Line with Insulated Fins
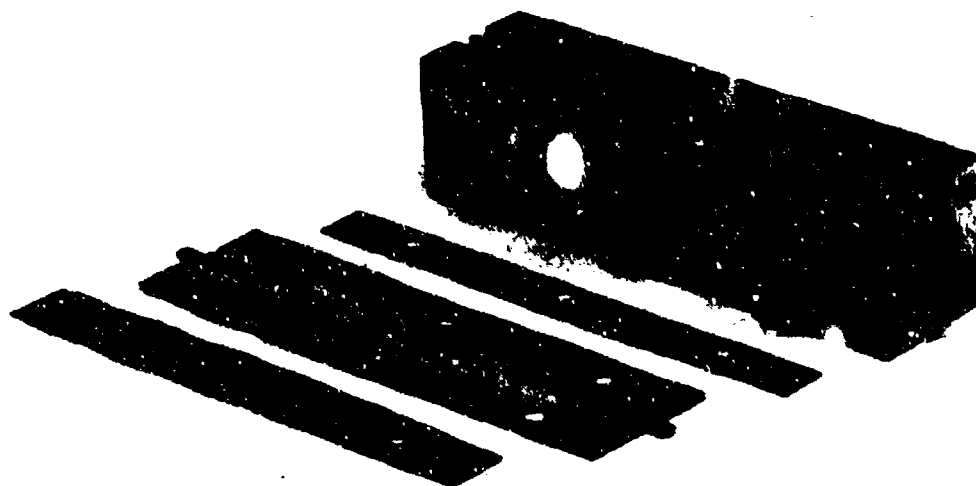
Figure 2. Fin-Line Test Fixture
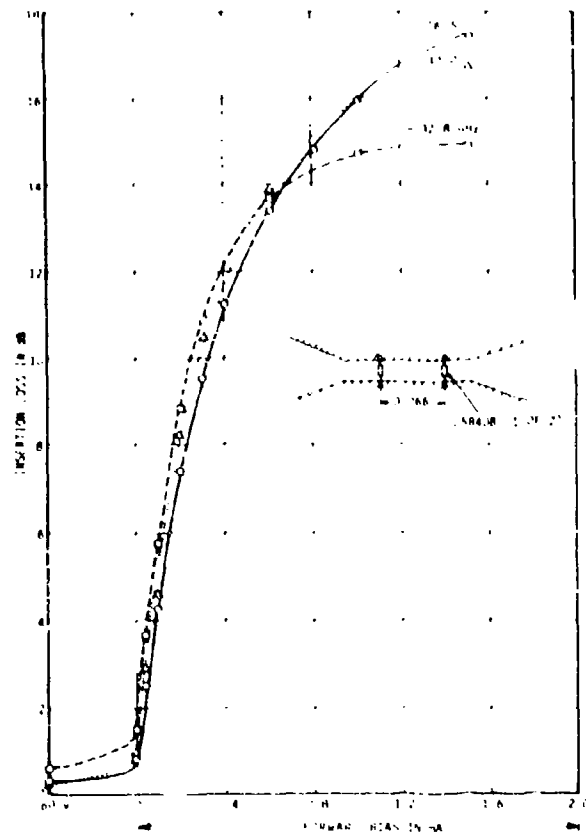
Figure 3. Insertion Loss of Fin-Line Attenuator
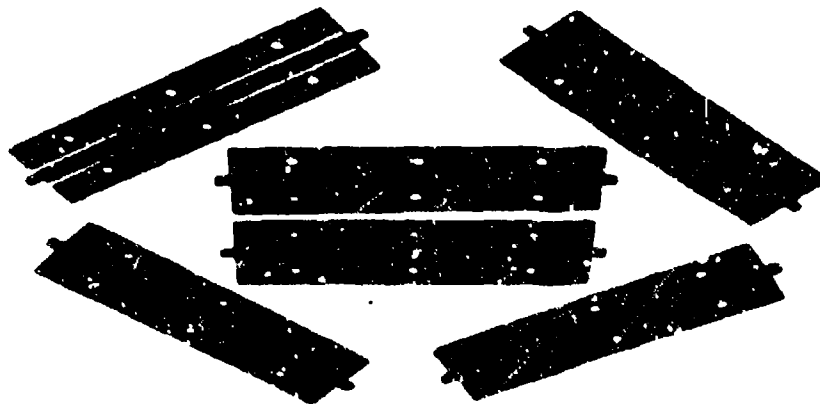
Figure 4. Filter Components
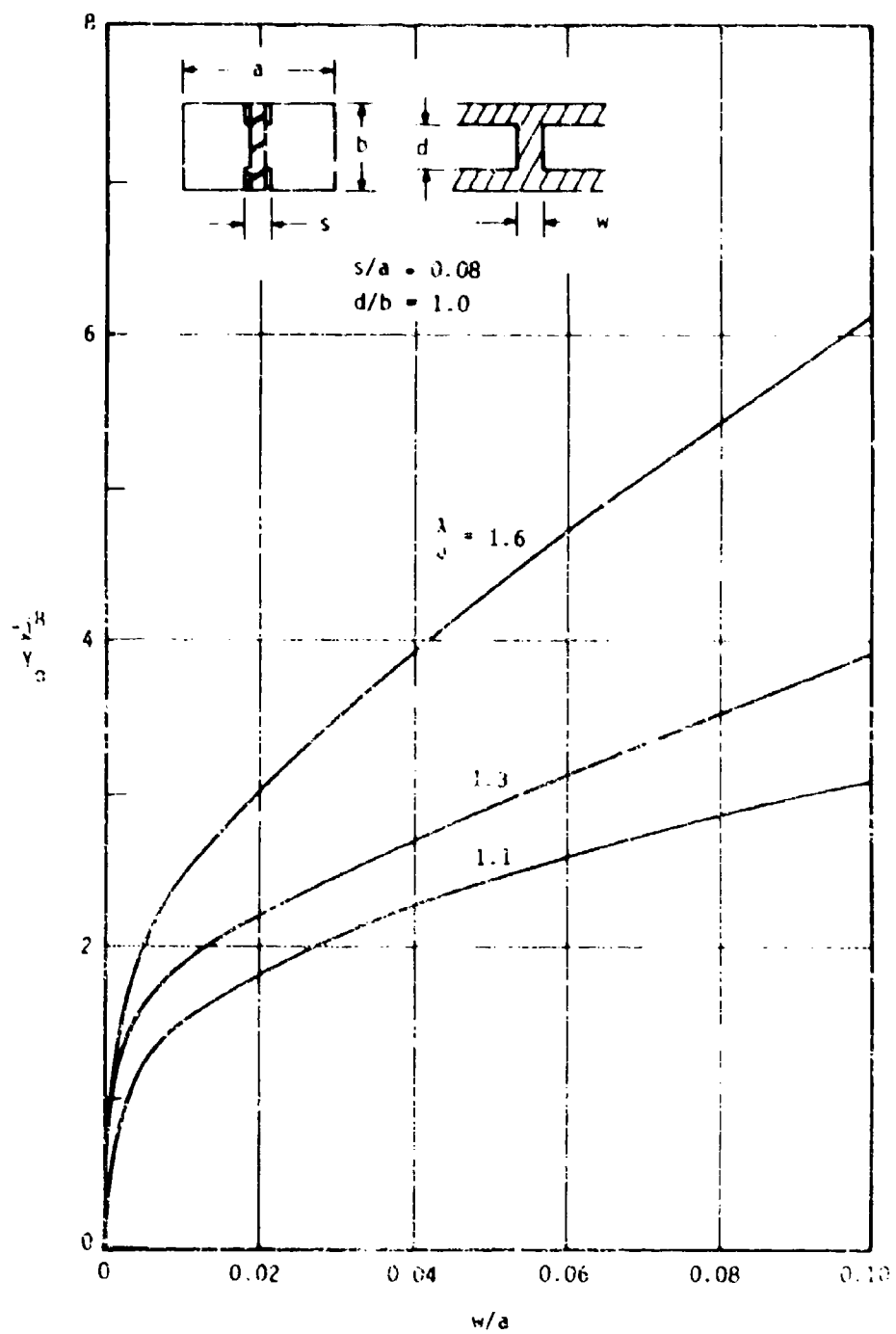
Figure 5.   Response of Four-Pole Filter

A WIDEBAND INTEGRATED CIRCUIT
DOWNCONVERTER FROM 36.0 GHz
TO C BAND

by

Harlan Howe, Jr.
G. Nicholas Larsen

MICROWAVE ASSOCIATES, INC
SOUTH AVENUE
BURLINGTON, MASSACHUSETTS

ABSTRACT

This paper describes the development of a 32.0 GHz to 36.0 GHz down-converter using planar transmission line techniques. The purpose of the program was twofold:

(1)   to develop these techniques for integrated circuits using photo-lithographic methods at millimeter frequencies and

(2)   build a millimeter wave down-converter utilizing these techniques to demonstrate the physical realizability of the approach.

These goals were achieved with the down-converter operating over the correct frequency band with an IF output of 4.0 - 8.0 GHz and a conversion loss of approximately 14.0 dB.

I.   INTRODUCTION

The purpose of the program was to advance technology leading the way to modernizing the high end of a wide-band receiver, such as the AN-TLR-10 using microwave integrated circuit techniques. Previous work has demonstrated that MIC's in the form of ceramic microstrip are an effective way of building microwave components through the frequency range of 18.0 GHz and, perhaps, higher. This program continued the investigation of the integratable circuit elements in order to permit microwave integrated circuits to be constructed at frequencies as high as 40.0 GHz. The demonstration vehicle chosen to establish feasibility of the techniques developed was a down-converter operating from 32.0 GHz to 36.0 GHz which would interface directly with a 4.0 to 8.0 GHz image rejection mixer circuit built in ceramic microstrip.

The following characteristics were established as goals:

Frequency Range (signal)	32.0 - 36.0 GHz
Local Oscillator	28 GHz (fixed)
IF	4.0 - 8.0 GHz

Tangential Sensitivity	-75 dBm (20 MHz IF)
1 dB compression point	-20 dBm minimum
Spurious Signal	75 dBm down
Final IF Output Frequency	60 MHz
Minimum MTBF	10,000 hours

2. TRANSMISSION LINES

Most of the transmission line in common use for microwave frequencies can be applied to the sub-millimeter wave region of 16.0 to 40.0 GHz. These include waveguide, ridge waveguide, circular waveguide, co-planar waveguide, and ceramic waveguide, as well as coaxial lines, microstrip, stripline, trapped inverted microstrip, slot-line, unbalanced suspended substrates, balanced suspended substrates and other more experimental forms of TEM-mode transmission lines. For the purposes of this program, it was felt that it was desirable to restrict an investigation to TEM- and pseudo-TEM-mode transmission line; both because of the long term potential for their increased bandwidth as well as their inherent flexibility to inter-face with active devices such as mixer and source diodes. In order to achieve true integration, we also felt that the technique to manufacture must be related to photo-lithographic and automatic chassis construction; thus, coaxial lines, except in areas of transitions were also rejected as a method of manufacture of the receiver. The dielectric losses of solid dielectric stripline make it unsuitable at frequencies above 18.0 GHz and, it is our judgment that slot-line techniques have not been developed to a sufficient degree to permit their use in a practical receiver at this time. This, then, reduced the choice to three transmission lines which we felt had possible promise for application to the receiver ceramic microstrip, TIM line, and suspended substrate lines.

Ceramic microstrip is a well established technique for microwave integrated circuits, but suffers from increased insertion losses at elevated frequencies; which, while not excessive, nevertheless degrade the perform-ance characteristics. More significantly, the reduction of the dimensions of distributed line components, the result of the high dielectric constant results in extremely tight tolerances which we felt would make the approach excessively expensive and incompatible with a cost effective design approach.

Trapped Inverted Microstrip, or TIM, is a novel type of transmission line invented at Microwave Associates for the purpose of reducing the radiation discontinuities compared to conventional microstrip, without having to pay the penalty of increased line loss. TIM line also possesses several other useful features and is potentially attractive transmission line medium for use in MIC technology. Although some earlier tests have been encouraging, it was decided that once again the extremely tight dimen-sional tolerances required fo component development in this frequency range plus moding problems related to the increased line widths necessary for this

construction as compared to ceramic microstrip ruled it out as a method of manufacture within the time frame of this program.

The transmission line technique chosen for the construction of the receiver was a balanced suspended substrate structure shown in Figure 1B. In this configuration a pair of equal potential conductors is placed on each side of the dielectric substrate support. It differs from the unbalanced substrate shown in Figure 1A, in that because of the equi-potential line registration virtually no field exists within the dielectric substrate, thus reducing, or eliminating, totally its contribution to line insertion loss. A further advantage accrues from the fact that the dielectric is air. The effective wavelength of the line is increased compared to other types of transmission line, thus improving the aspect ratio of components to be built at sub-millimeter frequency. A 0.004" thickness substrate, a 0.001" thick equi-potential conductor, a 0.044" channel height package was chosen as the basic transmission line. A test fixture was built which is shown in Figure 2. Insertion loss data for this transmission line was more than satisfactory and is shown in the loss curve of Figure 3. The original substrate material chosen was an epoxy glass composite, however, final substrate material used in the receiver was a woven teflon fiberglass material which provides stable support for the suspended line and can be processed with conventional photo-etching equipment thus reducing its cost of manufacture. The transmission line is suspended above the channel which is made by optical milling techniques in the basic chassis.

3. CIRCUIT FUNCTION

Since most interfacing equipment, as well as test equipment, is still made in waveguide rather than in a TEM mode transmission line, it was necessary to design the transition which would permit the waveguide to interface directly with the integrated package. A transition developed operated over an extremely wide range and actually provided satisfactory operation from 27.0 GHz to 38.0 GHz. This data is shown in Figure 4, as a plot of VSWR vs. frequency. Additional components developed for the receiver included a bandpass filter, a 90° hybrid which was converted into a balanced mixer and a directional coupler for test purposes. In order to provide image rejection over the RF band and to prevent spurious signals at lower frequencies from entering the receiver, a five-section bandpass filter was designed. This filter was built using short-circuited stubs spaced one-quarter wavelength along the line. The stubs which are nominally one quarter wavelength long the design frequency were transposed, in this case, to be three-quarter wavelength long stub in order to transform their impedance to a higher level, thus maintaining a reasonable aspect ratio and avoiding the problems of loading at the junctions of the line. A test filter was built using the previously developed waveguide transmission and its performance is shown in the curve of Figure 5.

UNBALANCED SUSPENDED SUBSTRATE

BALANCED SUSPENDED SUBSTRATE
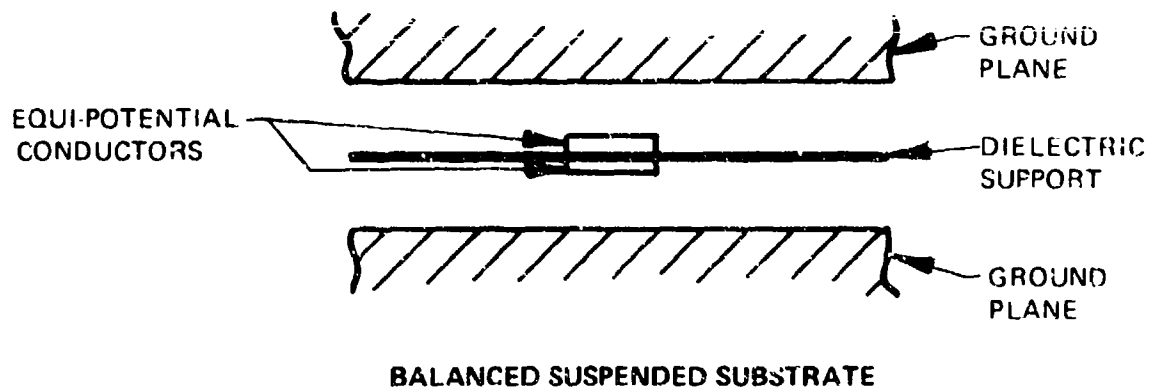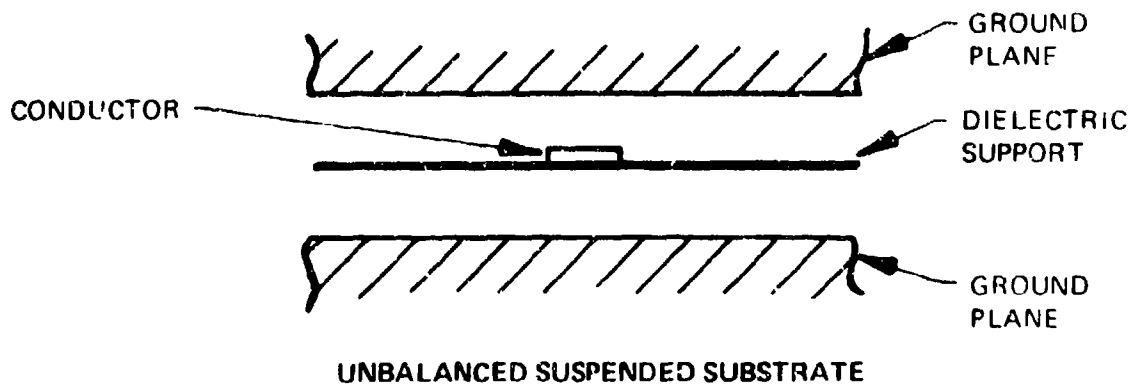
FIGURE 1

D 11574

FIGURE 2   2" LONG SUSPENDED SUBSTRATE TEST LINE
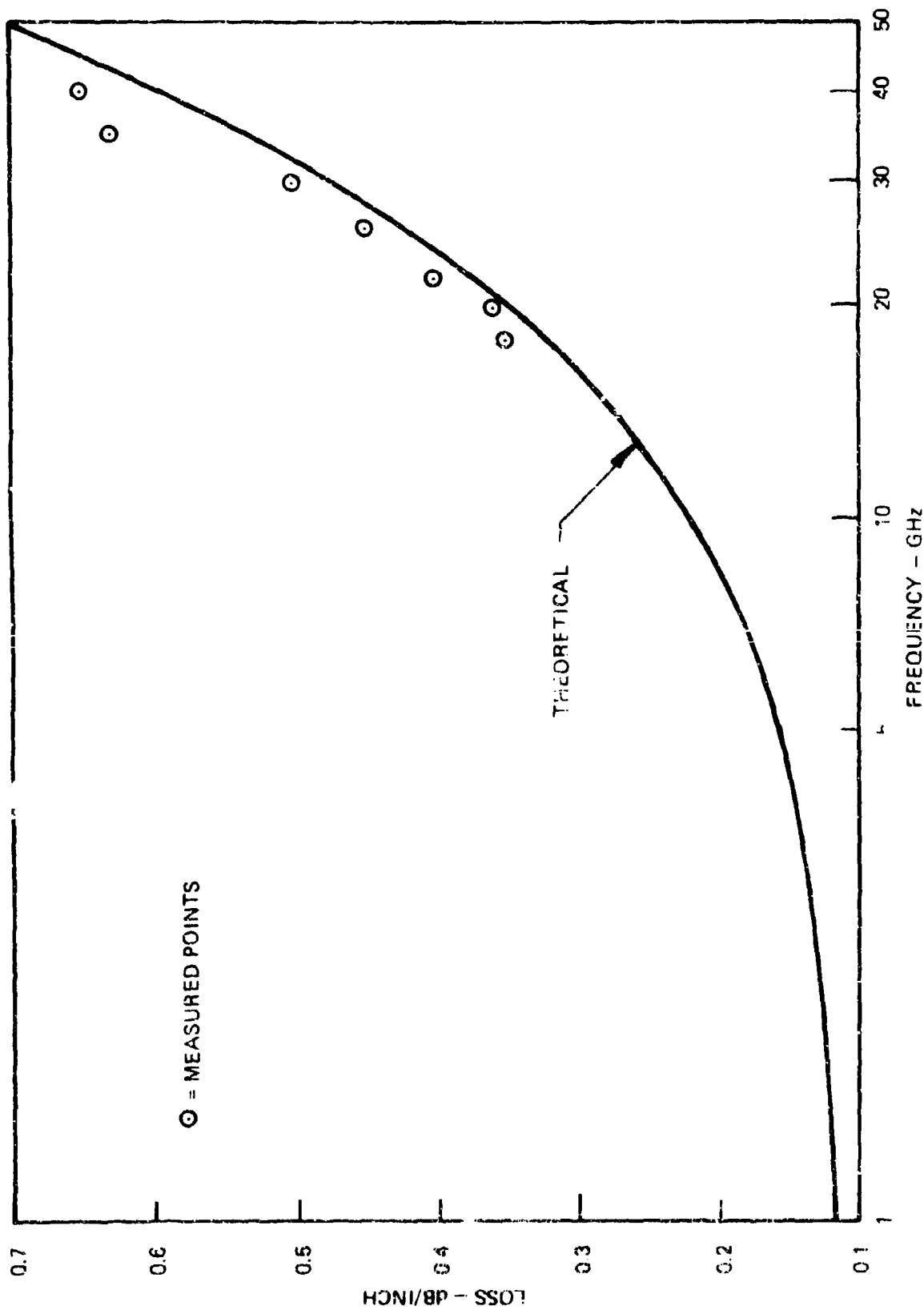
FIGURE 3   INSERTION LOSS VS. FREQUENCY FOR A 0.044 G.P.S.
            BALANCED SUSPENDED SUBSTRATE LINE

Figure 1. Integrated Fin-Line with Insulated Fins

Figure 2. Fin-Line Test Fixture

FIGURE 3   INSERTION LOSS VS. FREQUENCY FOR A 0.044 G.P.S.
BALANCED SUSPENDED SUBSTRATE LINE

⊙ = MEASURED POINTS

THEORETICAL

FREQUENCY – GHz

LOSS – dB/INCH

D-11628

FREQUENCY – GHz

VSWR
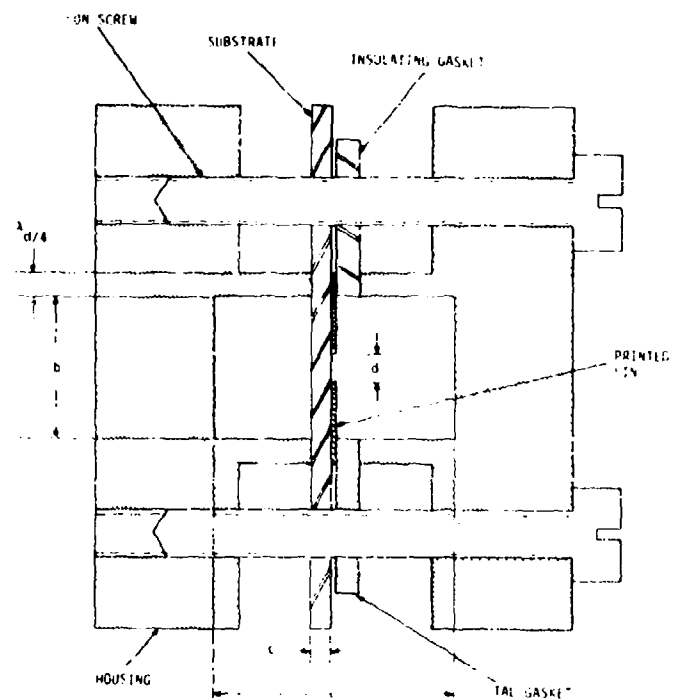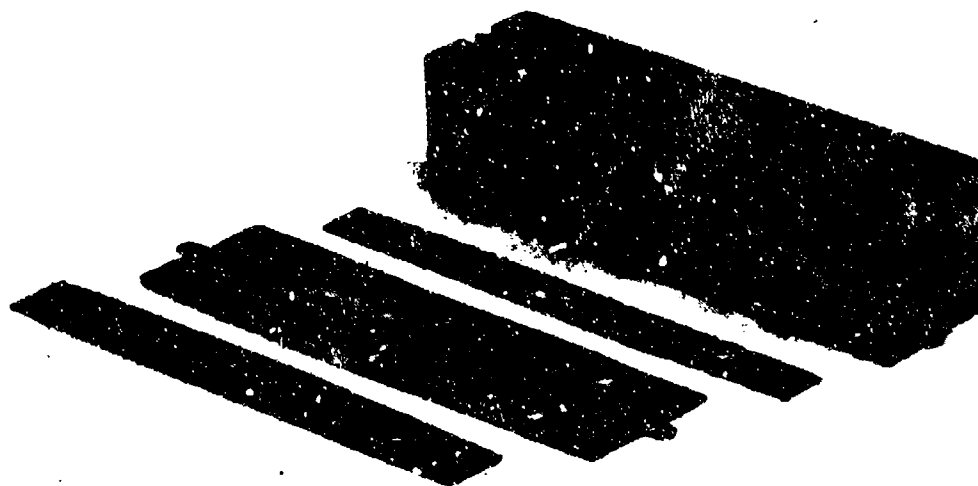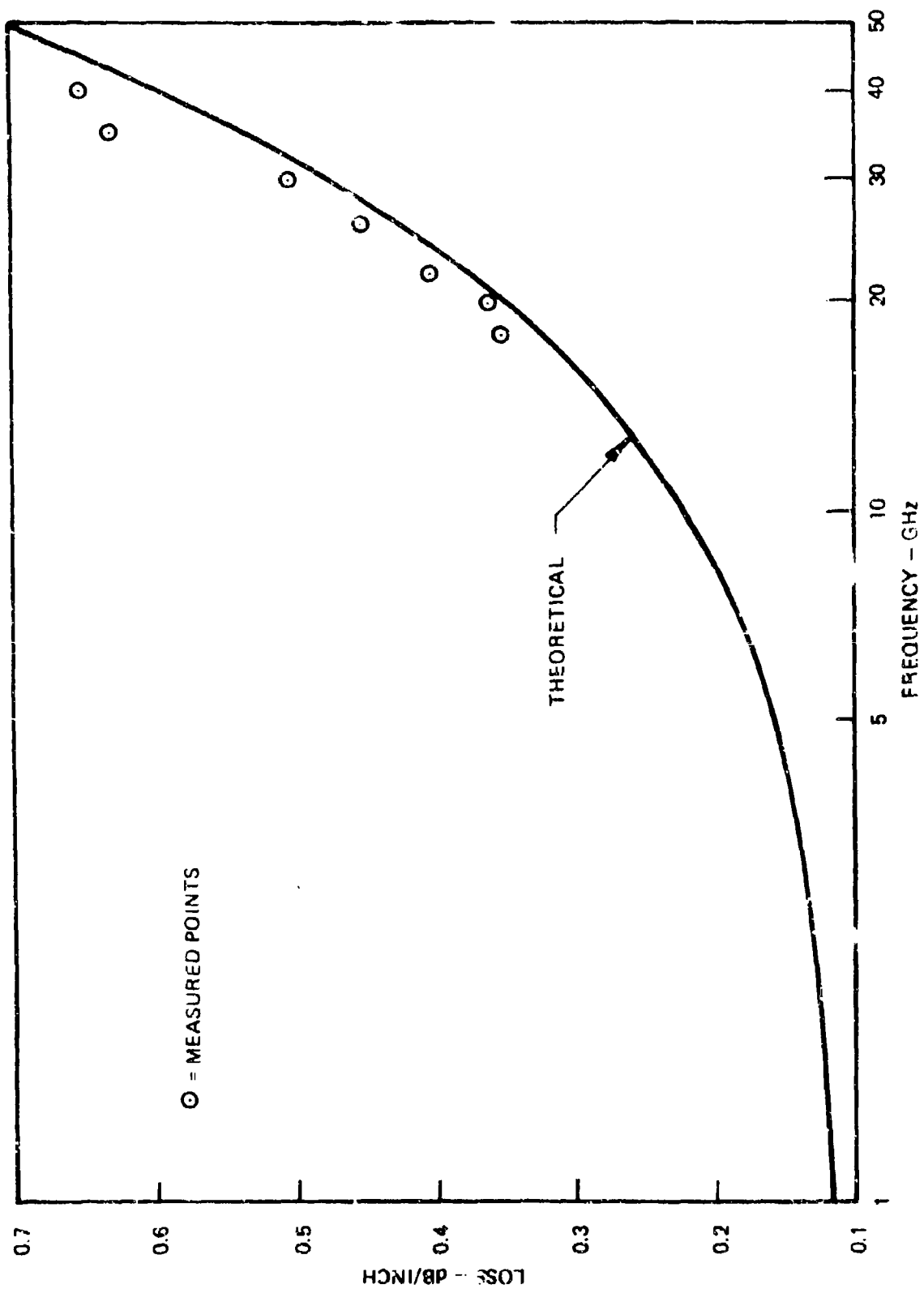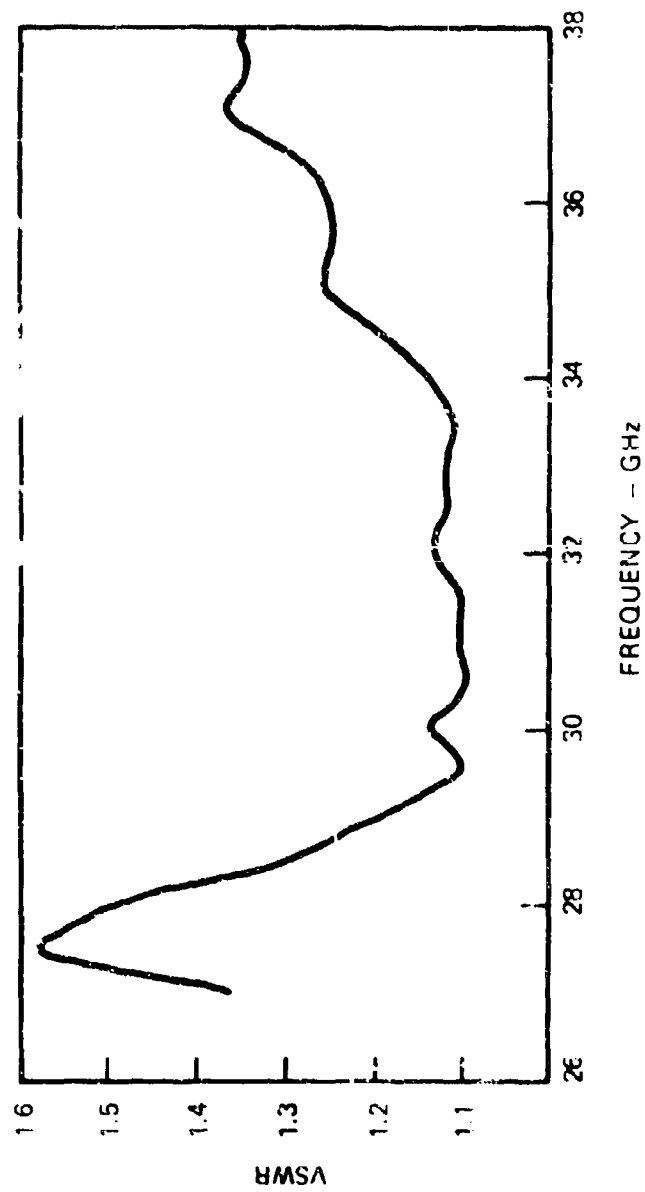
WR-28 WAVEGUIDE TO SUSPENDED SUBSTRATE LINE – PERFORMANCE

FIGURE 4.
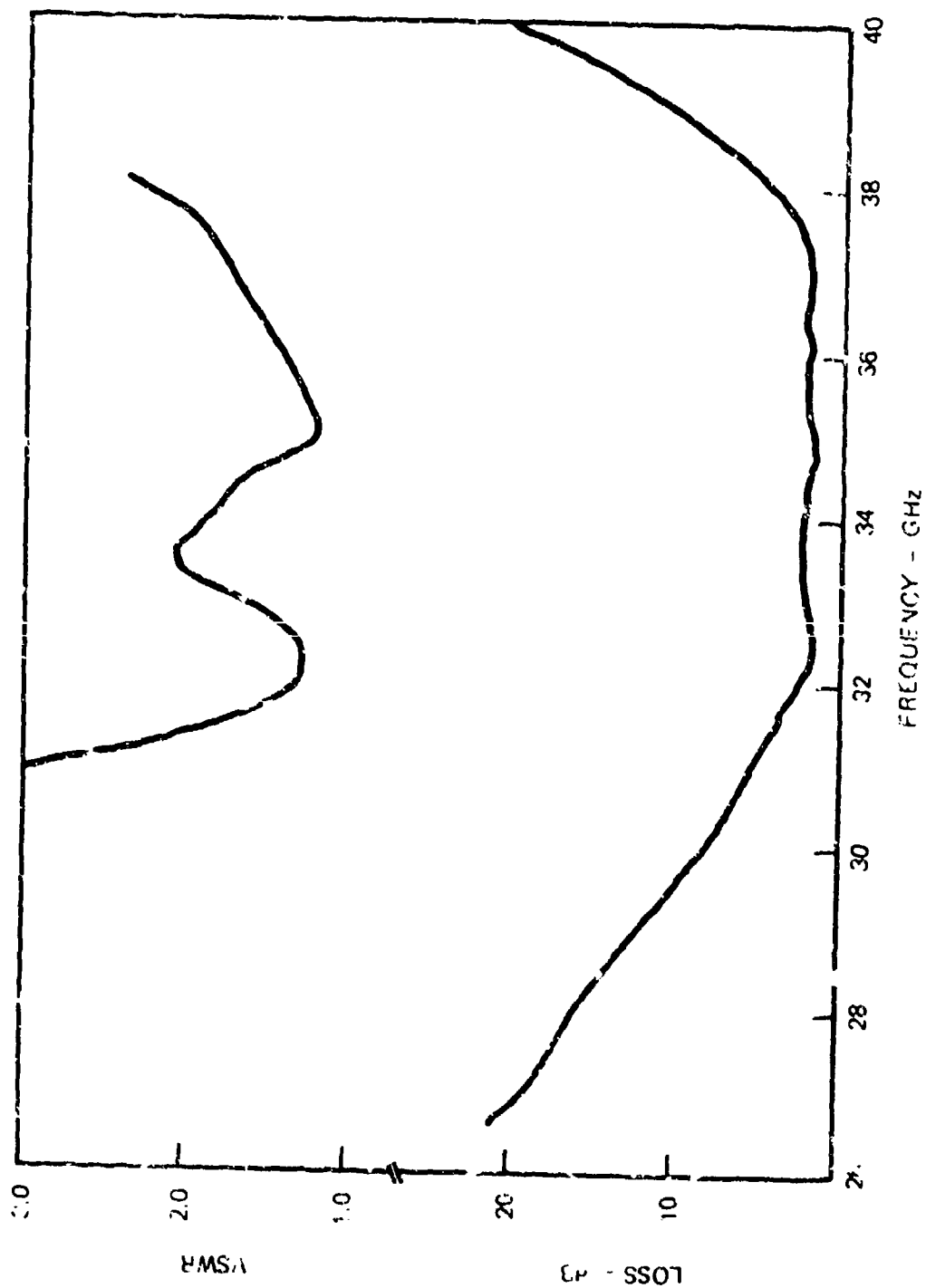
D-12316

FIGURE 5
BANDPASS FILTER RESPONSE

FREQUENCY – GHz

VSWR

LOSS – dB

D.12313

A quarter-wavelength side-coupled directional coupler was also fabricated in suspended substrate line to serve as a BIT input coupler. it demonstrated a flatness of ± 1.0 dB across the band and a VSWR contribution of typically less than 1.5 across the band. More significant to the development of the down-converter was a three-section branch-arm 90° hybrid. Although the bandwidth required for this program would normally indicate a two-arm hybrid, the advantages gained by the three-arm hybrid in terms of reduced interface capacity due to higher impedance branches was considered to be a significant advantage, and thus the more complicated design was used. The performance of this circuit was shown in the curves of Figure 6. This hybrid was then integrated with an open-circuit stub band reject filter which provided the necessary RF blocking for the diode configuration of the balanced mixer. The diodes chosen were specially selected low-capacity (0.07 pF) glass passivated beam lead Schottky diodes which were mounted on the substrates by thermal compression bonding techniques between the output arms of the 90° hybrid and the input of the bandstop filter assembly. External filter bias points were provided in order to permit individual diode monitoring, and/or dc bias.

4. INTEGRATED RECEIVER

All of the above circuit functions plus a waveguide Gunn oscillator and a microstrip image rejection mixer assembly were integrated in a final down-converter in accordance with the block diagram shown in Figure 7. The bandpass filter, directional coupler and balanced mixer along with the appropriate transitions and bias filtering was included in a single suspended substrate chassis. This is shown in the photograph of Figure 8. The Gunn oscillator was directly coupled to the substrate by means of the cavity to the suspended substrate transition and the output was fed through a 4.0 to 8.0 GHz preamplifier into an image rejection mixer assembly.

Figure 9 shows the overall finished assembly with all of these components. The measured electrical performance of the receiver showed good compliance with the program goals. A 4.0 GHz bandwidth was achieved with an IF bandwidth operating from 4.0 - 8.0 GHz in the first converter and at 60 MHz in the second converter. The conversion loss from 32.0 to 36.0 GHz to C-band is shown in Figure 10 and is typically 14.0 to 15.0 dB across the band with a maximum conversion loss of 18.0 dB occurring at 34.0 GHz. This measurement does not include any IF amplifier gain. This would permit a worst case tangential sensitivity of -76 dBm with a 20 MHz IF bandwidth. The 1 dB compression point occurs at approximately -5 dBm, thus permitting 70 dB dynamic range. Although provisions were made for dc biasing the diode it was found, in practice, that this was not necessary and that a common dc return between the two diodes could be used. The MTBF of the entire assembly, including the amplifier and image rejection mixer subassemblies, was calculated in accordance with MIL-STD-217A. The MTBF calculated for the assembly was 22,345 hours.
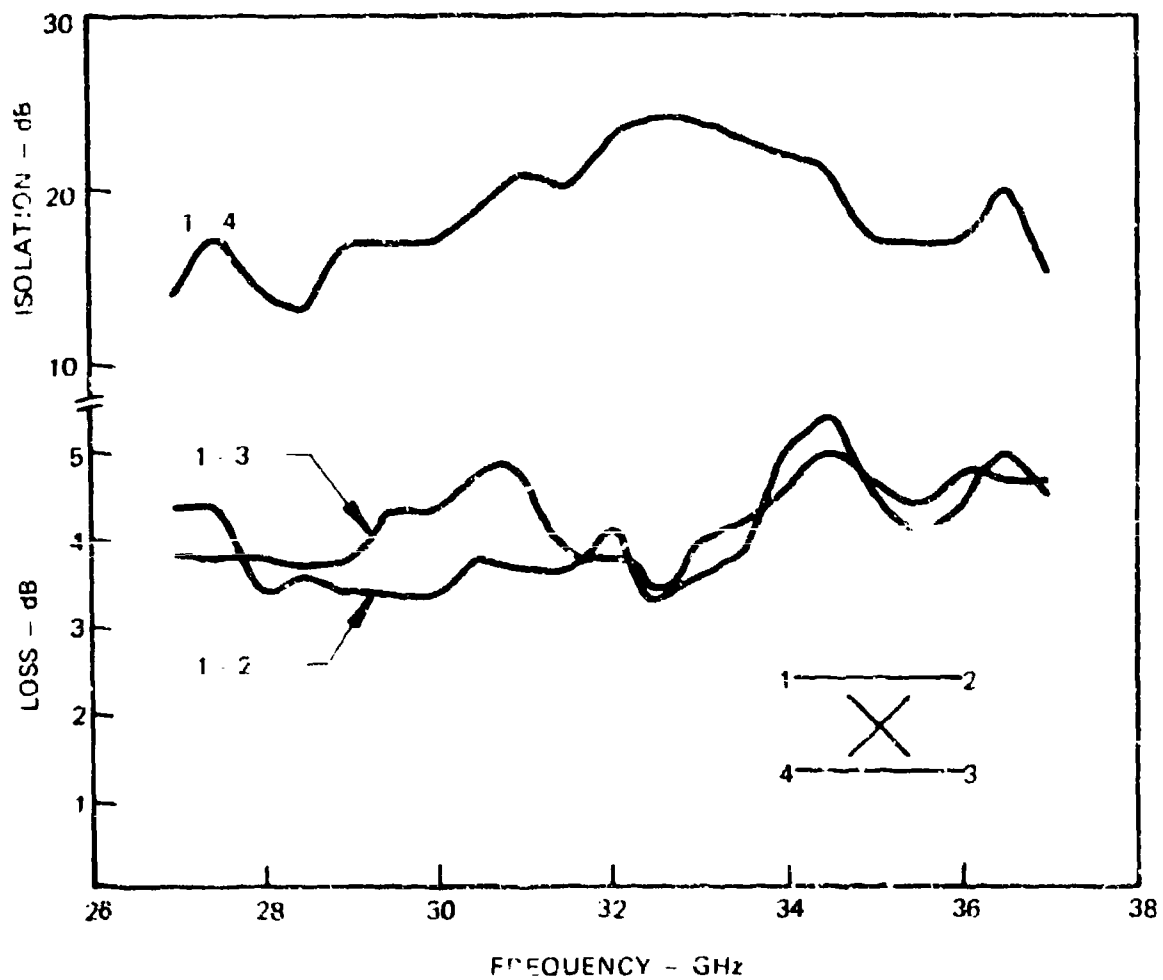
FIGURE 6

SUSPENDED SUBSTRATE HYBRID PERFORMANCE
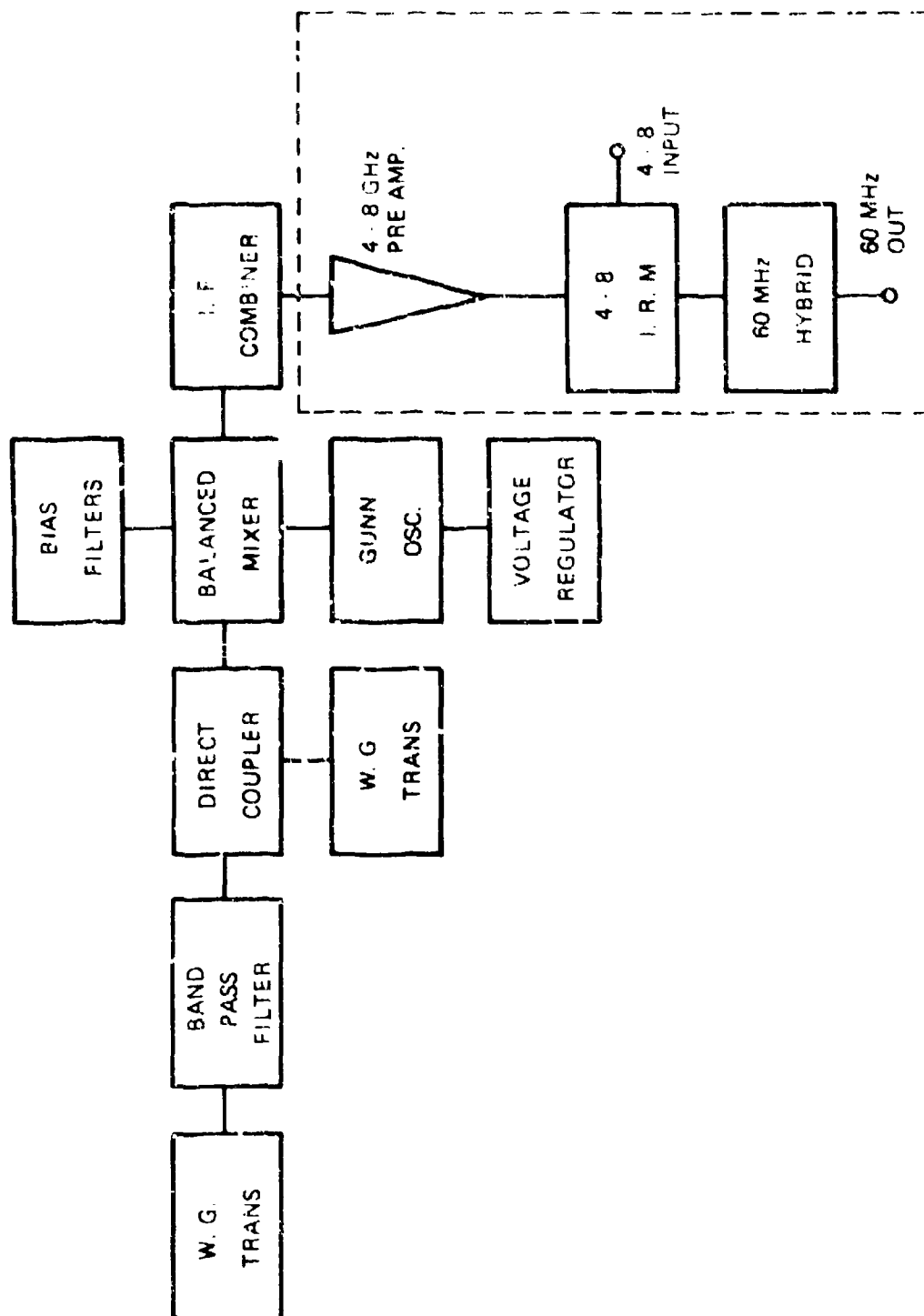
FIGURE 7   32 GHz – 36 GHz BLOCK DIAGRAM
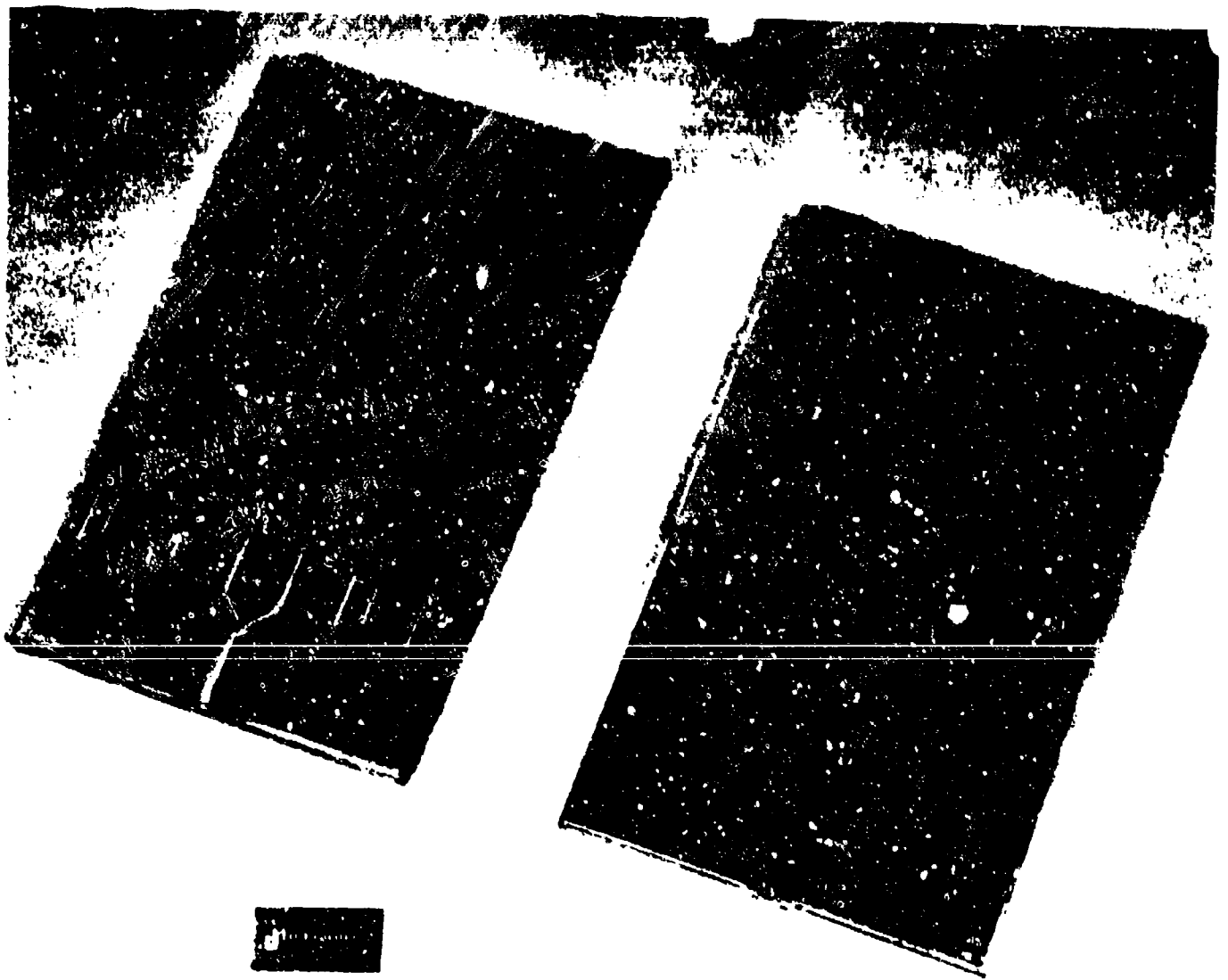
FIGURE 8   32 GHz TO 36 GHz INTEGRATED CONVERTOR CHASSIS AND CIRCUIT
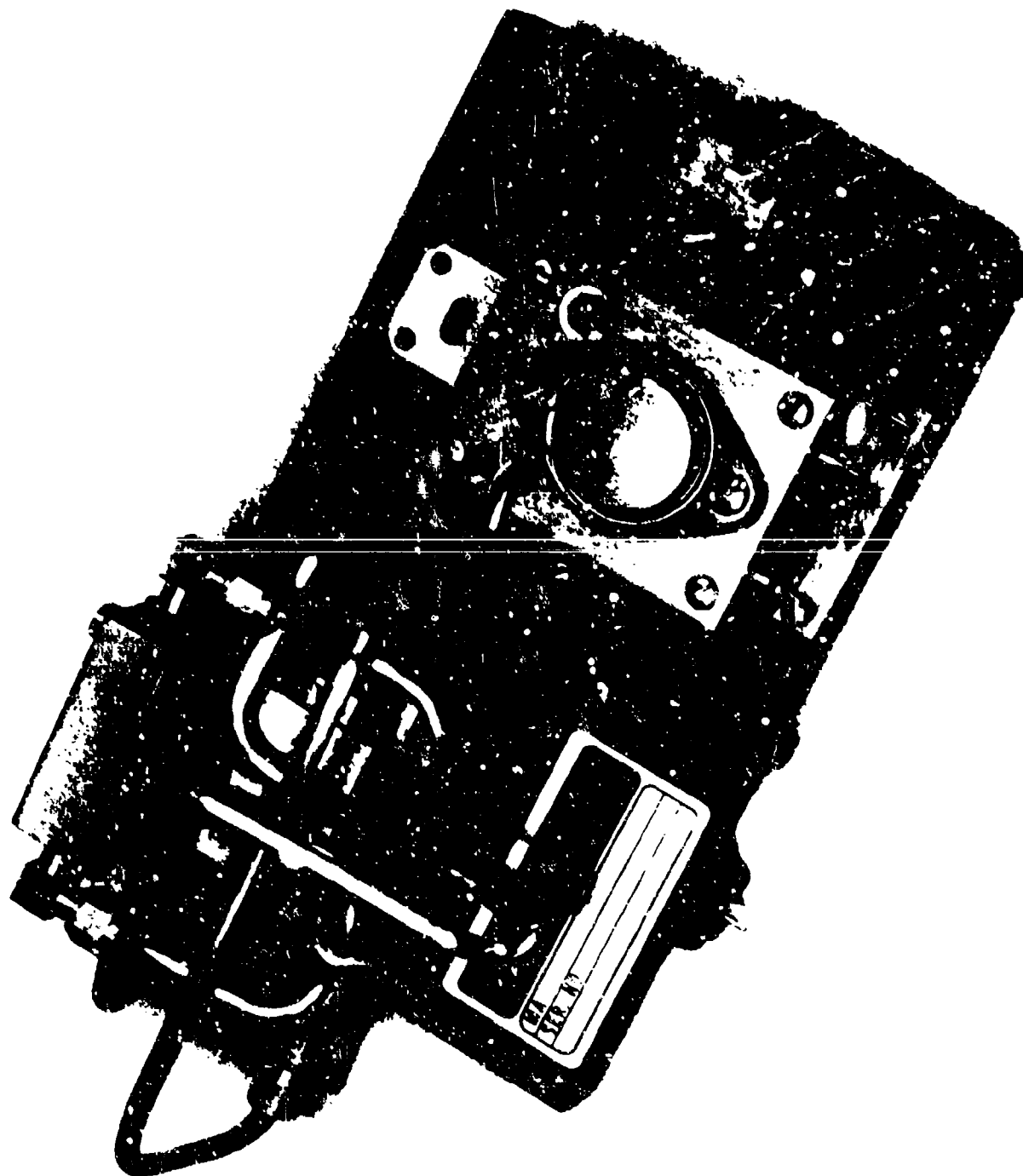
FIGURE 9   FINISHED INTERGRATED DOWN CONVERTOR
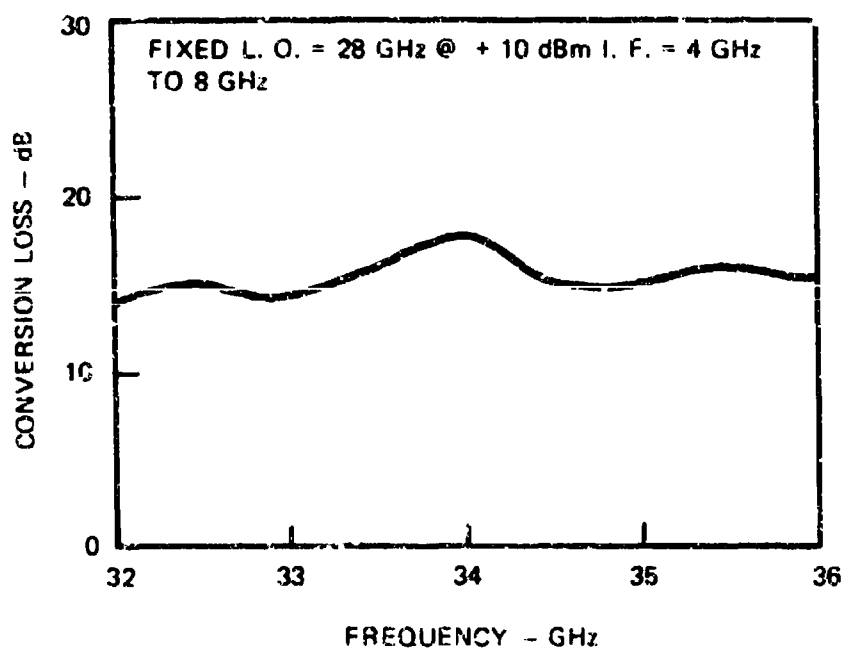
FIGURE 10 SYSTEM CONVERSION LOSS

5. ACKNOWLEDGEMENT

WIDEBAND MICROSTRIP COMPONENTS
AND THE IFM DISCRIMINATOR

by
D. L. Saul
Naval Electronics Laboratory Center
San Diego, California 92152

INTRODUCTION

This paper describes progress at NELC in the development of microwave integrated circuits and components for use in the lower ehf region. This work has been accomplished as part of a continuing MIC development effort under NELC's Independent Research and Independent Exploratory Development Program. The frequency region of interest under this portion of the Program extends from 20 to 110 GHz, although the results included here are based on work in the 26.5–40-GHz band.

One of the primary objectives of this effort has been development of components suitable for use in surveillance receivers. Of particular interest have been receivers of the instantaneous frequency measuring (IFM) type. To this end, a discriminator of a type suitable for IFM receiver use has been built in microstrip. This unit operates over the full 26.5–40-GHz band.

A number of individual components have been developed, including power splitters, 90° and 180° hybrid junctions of the branched-arm coupler and reverse-phase hybrid ring types, respectively, and waveguide-to-microstrip transitions.

THE CIRCUIT MEDIUM

Microstrip line fabricated on an irradiated polyolefin dielectric substrate offers certain advantages for applications in the subject frequency range. This material's low relative permittivity ($\varepsilon_r \approx 2.3$) allows circuits and components to be fabricated which are neither unreasonably small nor subject to dimensional constraints that might lead to extreme fabrication difficulties. The material is relatively inexpensive and easily obtained. In the form selected for this work, the dielectric material contains no woven fibers or other mechanical reinforcement. The dielectric is modified in its molecular structure during manufacture by means of an irradiating process claimed by the vendor to improve temperature behavior and mechanical stability. The resulting product is reportedly able to tolerate a much wider range of environmental conditions than unmodified polyolefin dielectrics.

No quantitative information is yet available regarding the loss tangent of this material at millimeter wavelengths. Experimental data gathered on microstrip line attenuation at frequencies up to 40 GHz suggest, however, that the loss tangent remains reasonably low at frequencies well above the conventional microwave bands. Data supplied by the manufacturer indicate a value of

$$\tan \delta = 2.7 \times 10^{-4}$$

based on a measurement performed at 9.47 GHz using a resonant cavity and cavity perturbation technique.

The dielectric used for this work is 0.010 inch thick, and is obtained in sheets with copper foil of 0.0014 inch thickness bonded to both sides. Circuits are made by a conventional photofabrication process. Photoresist is applied by spinning, and, after exposure and developing, excess copper is etched away by a solution of ferric chloride.

The copper foil is somewhat thicker than would be most favorable for work involving close dimensional tolerances. Maintaining accurate line width and circuit dimensions can be difficult because of the tendency of the etchant to undercut the exposed edges of conductors. The problem does not turn out to be as severe, however, as first appearances might suggest. Experience has shown that the width of microstrip lines can be maintained to within a mil or better if reasonable care is exercised throughout each step of fabrication.

A line width of 0.024 inch was adopted for microstrip line to give a characteristic impedance of 60 ohms.

TRANSITIONS

Since virtually all test equipment for use in the millimeter region is equipped with rectangular waveguide connections, it was necessary to fabricate waveguide-to-microstrip transitions. Since wideband operation was desired, a design utilizing a short length of rectangular waveguide containing a ridgeline transformer section was determined to be most suitable. Various examples were fabricated using Tchebycheff transformers with steps placed $\lambda/4$ apart, and others were made using smoothly tapered transformer sections. Figure 1(a) illustrates the construction of a unit with several $\lambda/4$ steps. The design found to be best suited for laboratory work, however, incorporates a ridgeline transformer section in which ridge height varies as the cosine function over the interval 0 to π. The length of the section is 1.4 inches. This design is illustrated in figure 1(b). A tab not shown in the illustration is provided at point A to connect the ridgeline to the microstrip. The lower wall of the waveguide extends outward slightly to facilitate connection to the groundplane on the substrate's under side. The corners of the ridge at the open end of the waveguide are chamfered to reduce the effect of capacitive discontinuity in the region of the point of contact.

In the final design, a small, cavity-like structure was installed at the open end of the waveguide after direct signal radiation was found to be occurring. This radiation, manifesting itself in the form of excessive transmission loss of as much as 1 dB near the upper end of the band, was observed to be coming from the vicinity of the point at which the microstrip line was connected to the transition. The radiation's physical mechanism remains under investigation, although a practical means of suppressing it has been devised. Excitation of one or more spurious surface wave modes may be responsible.

By way of performance, the measured VSWR of a pair of transitions and a 1-inch length of microstrip line is typically less than 1.2:1 over the full 26.5-49-GHz band. Each transition is observed to have an insertion loss of about 0.35 dB. The microstrip line itself exhibits a loss of about 0.31 dB per inch at 26.5 GHz, increasing gradually to about 0.46 dB per inch at 40 GHz.

THE DISCRIMINATOR

A discriminator of the type used for IFM receiver applications may be referred to as an instantaneous frequency discriminator (IFD), a term which serves to distinguish it from other types of discriminators such as those used for FM signal demodulation.[1]

In terms of practical application, the IFD's purpose is to respond to an input rf signal in such a way that the input signal's frequency and power level can be communicated to operator personnel in the form of a visual polar display. In such a display, the angle of a radial strobe has a one-to-one correspondence with a given input signal's frequency, and the length of the strobe's radius vector is proportional to the input signal's power level. Use of a single IFD to cover a very wide band of frequencies is often desirable from a practical standpoint, and capability to operate over a 3:2 band of frequencies is considered a reasonable goal for coverage in the subject frequency region.

Figure 2 shows the discriminator circuit in schematic form, and figure 3 shows the microstrip circuit layout. The circuit utilizes four hybrids of the reverse-phase ring type and one of the branched-arm coupler type. It will be noted that this circuit exploits the phase properties of the 180° and 90° hybrids in such a way that no separate phase shifter is needed to obtain the quadrature outputs necessary to produce a polar display of the type mentioned previously.

The IFD circuit's operation is best described mathematically. For the sake of convenience and simplicity, a convention is adopted such that phase delays along various signal paths of equal electrical lengths are omitted from the mathematical representations of signals, since these phase delays are arbitrary in nature and have no direct bearing on principles of circuit operation. The figures of merit of the detectors are also omitted for similar reasons.

Numbered and lettered references in the following discussion apply to figure 2.

The input signal V_i at point 1 can be expressed as

$$V_i = E_0(t) \cos \omega t$$

in which $E_0(t)$ is an arbitrary amplitude modulating function, ω is the radian frequency of the rf input signal, and t is time. Hybrid H_1 is connected to function as a power divider. Lines L_1 and L_2 are of unequal electrical lengths such that

$$L_2 - L_1 \quad \Delta L \neq 0 \quad .$$

The signals applied to H_2 and H_3 following the power split of H_1 can thus be represented as

$$\frac{E_0(t)}{\sqrt{2}} \cos (\omega t - \beta L_1)$$

and

$$\frac{E_0(t)}{\sqrt{2}} \cos (\omega t - \beta L_2) \quad .$$

respectively, with phase constant β defined as the rate of change of phase with respect to distance along a transmission line for fixed values of time. The value of β is given by

$$\beta = \frac{2\pi}{\lambda} \quad .$$

in which λ is wavelength.

Hybrids H_2 and H_3 are also connected to function as power dividers. Lines L_3, L_4, L_5, and L_6 all have equal electrical lengths. The outputs of H_2 and H_3 at the indicated reference points can thus be expressed as follows:

At point 4
At point 5 $\}$ $\dfrac{E_0(t)}{2} \cos(\omega t - \beta L_1)$.

At point 6
At point 7 $\}$ $\dfrac{E_0(t)}{2} \cos(\omega t - \beta L_2)$.

The purpose of hybrid H_4 is to recombine the signals passing along lines L_3 and L_5 from points 4 and 6. Since H_4 is a $180°$ hybrid, signals at points 8 and 9 can be represented by the following:

At point 8, $\dfrac{E_0(t)}{2\sqrt{2}} \cos(\omega t - \beta L_1) + \cos(\omega t - \beta L_2)$.

At point 9, $\dfrac{E_0(t)}{2\sqrt{2}} \cos(\omega t - \beta L_1) - \cos(\omega t - \beta L_2)$.

Using the trigonometric identity

$$\cos X + \cos Y = 2 \cos \tfrac{1}{2}(X + Y) \cos \tfrac{1}{2}(X - Y) \quad ,$$

the signal at point 8 may be expressed as

$$\dfrac{E_0(t)}{\sqrt{2}} \left\{ \cos[\omega t - \tfrac{1}{2}\beta(L_1 + L_2)] \right\} \cos \tfrac{1}{2}\beta \, \Delta L \quad .$$

Assuming square-law detection, the signal at point 12 is found to be

$$\dfrac{E_0^2(t)}{2} \cos^2 \tfrac{1}{2}(\beta\Delta L) \quad .$$

Using the trigonometric identity

$$\cos X - \cos Y = -2 \sin \tfrac{1}{2}(X + Y) \sin \tfrac{1}{2}(X - Y)$$

the signal at point 9 can be expressed as

$$\dfrac{E_0(t)}{\sqrt{2}} \left\{ \sin[\omega t - \tfrac{1}{2}\beta(L_1 + L_2)] \right\} \sin \tfrac{1}{2}(\beta\Delta L) \quad .$$

which, after square-law detection, yields

$$\dfrac{E_0^2(t)}{2} \sin^2 \tfrac{1}{2}(\beta\Delta L)$$

at point 13. Taking the difference of the detected signals at points 12 and 13 by means of differential amplifier A_1 and applying trigonometric identity

$$\cos^2 X - \sin^2 X = \cos 2X \quad .$$

it is found that Output A, at point 16, is

$$\text{Output A} = \frac{E_0^2(t)}{2} \cos \beta \Delta L \quad .$$

Since β has an approximately linear rf frequency dependence, Output A undergoes a cosine variation as the discriminator's input signal is varied in frequency. Note also that the output varies as the square of modulation amplitude and hence as the power level of the input signal.

Hybrid H_5 serves to recombine signals passing from points 5 and 7 along lines L_4 and L_6, respectively. By a mathematical process similar to the foregoing, output B at point 17 can be shown to be

$$\frac{E_0^2(t)}{2} \sin \beta \Delta L \quad .$$

thus providing the remaining member of a pair of quadrature outputs needed for the polar display.

The angle θ of the polar strobe is given by

$$\theta = \beta \Delta L \quad .$$

It is generally desirable to limit the angular variations of θ to a maximum of $360°$ to avoid ambiguity. For a frequency range of ω_1 to ω_2, this requires that

$$\frac{\Delta L}{V_0} (\omega_2 - \omega_1) \leqslant 2\pi \quad .$$

in which V_0 is propagation velocity in the transmission lines.

CONFIGURATION AND PERFORMANCE

For purposes of laboratory evaluation, the microstrip discriminator has initially been equipped with waveguide-mounted wideband detectors. This configuration is illustrated in figure 4. Future plans call for detectors to be mounted in hybrid IC form directly on the substrate.

Preliminary performance data are contained in figures 5 and 6. Figure 5 shows a polar plot of a frequency sweep from 26.5 to 40 GHz, with a marker each 0.5 GHz. Figure 6 is a plot of linearity, which shows a maximum deviation of about $\pm 20°$ from an ideal straight line. The preliminary nature of these performance data is again emphasized, and it should be noted that the discriminator is still under development. The information contained in figures 5 and 6 was, in fact, obtained approximately 2 weeks after the discriminator's first operation in the laboratory.

DISCRIMINATOR COMPONENTS

The reverse-phase hybrid ring has been used in various forms at lower frequencies for many years. In such a hybrid ring, wideband performance is obtained by replacing the conventional hybrid ring's $3\lambda/4$ arm with a $\lambda/4$ arm, including a frequency-insensitive reversal of phase.[2] In microstrip, this can be accomplished by fabricating a ring structure with four $\lambda/4$ arms and installing a "twist" in one of the arms for the purpose of phase reversal. The twist consists of a short length of parallel-plate line which is physically twisted to invert the ends of the line. It has been found that microstrip line can be tapered off in a very short distance to form parallel-plate line for the purpose of making the required twist. The phase reversal can thus be introduced without serious loss of performance. This technique was developed J. Keindel of NELC.

Performance of the 26.5–40-GHz reverse-phase hybrid ring is quite good over the entire band, and probably beyond. Octave bandwidths have been achieved at lower frequencies with hybrids of similar design. Hybrids of the type used in the discriminator have been found to provide isolation of 20 dB or better throughout the band while maintaining a uniformity of power split within 1 dB. Input VSW is typically less than 1.3:1 throughout the band with three ports terminated in their characteristic impedance.

The branched-arm coupler used in the present discriminator circuit has considerably less bandwidth capability than the reverse-phase hybrid rings. Although a reasonably good power split is obtainable with such a unit over a full waveguide band, the VSWR increases rather sharply near the band edges. Linearity of the discriminator would probably be improved if a better wideband $90°$ hybrid could be placed in the circuit. A hybrid utilizing a coupled-line structure might offer improvement if fabrication difficulties could be overcome.

REFERENCES

1. Wiley, R. G., and Williams, E. M., "Spectrum Display I, Instantaneous," *Microwaves*, August 1970, p. 44–47.

2. Tyminski, W. V., and Hylas, A. E. "A Wide-Band Hybrid Ring for UHF," *Proceedings of the IRE*, January 1953, p. 81–87
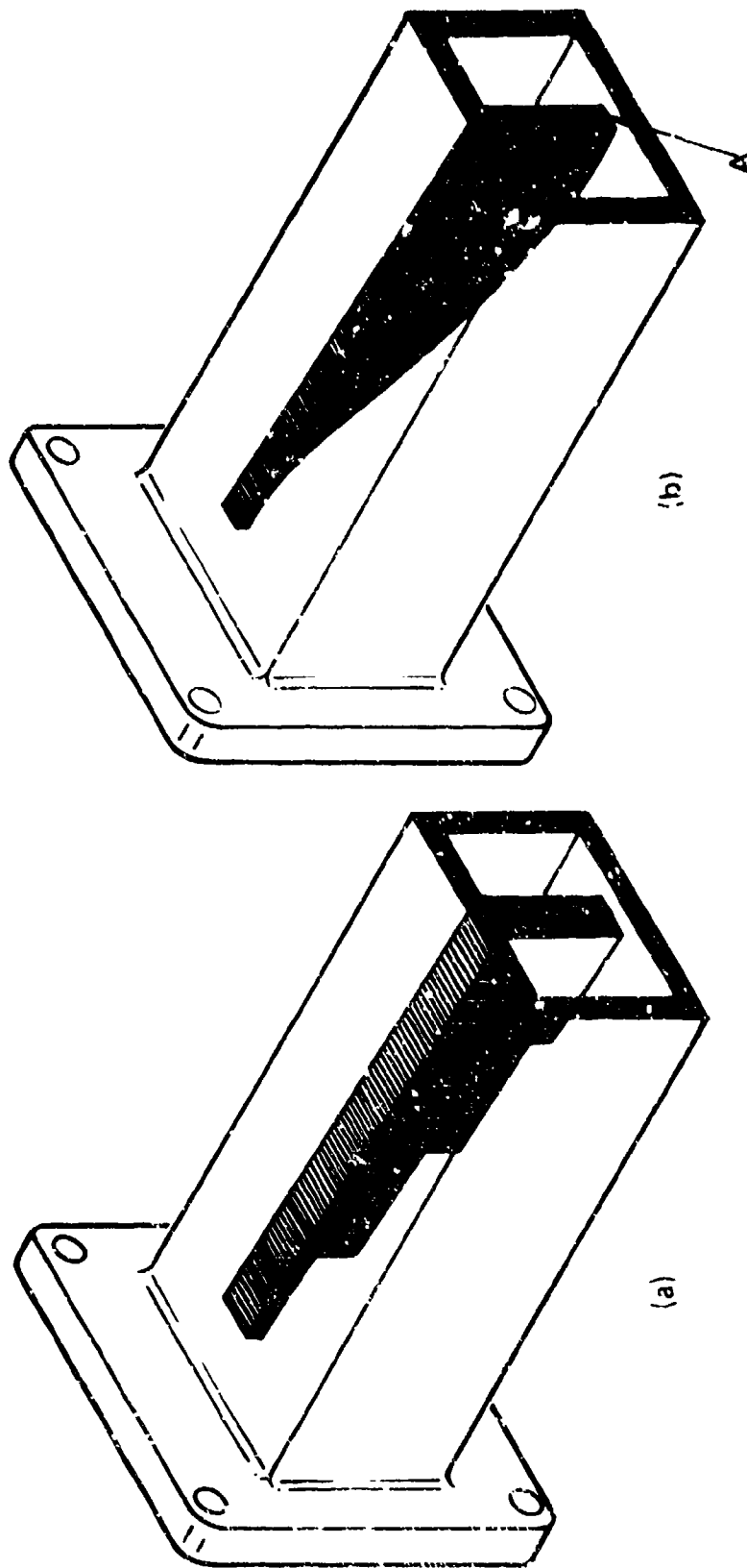
Figure 1. Waveguide-to-microstrip transitions.

(a)

(b)

A
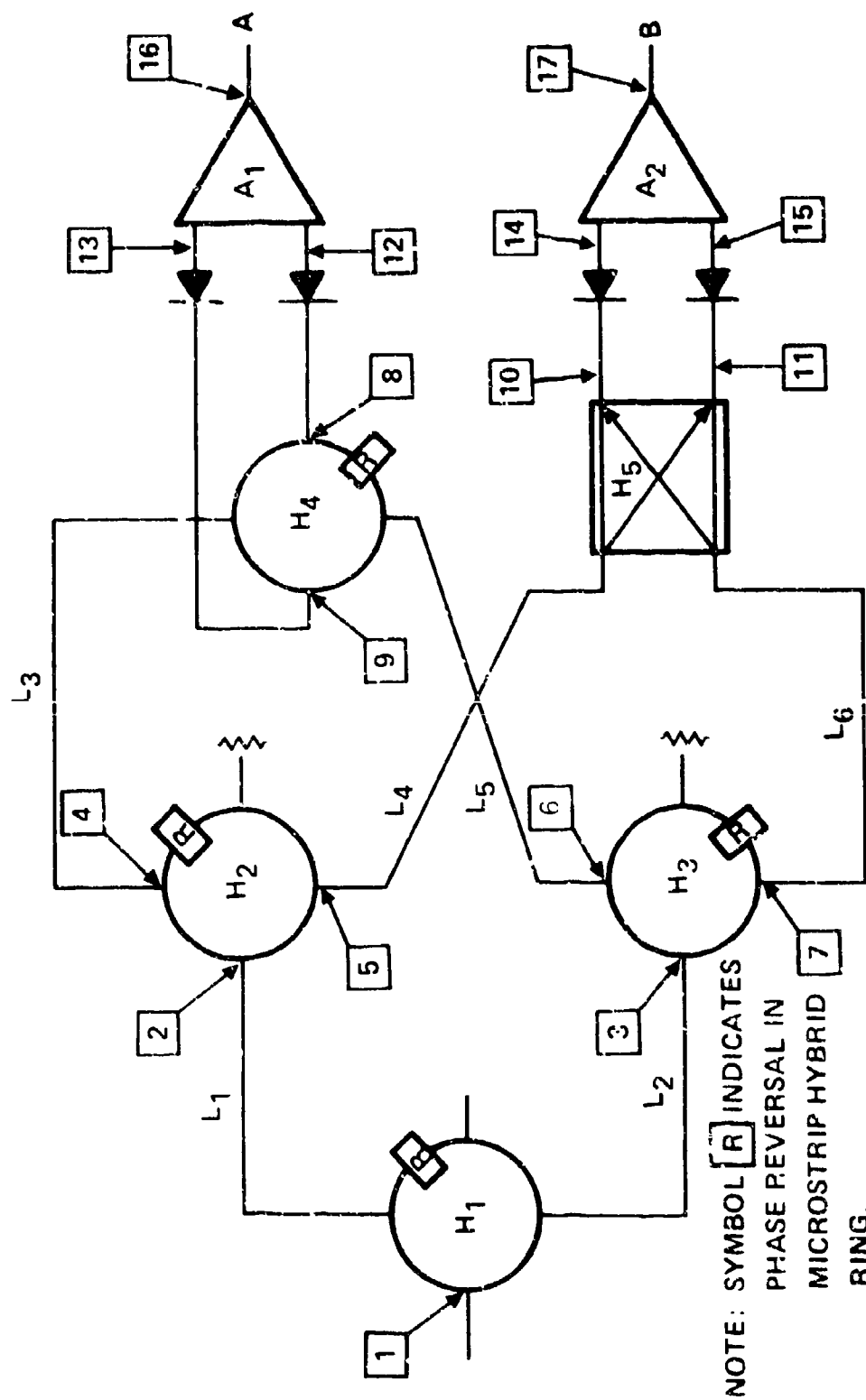
Figure 2. Schematic diagram of discriminator.

NOTE: SYMBOL [R] INDICATES
PHASE REVERSAL IN
MICROSTRIP HYBRID
RING.
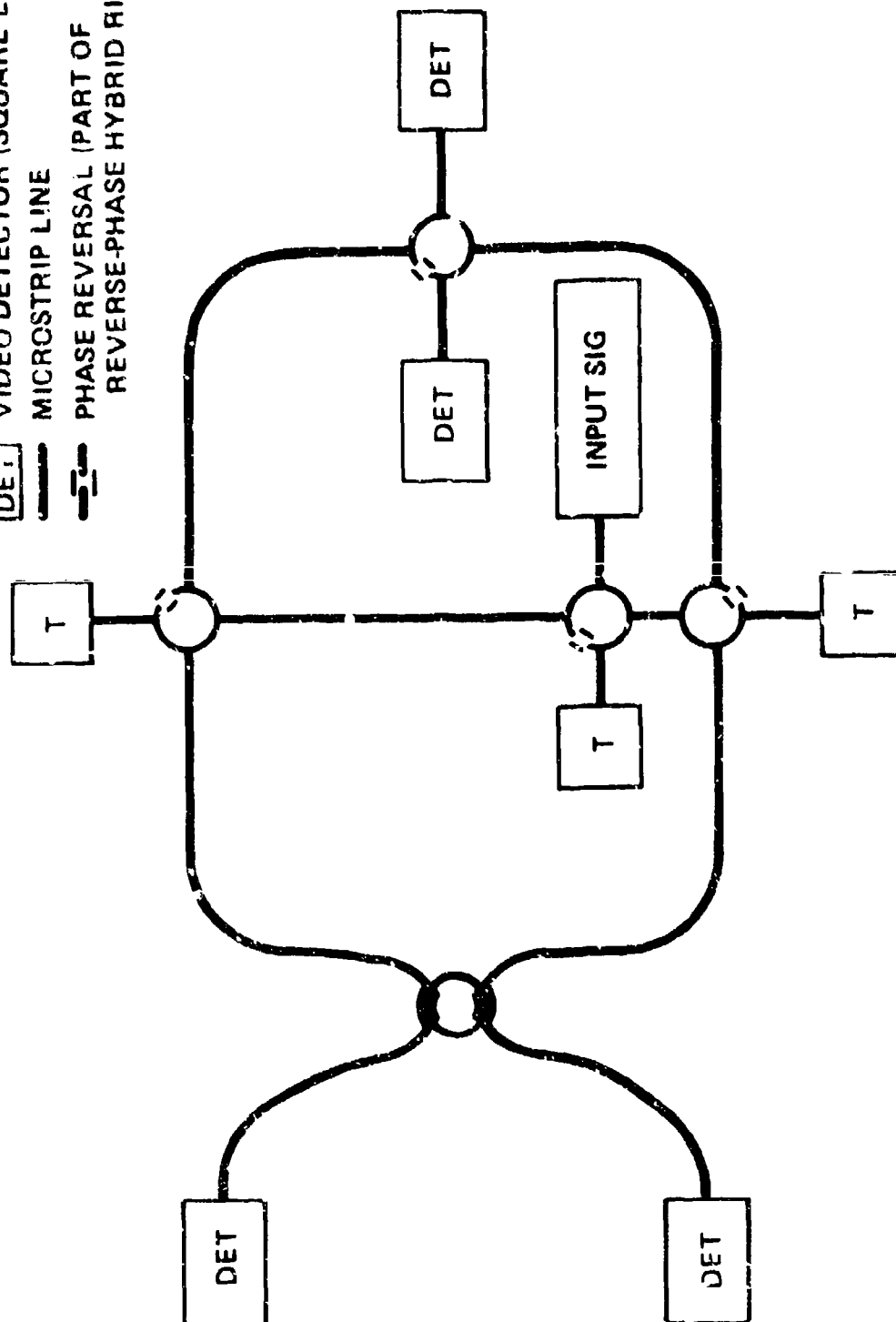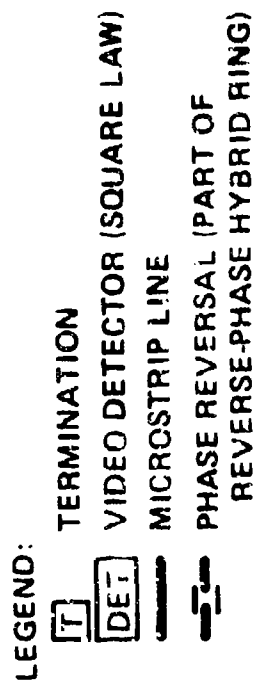
Figure 3. Microstrip circuit layout.

LEGEND:

[T] TERMINATION
[DET] VIDEO DETECTOR (SQUARE LAW)
— MICROSTRIP LINE
↗↘ PHASE REVERSAL (PART OF REVERSE-PHASE HYBRID RING)

D4-9

Figure 4. Microst... discriminator.

40 GHz

26.5 GHz
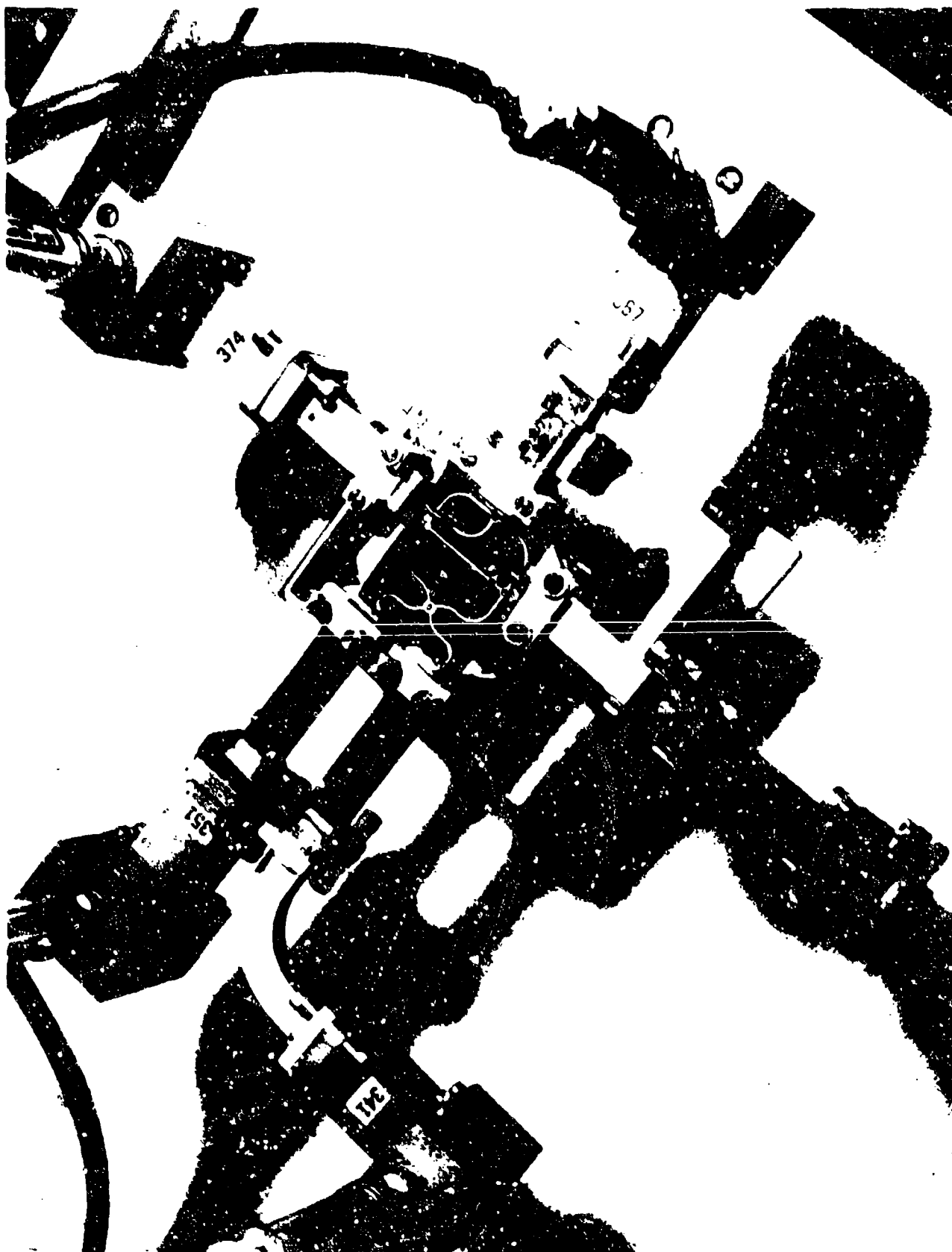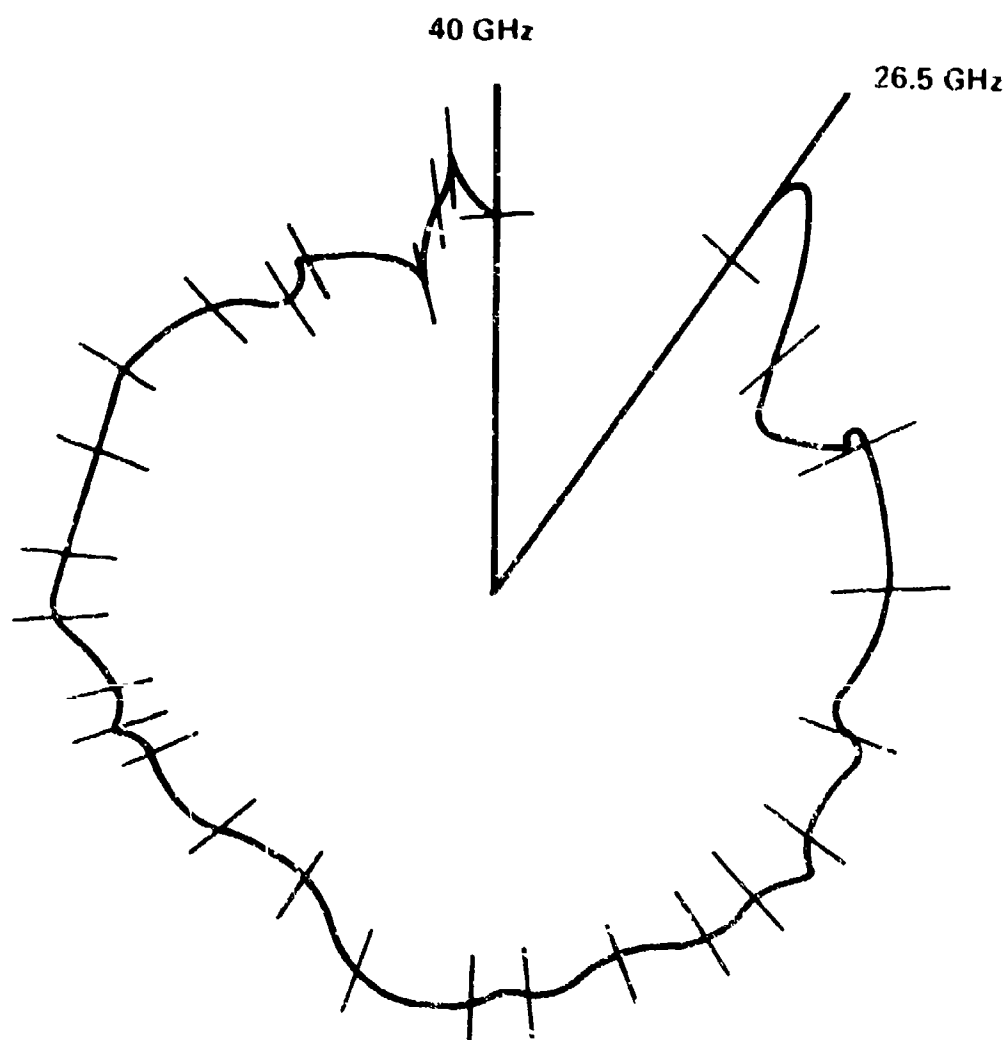
Figure 5. Polar plot of frequency.
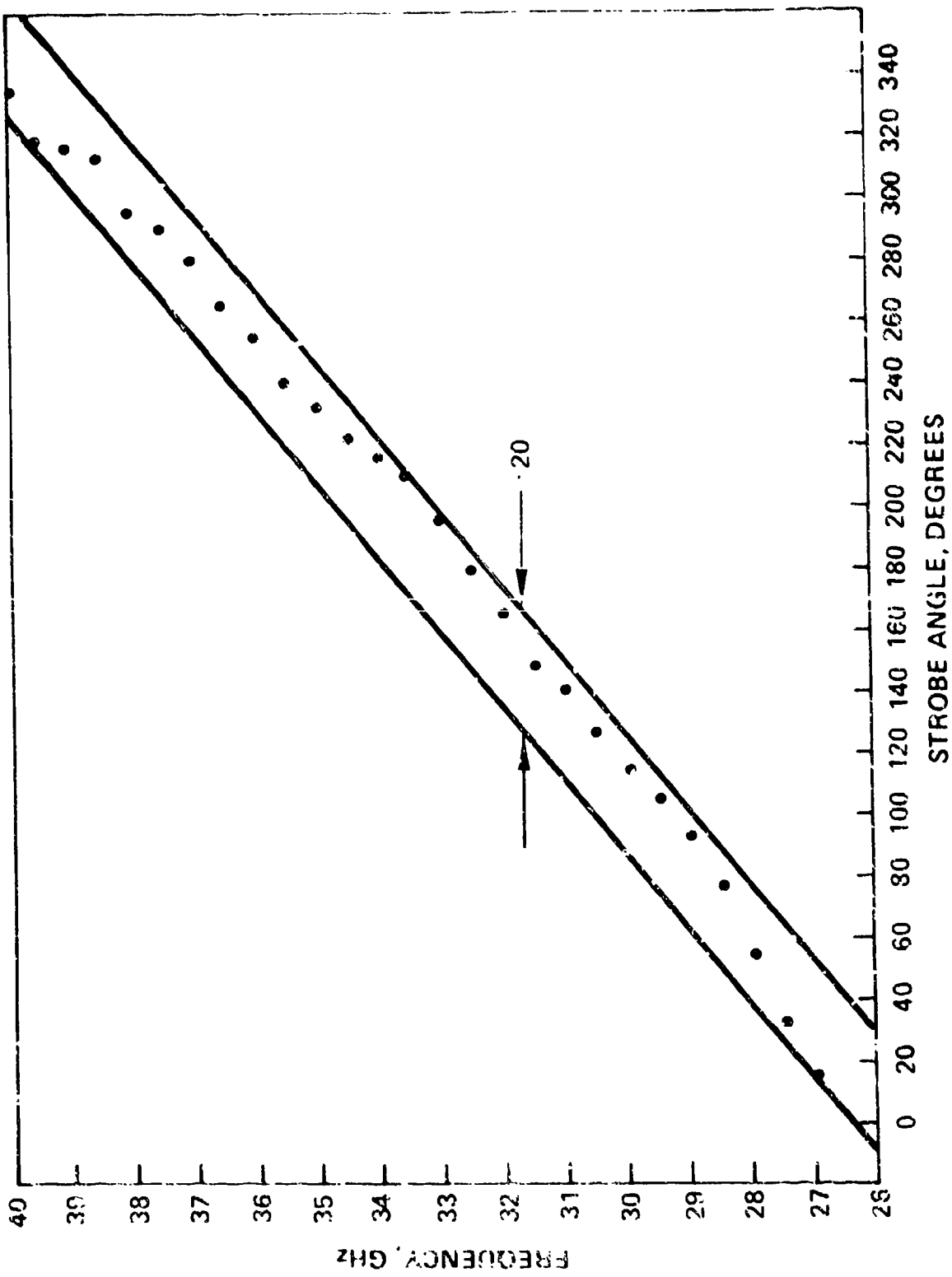
Figure 6. Discriminator linearity.

FREQUENCY, GHz

STROBE ANGLE, DEGREES

MILLIMETER WAVE SOLID STATE

RECEIVER AND TRANSMITTER COMPONENT DEVELOPMENT

by

J. E. Raue, F. J. Bayuk, A. I. Ohashi and L. T. Yuan

TRW Systems
Redondo Beach, CA 90278

INTRODUCTION

Increasing interest by the military in the EHF band, particularly in the 35 to 40 GHz and 55 to 65 GHz bands, both for communications and electronic warfare applications, in high performance systems and subsystems underscores the need for developing critical component technology in these frequency bands. These include transmitter components such as solid state amplifiers, power combining techniques, upconverters and frequency sources, as well as receiver components such as mixers and LO sources. In addition, supporting components such as filters, hybrids, circulators, switches, etc., are of interest.

TRW's development emphasis has been on high performance, broadband components. These state-of-the-art millimeter wave components have been generally designed for wideband operation in order to provide maximum flexibility for applications (spread spectrum communications, frequency hopping radars, high data rate analog and digital systems, broadband radiometers) and · operate over a temperature range.

TRANSMITTER COMPONENTS

State-of-the-art performance of several key transmitter components is described.

Broadband Varactor Doubler/Upconverter

This component was designed as an upper sideband doubler/upconverter capable of efficiently upconverting a 2 GHz wide S-band signal to Ka-band. This unit represents two components, a frequency doubler and an upconverter combined into one - using a Ku-band pump (at approximately 17.5 GHz) an S-band signal (2 to 4 GHz) is upconverted to a Ka-band output at 37-39 GHz.

This component is shown in Figure 1. The three ports, waveguide output and pump, as well as the coaxial IF input port, are clearly visible. This unit exhibits a 1 dB bandwidth over 2 GHz, with an IF to RF conversion loss of less than 3 dB and an RF conversion efficiency of 12 dB, including isolator and filter losses. The RF output power is 5 mW.
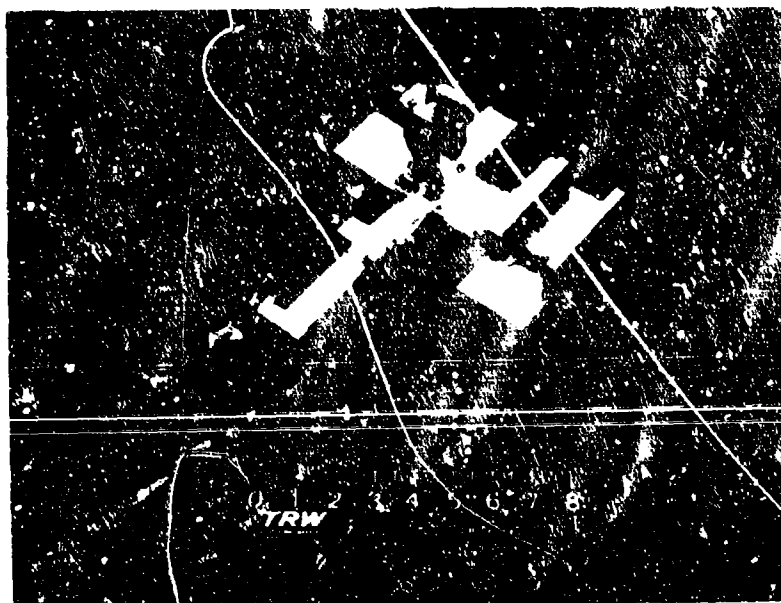
Figure 1. S-to-Ka-Band Upconverter with 2 GHz of Bandwidth.

Low Q Ka-Band Power Combiner

A series of Ka-band cylincrica! resonator type combiners have been developing as depicted in Figure 2. These include bo. waveguide coupled
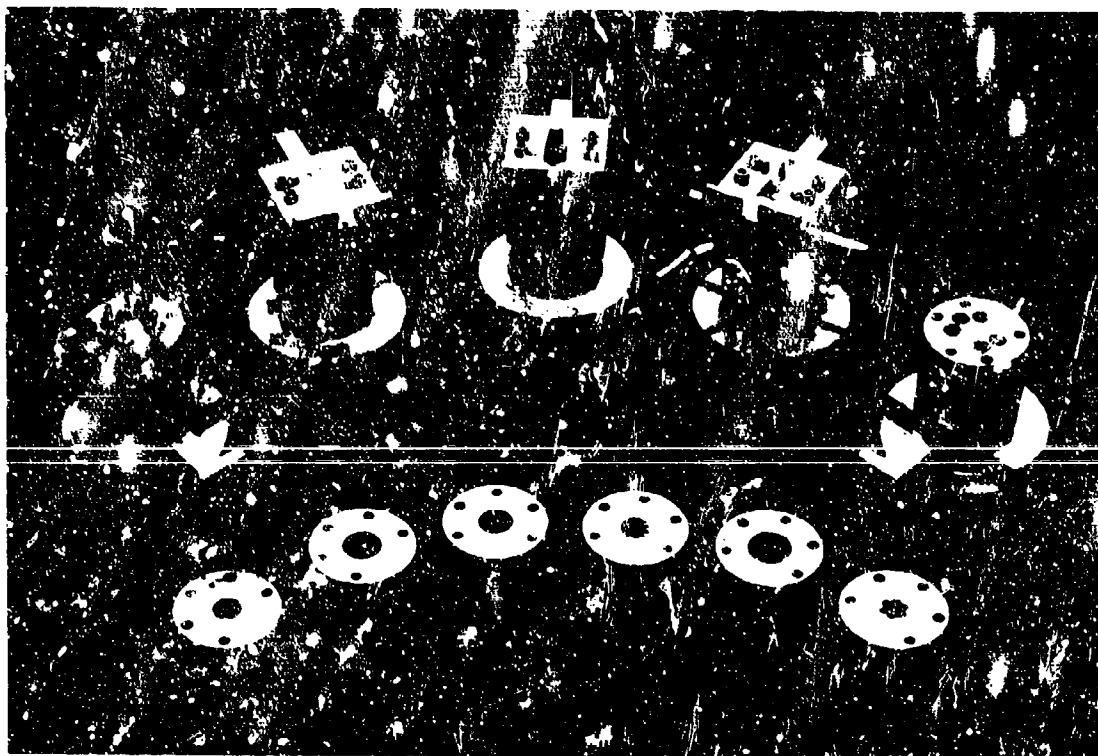
(extreme .eft and right) and coaxial line coupled combiners (center). These circuits which combine power from six individual coaxial circuits periphaily spaced around and magnetically coupled to the resonant cavity have been operated both in the fundamental TM_{010} mode as well as in the TM_{020} mode, with comparable results at 33 and 37 GHz. Utilizing six typical 100 mW diodes, total output power of 500 to 600 mW was obtained at operating junction temperatures below $20'^{0}C$. Operated as injection locked amplifiers, external Q's as low as 20 have been measured.

Avalanche Amplifiers

A variety of millimeter wave avalanche amplifiers have been developed, both at 35-40 GHz and 55-65 GHz range, as summarized in Table 1.

Table 1. Avalanche Amplifier Performance Summary

Frequency GHz	Output Power mW	Efficiency	ΔT_j °C	Gain dB	Bandwidth	G x BW	Amplifier Mode
37	200	3.5%	175°C	13	2.6 GHz	(Two-Stage)	Negative Resistance
37	300	7.0%	180°C	25	0.2 GHz	6 GHz	Injection Locked
64	150	6.4%	175°C	12	1 GHz	4 GHz	Negative Resistance
55-65	100-200	5-7%	200°C	23	1.3GHz	18 GHz	Injection Locked

Utilizing single drift Si diodes, amplifiers have been developed to operate in the negative resistance and injection locked mode. Emphasis is on reliable operation at reasonable junction temperatures. State-of-the-art performance was achieved at V-band with an amplifier exhibiting 6.4 percent power added efficiency with a junction temperature rise of 175°C, as well as with an injection locked amplifier with 1.3 GHz of locking bandwidth at a gain level of 23 dB, for a voltage gain-bandwidth product of 18 GHz.

On the receiver side, high performance front ends have been developed at both Ka and V-bands. Typical performance of the Ka-band balanced mixer preamplifier, for example, is 7.5 to 8 dB noise figure (SSB) with an IF centered at 600 MHz (measured over 400 MHz of bandwidth). This component, including short slot hybrid, is shown in Figure 3. At V-band a compact
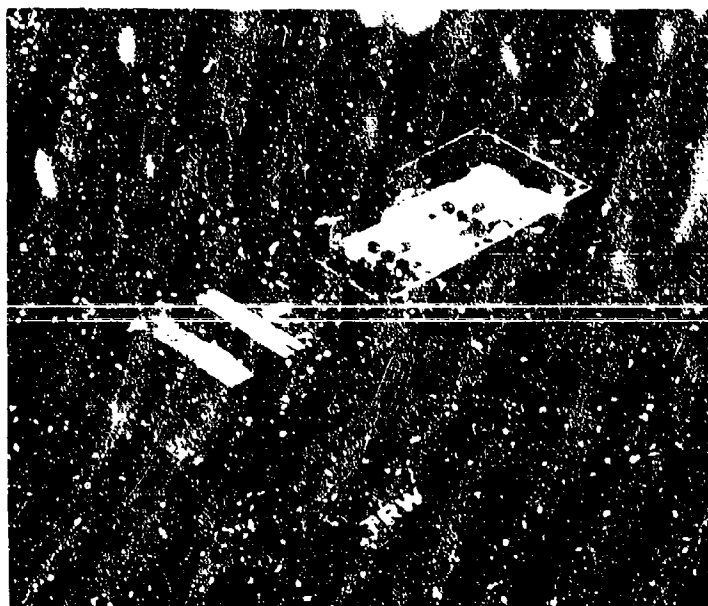
Figure 3.   Ka-Band Balanced Mixer Preamplifier Receiver Front End

mixer-preamplifier was developed with 9 dB SSB noise figure measured over a 600 MHz IF frequency range (centered at 1 GHz).
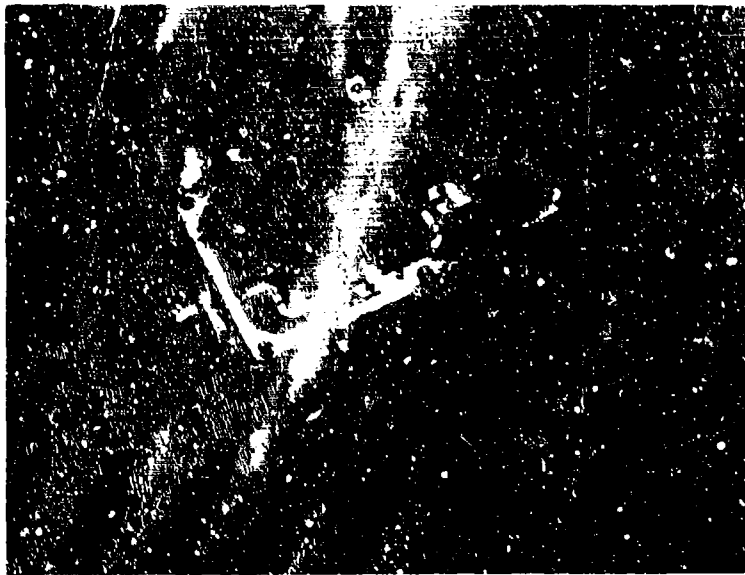
Figure 4. V-Band (55-65 GHz) Balanced Mixer Preamplifier

The IF amplifier of the Ka-band unit utilized alumina substrate, the V-band unit features a 1 x 1/2" sapphire substrate, GaAs mixer diodes are used in the V-band unit, the Ka-band unit utilizes Si mixer diodes. Both typically operate with LO power levels of 5 mW.

PASSIVE COMPONENTS

A number of key passive components are required in developing complete RF transmitter and receiver subsystems, including filters, circulators, transitions and 3 dB hybrids. Table 2 summarizes the performance of these components. The unique common features of these components are that they are all electroformed and fixed tuned. Emphasis in design was placed on truly high performance and high reliability - both were achieved. For example, two Ka-band short slot hybrids are shown in Figure 5, flanking a Ku-band split-block hybrid. The electroformed Ka-band hybrids exhibit a design bandwidth of 5 GHz, a maximum power unbalance of 0.25 dB, a minimum of 25 dB isolation and a 1.1 VSWR.

TABLE 4.   PERFORMANCE SUMMARY OF ELECTROFORMED PASSIVE COMPONENTS

Component	Center Frequency (GHz)	Bandwidth	Insertion Loss (dB)	Isolation (dB)	VSWR
3 dB Short Slot Hybrid	30-37	4 GHz	0.2	25	1.1
Fixed Tuned Band-Pass Filters	30-38	400 MHz	0.2	---	1.1
	55-65	200 MHz	0.3	---	1.2
High Pass Filters	30-38	---	0.1?	30*	1.?
Circulators	55-65	2 GHz	0.3	0	1.15
WG-Coaxial Transition	3	5 GHz	0.2	---	1.2

*1 GHz Below Design Pass Frequency
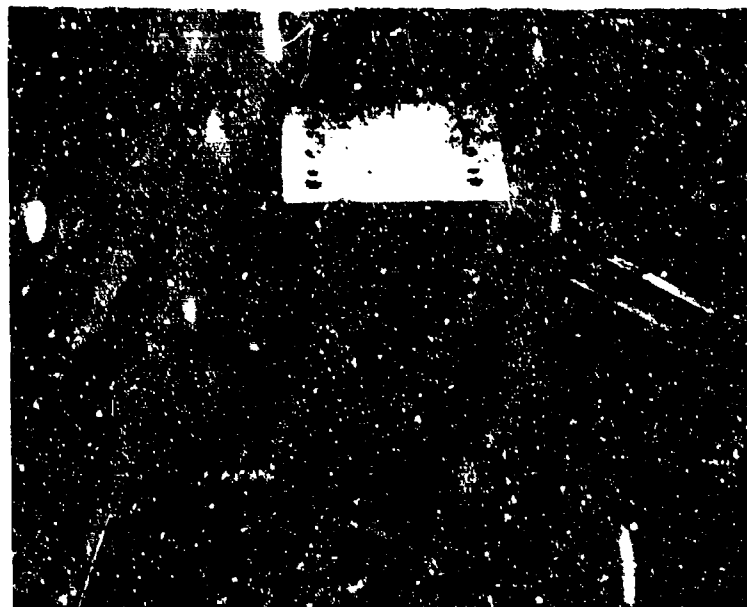
Figure 5.   3 dB Short Slot Hybrids

An electroformed 55 to 65 GHz circulator is shown in Figure 6. This turnstile Y-junction design typically has a bandwidth of 2 GHz, an insertion loss of 0.3 dB and a maximum VSWR of 1.2. No dielectric material of any kind is used for matching, coupling or ferrite support.
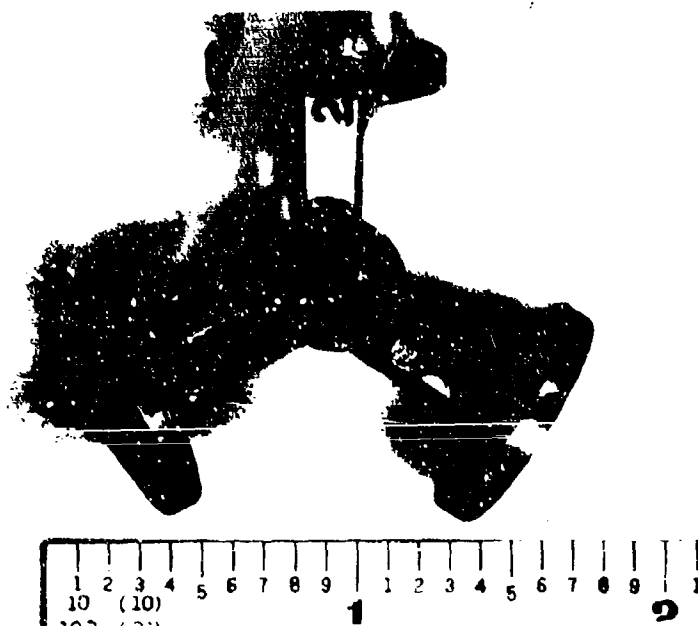
Figure 6. V-Band Waveguide Junction Circulator

The fixed tuned filter capability at TRW encompasses high pass and bandpass filters, including three and five section filter designs. Total absence of tuning screws results in lowest insertion loss and highest unloaded Q. Unloaded Q's of 80 percent of theoretical have been repeatably achieved.

Figure 7 shows two V-Band fixed tuned bandpass filters, one filter cut open for view. The fixed tune filter capability was originally established
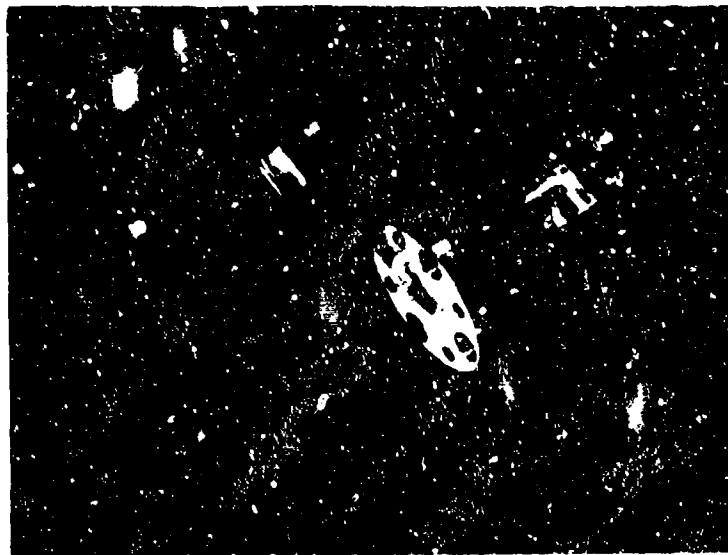
Figure 7. Fixed Tuned V-Band Bandpass Filter

at V-Band and subsequently scaled down to Ka-band and further developed. Some typical performance data is shown in Figure 8. This unique design capability has recently been expanded to include a range of bandwidth from 0.25 to 6 percent.

All components have been evaluated over temperature ranges typically 50 to 100°C with only minimal changes in performance.

ACKNOWLEDGEMENT
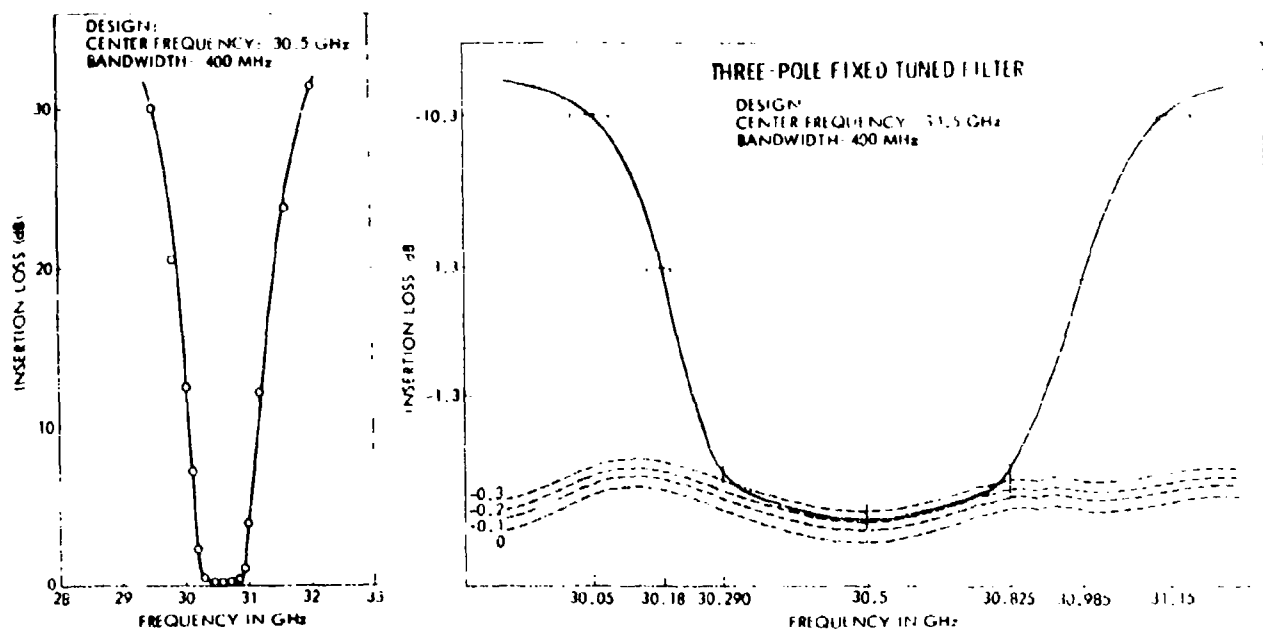
(a) Three-Section Filters, Including Expanded Scale
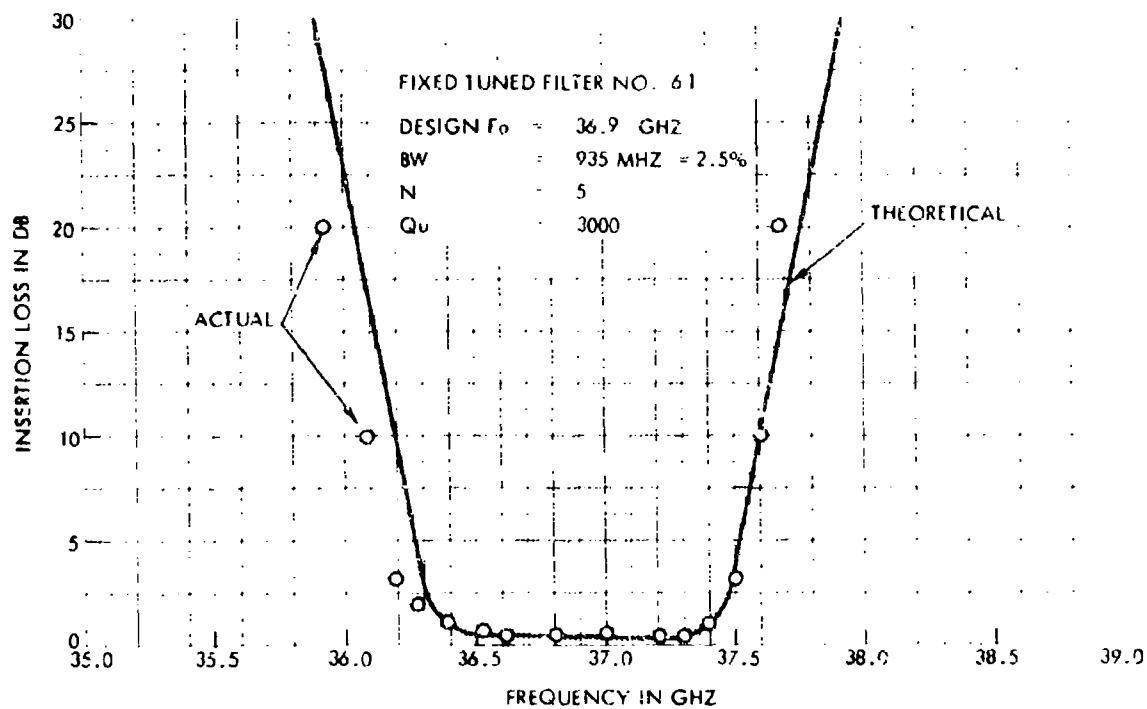
(b) Five-Section Filter

Figure 8. Comparison of Theoretical and Measured Response of Fixed Tuned Bandpass Filter

JOSEPHSON-EFFECT DETECTORS
AT MILLIMETER AND SUBMILLIMETER WAVELENGTHS
by
Richard G. Brandt
Office of Naval Research
1030 E. Green St.
Pasadena, CA 91106

INTRODUCTION

A Josephson junction consists of two superconductors which are weakly
connected so that electron pairs (which are the current carriers) can flow
from one superconductor to the other. The junction can take the form of a
sharp metal point making contact with a metal block, two metal films sepa-
rated by a thin oxide barrier or a single metal film whose width or current-
carrying capacity is locally reduced.

One remarkable aspect of such junctions, called the dc Josephson effect,
is the fact that a steady current can flow through the junction in the
absence of an applied voltage. At voltages large enough to break the
electron pairs, the junction becomes an ordinary ohmic device. At
voltages less than required to destroy the superconductivity, the current
which flows oscillates at a frequency proportional to the voltage.
This phenomenon is known as the ac Josephson effect and is important for
detection since extremely weak external signals can interact with this in-
ternal oscillation giving rise to various frequency conversion processes,
such as mixing, rectification, and parametric amplification. The upper fre-
quency limit for such processes is in the submillimeter range when the
photons become sufficiently energetic to break electron pairs.

Equivalent circuit representations are available for analyzing the
behavior of Josephson junctions in detector configurations. In the simplest
model the Josephson junction is represented by a perfect Josephson element
shunted by a small constant resistance. The Josephson element is highly
nonlinear: the current through the element is proportional to the sine
function of the time-integrated voltage across the element. Analog simu-
lations have been especially valuable in studying such circuits and have
provided the understanding necessary to construct well engineered devices.

DETECTOR PERFORMANCE

In Table I a comparison is made of the best operating characteristics that have been achieved at 1 mm wavelength for various incoherent detectors, both superconductor and semiconductor types. The superconductor bolometer has both the lowest NEP and the largest input bandwidth for this class of detectors which gives it the capability of resolving target temperature differences smaller than 10^{-2} K for a 1 second integration time. The sensitivity of this device is expected to remain constant throughout the millimeter range. The only disadvantage of the superconductor bolometer is its relatively slow response time of 10 to 100 ms.

Table II gives a comparison of various coherent detectors at 1 mm wavelength. The performance of GaAs mixers is seriously degraded above microwave frequencies. The InSb hot-electron mixer cooled to liquid helium temperature has very high sensitivity up to 1000 GHz, but is inherently a very narrowband (2 MHz) device. It is predicted that the same NEP (2×10^{-17} W/$\sqrt{Hz}$) can be achieved with a Josephson mixer which would have somewhat greater bandwidth (20 MHz). This performance has been demonstrated at 36 GHz, and preliminary measurements at 144 GHz are encouraging.

SUMMARY

Josephson-effect detectors have become competitive with semiconductor devices in the millimeter region. Continuing research on superconductor detectors, particularly on parametric amplification devices, could lead to further substantial improvements. In view of the Navy's commitment to development of cryogenic ship propulsion machinery, serious consideration should be given to use of Josephson-effect detectors in future millimeter-wave systems.

REFERENCES

1. Proceedings of the International Conference on the Detection and Emission of Electromagnetic Radiation by Josephson Junctions, Revue de Physique Appliquee, vol. 9 (1974).

2. A. A. Penzias and C. A. Burrus, Annual Reviews of Astronomy and Astrophysics 11, 51 (1973).

Table I

INCOHERENT DETECTORS

AT 1 MM WAVELENGTH

TYPE	OPERATING TEMPERATURE	NEP	BANDWIDTH	ΔT_{min}	RESPONSE TIME
SEMICONDUCTOR BOLOMETER	77 K	10^{-13} W/$\sqrt{Hz}$	>30 GHz	.25 K/$\sqrt{Hz}$	1 s
SUPERCONDUCTOR BOLOMETER*	1.7 K	5×10^{-15} W/$\sqrt{Hz}$	>30 GHz	<.01 K/$\sqrt{Hz}$	<.1 s
JOSEPHSON VIDEO DETECTOR	4.2 K	10^{-14} W/$\sqrt{Hz}$	3-30 GHz	.25 K/$\sqrt{Hz}$	$<10^{-8}$ s
JOSEPHSON REGENERATIVE DETECTOR	4.2 K	5×10^{-15} W/$\sqrt{Hz}$	300 MHz	1 K/$\sqrt{Hz}$	$<10^{-8}$ s

*MEASURED ELECTRICAL NEP ASSUMED VALID FOR 300 GHz RADIATION.

Table II

COHERENT DETECTORS

AT 1 MM WAVELENGTH

TYPE	OPERATING TEMPERATURE	MIXER TEMPERATURE	BANDWIDTH	NEP	ΔT_{min}
GaAs MIXER	290 K	6000 K	100 MHz	$2 \times 10^{-15} W/\sqrt{Hz}$	$1.4 \ K/\sqrt{Hz}$
GaAs MIXER*	77 K	2000 K	500 MHz	$1 \times 10^{-15} W/\sqrt{Hz}$	$2 \ K/\sqrt{Hz}$
InSb MIXER	4.2 K	500 K	2 MHz	$2 \times 10^{-17} W/\sqrt{Hz}$	$.7 \ K/\sqrt{Hz}$
JOSEPHSON MIXER**	4.2 K	200 K	20 MHz	$2 \times 10^{-17} W/\sqrt{Hz}$	$.07 \ K/\sqrt{Hz}$

*ESTIMATED PERFORMANCE. NOT YET MEASURED.

**MEASUREMENTS AT 36 GHz. FREQUENCY INDEPENDENT EXTRAPOLATION. COUPLING PROBLEM MORE DIFFICULT
AT 300 GHz. JUNCTION CAPACITANCE MUST BE MINIMIZED, BUT POSSIBLE SOLUTIONS ARE AVAILABLE.

RECIPROCAL AND NONRECIPROCAL PHASERS FOR USE AT MILLIMETER WAVELENGTHS

Lawrence R. Whicker and Charles W. Young, Jr.
Naval Research Laboratory
Washington, D.C. 20375

INTRODUCTION

High performance millimeter wavelength phase shifters are needed for electronically scanned phased array antennas, and for performing various control functions such as switching in radar, communications, and electronic warfare systems. As at lower frequencies, there are presently two phaser configurations which are suited for use in the 20-100 GHz range. These phaser types are the latching, toroidal, nonreciprocal phaser (1-3) and the latching, dual-mode reciprocal phaser. (4-5)

In this paper, the present state-of-the-art for toroidal, nonreciprocal phasers and dual mode phasers are reviewed and projected performance for these phaser types are presented. Additionally, a current program at the Naval Research Laboratory is described. This program is attempting to broaden the operating bandwidth of the toroidal nonreciprocal phase shifter to cover the 26-40 GHz range.

THE TOROIDAL NONRECIPROCAL PHASER

Work on the toroidal, nonreciprocal phaser has been underway in the United States since early in 1963. The basic operating mechanism of this type of phaser is reviewed in Figure 1. Figure 1(a) shows the ferrimagnetic toroid centered in either a standard or reduced width waveguide, Figures 1(b) and 1(c) review the two types of construction which are normally utilized. Computer programs are utilized to optimize the phaser designs at center frequencies ranging from about 3 to 35 GHz. In designing such phasers, it is desired to select a ferrimagnetic material such that a fixed remanent flux density to operating frequency is maintained. However, at frequencies above about 35 GHz, this cannot be done. The choice then is to use materials having the largest possible saturation magnetization while maintaining a good squareness ratio. Nickel zinc ferrites and Lithium titanium ferrites offer the highest available saturation moment of about 5,000 gauss.

Present Performance

In 1966, Stern and Agrios (6) reported on a 35 GHz high power switch using 90° phase shifter elements. A similar geometry was used by Whicker, Degenford and Wantuch (7-8) in investigating phase shifters in the 35-94 GHz region. The geometry used in 35 GHz and 75 GHz designs are shown in Figure 2. Phase shift data obtained using two Nickel Zinc materials are shown in Figures 3-4. Several 35 GHz phasers have been subsequently been fabricated. Phase shifter properties for 35 GHz units and projected performance for a 75 GHz unit are listed in Table I. It should be noted that because of severe tolerances and present machining capability, the data listed in Figure 4 is not for a truly optimized 75 GHz phaser. It appears that toroidal designs are best suited for use below about 60 GHz.

Table I
NONRECIPROCAL PHASE SHIFTER PERFORMANCE

f_c	34.5 GHz	75.5 GHz
Bandwidth	34 - 35 GHz	77 - 77 GHz
Insertion Loss	1.5 dB	3.5 - 4.0 dB
VSWR:	<1.25	<1.25
Switching:	3 Bit or Flux Transfer	3 Bit or Flux Transfer
Length:	3 inches	4 inches

DUAL MODE RECIPROCAL PHASER

In looking for a phaser geometry which might be less tolerance sensitive than the toroidal type, the dual mode reciprocal phaser is considered to be a good candidate. A test phaser has been fabricated. (9) In this phaser a center frequency of 35 GHz has been used. The phaser design is shown in Figure 5. The basic concept is shown schematically in Figure 5(a). Here, linearly polarized energy in rectangular waveguide is passed through nonreciprocal polarizers and is converted to either left or right circular polarized energy in quadrantally symmetric waveguide, is phase shifted and reconverted to linear polarization in rectangular waveguide. As indicated in the figure, a metal fixture-housing is used which

provides access to the phaser for tuning of the nonreciprocal polarizers.

Phase shift data for the 35 GHz unit are given in Figure 6. The other performance parameters for the phaser unit are as follows:

Bandwidth	34 - 36 GHz
Insertion Loss	< 2.2 dB
VSWR	< 1.3
Length	< 7 inches

Other than precision grinding of the ferrite rod which forms the body of the phaser element, only standard tolerance parts have been used. Computer computational techniques have been used in designing and predicting the performance of this unit.

In addition to the 35 GHz phaser design, computer designs for phasers centered at 55 and 95 GHz have been prepared. The predicted loss characteristics for these phasers are summarized in Table II. It is interesting to note that material dielectric losses predominate at the higher frequencies. In general, the dual mode phaser appears better suited for use above 35 GHz than the toroidal type. Loss restrictions rather than tolerance problems are expected to provide an upper frequency bound for use of this phaser.

TABLE II

CALCULATED LOSS FOR DUAL-MODE PHASERS

	FREQ. (GHz)	COND. LOSS (dB)	DIEL. LOSS (dB)	MAG. LOSS (dB)	TOTAL LOSS (dB)
35 GHz PHASER	33.0	.647742	.671986	.455419	1.775147
	34.0	.617772	.680277	.422221	1.720220
	35.0	.591495	.689357	.392912	1.673754
	36.0	.568277	.699191	.366848	1.616875
	37.0	.547628	.715052	.332770	1.585960
55 GHz PHASER	50.0	1.010916	.996375	.224717	2.232006
	52.0	.946206	1.010553	.202189	2.158951
	54.0	.892059	1.027143	.183219	2.102711
	56.0	.846123	1.046387	.167035	2.059543
	58.0	.806698	1.066971	.153073	2.026749
	60.0	.772529	1.088862	.140919	2.002315
95 GHz PHASER	90.0	1.583211	1.749832	.066403	3.399442
	92.0	1.531693	1.766884	.062749	3.361328
	94.0	1.484813	1.785147	.059417	3.329370
	96.0	1.441991	1.804462	.056367	3.302827
	98.0	1.402732	1.824697	.053565	3.280996
	100.0	1.366524	1.845743	.050983	3.263345

NRL BROADBAND PHASER DEVELOPMENT

A system requirement has dictated the necessity for a fast switching (< 1µsecond switching) phaser to operate over the 26.0-40 GHz band. The switching speed requirement, in turn, precludes the use of th dual mode phaser and leaves the nonreciprocal toroidal phaser as the only candidate.

Computer computational techniques have been utilized to investigate the bandwidth characteristics for candidate geometries. Figure 7 gives plots of phase shift activity as a function of ferrite toroid geometry and as a function of dielectric loading within the toroid slot, Figure 8, shows the amount of variation in differential phase shift which may be obtained by selecting a fixed dielectric loading and slo. width (ϵ_d = 16, t ≈ 0.015 inches). As indicated, a toroid width of 0.053 in. provides the flattest differential phase shift across the 26-40 GHz band.

At this time, the computer design of the phaser element has been completed and present efforts are addressing the fabrication problems associated with the physical realization of this phaser. As with lower frequency to oidal phasers, two main problem areas are encountered. These include:

1. Intimate contact between the waveguide walls and the ferrite toroid are required. Air gaps or uneven areas introduce insertion loss spikes across the bandwidth of the device.

2. The Nickel Zinc ferrite material which has been used to date is magne ostrictive. Excess pressure exerted on the toroid can produce undesired changes in loss and phase shift.

Structures which are being investigated are shown in Figure 9. Thus far, the results obtained with the structures shown in Figures 9(a) and 9(b) have been encouraging. Experiments with the structure shown in Figure 9(c) will be initiated shortly. In the present experiments, Nickel Zinc materials have been used. Experiments using high saturation moment Lithium Titanium ferrites which are less magnetostrictive will be started within the next few months.

CONCLUSIONS

Based on past and present experiments, it appears that good quality ferrite phasers may be realized to operate throughout the 20-100 GHz region. The toroidal, nonreciprocal phaser is best suited for use below about 50 GHz. Above this frequency, manufacturing tolerances become untolerable. The dual mode reciprocal phaser can readily be fabricated to operate throughout the 20-100 GHz region. Material losses tend to become excessive, however, near 100 GHz.

A present NRL program is attempting to realize a broadband, nonreciprocal toroidal phaser to operate across the 26-40 GHz band. A computer design of the phaser has been realized and preliminary electrical measurements are encouraging.

REFERENCES

1. M.A.Treuhaft, L.M.Silber, "Use of Microwave Ferrite Toroids to Eliminate External Magnets and Reduce Switching Power," Proc.IRE, Vol.46, Aug 1958, pp.15-38

2. J.A.Kempic, R.K.Jones, "A Temperature Stable High Power C-Band Digital Phase Shifter," 1965 NEREM Record, pp.12-13

3. L.R.Whicker, "Recent Advances in Digital Latching Ferrite Devices," 1966 IEEE International Conv. Record, Vol.14, Pt.5, pp.49-51

4. C.R.Boyd, Jr., "A Dual-Mode Latching, Reciprocal Ferrite Phase Shifter," IEEE Trans.MTT-18, Dec 1970, pp.1119-1124

5. C.R.Boyd, Jr., L.R.Whicker, R.W.Jansen, "Study of Insertion-Phase Variation in a Class of Ferrite Phasers," IEEE Trans.MTT-18, Dec 1970, pp.1084-1089

6. R.A.Stern, J.P.Agrios, "A Fast Millimeter Ferrite Latching Switch," 1966 G-MTT Symposium Digest, pp.219-223

7. L.R.Whicker, J.E.Degenford, E.Wantuch, "Millimeter Wavelength Latching Ferrite Phase Shifters," 1967 NEREM Record, pp.60-61

REFERENCES--continued

8. E.Wantuch, J.E.Degenford, L.R.Whicker, "Modified Nickel Zinc Ferrites with High Saturation Magnetization and Improved Hysteresis Properties," Jour.of Applied Physics, Vol.39, No.2, Part 1, February 1969, pp.723-725

9. L.R.Whicker, C.R.Boyd, Jr., "A New Reciprocal Phaser for use at Millimeter Wavelengths," IEEE Trans.MTT-19, Dec.1971, pp.944-945

CONDUCTOR FOR DC
LATCHING PULSE

REMANENCE
POINT B_{r_2}

CLOSE LOOP
FERRITE TOROID

REMANENCE
POINT B_{r_1}

HYSTERESIS LOOP
FOR FERRITE
MATERIAL
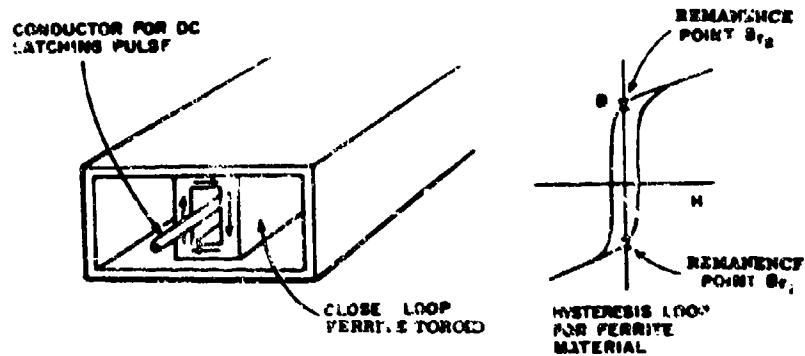
(a) Switching of ferrite toroid waveguide

DIELECTRIC MATCHING
TRANSFORMER

DIELECTRIC
SPACERS

LATCHING
CONDUCTOR

FERRITE TOROID
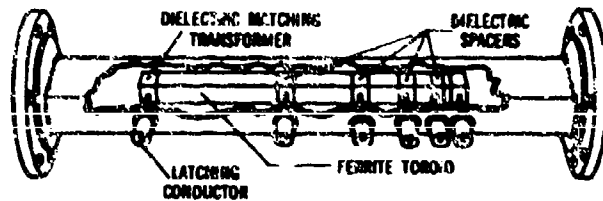
(b) Five bit nonreciprocal phaser

DIELECTRIC
MATCHING
TRANSFORMER

FERRITE
TOROID

LATCHING
CONDUCTOR
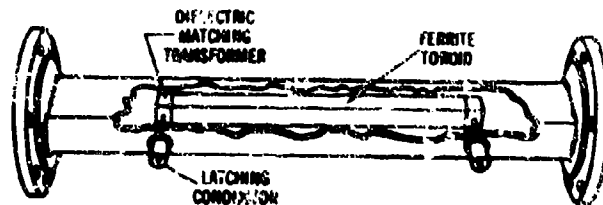
(c) Single Toroid Phaser--To Be Switched By Flux Transfer Techniques

FIGURE 1
NONRECIPROCAL TOROIDAL PHASER

UNCLASSIFIED
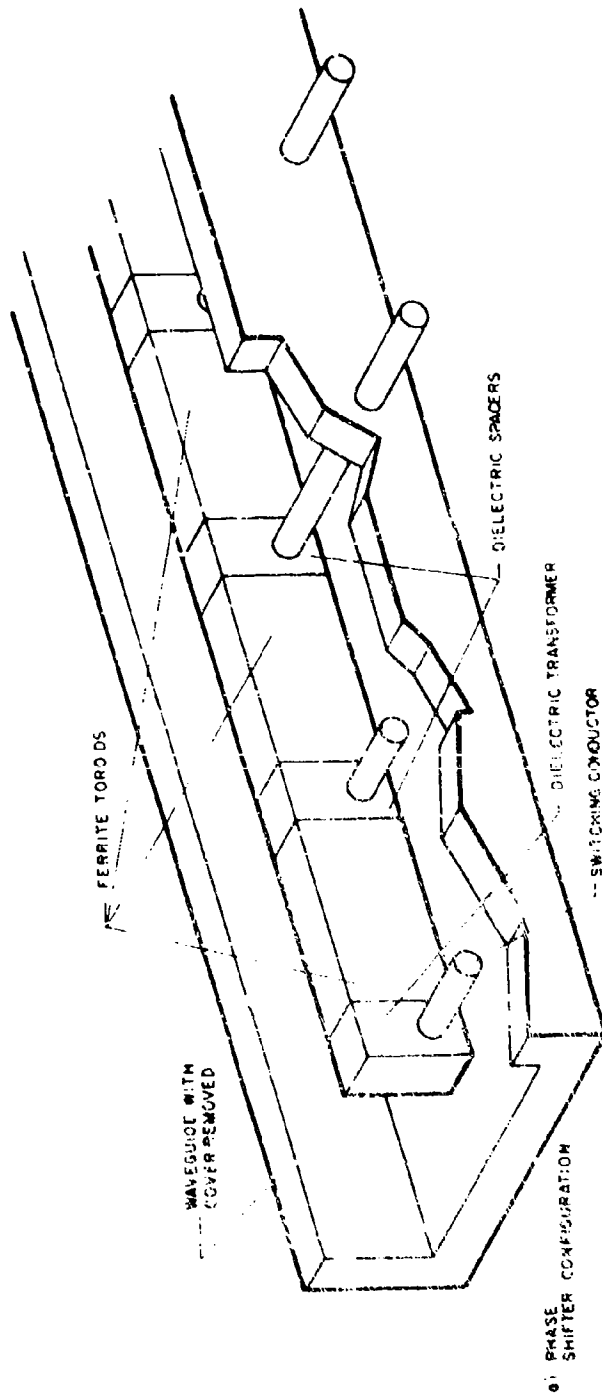
S7034-VC-3

FERRITE TOROIDS

WAVEGUIDE WITH COVER REMOVED

DIELECTRIC SPACERS

DIELECTRIC TRANSFORMER

SWITCHING CONDUCTOR

a) PHASE SHIFTER CONFIGURATION

b) TOROID CROSS SECTION
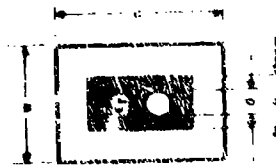
fo (GHz)	h (in)	w (in)	d (in)	g (in)	df
35	.120	.054	.013	.005	.44
95	.061	.029	.008	.003	.13

FIGURE 2
MILLIMETER PHASE SHIFTER CONFIGURATIONS

D7-9

IMPROVED Nb Zn, F.M.=375%/DB

TE2-III, E.M.=270%/DB

FREQUENCY (GHz)

34.0 34.5 35.0

DIFFERENTIAL PHASE SHIFT (DEGREES/INCH)

200 180 160 140 120 100 80
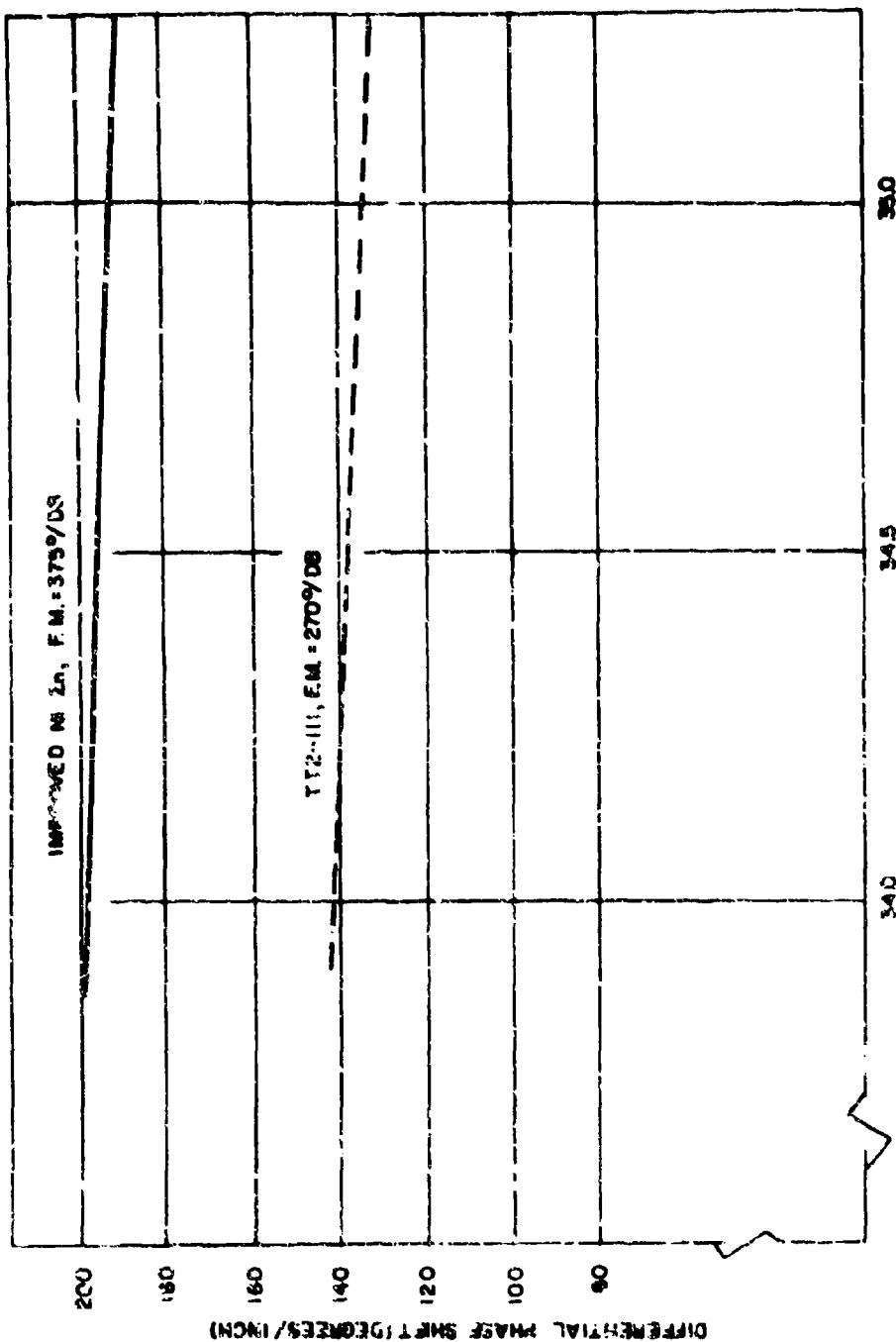
FIGURE 3

PHASE SHIFT VS. FREQUENCY DATA FOR 35 GHz PHASER
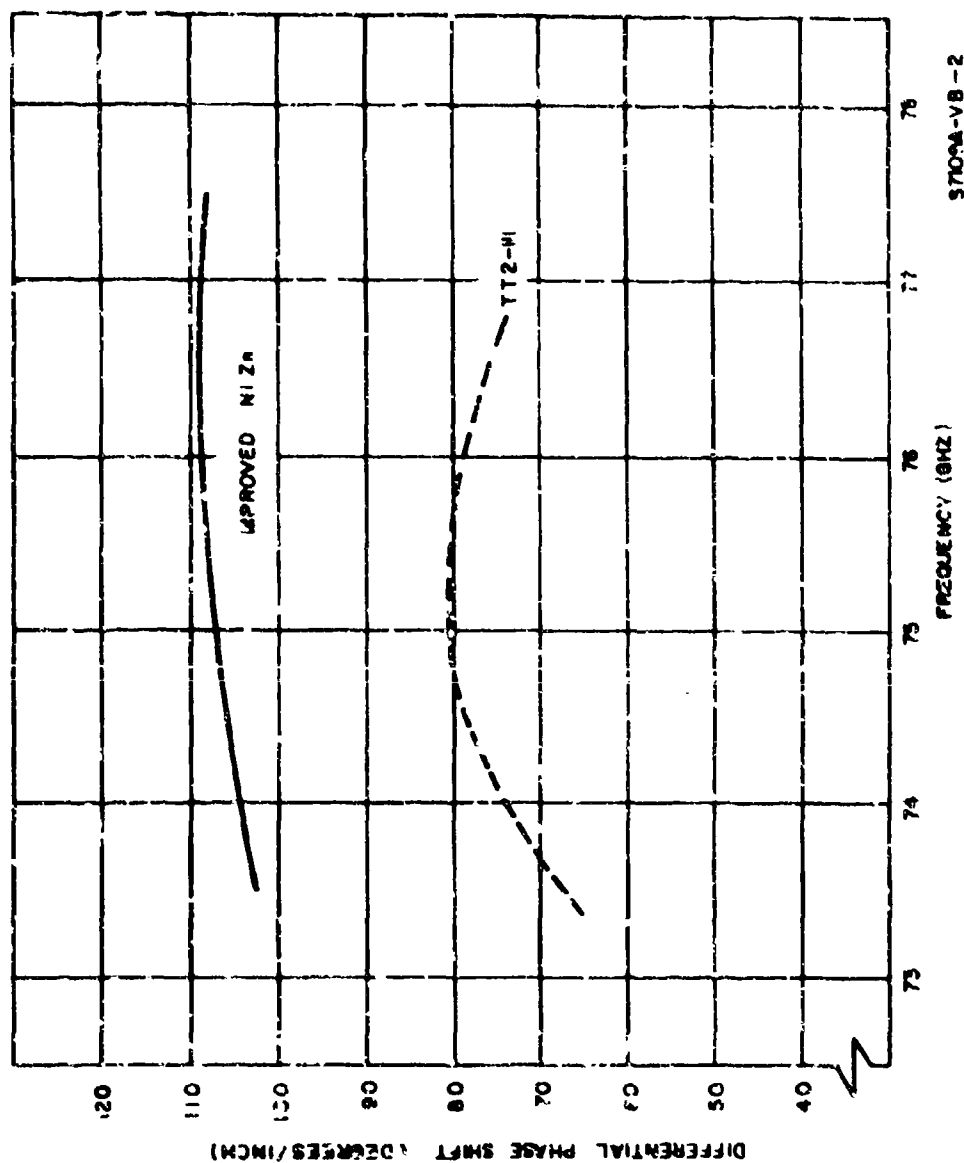
FIGURE 4
PHASE SHIFT VS. FREQUENCY DATA FOR 75 GHz PHASER
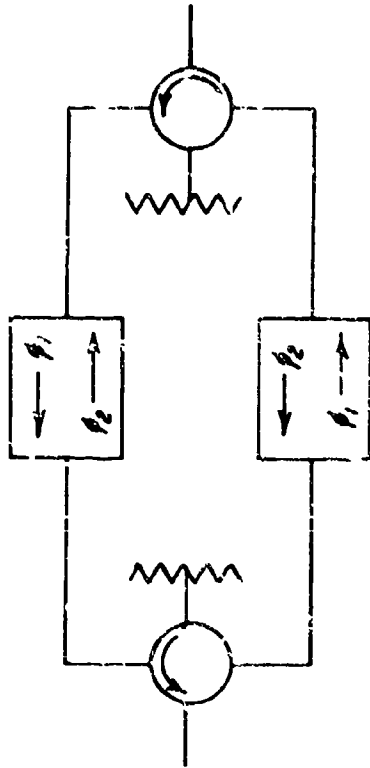
(a) BASIC CONCEPT OF DUAL MODE PHASER
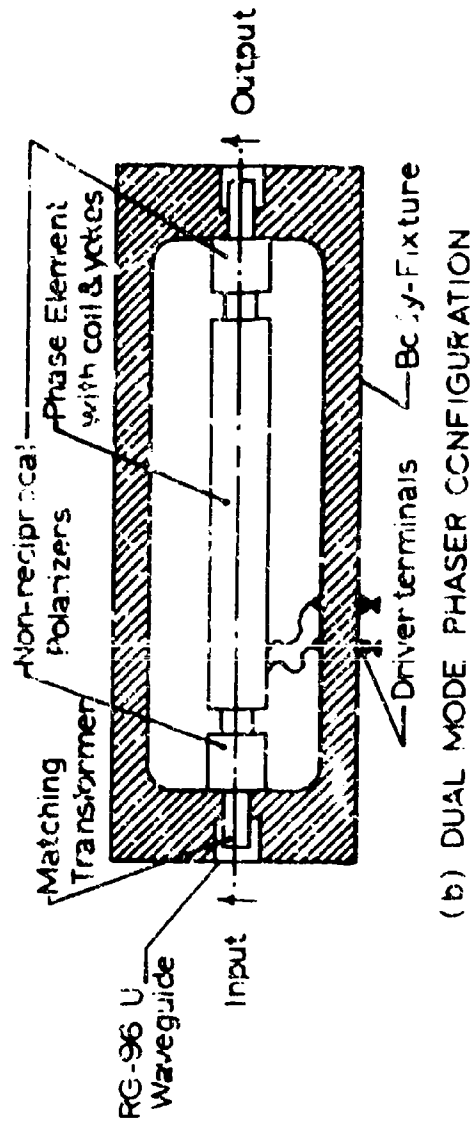
(b) DUAL MODE PHASER CONFIGURATION

Input

Output

RG-96 U
Waveguide

Matching
Transformer

Non-reciprocal
Polarizers

Phase Element
with coil & yokes

Driver terminals

Body-Fixture

FIGURE 5
DUAL MODE PHASER
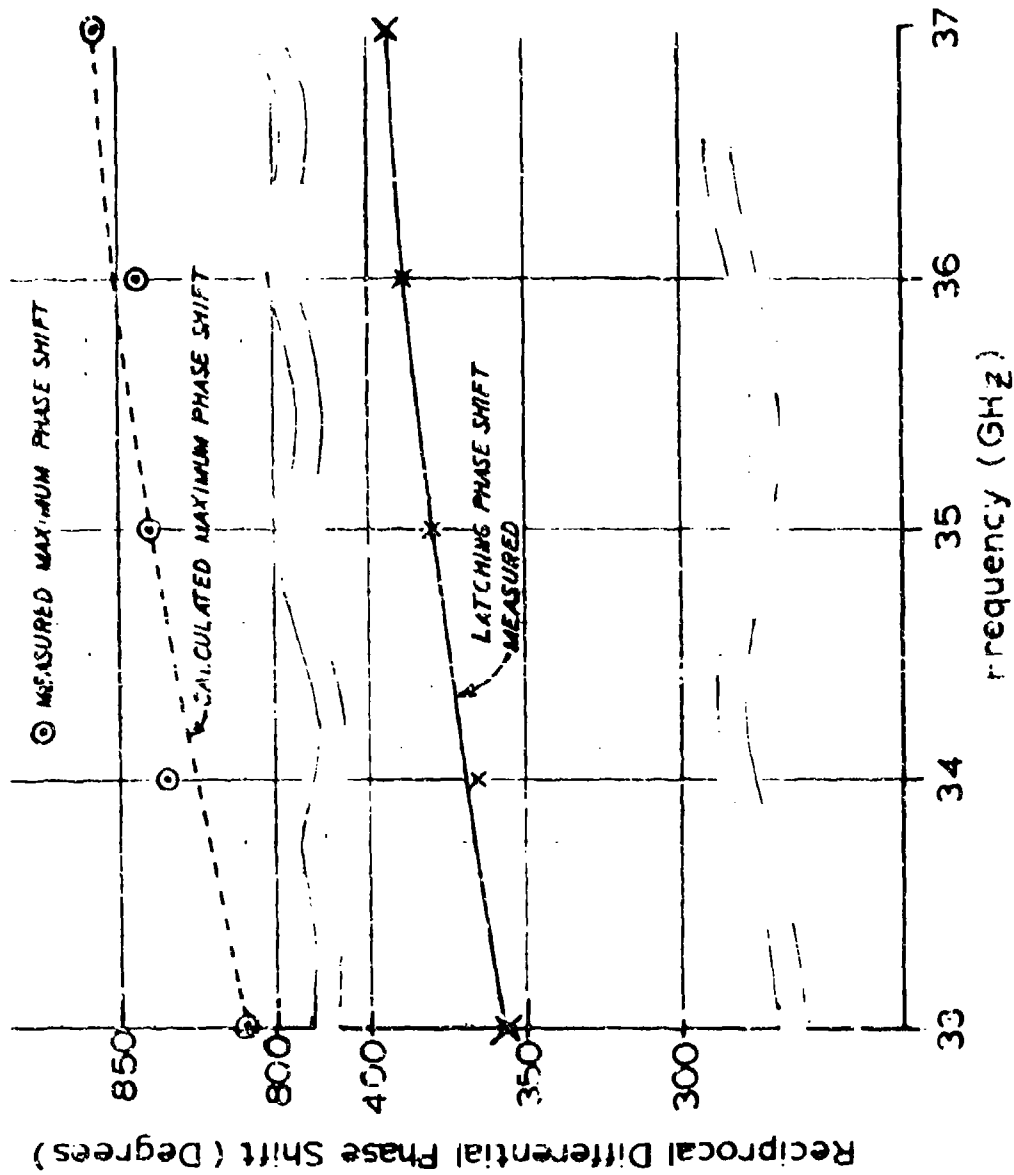
FIGURE 6
PHASE SHIFT DATA FOR DUAL MODE PHASER

-12
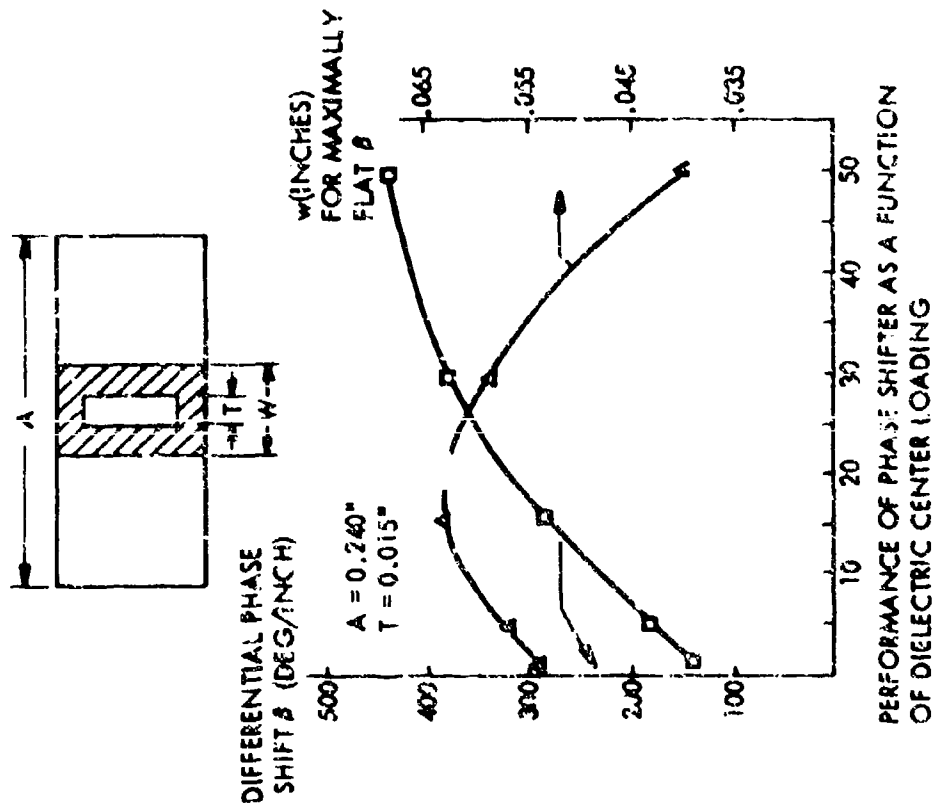
FIGURE 7

PHASE SHIFT ACTIVITY VS. DIELECTRIC CENTER LOADING
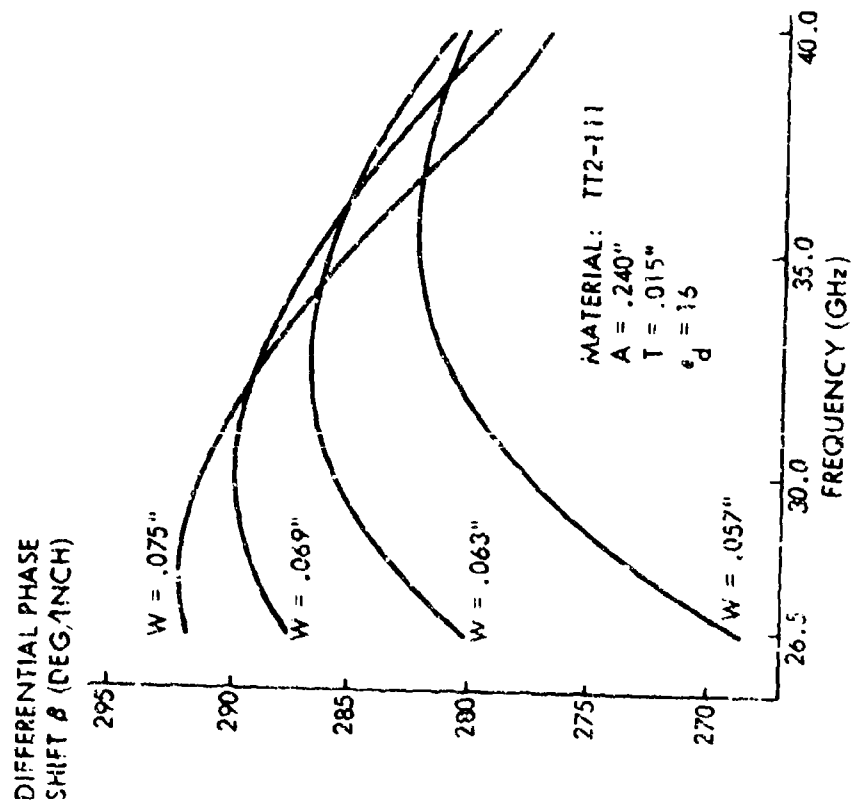
FIGURE 8
PHASE SHIFT VS. FREQUENCY FOR VARIOUS TOROID WIDTHS
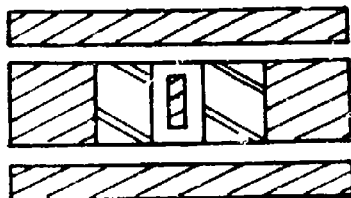
1. Toroid and side walls are glued together using polystyrene spacers.

2. Four mating surfaces are ground and polished.

(a)
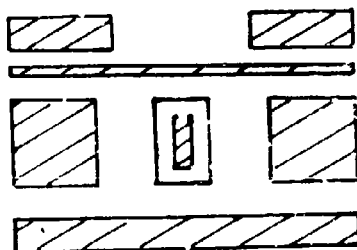
1. Top and bottom walls of ferrite toroid are metalized (Cr-Au)

2. Flexible top wall in area of toroid is used.

(b)
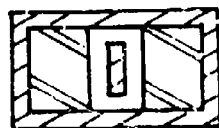
Waveguide wall is plated or electroformed directly about ferrite and alumina structure.

(c)

FIGURE 9
CONSTRUCTION DETAILS FOR BROADBAND PHASERS

A 95-GHz PRETRIGGERED RECEIVER PROTECTOR

by

H. Goldie
Westinghouse Defense and Electronic Systems Center
Systems Development Division
Electromagnetic Technology Laboratory
Baltimore, Maryland 21203

The purpose of this effort is to develop a radar receiver protector (RP) that will perform simultaneously the dual function of a millimeter-wave receiver protector and a high-current video switch. At present there is no device which can provide low loss protection at 95 GHz with 50 dB or more of broadband (60-100 GHz) isolation. The need for broadband isolation is due to the spurious moding of millimeter-wave multi-kilowatt magnetrons.

The device shown in figure 1 consists of 6:1 oversized WR-12 waveguide filled with low-pressure hydrogen gas, slotted sidewalls in the waveguide for orthogonal beam-current passage, a pair of impedance-matching tapers (figure 2) within the vacuum envelope, and specially developed wide-band, low-loss, high-temperature pr   windows. The waveguide serves the dual purpose of guiding the ri   ve and acting as a trigger grid to actuate the beam. A convergence cone, located between the waveguide sidewall and the cathode, is used to compress the beam in order to obtain high plasma densities without using excessive beam currents or externally applied magnetic fields.[1]

1. A Singh and J. Rowe, "Enhancement of Plasma Density in an Arc Discharge," J. Appl. Phys., (November 1967).

The resultant enhancement ratio of the plasma density at the cone exit relative to the value at the cone entrance has been measured using Langmuir probes under conditions where electron losses to the metallic cone wall are small. The plasma density enhancement method is compatible with small waveguide size because the plasma enhancement ratio, above a certain minimum cone exit area and except for a slight dependence on electron temperature, is proportional to the cone entrance-to-exit area ratio. Thus, the cone exit area is made compatible with the total area of the waveguide sidewall slot openings necessary for beam current passage.

Preliminary results concerning the theory, development, and low RF power evaluation of a 95-GHz plasma waveguide switch (PWS) were presented at the 1970 IEDM;[2] the basic model for the analysis of small-signal attenuation is shown in figure 3 and the computer-run solutions are shown in figure 4. The present paper concerns high-power experiments using an 8-kW, 95-GHz pulsed magnetron to obtain data on the PWS when used as a pretriggered receiver protector. The results show spike and flat leakage power levels of 20 mW for RF power levels up to 4 kW and under 1 mW for power levels of 1 kW; recovery times under 0.5 microsecond have been obtained. The external RF characteristics of the RP are dependent on the pre-excitation beam current magnitude. The beam current is controlled over a range of 5 to 100 amperes peak to obtain a predetermined fixed degree of RF isolation.

The fixed isolation, measured with a low-amplitude 95-GHz probing wave, represents the minimum attenuation of the pretriggered device with the beam on. The data is given in figures 5, 6, and 7. Previous measurements using Langmuir probes have shown the electron density

---

2. H. Goldie, "A 60 to 96 GHz Fast Acting Plasma Waveguide Switch," IEEE-70-C45-ED, (October 1970), page 40.

under these conditions to be approximately 10^{15} e/cc. With the 4-kW
RF pulse incident on the device (figure 8), an intense RF field is super-
imposed on the pretriggered dc field, resulting in an increase in plasma
density with a consequent increase in RF isolation. The high-power
data is shown in figures 9 to 11. The beam is pretriggered by a few
microseconds to allow the buildup of electrons to equilibrium values
prior to the RF pulse arrival. In our experiments, RF pulsewidths be-
tween 20 and 200 nanoseconds were used at PRF's from 100 to 1 kHz,
and total gas admixture pressures of approximately 100 to 400 mtorr
were used.

RP insertion loss has been reduced to 0.8 dB, as shown in
figures 12 and 13, by developing an RF choke whose diameter is much
less than the diameter of the glass-bonded mica window. This pre-
vented any significant RF current from reaching the glass bonding at
the window periphery, thus keeping insertion loss down to 0.2 dB/
window. The windows were individually tested at 3 kW after low-power
evaluation and hermetic sealing.

The RP design has evolved to include a keepalive electrode that
draws a constant but small current of 50 mA. This creates a glow
discharge which establishes a virtual cathode a short distance from the
actual cathode. Experiments show improved starting characteristics
with relatively small pulse-to-pulse jitter; additionally, a longer
cathode life is expected relative to the no-keepalive design due to
reduced back ion bombardment.

The RP is so designed that low-level insertion loss tests can be
run separately on the windows and on the waveguide body prior to
committing the windows to the device in the final brazing process. Ex-
perimental data to optimize isolation and recovery time will also be
discussed.

Figure 14 depicts a fail/safe circuit using the PWS as a pre-triggered RP and a dc switch. Experiments were performed at X-band to demonstrate feasibility. Figure 15 shows the actual front end to be used in a millimeter-wave radar; overall noise figure is about 9 dB, and gain is about 20 dB when measured from the input port of the RP to the output port of the 1-1.5 GHz IF preamplifier.
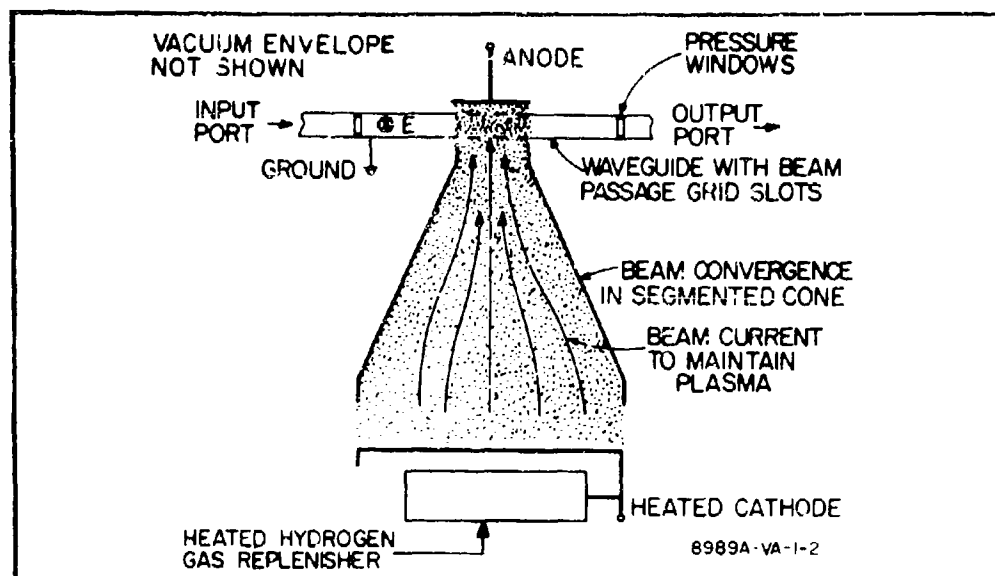
Figure 1a. Functional Sketch of Millimeter-Wave Plasma Waveguide Switch
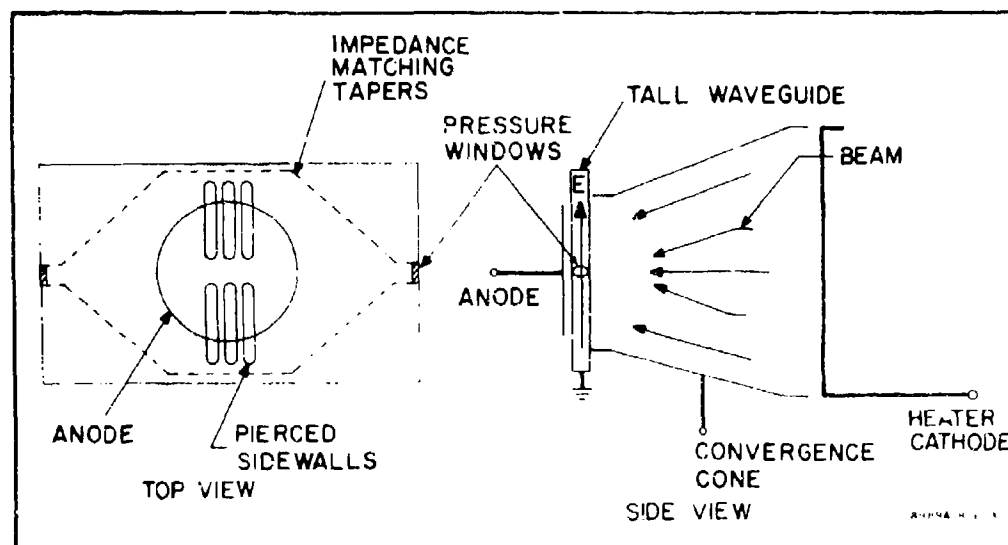
Figure 1b. Diagram of Millimeter-Wave Plasma Waveguide Switch

A. SLOTS

B. COMPLETE WAVEGUIDE
IN SECTIONAL VIEW

:'1-0903-BB-6

Figure 2. Photo of Body Showing Waveguide Sidewall Geometry for
Beam Passage and Two Impedance Transformers
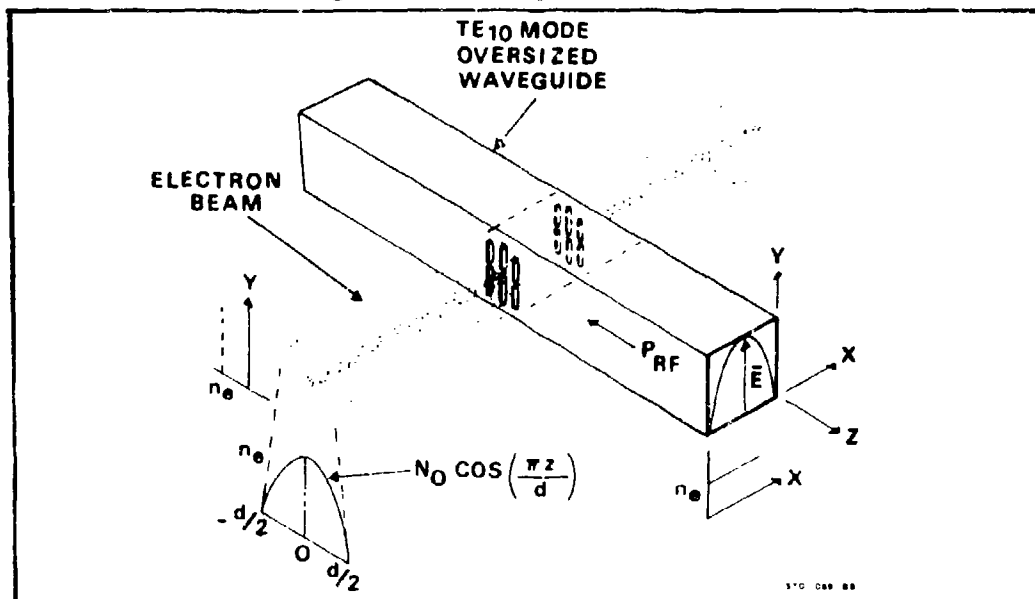
Figure 3. Model Used for Computation of Small-Signal Attenuation as
a Function of Electron Density and Frequency from Computer
Solutions of Wave-Plasma Transmission Equations
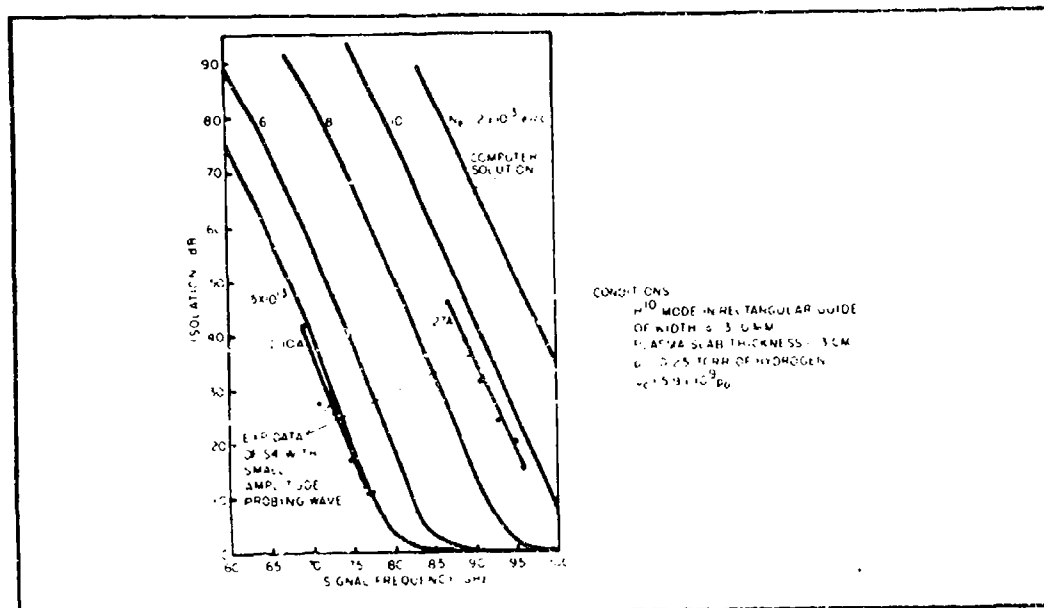
Figure 4. Comparison of Computer-Run Results of Small-Signal
Wave-Plasma Interaction Theory with Small-Signal
Measured Attenuation Data
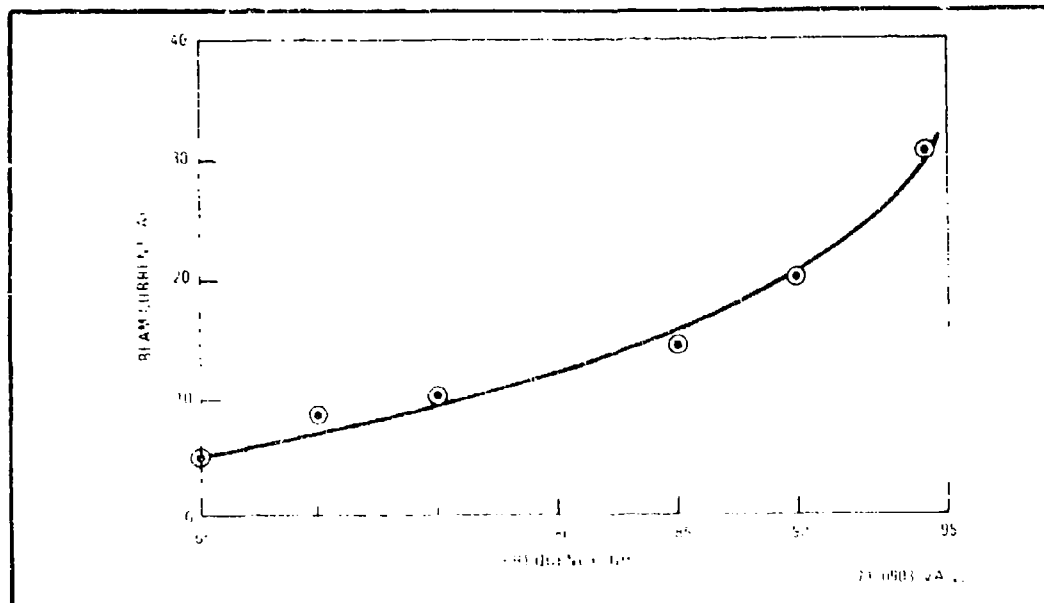
Figure 5. Required Beam Current to Maintain a Small-Signal
Attenuation of 30 db. Data Taken Using a 1-mW Probing Signal.
Gas Fill of 40 m. of Krypton plus 1 m. of H₂. 3 μsec Beam Pulse Duration

Small Signal Attenuation - 17-dB
Dynamic Range Shown.
Actual Attenuation over 30 dB.

Anode Voltage = 5 kV/cm

Beam Current = 50 A/cm

X = 1 μsec/cm

PRF = 1 kHz

S10

74-0194-PA-1
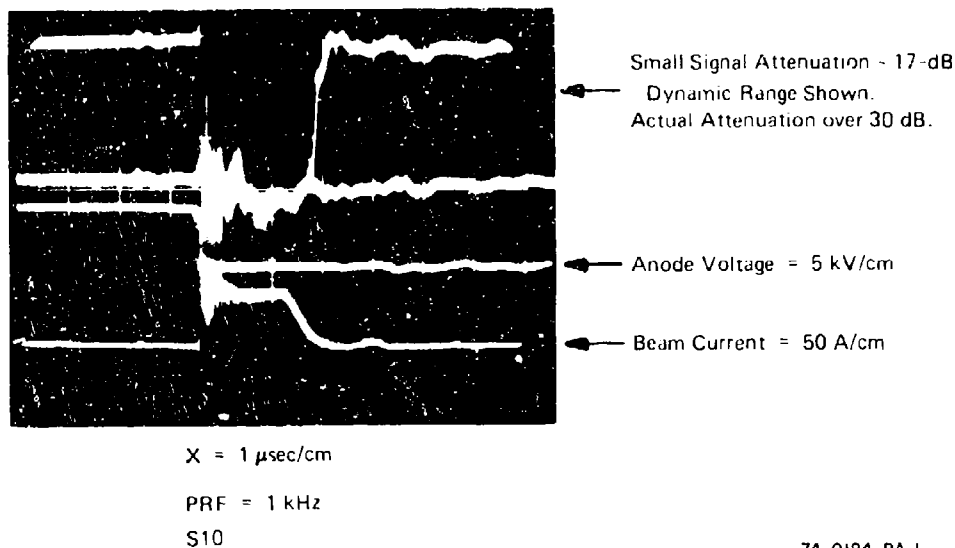
Figure 6. Upper Trace Shows Interrupted 1-mW CW Probing Wave at 70 GHz. Switch-on Time ≤ 0.25 μ sec and Recovery Time ≤ 0.25 μ sec. Small Signal Attenuation ≥ 30 dB for 2 μ sec.

CW milliwatt power detected at load. Interupted CW is due to PWS triggered to "on" position. Y axis shows approximately 15 dB attenuation; actual attenuation is 34 dB.

PWS beam current strength is 50A, 3-μsec duration. Y axis is 20 A/cm.

71-0903-BB-20
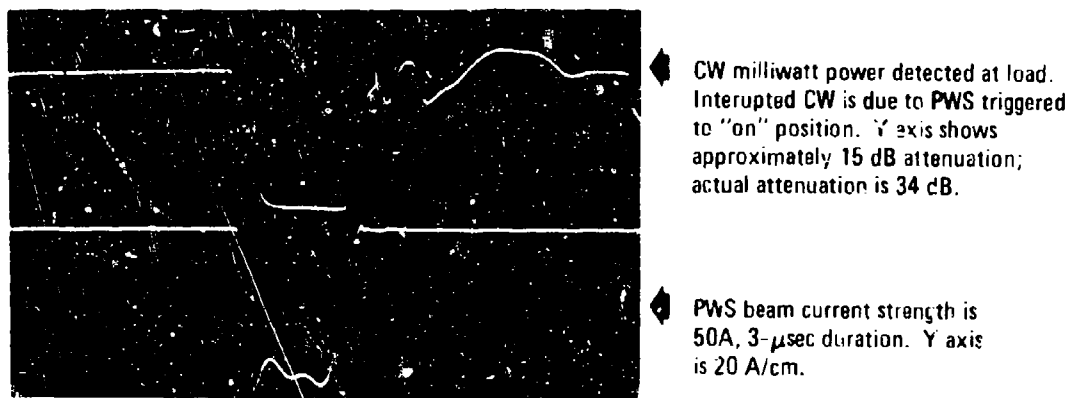
Figure 7. Isolation and Switching Times for S5 at 96 GHz

UNCLASSIFIED

Circulator-Inline RP Duplexer Radar Configuration
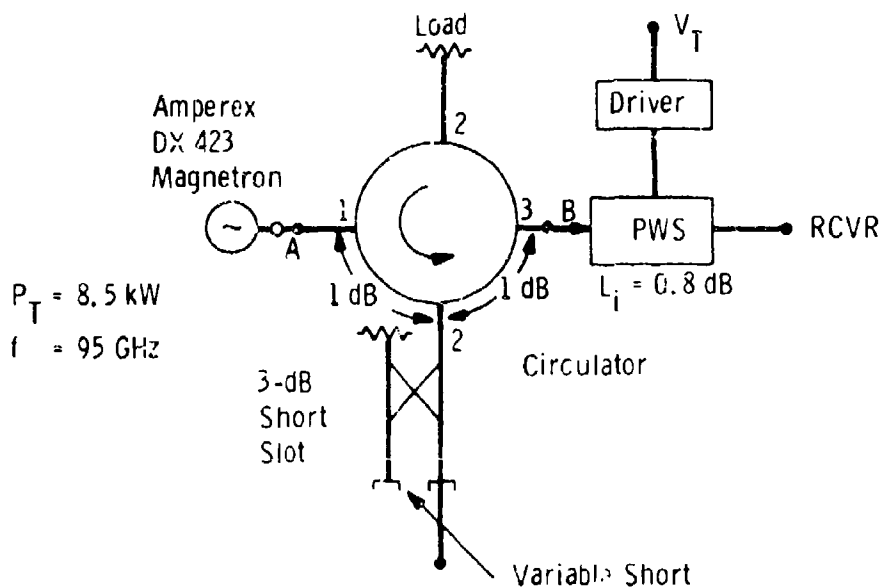
Minimum loss between points A and B was measured at 95 GHz to be 3.7 dB.
The variable impedance at port 2 gave a 33-dB variation in power range.

Total System T-R Losses:

Transmit Losses = 1 dB
Receive Losses = 1.8 dB
                  2.8 dB

Figure 8. Simulated Radar Experiment Using PWS as a
Pretriggered Receiver Protector

UNCLASSIFIED

D8-9

Beam Current:
40 A/7 μsec →

Detected RF Pulse:
4 kW/200 nsec →

Leakage Spike:
100 mW/10 nsec →

X = 1 μsec/cm

X = 40 nsec/cm

S9

PRF = 1 kHz

f = 95.7 GHz
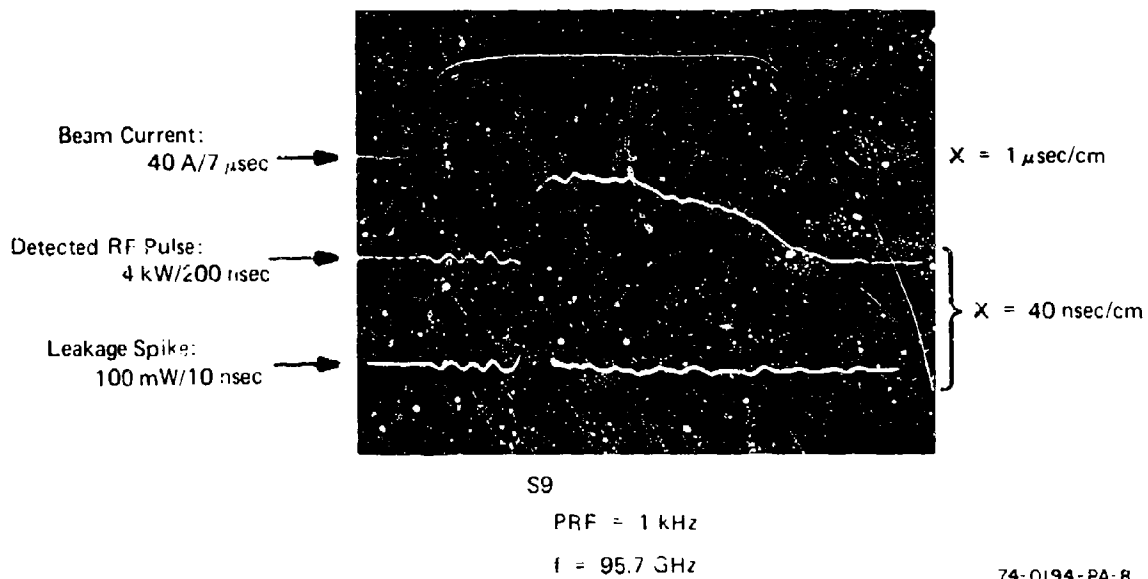
74-0194-PA-8

Figure 9. Input and Output RF Waveforms at 40-Amp
Beam Current
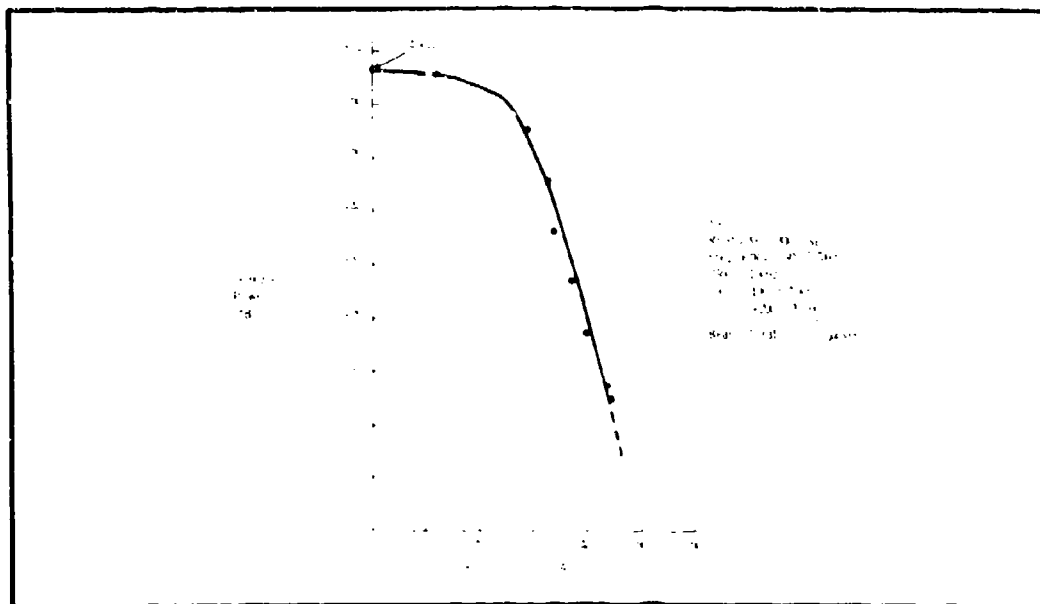
Figure 10. Leakage Power as a Function of Beam Current
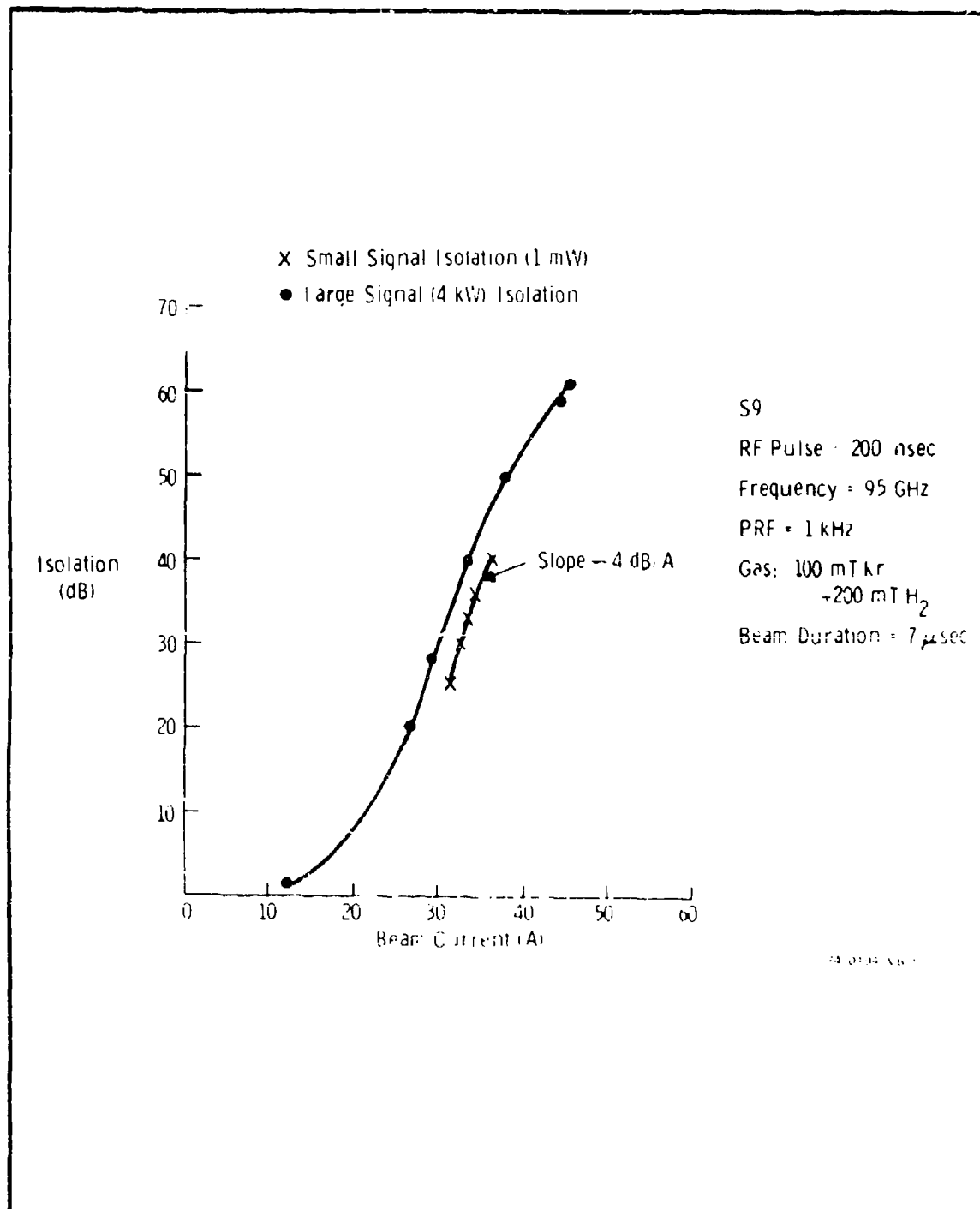
Figure 11. RF Attenuation as a Function of Beam Current
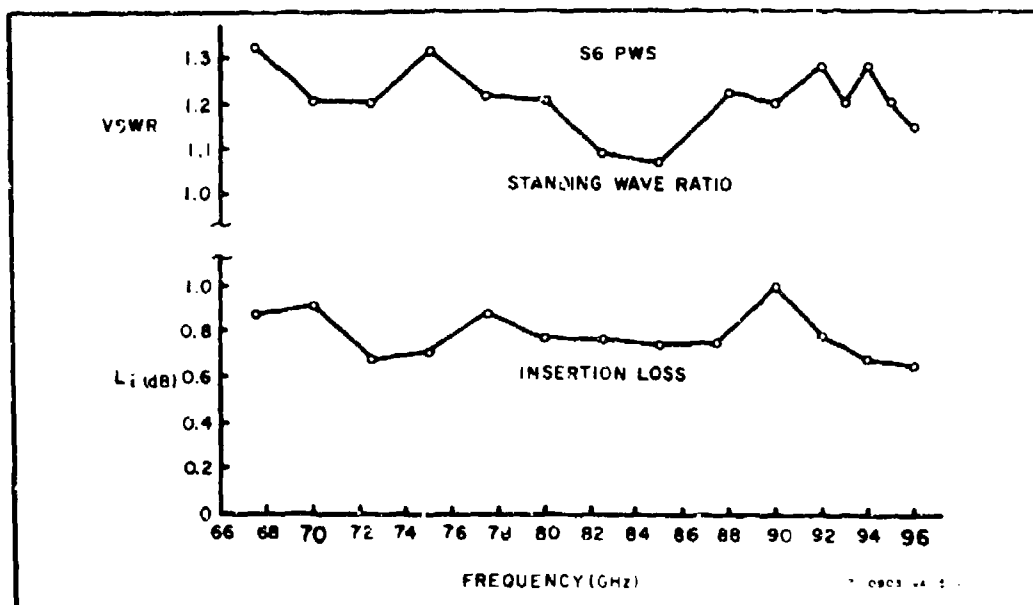
Figure 12. Measured Point-by-Point VSWR and Cold Loss Data of S6
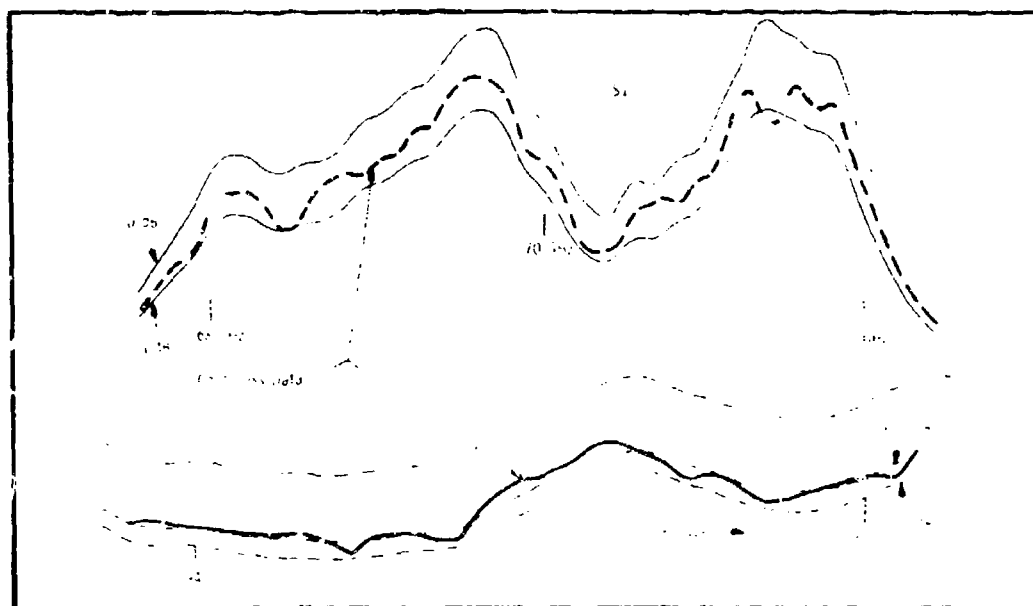
Figure 13. Swept Insertion Loss Data as a Function of Frequency in Cold State
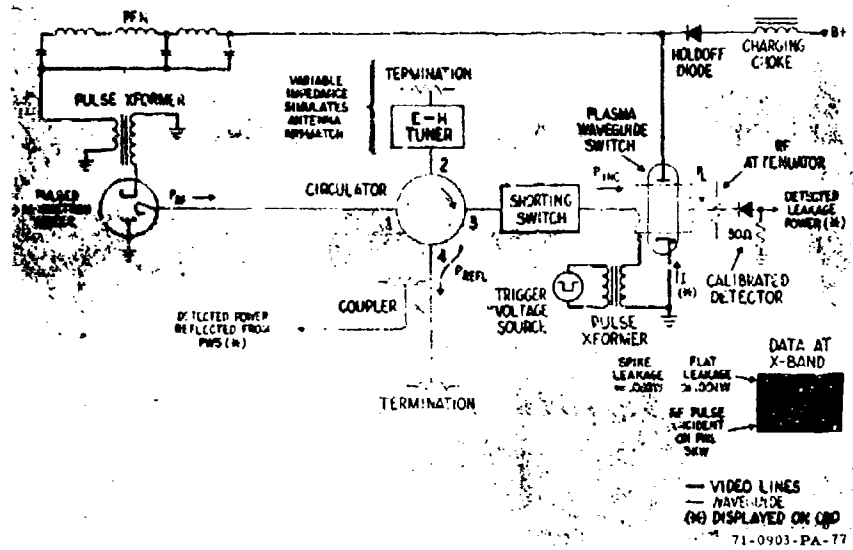
Figure 14. Fail/Safe Receiver Protection Experiment Performed at
X-Band (9.5 GHz) to Demonstrate Application of PWS to Radar Use
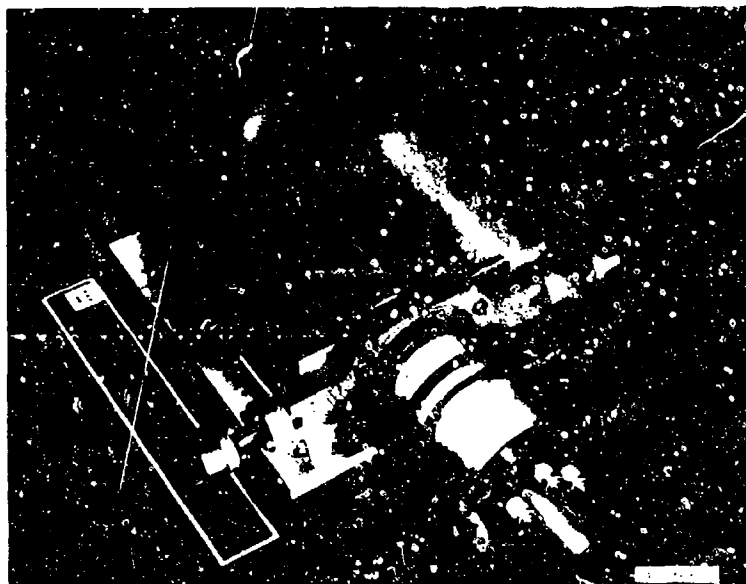
Figure 15. Millimeter-Wave Front End Showing PWS Used as a
Receiver Protector, Single-Ended Mixer (LO Not Shown),
and 1-1.5 GHz IF Preamplifier

A New 40 GHz Coaxial Connector
by
M. A. Maury, Jr. and W. A. Wambach
Maury Microwave Corp.
Cucamonga, Cal. 91730

INTRODUCTION

A new minature coax connector has been designed and developed to fill
the gap between connectors currently on the market and 40 GHz. This new
connector, "MPC2," permits coaxitube cable assemblies and waveguide to
coax adaptors to operate higher order mode free to 40 GHz whereas currently
available connectors begin to exhibit higher order mode resonances in the
vicinity of 36 to 38 GHz.

INTERFACE

Refer to figure 1, interface specifications of the MPC2. The dimen-
sions of the dielectric have been chosen to yield both an exact 50 ohm
line and a TE_{11} mode cutoff of 43.1 GHz. (1) The dielectric and center
conductor interface yield a near perfect coplaner junction when the male
and female MPC2 connectors are mated. The outside of the MPC2 resembles
a standard SMA connector but mating between the two is not mechanically
possible.

ELECTRICAL CHARACTERISTICS

Figure 2 is a TDR plot of a MPC2, an OSM, and an OSSM connector
mated pair on .086 dia. coaxitube cable assemblies. Clearly the new MPC2
interface is a better compensated junction impedance wise than either OSM
or OSSM connectors for .086 coaxitube applications. Because of the choice
of a TE_{11} mode cutoff of 43.1 GHz the MPC2 is safely useable to 40 GHz
when used with air lines or coaxial cable which do not permit TE_{11} mode
propagation below 40 GHz.

An application of the MPC2 interface has been made in a .086 dia.
coaxitube cable connector which permits low VSWR, low loss 40 GHz
cable assemblies. A feature of this connector is that the impedance

matching transformer (See figure 3) between the coaxitube cable line size
and MPC2 connector line size can be visually and mechanically inspected
after the final soldering process. This inspection ability eliminates
excessive heating effects as a cause of cable assembly rejections at a
higher inspection level. The final assembly of the connector to the
cable consists of mechanically threading on precision machined outer
conductor and connector shell parts. The dielectric and center conductor
interface are gaugable for compliance to the MPC2 interface of figure 1.
A connector gauge kit to inspect these parameters has also been developed
(See figure 4). Figures 5 and 6 show the VSWR and insertion loss char-
acteristics of a typical cable assembly. No resonances of high VSWR or
loss are present to indicate the existance of higher order modes.

An application of the MPC2 interface has been made in a bulkhead
mounted connector. This connector has been designed to interface with
proprietary coax to waveguide junction designs which require a .116
outer conductor and .050 dia. center conductor coaxial air transmission
line input. The dielectric bead support in this connector is mode free
to beyond 40 GHz.

Analysis of this dielectric bead in the manner of reference (2)
predicts a resonant frequency at 41.7 GHz, well above the upper limit
of 40 GHz. Figures 7 and 8 show the VSWR and insertion loss character-
istics of a typical WR28 waveguide to coax adaptor with the new MPC2
connector. No resonances of high VSWR or loss are present to indicate
the existance of higher order modes.

Figure 10 shows the VSWR characteristics of a WRD180C24 double
ridged waveguide to coax adapter (Figure 9) with the new MPC2 connector.
Again, no sharp resonances are present. This device allows the direct
connection of .086 coaxitube cable assemblies to low loss, broadband
(18 to 40 GHz) waveguide systems.

TEST METHODS

The VSWR and insertion loss responses of figures 5-6 were made
with the test set up of figure 11, and responses of figures 7, 8 and

10 with the test set up of figure 12. In measuring VSWR the test port was terminated in a precision 50 ohm coaxial air line with a built in sliding absorber. In measuring insertion loss the test port was terminated in an open circuit. In all cases, connector and dielectric bead orientation were varied in case a resonance existed which was orientation sensitive.

FUTURE APPLICATIONS

The applications of any coaxial connector are obvious. The application of the MPC2 is to systems which must operate to 40 GHz with no "dead" spots or frequencies at which systems characteristics are radically different from the typical. A comprehensive product line of connectors, components and measurement instruments featuring the MPC2 connector is currently under development in order to realize full utilization of this new connector to 40 GHz. Work is currently under way on a microstrip version of the MPC2, and on broadband 12-40 GHz double ridged waveguide transitions. Also, further measurements are planned to determine exact resonance frequencies above 40 GHz, and mated pair loss and VSWR characteristics of the coaxitube and bulkhead mounted versions of the MPC2.
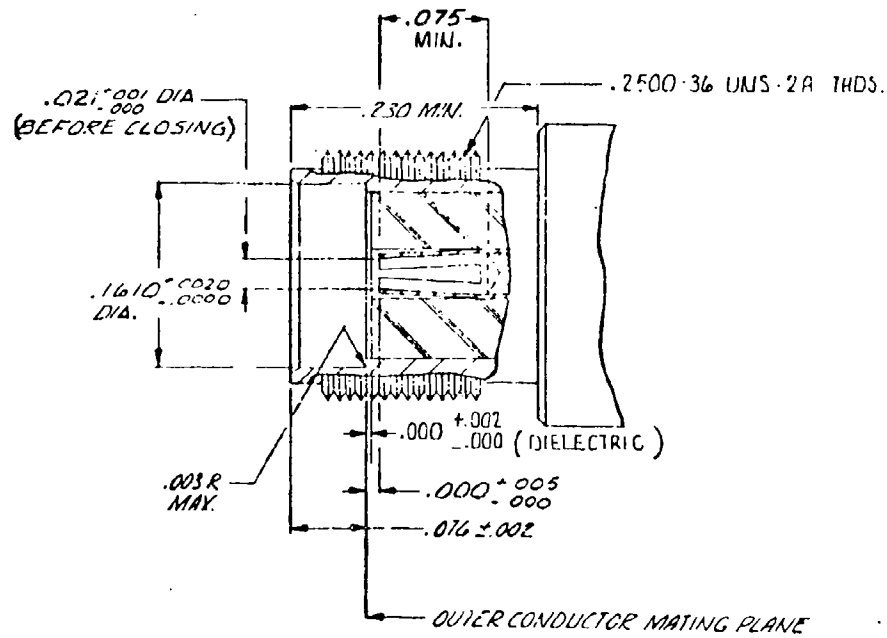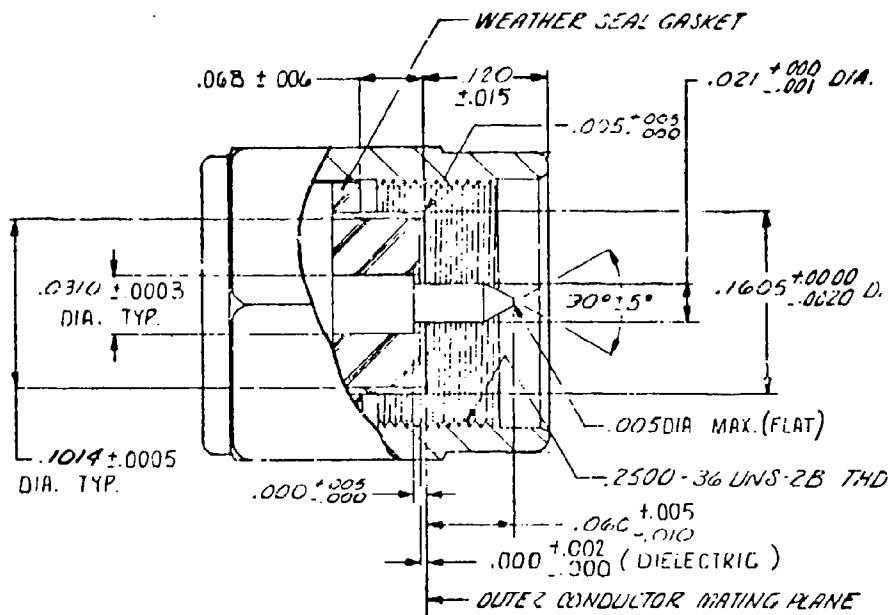
a)   female connector

b)   male connector

FIGURE 1

MPC2 Connector Interface
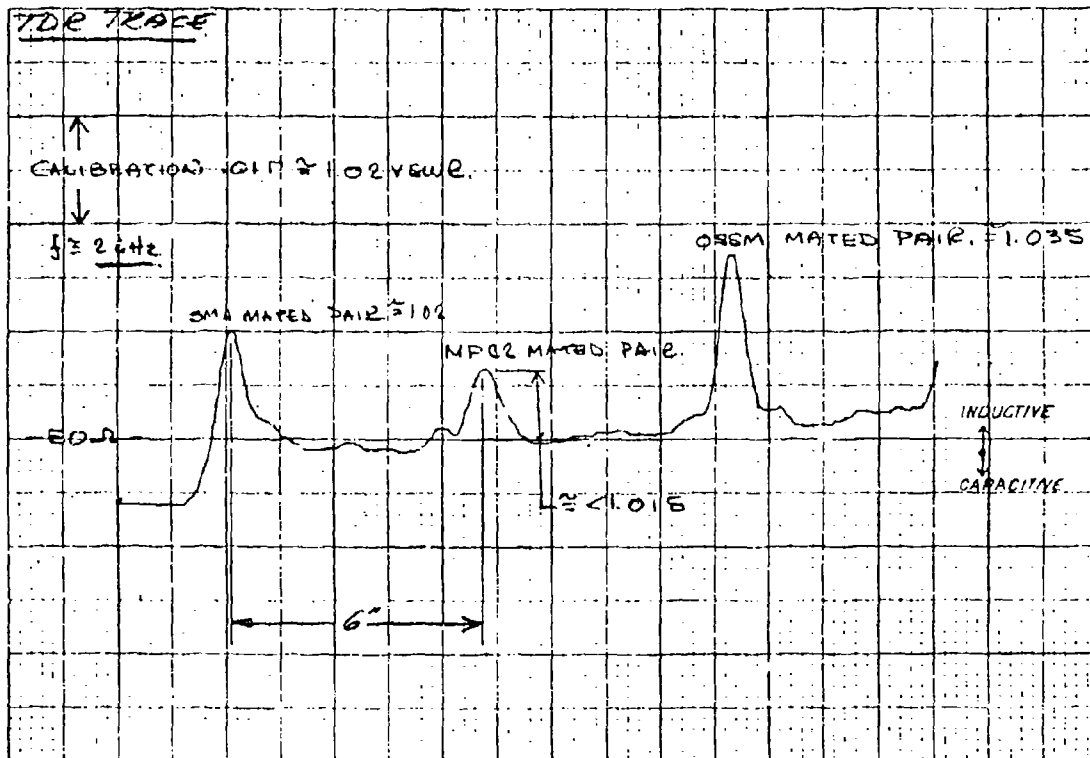
FIGURE NO. 2
TDR response, OSM, OSSM and MPC2
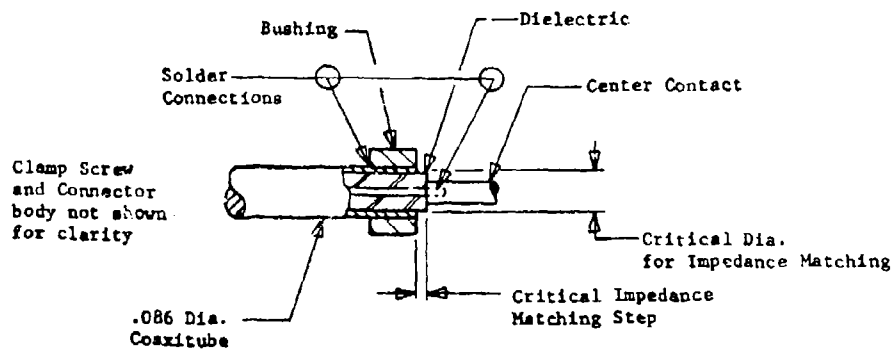
FIGURE NO. 3
MPC2 Connector, coaxitube impedance matching step
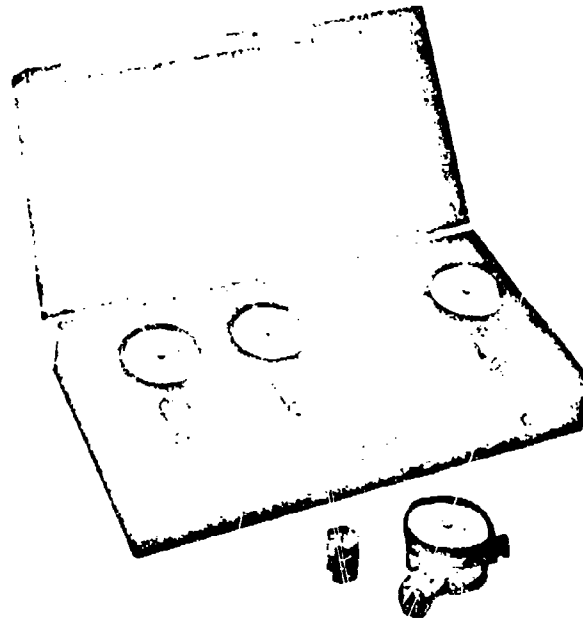
FIGURE NO. 4
MPC2 Connector Gauge, MMC Model No. A629
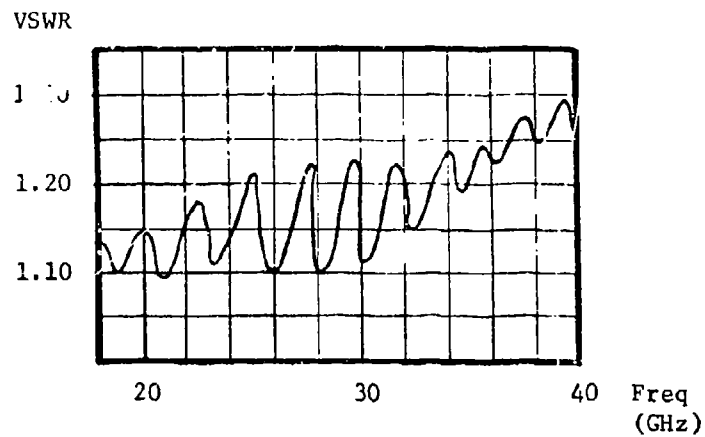
FIGURE NO. 5
Typical VSWR response .086 dia. coaxitube cable
assembly with MPC2 connectors.

Loss Variation (Normalized to Cable Loss)
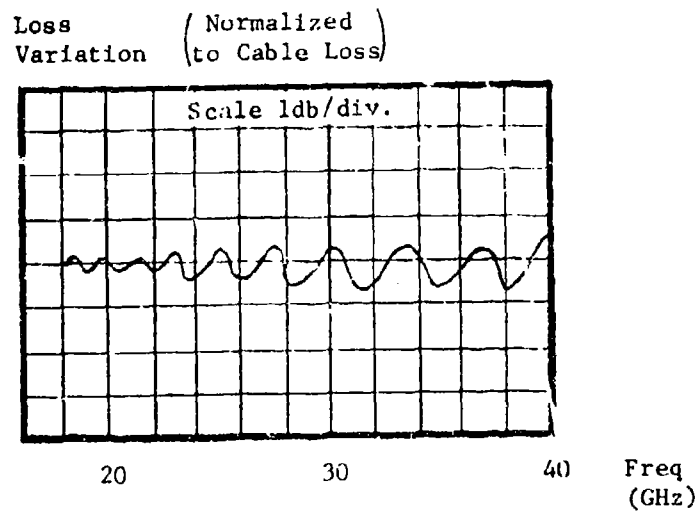
FIGURE NO. 6
.086 dia. coaxicable assembly, MPC2
connector, loss variation
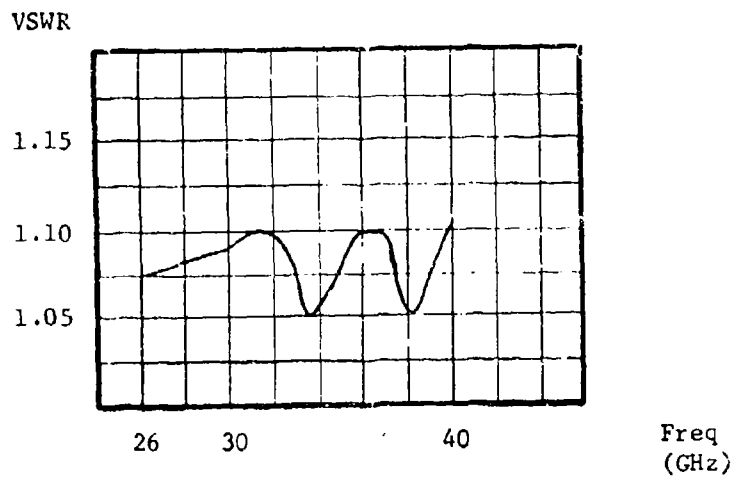
VSWR

FIGURE NO. 7
Typical VSWR response, WR28 waveguide
to MPC2 adaptor
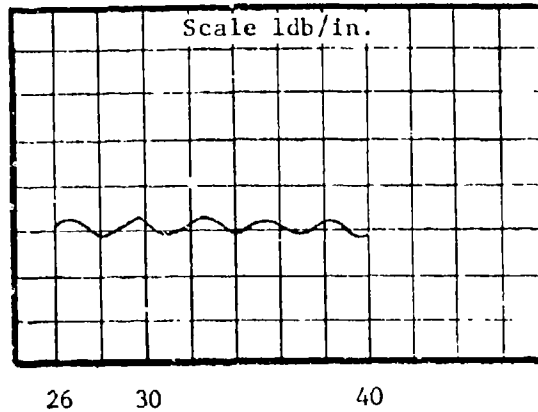
Loss Variation

FIGURE NO. 8

WR28 Waveguide to MPC2 Adaptor Loss Variation

FIGURE NO. 9

WRD180C24 to MPC2 Adaptor
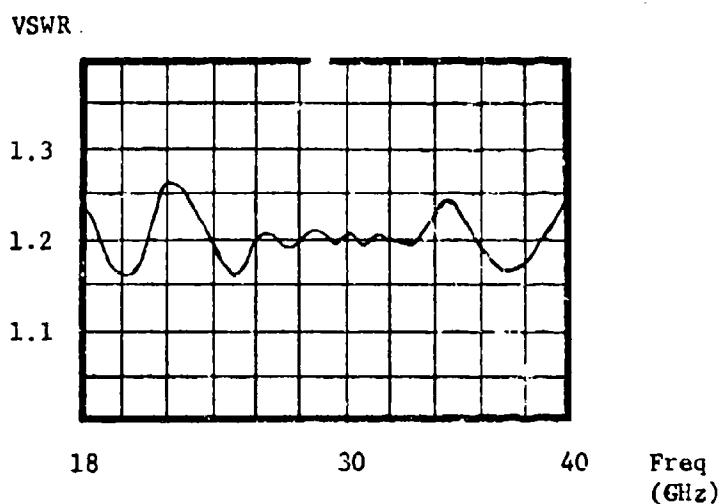
VSWR

FIGURE NO. 10
Typical VSWR response, WRD180C24
Waveguide to MPC2 adaptor
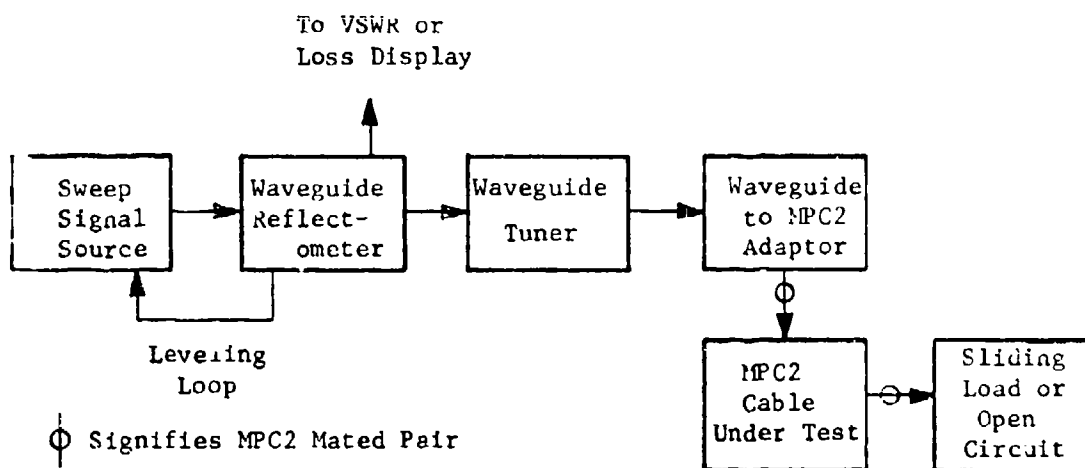
FIGURE NO. 11
Test set up to measure VSWR and loss
of MPC2 cable assembly
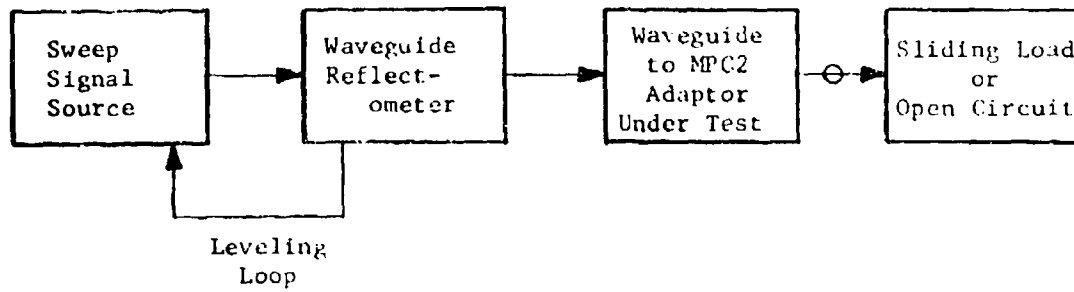
φ Signifies MPC2 Mated Pair

FIGURE NO. 12
Test set up to measure VSWR and loss of
waveguide to MPC2 adaptor

FOOTNOTES:

(1) N. Marcuvitz, Waveguide Handbook, MIT Radiation Lab Series,
     Vol. 10, McGraw Hill, New York, 1951, pp. 77.

(2) 'The GR Experimenter," August 1966, pp. 10-13.
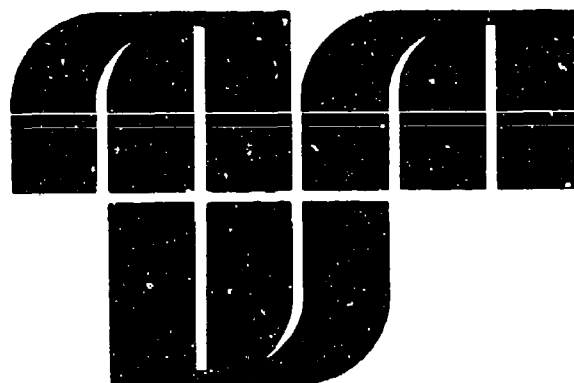
SESSION E

Standards and
Measurements;
Tubes; Radomes

MILLIMETER WAVE METROLOGY CAPABILITIES AT NBS

by

C.K.S. Miller
National Bureau of Standards
Boulder, Colorado 80302

INTRODUCTION

In the millimeter wave region between 20 and 100 GHz, the Electromagnetics Division of the National Bureau of Standards, Boulder, Colorado, has metrology capabilities in two frequency ranges. In the 20 to 40 GHz range partial coverage of measurands exist, whereas a more complete coverage exists in the 56.5 to 64.5 GHz range. This paper will highlight the recently developed capabilities in the higher frequency range (56.5 to 64.5 GHz) and only briefly touch upon the long-existing capabilities in the lower range. These capabilities are applied by NBS to measurement needs of the technical community in various ways ranging from regular calibration services to applied measurements wherein we take equipment and people to the customer's site.

CAPABILITIES IN THE 20 TO 40 GHz RANGE

Power

Low-level CW power can be measured in the 0.1 to 10 mW range. A regular calibration service is available for WR42 and WR28 waveguide bolometer units with barretter-type or thermistor-type elements and for WR42 waveguide bolometer-coupler units

with coupling ratios from 3 to 20 dB [1]. These services are
based on microcalorimeters that have been especially developed
at NBS to serve as reference power standards. Using these
basic capabilities higher power levels can be measured using
relatively simple extension techniques [2]. The actual in-
accuracies obtained are dependent upon the measurement proc-
esses used, but it is possible to achieve inaccuracies of
± 0.5% to 2.0%.

Reflection Coefficient Magnitude

Reflection coefficient magnitude measurements of waveguide
reflectors and of non-reflecting waveguide ports are available
in a regular calibration service for WR42 waveguide and in a
special calibration service for WR28 waveguide. Reflecting
waveguide ports are sometimes called standard mismatches and
the term non-reflecting waveguide port is used to indicate
that the waveguide port has been designed or adjusted with the
intent to produce a reflection coefficient magnitude, $|\Gamma|$,
equal to zero. Accurate measurements require the connector
flanges in good condition and the interior surfaces of the
waveguide accurately joined; however, accurate joining depends
upon such factors as the alignment of bolt holes, paint on the
back of the flange that can affect the seating of the bolt on
its bearing surface, and smoothness of connecting surfaces. Meas-
urements using flanges in good condition and accurately joined
can provide maximum inaccuracies as small as $\pm(0.0004 + 0.0017|\Gamma|)$
[1].

Attenuation

Attenuation measurements are available in regular calibration services in both WR42 and WR28 waveguide on variable and fixed waveguide attenuators. For attenuation difference of variable attenuators, the inaccuracies of the calibration service are for ±(0.05 dB or 0.5%), whichever is greater in the 0 to 50 dB range. For the measurement of insertion loss of variable or fixed attenuators, the inaccuracies of the calibration service are closer to 1% for WR42 waveguide and 2% for WR28 waveguide sizes [1]. In general, no high quality attenuators are available commercially that warrant a more accurate calibration service in this frequency range, but improved attenuation measurement systems have been developed [3,4] and could be implemented in this frequency range.

Noise

No noise reference standards have been developed to this date in this frequency range. Although noise measurement services could be developed readily, the minimal demand so far has not warranted the expenditure that would be required.

Antenna

No established antenna gain or pattern measurement capabilities exist for this frequency range. It is possible that antenna measurement services could be established without

much effort since the basic facilities exist and relatively few components would need to be added to extend their usefulness to these frequencies.

CAPABILITIES IN THE 56.5 TO 64.5 GHz RANGE

Metrology capabilities in this region are limited in frequency coverage from 56.5 to 64.5 GHz due primarily to the commercially available isolators and oscillators obtained when these capabilities were developed in WR15 waveguide. This frequency limitation does not apply to NBS developed reference standards which are useable from 50 to 75 GHz.

The available calibration services in this frequency range were initially announced in February 1972 [5].

Power

A microcalorimeter has been developed that serves as the NBS reference standard for power measurements [6]. The calorimeter has undergone a detailed error analysis that permits the determination of the effective efficiency of a standard bolometer unit to within a total estimated inaccuracy of $\pm$ 0.28% [6]. This total inaccuracy is composed of a systematic uncertainty of $\pm$ 0.23% and of a random uncertainty (3σ) of $\pm$ 0.05%.

Using this microcalorimeter with a transfer system it is possible to calibrate WR15 feed-through type power meters to a total estimated inaccuracy of approximately $\pm$ 1.1% for bolometer-coupler unit calibrations. A measurement technique

was implemented to evaluate a combination of two couplers to
allow for power measurements to power levels of 100 watts to an
estimated inaccuracy of ± 1.2% [7]. The end result of this
effort is that NBS can help you measure power levels from 1 mW
to 100 watts by planning a measurement with you and if need
be to bring our staff and equipment to your facility.

Reflection Coefficient Magnitude

A measurement system has been developed to measure both
reflection coefficient magnitude and attenuation [8]. The
system is based upon a 30 MHz waveguide below-cutoff attenuator
standard. A description of the system is included in NBS
Technical Note 619 together with machine drawings that provide
information on how to build such a system and the necessary
hardware that is not commercially available. The document also
discusses precision and systematic error along with equations
for estimating the limits of the error.

Basically this measurement system provides a tuned reflec-
tometer that measures the magnitude of reflection coefficient
$|\Gamma|$ to better than $\pm 0.001(1 + 3|\Gamma|)$ over the range from 0.001
to 0.99. The accuracy of a reflection coefficient measurement
is limited to the dimensional tolerances achieved in fabricating
the input waveguide section. The NBS system has an input
waveguide section whose internal dimensional tolerances are
approximately ± 15 millionths of an inch (0.38 microns); this
compares to commercial tolerances of 0.001 inch (25.4 microns).

Attenuation

The above measurement system [8] can measure attenuation difference of variable attenuators to $\pm(0.05$ dB or $0.5\%)$, which-ever is greater in the 0 to 50 dB range. It can also measure the insertion loss of fixed or variable attenuators to better than $\pm$ 2%.

In order to provide a capability to resolve precisely dif-ferences of attenuation in support of noise and antenna measure-ments, two attenuators with improved readouts were developed. An identical pair of commercial rotary-vane attenuators were modified to provide readouts in degrees of rotation of the center-vane of each attenuator. In the finished form one attenuator was significantly larger than the other and both were larger than their commercial counterparts. The smaller attenuator [9] can resolve the rotation of the center vane to 0.01 degree while the larger attenuator indicates the near-est 0.0005 degree. When properly aligned [10] the maximum attenuation values attained for these two attenuators were greater than 65 dB, which means they can resolve attenuation difference values to 0.005 dB. These attenuators track the mathematical law for rotary-vane attenuators very closely allowing the use of tables [11] to obtain their attenuation values.

Noise

A reference standard has been developed for thermal noise measurements. This WR15 standard was designed to operate

at the silver point (963.19°C) which gives an output noise temperature of about 1235 kelvins with an estimated inaccuracy of ± 2 kelvins. The details of its design, construction, and performance with an error analysis have been published [12]. This standard is useable from 50 to 75 GHz although its accuracy will vary to a small degree across this frequency range.

A total power radiometer has been developed as a comparator in order to compare the reference noise standard with an unknown. A special calibration service using these two is available and provides a measurement of the noise output of a noise-tube mount to approximately ± 2% if the reflection coefficient magnitude is less than 0.05 [13].

However, commercially available WR15 waveguide noise-tube mounts were found to have very poor reflection coefficient magnitudes and unstable noise outputs making them unsatisfactory for noise measurements. For this reason, NBS undertook to design a new noise-tube mount using a commercially available ceramic argon-filled tube [14]. This WR15 waveguide noise source design is now commercially available and has a reflection coefficient magnitude of 0.05 and a noise output instability of less than 0.005 dB at 150 ma operating current.

A computer-controlled system has been developed to provide the capability of automatically measuring a noise factor (or noise figure) to an inaccuracy of less than ± 0.2 dB or ± 0.1 dB if the value is less than 10 dB [15]. To achieve this accuracy, the output noise power ratio of an amplifier for a known input

noise power ratio must be measured to less than ± 0.01 dB.
This having been done, it is now possible to get better noise
factor (or noise figure) measurements at these frequencies
than at microwave frequencies. This measurement system is
portable and versatile and has been used to evaluate the sys-
tem gain to system noise temperature of satellite ground sta-
tions. It has allowed manufacturers of millimeter wave mixers
to assess the characteristics of a mixer for different local
oscillator power levels and types of local oscillator.

To achieve state-of-the-art noise factor (or noise figure)
measurements requires that adequate consideration be given to
the precise measurement of amplifier noise during the design
stages of equipment development so that precise noise measure-
ments can in fact be obtained on the final product and in the
final system application [16,17].

Antenna

On-axis antenna gain measurement capability with limited
pattern information has also been developed [18]. Two techniques
are employed. An indoor facility using a near-field technique
can measure an 18 inch diameter disk antenna to within ± 3.5%.
An outdoor facility using an extrapolation range can measure an
18 inch diameter disk antenna to within ± 4.5%. These capa-
bilities are more thoroughly covered in the next presentation.

Flanges

In this frequency range, the quality of flanges used on equipment is critical to the final product. At NBS, it was found that significant problems occur due to the lack of adequate military specifications of WR15 waveguide flanges. For this reason a study was conducted at 60 GHz to assess effects of variations in the flanges generally used in WR15 waveguide equipment [19]. The study revealed that 1) plain brass flanges had lower loss than any coated flanges, 2) standardization of the locations of pins and holes to a close tolerance is crucial, 3) for low loss requirements a differently designed flange with a rectangular boss the size of the waveguide may be preferable, 4) lapped flanges were more repeatable, and 5) uniformity in tightening torque of the bolts was important.

CONCLUSIONS

This paper highlights current millimeter wave measurement capabilities of the Electromagnetics Division of NBS. It is recognized that although these capabilities are limited in frequency range, magnitude, and accuracy they are more accurate than any other known millimeter wave metrology capabilities. The development of further metrology capabilities for additional quantities and additional frequency ranges is needed to fully utilize the millimeter wave frequencies. Future work should include automating these existing measurement capabilities while developing new capabilities. Automation is

necessary to facilitate the coverage of the enormous frequency
spectrum covered in each waveguide size of the millimeter wave
frequency spectrum. No new NBS metrology developments are in
progress at present although this could change if it was evident that national program needs demand it.

REFERENCES

[1] Calibration and Test Services of the NBS, National Bureau of Standards (U.S.), Special Publication 250 (December 1970).

[2] Bramall, Kenneth E., Accurate Microwave High Power Measurements Using a Cascaded Coupler Method, J. Res. Nat. Bur. Stand. (U.S.), 75C, Nos. 3 & 4 (December 1971).

[3] Schafer, G.E., and Bowman, R.R., A Modulated Sub-Carrier Technique of Measuring Microwave Attenuation, Proc. IEE (London), 109, Part B., Suppl. 23, 783-786 (May 1962).

[4] Larson, Wilbur and Campbell, Eugene, Microwave Attenuation Measurement System (Series Substitution), Nat. Bur. Stand. (U.S.), Tech. Note 647, 28 pages (February 1974).

[5] Measurement Users Bulletin No. 3, Supplement to Nat. Bur. Stand. (U.S.) Special Publication 250 (February 1973).

[6] Harvey, M.E., WR15 Microwave Calorimeter and Bolometer Unit, Nat. Bur. Stand. (U.S.), Tech. Note 618, 41 pages (May 1972).

[7] Weidman, M.P., Calibration and Application of WR15 Feed-Through Type Power Meters, 45 pages (unpublished NBS report).

[8] Yates, B.C., and Larson, W., Millimeter Attenuation and Reflection Coefficient Measurement System, Nat. Bur. Stand. (U.S.), Tech. Note 619, 175 pages (July 1972).

[9] Foote, W.J. and Hunter, R.D., Improved Gearing for Rotary-Vane Attenuators, Rev. of Sci. Instruments, 43, No. 7, 1042-1043 (July 1972).

[10] Larson, W., Analysis of Rotationally Misaligned Stators in the Rotary-Vane Attenuator, IEEE Trans. on I&M, IM-6, No. 3, 225-231 (Sept. 1967).

[11] Larson, W., Table of Attenuation as a Function of Vane Angle for Rotary-Vane Attenuators, Nat. Bur. Stand. (U.S.), Tech. Note 229, __ pages (January 1965).

[12] Daywitt, W.C., Foote, W.J., and Campbell, E., WR15 Thermal Noise Standard, Nat. Bur. Stand. (U.S.), Tech. Note 615, 154 pages (March 1972).

Daywitt, W.C., A Reference Noise Standard for Millimeter Waves, IEEE Trans. on MTT, MTT-21, No. 12, 845-847 (Dec. 1973).

[13] Wait, D.F., Error Analysis of the WR15 Noise Temperature Calibration Service, (in preparation).

[14] Miller, C.K.S. and Kanda, M., A Noise Tube Mount for Millimeter Waves, (in preparation).

[15] Boyle, D.R., Clague, F.R., Reeve, G.R., Wait, D.F., and Kanda, M., An Automated Precision Noise Figure Measurement System at 60 GHz, IEEE Trans. on I&M, IM-21, No. 4., 543-549 (Nov. 1972).

[16] Wait, D.F., Considerations for the Precise Measurement of Amplifier Noise, Nat. Bur. Stand. (U.S.), Tech. Note 640, 129 pages (August 1973).

Wait, D.F., Measurement of Amplifier Noise, Microwave Journal, 16, No. 1, 25-29 (January 1973).

[17] Engen, G.F., Mismatch Considerations in Evaluating Amplifier Noise Performance, IEEE Trans. on I&M, IM-22, No. 3, 274-278 (Sept. 1973).

[18] Newell, A.C., Baird, R.C., and Wacker, P.F., Accurate Measurement of Antenna Gain and Polarization at Reduced Distances by an Extrapolation Technique, IEEE Trans. A&P, AP-21, No. 4, 418-431 (July 1973).

[19] Yates, B.C. and Counas, G.J., Summary of WR15 Flange Evaluation at 60 GHz, Nat. Bur. Stand. (U.S.), Tech. Note 642, 32 pages (October 1973).

The Accurate Determination of Millimeter-Wave Antenna
Characteristics by Deconvolution and Extrapolation Techniques
by
R.C. Baird and D.M. Kerns
National Bureau of Standards
Boulder, Colorado 80302

SUMMARY

1.0 Introduction

The recent availability of mm-wave oscillators with adequate power
has resulted in a rapid expansion in the use of mm-wave systems for space
and satellite communications and other applications requiring high gain
antennas of relatively small physical size. These systems are generally
sophisticated and expensive, and close tolerances are required on several
parameters, including antenna power gain. For some systems, the antenna
polarization and pattern must also be well known. Consequently, high-
accuracy antenna calibrations are required to avoid expensive overdesign
and to assure adequate performance of the overall systems. Requirements
for gain calibrations with total uncertainties (3σ) of 0.1 dB or less are not
uncommon, and it is difficult to measure the gain of any antenna to this accu-
racy.

The most common method of determining antenna gain and polarization
is a substitution technique, where the response of the test antenna to an in-
cident "plane-wave" field is compared with that of one or more standard an-
tennas. With conventional "far-field" antenna ranges, the plane-wave con-
dition is approximated by using large separation distances between the trans-
mitting and receiving sites. (An optional approach to obtaining an approx-
imate plane wave is the "compact range" technique described by Johnson
et al. [1,2]) However, for high gain antennas, ranges of sufficient length may
not be available. This is especially true when high accuracy is desired. For
example, to reduce the proximity correction of a typical standard gain horn
to less than 0.1 dB requires a distance of about 16 (not 2) a^2/λ, where a is

the largest aperture dimension and λ is the free space wavelength. At such large distances the errors due to ground reflections and scattering from other objects can be significant. Additional errors can occur if the test and unknown antennas have significantly different gains, patterns, or polarization characteristics. Further, even if the errors due to all of the above effects could be brought under control, one would still be faced with the problem of accurately determining the gain of the standard antenna. The strong atmospheric attenuation (more than 10 dB/km at some frequencies) precludes the use of the far-field three-antenna method of determining absolute gain over much of the mm-wave frequency range. In addition, calculated gain and polarization values of a "standard" antenna do not in general, provide a satisfactory basis for high accuracy measurements. Due to computational approximations and imperfect fabrication, the calculated values are usually outside the error limits of (highly) accurate measurements, although the computational accuracy may be better for certain specialized cases [3].

This summary presents samples of the experimental results of two recently developed techniques for accurately determining absolute gain, polarization, and pattern from data obtained at greatly reduced distances. Both methods are based on a relatively new theoretical approach (developed by D.M. Kerns of the National Bureau of Standards) which we refer to as the "plane-wave scattering-matrix theory of antennas and antenna-antenna interactions". The theory is essentially free of restrictive assumptions and built-in approximations and the measurement results have demonstrated that high accuracy is attainable. Further, the methods are applicable to any type of directive antenna, including phased arrays. The techniques are useful at all microwave frequencies, but are especially valuable at mm-wave frequencies where high-gain antennas are physically small enough to work with in the laboratory, and where the large Rayleigh distances and atmospheric attenuation make conventional measurements particularly difficult.

---

* A recent survey paper by Johnson et al. [2] discusses several other approaches to the problem of determining far-field antenna patterns from near-field measurements and gives many references. Some of the approaches may now be of only historical interest.

2.0 Deconvolution Technique

The planar scan-deconvolution technique was formulated for antennas by Kerns [4]. Experimental results have been given by Baird et al. [5] and by Joy and Paris [6]. Here we shall outline very briefly some of the main qualitative and quantitative features of the technique.

For this discussion (as well as for the discussion of the extrapolation technique below) a few preliminary definitions are essential. The propagation vector $\underline{k}$ for plane waves in space is resolved into a transverse (x,y) part $\underline{K}$ and an axial part $\gamma \underline{e}_z$ ($\underline{k} = \underline{K} + \gamma \underline{e}_z$) and is subject to $\underline{k} \cdot \underline{k} = \omega^2 \mu\epsilon$. We employ a pair of two-component vector functions, $\underline{S}_{10}(\underline{K})$ and $\underline{S}'_{02}(\underline{K})$, representing respectively the transmitting characteristics of a transmitting antenna and the receiving characteristics of a receiving antenna; the independent variable $\underline{K}$ serves to specify the direction associated with each spectral component. Without attempting to give complete definitions we note that the far-field vectorial pattern of the transmitting antenna, hence the power gain and polarization characteristics, can be computed from $\underline{S}_{10}(\underline{K})$.
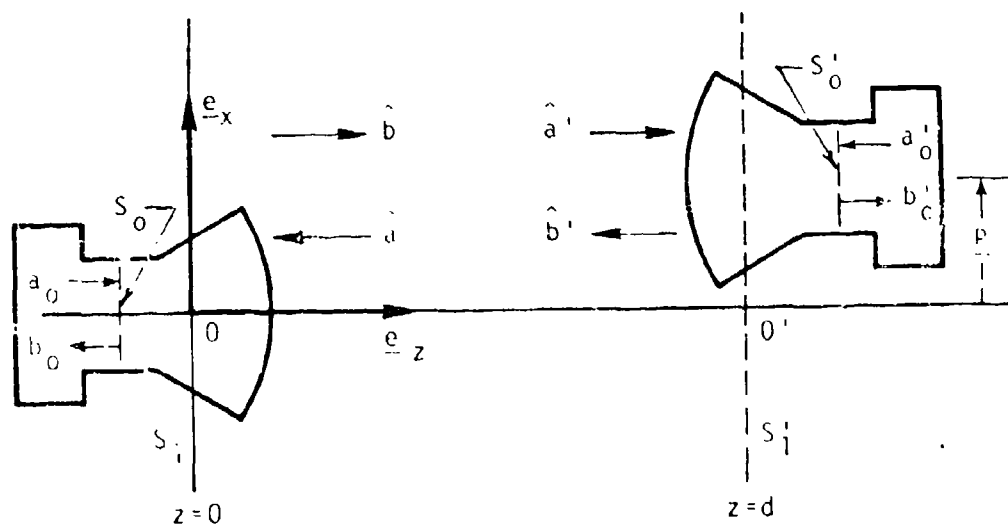
Fig. 1. Arrangement for transverse scanning: d is fixed, $\underline{P}$ is variable.

In describing the deconvolution technique we suppose that the radiating characteristic $\underline{S}_{10}(\underline{K})$ of the transmitting antenna shown schematically on the left in Figure 1 is to be determined with a known receiving antenna

(i.e., one with $\underline{S}'_{02}(\underline{K})$ known) on the right, which is used to scan the field of the transmitting antenna in a transverse plane (z = const) a short distance ($d \ll a^2/\lambda$) away from the transmitting antenna. If (as is required in this technique) multiple reflections between antennas are negligible, then the radiated spectrum $\underline{S}_{10}(\underline{K})$ is given rigorously in terms of the Fourier transform of the transverse $\underline{E}$ in the measurement plane. What we may call an ideal probe would measure one of the transverse components of $\underline{E}$ directly, even in the near field; an actual probe, however, yields a response $b'_o(\underline{P})$ given by a convolution integral involving both the structure of the field and the characteristics of the probe itself. The convolution integral is represented in the spatial frequency domain by

$$ b'_o(\underline{P}) = a_o F' \int\int_{-\infty}^{\infty} \underline{S}_{10}(\underline{K}) \cdot \underline{S}'_{02}(\underline{K}) e^{i\gamma d} e^{i\underline{K}\cdot\underline{P}} dk_x \, dk_y \tag{1} $$

where $\underline{P}$ is a transverse vector specifying the displacement of the probe (Fig. 1), a_o is the input wave-amplitude at the transmitter, and F' is a mismatch factor associated with the receiving antenna and its load. Deconvolution is effected by Fourier transformation and yields

$$ \underline{S}_{10}(\underline{K}) \cdot \underline{S}'_{02}(\underline{K}) = \frac{e^{-i\gamma d}}{4\pi^2 a_o F'} \int\int_{-\infty}^{\infty} b'_o(\underline{P}) e^{-i\underline{K}\cdot\underline{P}} dx\,dy \tag{2} $$

Using band limits $k_1 = 2\pi/\lambda_1$ and $k_2 = 2\pi/\lambda_2$ for k_x and k_y, respectively, and applying a two-dimensional, spatial sampling theorem enables us to replace the above integral by a sum,

$$ \underline{S}_{10}(\underline{K}) \cdot \underline{S}'_{02}(\underline{K}) \cdot \frac{e^{-i\gamma d}}{4 k_1 k_2 F' a_o} \sum_{r,s} b'_o(\underline{P}_{rs}) e^{-i\underline{K}\cdot\underline{P}_{rs}} \tag{3} $$

Here, the vectors $\underline{P}_{rs} = \frac{1}{2} r \lambda_1 \underline{e}_x + \frac{1}{2} s \lambda_2 \underline{e}_y$ (with r, s = ... -2, -1, 0, 1, 2...) define the measurement lattice, the $b'_o(\underline{P}_{rs})$ are the (complex) values of probe

output directly observed at the points of the lattice, and the summation goes over the points of the lattice. The great virtues of (3) are that data can be taken at the points of a discrete lattice without loss of desired information and that the highly efficient fast Fourier transform algorithm is rigorously applicable to evaluation of the sum. The theorem requires an infinite lattice, but in practice we have found that taking data over an area somewhat larger than the transmitting antenna aperture is sufficient to insure full accuracy in the results.

We should note that (3) determines only one linear combination of the two components of the unknown $S_{10}(\underline{K})$ for each value of $\underline{K}$. In general, one must make two complete transverse scans using measuring antennas chosen to give independent linear combinations. (In many cases a single antenna used in two orientations 90 degrees apart would suffice.) Thus one obtains pairs of linear equations that can be solved for the components of $S_{10}(\underline{K})$ with $\underline{K}$ in the role of a parameter.

Band limits $k_1 = k_2 = k$ have been found satisfactory as a rule of thumb when essentially complete pattern information is desired. These band limits correspond to $\lambda/2$ as an approximate minimum spacing of measurement points and mean that a relatively large number of data are required--typically phase and amplitude for approximately 4,000 to 40,000 points.

Efficient application of the technique practically demands use of an automated precision scanner and requires computer capability to process such large numbers of data. At NBS the previous partially automated scanner is being replaced by a larger, more fully automated mechanism capable of rapidly acquiring data over an area up to 4.5 meters square.[*] (In a typical mm-wave application, such as that discussed in the next paragraph, data from 128 x 128 points in a $60 \times 60 \text{ cm}^2$ area should be obtainable in less than half an hour.) Computation times are nominal, ranging from 15 to 60 seconds on a modern

---

[*] In both the deconvolution and the extrapolation technique, normalization of probe output (b') to transmitting antenna input (a_0) is required. In the facilities for the two techniques, provision is made for bringing source and receiver close together (with the antennas not in place!) so that this normalization can be easily and properly effected.
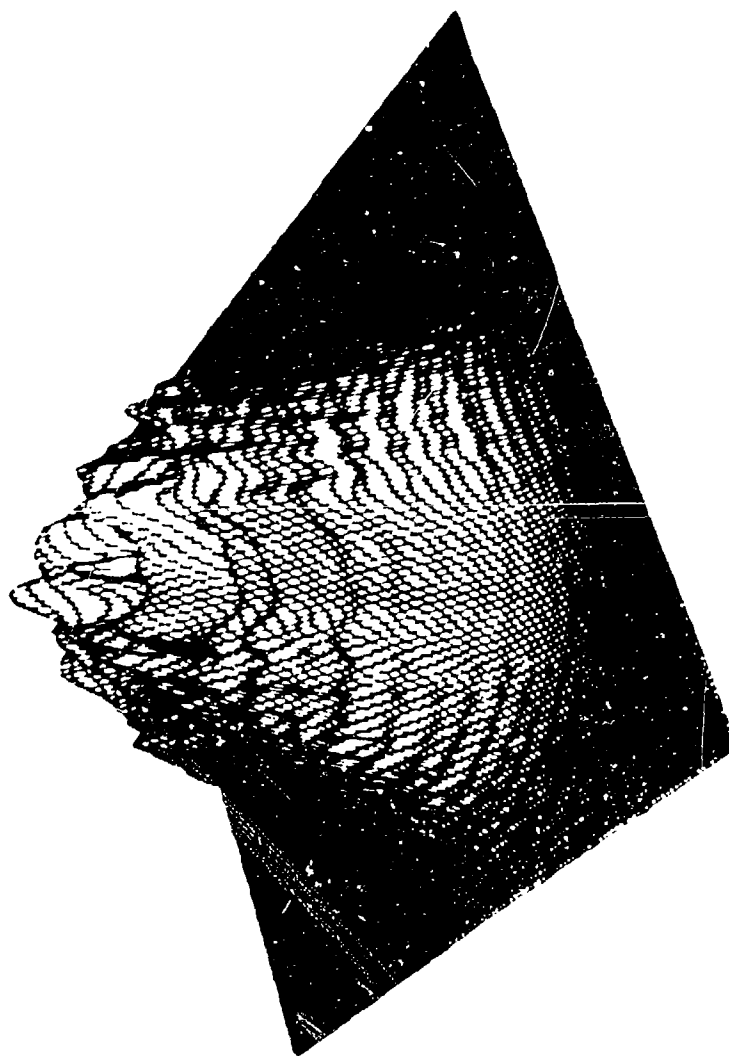
Fig. 2. Magnitude of $b'_o(\underline{P})$ over scan area.
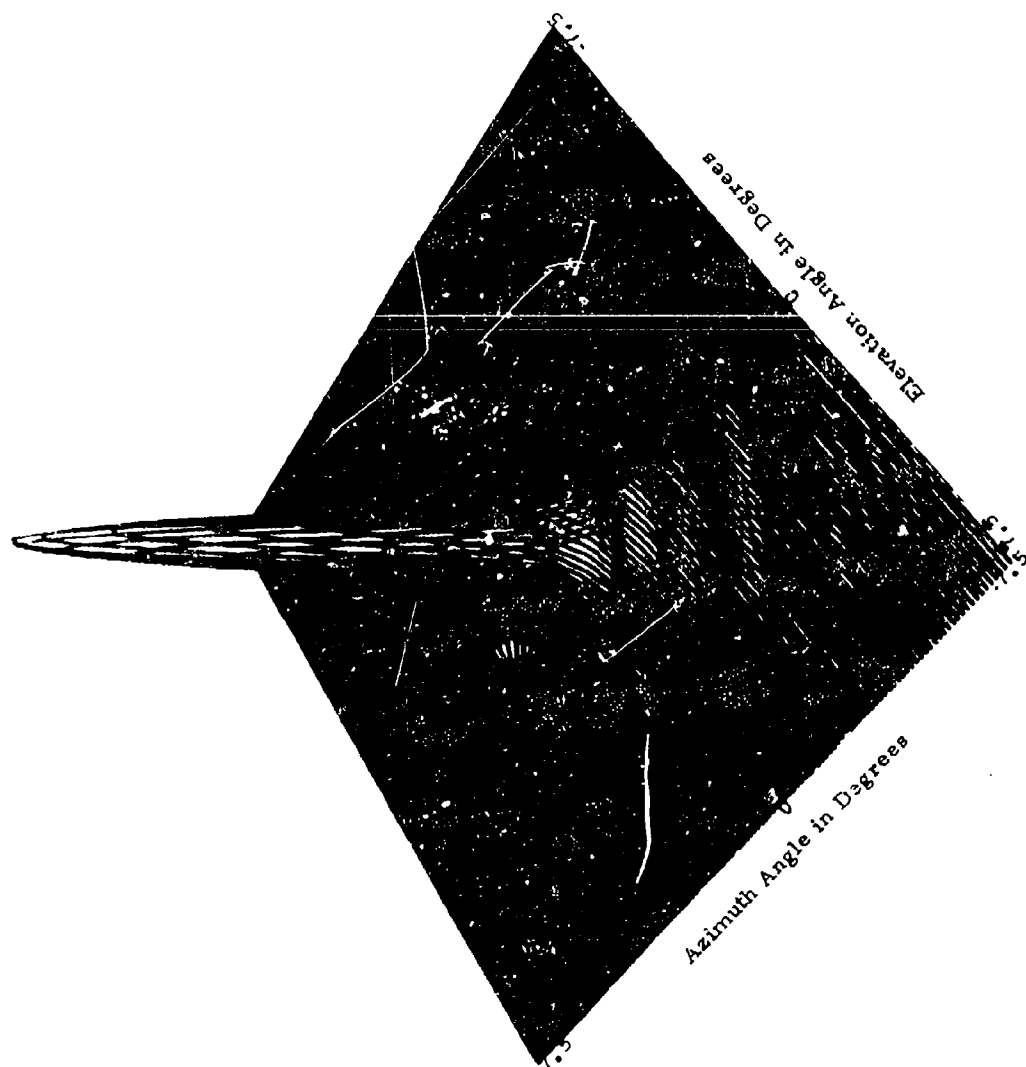
Fig. 3. Magnitude of far-field computed from near-field data.

high speed computer. This includes all data processing and computation ex-
cept that involved in the production of   perspective plots of the type shown
in Figs. 2 and 3, which may require 30 seconds to several minutes of lower-
cost computer time.

Figures 2 and 3 show graphically the character of the input and output
data for a Cassegrain antenna 46 cm in diameter operated at approximately
60 GHz. Data were taken in a plane approximately 50 cm away from the
antenna, using a small standard-gain horn oriented for (approximate) polar-
ization match. In Fig. 2 are plotted the values of $|b'_o(P)_{rs})|$ so obtained;
these data may or may not closely resemble a plot of the magnitude of the
corresponding transverse component of $\underline{E}$. Fig. 3 pictures the far-field
magnitude calculated from the near-field data. The on-axis power gain was
found to be 46.42 ± 0.19 dB (3σ). In this example both the contribution of
cross-polarization and the probe-pattern correction were negligible in the
narrow angular region of interest. Of course the correction for probe gain
on axis was not negligible; in fact the uncertainty in the probe gain contrib-
uted a large share of the uncertainty in the reported antenna gain. (Signif-
icantly better accuracy in probe gain and pattern determination is now poss-
ible.)

3.0   Extrapolation Method

The second method is known as an extrapolation technique and is used
primarily to determine on-axis gain and polarization to high accuracy (it can
also be used to advantage for less accurate measurements). This method is
not as well suited to pattern measurements, although pattern information
can be obtained.   The theoretical basis was developed by Wacker [7], and
its application to accurate antenna measurements has been described very
briefly by Newell and Kerns [8] and more fully, in an experimentally
oriented paper, by Newell et al. [9].

The main result of the extrapolation theory is, that for any two essen-
tially arbitrary antennas (see Fig. 1), the received signal $b'_o(d)$ can be
accurately represented as a function of separation distance d by the series

E2-8

$$b_o'(d) = a_o F' \left\{ \frac{e^{ikd}}{d} \left(A_{00} + \frac{A_{01}}{d} + \frac{A_{02}}{d^2} + \frac{A_{03}}{d^3} + \ldots \right) \right.$$

$$\left. + \frac{e^{3ikd}}{d^3} \left(A_{10} + \frac{A_{11}}{d} + \frac{A_{12}}{d^2} + \ldots \right) + \frac{e^{5ikd}}{d^5} \left(A_{20} + \ldots \right) + \ldots \right\}, \tag{4}$$

where the A's are complex coefficients. Equation (4) includes both proximity effects and multiple reflections between antennas without approximation and is an asymptotic function of the separation distance. Specifically, the first series represents the direct transmission signal, the second series the first order multiple reflection between the two antennas, and the other series the higher order multiple reflections. It is evident that, at sufficiently large distances, the only significant term in the series is the one involving A_{00}. Further, it can be shown [9] that

$$A_{00} = -2\pi ik \, \underline{S}_{10}(0) \, \underline{S}_{02}'(0) \tag{5}$$

evaluated on axis (i.e., with $\underline{K} = 0$). If either $\underline{S}_{10}(0)$ or $\underline{S}_{02}'(0)$ is known, the unknown vector can be obtained from two independent determinations of A_{00} which give two simultaneous equations like (5). Hence, the immediate measurement objective is the determination of A_{00}.

In conventional far-field measurements, d is made large enough so that the only significant term in (4) is that involving A_{00}. The basic idea of the extrapolation technique is to observe b_o' as a function of d and to fit this function with as many terms of (4) as may be significant, and so to determine a good value for A_{00} in particular. The term "extrapolation" is, of course, derived from the fact that measurements are carried out at finite distances and used to obtain results valid for infinite separation. The actual distance interval over which measurements are made will depend on the antennas and the desired accuracy, but will usually lie somewhere between $0.2a^2/\lambda$ and $2a^2/\lambda$.

The two "independent" measurements are achieved in many cases by rotating one antenna about its axis by 90°, as mentioned in the deconvolution

method. If a suitable known antenna is not available then the "three-antenna method" can be employed to determine the absolute gain and polarization of a standard. In this approach, two independent measurements are required for each of three pair-wise combinations of the three antennas, which provide six simultaneous equations that can be solved for the desired quantities.

This method requires a special range with provision for accurate longitudinal movement of one or both antenna tow rs. However, the range dimensions are only 1/5 to 1/10 as large as would be required with a conventional range to obtain equal accuracy, so many antennas can be measured on a relatively small indoor range. The NBS presently has both a 5 meter indoor range and a 60 meter outdoor range. Angular alignment can be maintained within 0.02^{o} and transverse displacements are less than 1 or 2 millimeters on the outdoor range; the corresponding figures for the indoor range are 0.01^{o} and 0.5 millimeters.

The first step in the measurement process is to connect the generator and load ports together to obtain a reference signal (see footnote page E2-6). The antennas are then installed and the received signal b'_o is recorded as a function of separation distance. Figure 4 displays some typical data. The oscillations are due to multiple reflections between the antennas (because of the large height-to-distance ratio ground reflections are not observed in many cases). In the fitting process, the values of $\left| b'_o(d)d \exp(-ikd)/(a_o F') \right|^2$ were averaged locally, and the averaged curve was fitted with a polynomial in $1/d$ (ordinarily 4 or 5 terms will suffice). This procedure determines $\left| A_{00} \right|$; the phase of A_{00} is determined separately (see [9]). An example of the type of results obtained by the fitting procedure is given in Fig. 5, which shows the measured data for an X-band conical horn fitted with a 5-term polynomial. The magnified differences between the measured and fitted curve qualitatively indicate the goodness of fit.

The gain of this horn was determined to be 22.05 ± 0.08 dB, which should be compared respectively with values of 22.10 ± 0.15 dB and 22.02 ± 0.10 dB determined by the deconvolution method and a far-field pattern integration method (including correction for antenna loss) [10]. The gain of the mm-wave
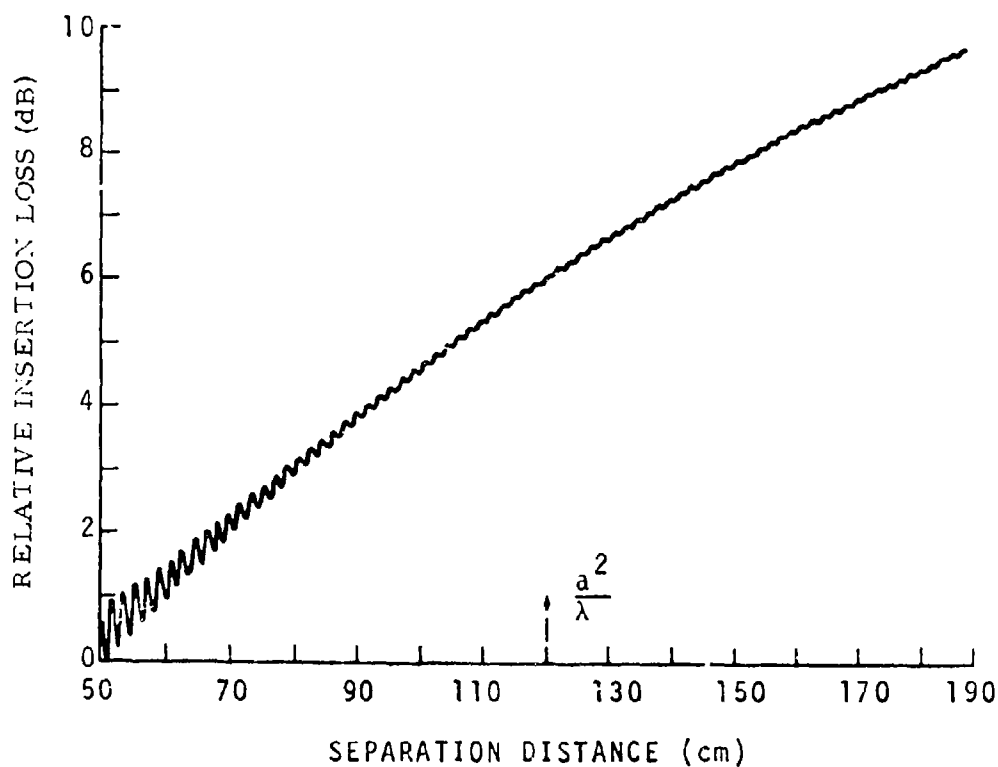
Fig. 4. Extrapolation data for two X-band standard gain horns.
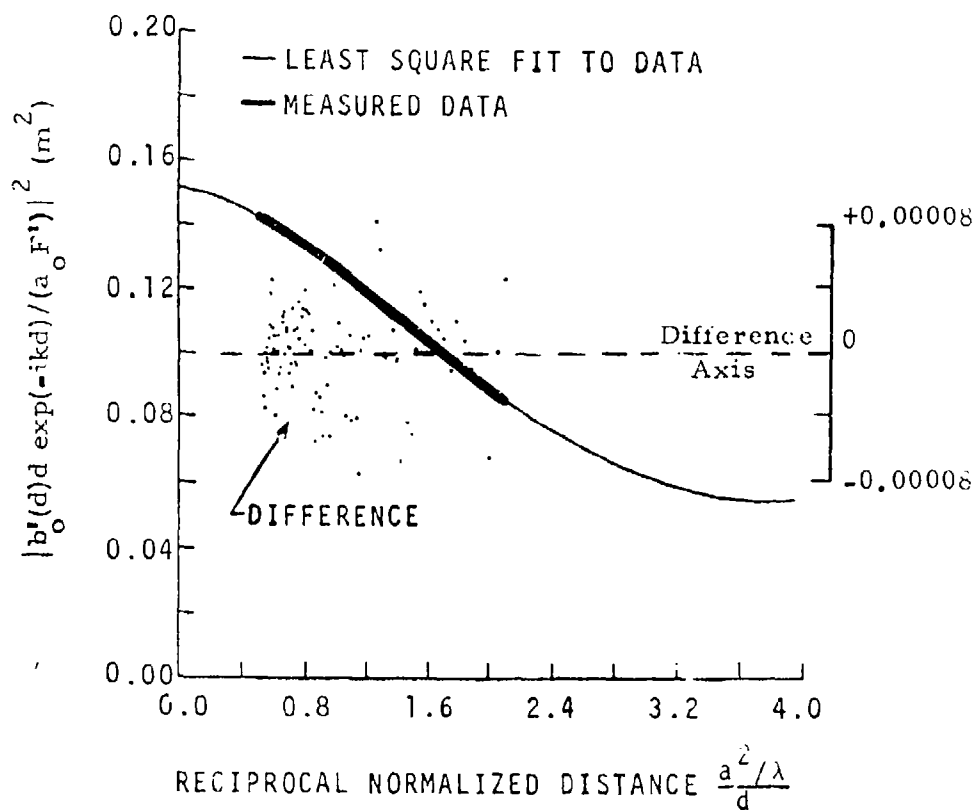
Fig. 5. Measured data, 5-term polynomial fit, and residuals for X-band conical horn (gain ≈22 dB).

antenna described in section 2.0 was determined by the extrapolation technique to be 46.26 ± 0.23 dB compared to a value of 46.42 ± 0.19 for the deconvolution method. In the extrapolation measurement, the larger errors for the mm-wave antenna were due to the relatively large uncertainty in the correction for atmospheric effects. All of the above uncertainties are 3σ values. We emphasize that the results presented here are only a sample of the many and varied measurements which have been performed at the NBS with these techniques.

REFERENCES

[1] R.C. Johnson, "Compact range techniques and measurements," IEEE Trans. Antennas Propagat., vol. AP-17, no. 5, pp.568-576, Sept. 1969.

[2] Richard C. Johnson, H. Allen Ecker, and J. Searcy Hollis, "Determination of far-field antenna patterns from near-field measurements," Proc. IEEE, vol. 61, no. 12, pp. 1668-1694, Dec. 1973.

[3] E.V. Jull, "Errors in the predicted gain of pyramidal horns," IEEE Trans. Antennas Propagat., vol. AP-21, pp. 25-31, Jan. 1973.

[4] D.M. Kerns, "Correction of near-field antenna measurements made with an arbitrary but known measuring antenna," Electron. Lett., vol. 6, pp. 346-347, May 1970.

[5] R.C. Baird, A.C. Newell, P.F. Wacker, and D.M. Kerns, "Recent experimental results in near-field antenna measurements," Electron. Lett., vol. 6, pp. 349-351, May 1970.

[6] E.B. Joy and D.T. Paris, "Spatial sampling and filtering in near-field measurements," IEEE Trans. Antennas Propagat., vol. AP-20, pp. 253-261, May 1972.

[7] P.F. Wacker, "Theory and numerical techniques for accurate extrapolation of near-zone antenna and scattering measurements," NBS, Boulder, Colo., unpublished rep., Apr. 1972.

[8] A.C. Newell and D.M. Kerns, "Determination of both polarization and power gain of antennas by a generalized 3-antenna measurement method," Electron. Lett., vol. 7, pp. 68-70, Feb. 11, 1971.

[9] Allen C. Newell, Ramon C. Baird, and Paul F. Wacker, "Accurate measurement of antenna gain and polarization at reduced distances by an extrapolation technique," IEEE Trans. Antennas Propagat., vol. AP-21, no. 4, pp. 418-431, July 1973.

[10] Arthur C. Ludwig and Richard A Norman, "A new method for calculating correction factors for near-field gain measurements," IEEE Trans. Antennas Propagat., vol. AP-21, no. 5, September 1973.

DUAL POLARIZED RADAR CROSS SECTION MEASUREMENTS

AT MILLIMETER WAVELENGTHS

by

E. E. Martin and T. M. Miller

Radar Divison

Engineering Experiment Station

Georgia Institute of Technology

Atlanta, Georgia 30332

INTRODUCTION

Significant advantages may be gained by the operation of a radar
system in the millimeter wave region. Important advantages are the
improved angular resolution, superior Doppler characteristics, poten-
tially increased target radar cross section, reduction in equipment
size and weight and the possibility of improved cost-effectiveness.

Important considerations in the application of millimeter wave
radar are the characteristics of the backscatter signal to be processed.
To properly define the radar parameters required to accomplish a partic-
ular mission, it is necessary to have good estimates of the average value,
variability, polarization properties, Doppler characteristics, etc., for
target and clutter.

The Radar Division of the Engineering Experiment Station at Georgia
Tech has recently developed a dual-polarized instrumentation radar at
70 GHz based on previous multi-polarization radars [1]. The 70 GHz radar
operates in a synchronized mode with a dual-polarized 16 GHz radar.
Thus, dual-polarized backscatter characteristics of targets and clutter
at 16 GHz and 70 GHz can be compared under idential conditions.

Automated computer analysis capability has been used to determine
statistical characteristics of the backscatter for 16 and 70 GHz. The
analysis capability includes plots of time series, probability density
and distribution functions, auto- and cross-coverience functions, and
power density spectrum functions.

This paper describes the dual-polarized measurement radar and presents initial measurement results comparing backscatter charaacteriaitcs at 16 and 70 GHz using the automated computer analysis capability.

POLARIZATION PROPERTIES OF TARGETS

Amplitude, phase, range and polarization information is available from pulsed radar signals. Although often not fully exploited in radar, polarization properties may offer significant advantages in discrimination [2]. However, to take advantage of the available polarization information, a certain amount of sophistication within the radar and its associated signal processor is implied. For many years the Radar Division of the Engineering Experiment Station at Georgia Tech has been conducting at 10 and 16 GHz polarization reflectivity measurements of targets and clutter to determine the radar polarization discrimination potential for a wide range of applications.

The polarization of a radar signal reflected from an object is a function of the polarization of the illuminating wave and the geometrical properties of the target. The resultant field of the scattered wave, $\overline{E}^s$, may be described in terms of the polarization scattering matrix as

$$\overline{E}^s = \begin{bmatrix} E_\theta^s \\ E_\varphi^s \end{bmatrix} = \begin{bmatrix} a_{11} & a_{12} \\ a_{21} & a_{22} \end{bmatrix} \begin{bmatrix} E_\theta^t \\ E_\varphi^t \end{bmatrix} \frac{e^{-jkR}}{\sqrt{4\pi R^2}}$$

where

$$R = \text{range}$$
$$k = 2\pi/\lambda$$

and E_θ^s and E_φ^s are the scattered field components and E_θ^t and E_φ^t are the transmitted field components polarized in the θ and φ directions, respectively. The elements of the polarization scattering matrix are complex terms representing the amplitude and phase scattering properties of the target for the two orthogonal polarization components. For the special case of linear horizontal and vertical polarizations, the matrix may be

written as

$$\overline{\overline{A}} = \begin{bmatrix} a_{HH} & a_{VH} \\ a_{HV} & a_{VV} \end{bmatrix}$$

where the subscripts represent the transmitted and received polarization, respectively.

The polarization scattering matrix is entirely a property of the target and its spatial orientation and completely describes the scattered fields from the target. If the elements of the polarization scattering matrix are known, the radar cross section for any given combination of transmitting and receiving polarizations can be computed. For example, in the simple case of the radar cross section corresponding to the matrix elements of the first column the result would be

$$\sigma_{HH} = |a_{HH}|^2$$

and

$$\sigma_{HV} = |a_{HV}|^2$$

For simple radar targets the coefficients of the scattering matrix may be calculated. However, as targets become more complex such calculations become impractical and evaluation of the coefficients must be accomplished through direct measurements.

MEASUREMENT EQUIPMENT

K_u-band Radar

Dual-polarized measurements of radar reflectivity were made simultaneously at 16.2 GHz and at 69.8 GHz. The 16.2 GHz measurements were made with the Georgia Tech GT-2 Mobile Radar. This radar is permanently installed in a van equipped with a self-contained 15 KVA, 60 Hz gasoline

powered generator. The K_u-band radar generates a 60 ns pulse with 4 KW peak power. The antenna used for these measurements was a 9 inch paraboloidal dish with a 5.2 degree beamwidth and a dual-polarized feed. Horizontal polarization was selected for the transmitted wave. Both the horizontal and vertical components of the backscattered wave are received by the antenna and routed to the proper receiver channel by a dual mode coupler located at the antenna feed. The radar receiver consists of two idential receive channels. Each mixer, supplied by a common local oscillator, is followed by I.F. attenuators and logarithmic I.F. amplifiers.

E-band Radar

A 69.8 GHz radar was modified to provide for dual-polarized radar reflectivity measurements. The modification consisted of repackaging and adding a separate cross (orthogonal) signal channel to the receiver. This system configuration is similar to the K_u-band radar with the exception of the precision R.F. attenuators, isolators in the local oscillator feeds, and a common transmit-receive antenna. Three separate antennas were used in this system: one each for receiving the horizontally and vertically polarized components in the reflected wave and one for transmitting the horizontally polarized transmitted wave. The three antennas are identical horns having beamwidths of approximately 6 degrees and gains of 29 dB. This antenna configuration was chosen because of the greater polarization isolation achievable in the receiver channels and low coupling between the receiver and transmitter. The transmitter generated a 50 ns pulse with a peak power of 400 watts. Table I lists the system parameters of this radar.

Timing and sampling pulses for the two radars are generated in the video processor unit. Range gates for the two radars are independently set to the peak of the respective video signal. The video is sampled, and the value is held by charging a capacitor which holds this charge until updated by the next sample pulse. This boxcar signal is then buffered and level shifted before being recorded on FM magnetic tape for subsequent computer processing.

TABLE I

PARAMETERS OF 70 GHz RADAR

TRANSMITTER

Frequency	69.8 GHz
Peak Power	400 watts
prf	0-5 KHz
Pulse Width	50 ns

ANTENNA

Type	3 horns
Polarization	Horizontal/Vertical
Polarization Isolation	>30 dB
Beamwidth	6 x 6.6 degrees
Aperture Size	2.0 x 1.4 inch
Slant Length	11.94 inch

RECEIVER

Mixer	Single Schottky Diode
I.F.	60 MHz log detection
Sensitivity	-77 dBm
Dynamic Range	70 dB

MEASUREMENTS

Calibration Procedure

Calibration of the data was accomplished by using a 6 inch by 12 inch diplane with main beam radar cross sections of 22.99 dB above one square meter (dBsm) at 16.2 GHz and 34.68 dBsm at 69.8 GHz as an absolute radar cross section reference. The diplane was located 200 feet from the radar with the flat plate intersection line oriented at 22.5 degrees from the vertical. Equal amplitude signals, received by the parallel and cross polarized antennas, are used as the reference signal for radar cross section calibration. Attenuation was added simultaneously to each channel in 10 dB increments over a 70 dB dynamic range. With the 3 dB reduction in radar cross section due to rotation of the diplane, the calibration radar cross sections are 19.99 dBsm and 31.68 dBsm for frequencies of 16.2 GHz and 69.8 GHz, respectively. Calibrations of the radars were made immediately prior to each series of runs.

Radar Targets

Radar targets which have been observed include dense pine groves, isolated trees, power and lamp poles, moving automobiles and flat plates of different geometrical shapes. During a data run, the sampled signals from a given range cell were simultaneously received and recorded by FM on magnetic tape for the parallel and cross polarized returns from each radar. Therefore, identical conditions exist at the target, allowing direct comparisons of the data for the two frequencies.

Measurement Data

Of the targets which have been observed, the pine grove presents the most interesting set of data. The radar antennas were 10 feet above ground level and illuminated the pine trees at an azimuthal incident angle of 42 degrees. Three contiguous 10 second samples of data were selected for analysis. The effect of wind velocity on tree clutter is easily seen in both the time and spectral plots during the total 30 second interval. The wind velocity was approximately 1 to 2 mph during the first 12 seconds of data, changing to an almost complete calm

E3-6

condition for the next 12 seconds and again changing to 1 to 2 mph during the last six seconds. Radar cross section vs. time and power spectral density plots for the three contiguous sections of data for the two frequencies are shown in Figures 1 through 3. The ability of this particular tree clutter to depolarize on reflection may also be seen by comparing time plots of the parallel and cross channel data for a given radar.

The autocovariance functions which indicate the time required for the received signal to decorrelate, for both parallel and cross polarized returns at the two frequencies for the data in Figures 1 through 3 are showns in Figures 4 through 6, respectively. For the 70 GHz radar there is no significant difference between data samples. However, decorrelation occurs much more rapidly at 70 GHz than at 16 GHz.

Cumulative distributions taken over a one minute period were computed and are shown in Figure 7. The distributions include the 30 seconds of data shown in figures 1 thru 3. Variability of the data and median values may readily be determined from these distributions. The maximum, minimum and median values for data collected on several targets are shown in Table II.

Of possible interest to both the automotive industry and the military, is the radar cross section of vehicles. Figure 8 shows a set of time and power spectral density plots for an automobile moving through the radar beam. These data were acquired by setting the sample gate to a fixed range cell and allowing an automobile to move away from the radar. The radars were located above a roadway and the antennas were pointed down at an angle of 17 degrees. Approximately 2 seconds were required for the automobile to pass through the range cell. Because the range resolution of the 16 GHz radar is slightly longer than that of the 70 GHz radar, a completely clear range cell could not be found at the measurement site. The doppler frequency generated by the automobile passing through a range cell containing a smaller

E3-7
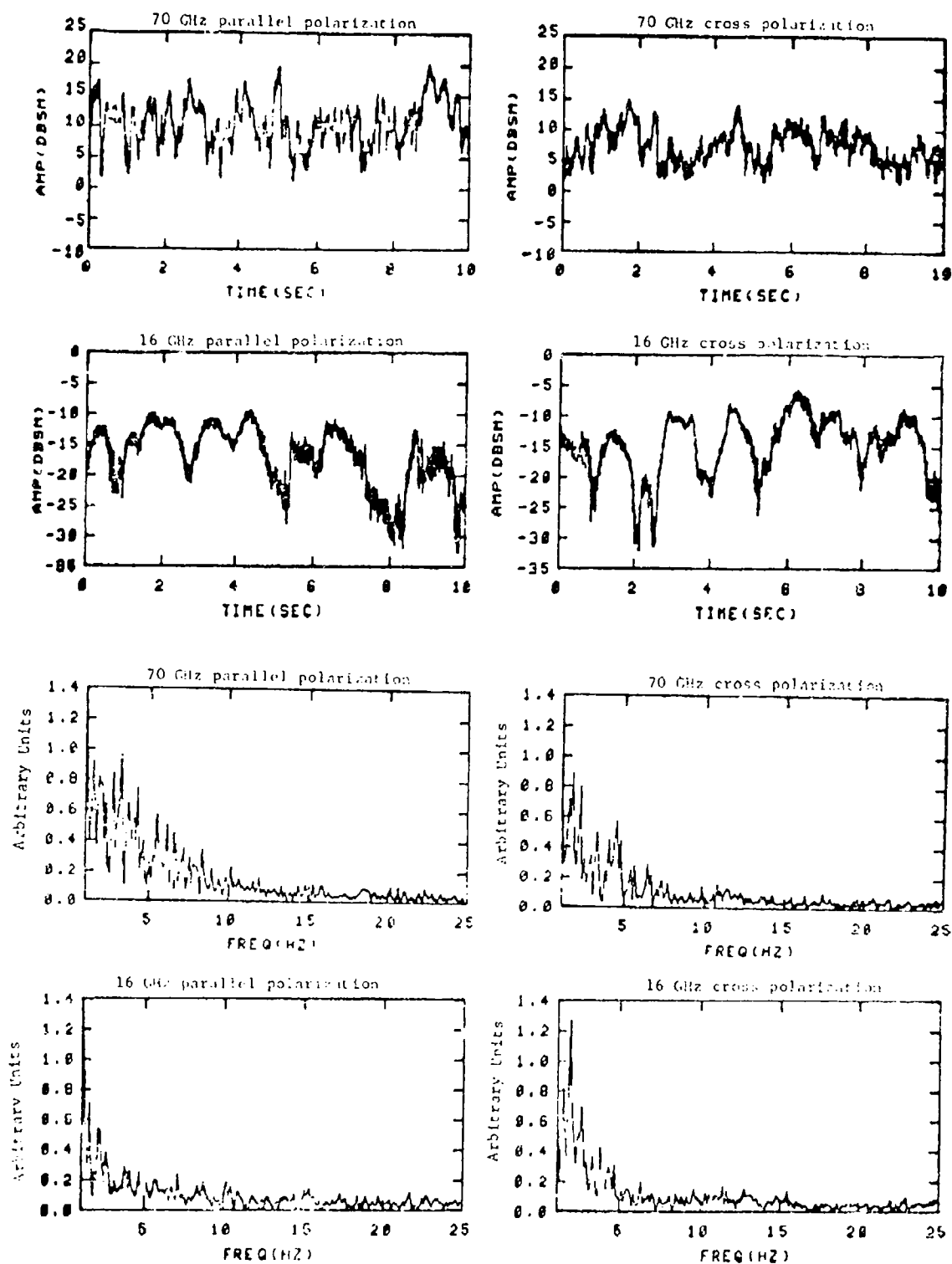
Figure 1. Radar cross section vs. time and power density spectrums of pine tree clutter for first 10 seconds of data.
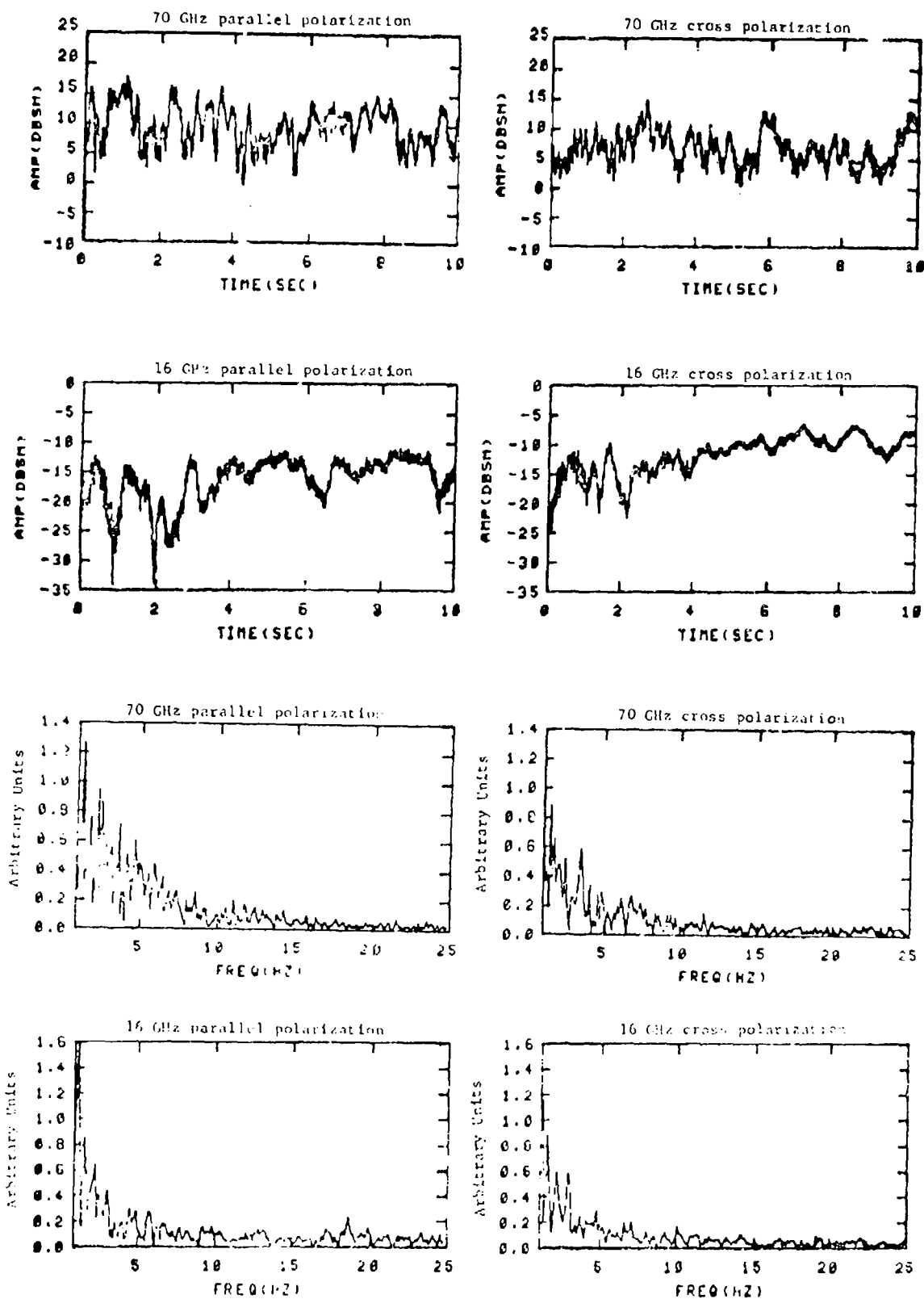
Figure 2. Radar cross section vs. time and power density spectrums of pine tree clutter for second 10 seconds of data.
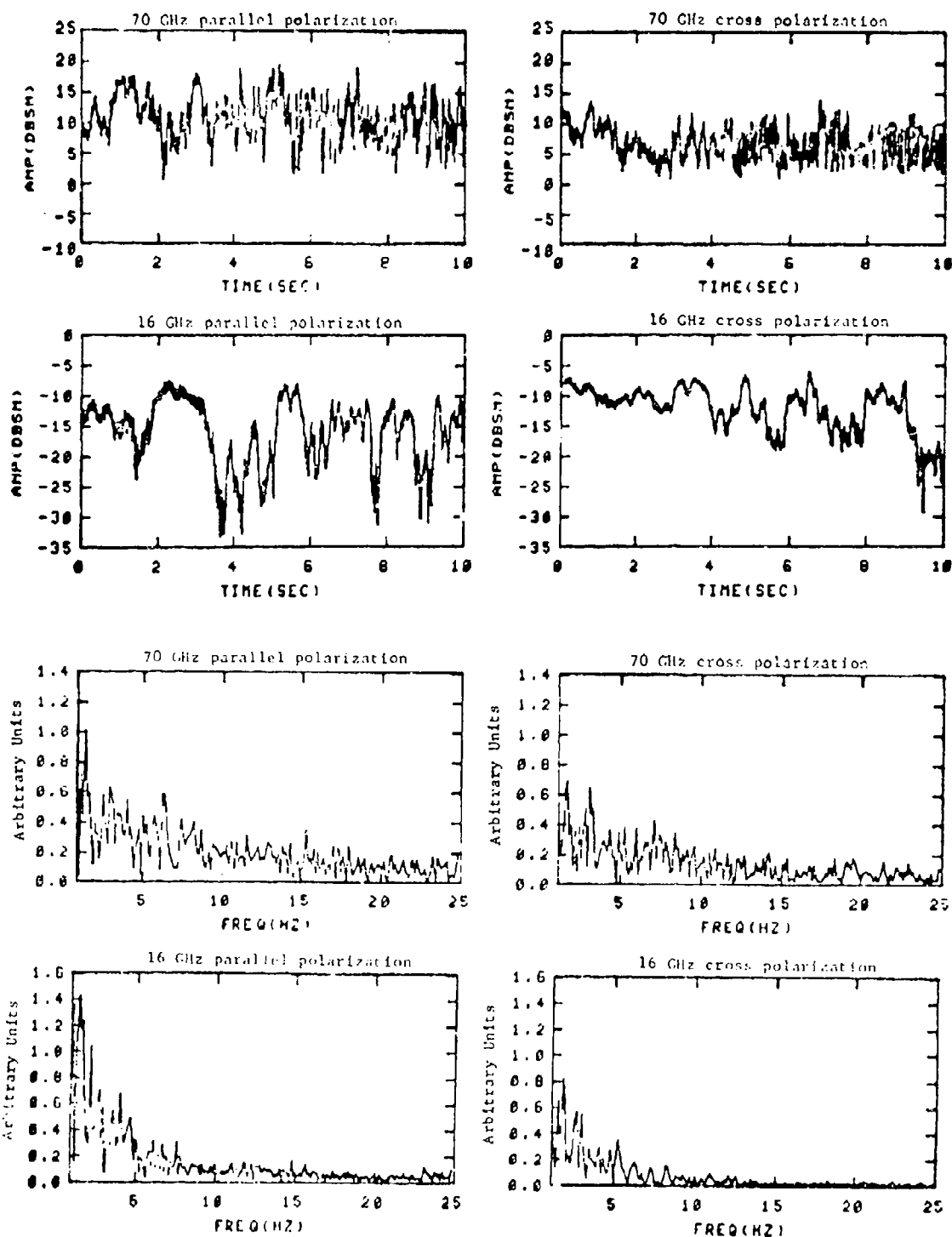
Figure 3. Radar cross section vs. time and power density spectrums
of pine tree clutter for third ten seconds of data.
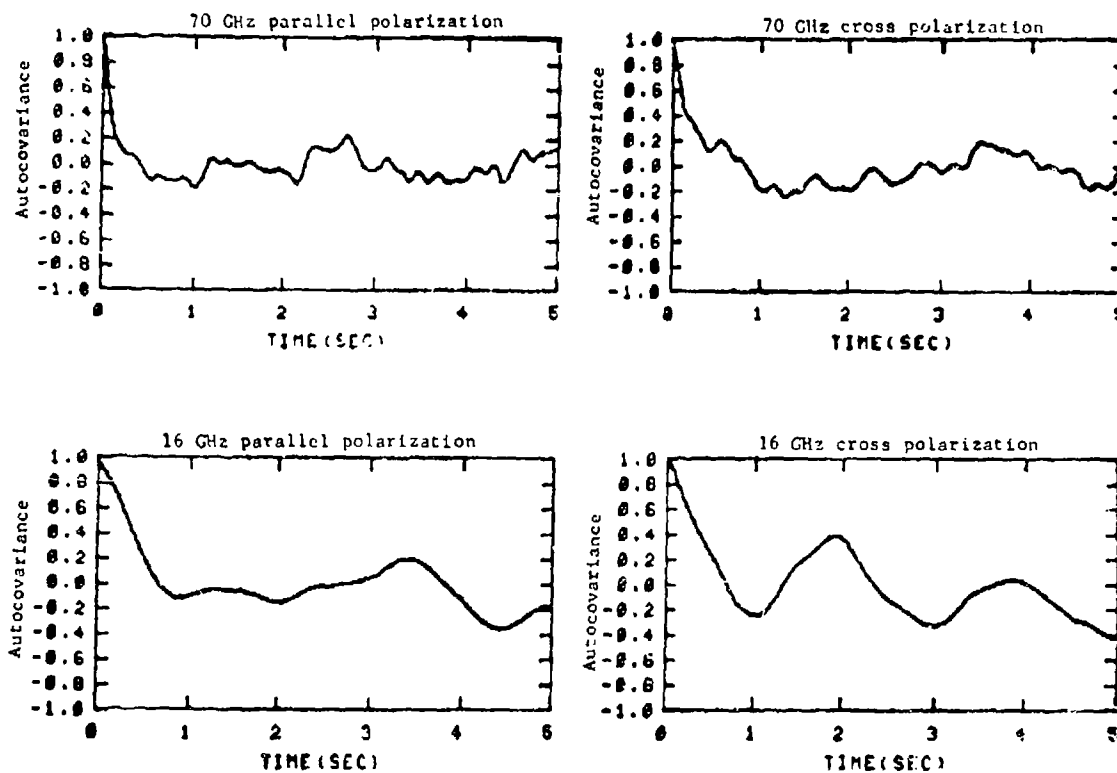
Figure 4. Autocovariance functions of pine tree clutter
for first 10 seconds of data.
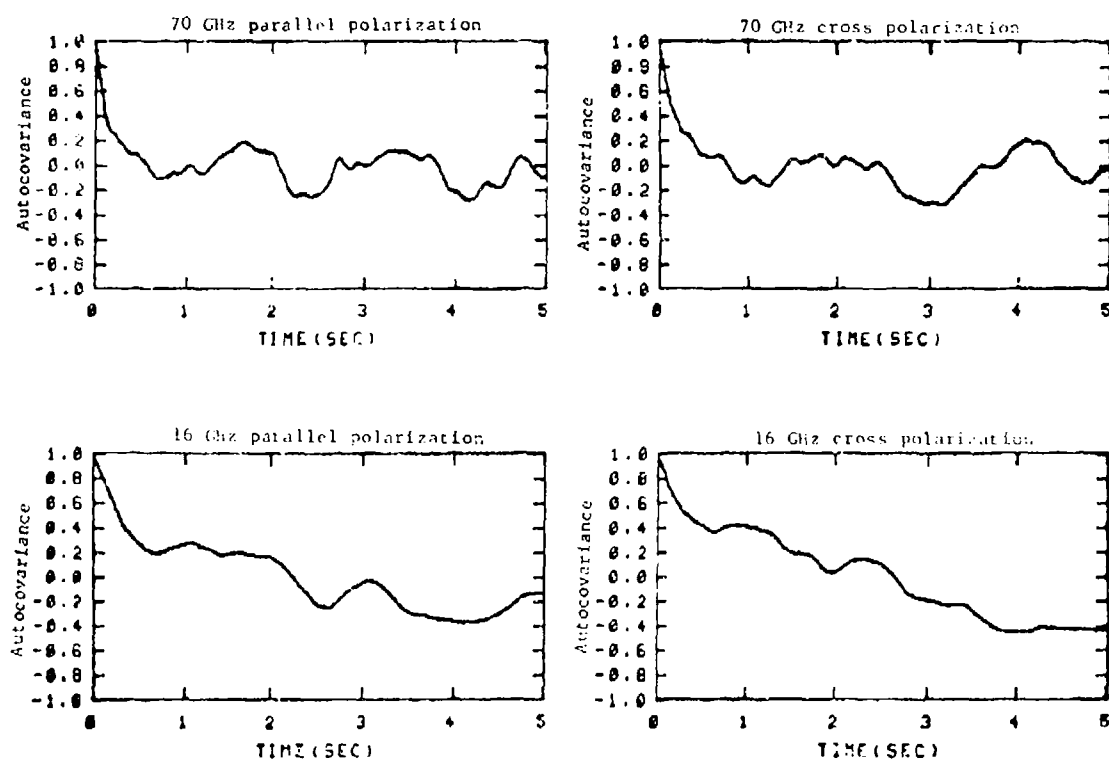
Figure 5.   Autocovariance functions of pine tree clutter
for second 10 seconds of data.
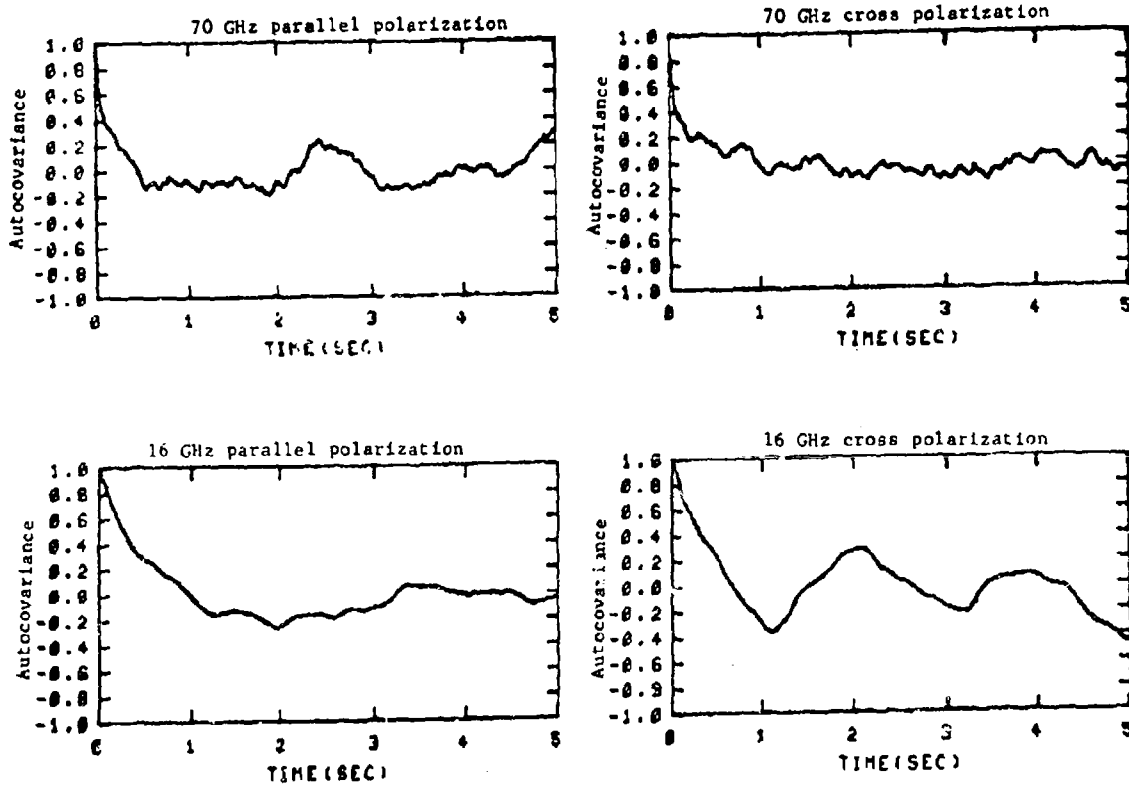
Figure 6. Autocovariance functions of pine tree clutter for third 10 seconds of data.
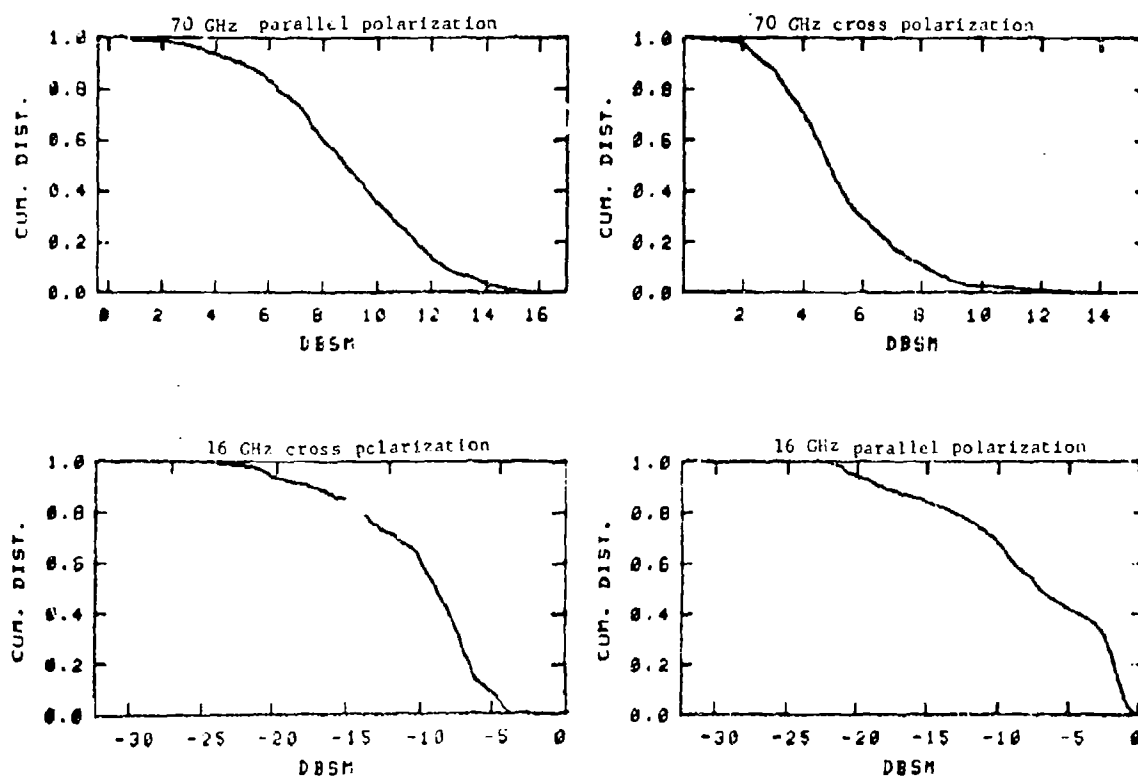
Figure 7. Cumulative distribution for a sixty second sample
of pine tree clutter.

TABLE II

MAXIMUM, MINIMUM AND MEDIAN VALUES OF
RADAR CROSS SECTION IN DBSM FOR SELECTED TARGETS

Target	Freq GHZ	Parallel Pol			Cross Pol		
		Max	Min	Mean	Max	Min	Mean
Wooden power pole	16	1.8	-11.6	-3.9	-0.8	-13.5	-4.7
	70	11.7	-4.0	6.5	-1.7	-15.8	-8 6
Wooden power pole with transformers	16	9.6	5.1	7.4	1.7	-0.1	.84
	70	24.8	18.9	22.9	6.2	-6.4	1.6
Metal lamp pole	16	7.3	-3.4	2.6	3.5	-10.2	-2.0
	70	27.1	18.9	23.6	8.3	-5.9	1.8
Brick building	16	34.6	30.3	32.7	20.5	13.0	16.9
	70	37.6	25.2	33.3	27.5	14.6	21.4
Isolated tree	16	-21.3	-61.4	-34.2	-21.2	-45.9	-28.1
	70	-5.6	-30.5	-16.4	-13.5	-30.3	-22.1
Pine grove	16	-5.3	-30.8	-10.4	-0.2	-31.0	-10.1
	70	15.8	0.9	9.1	14.1	-0.2	4.9
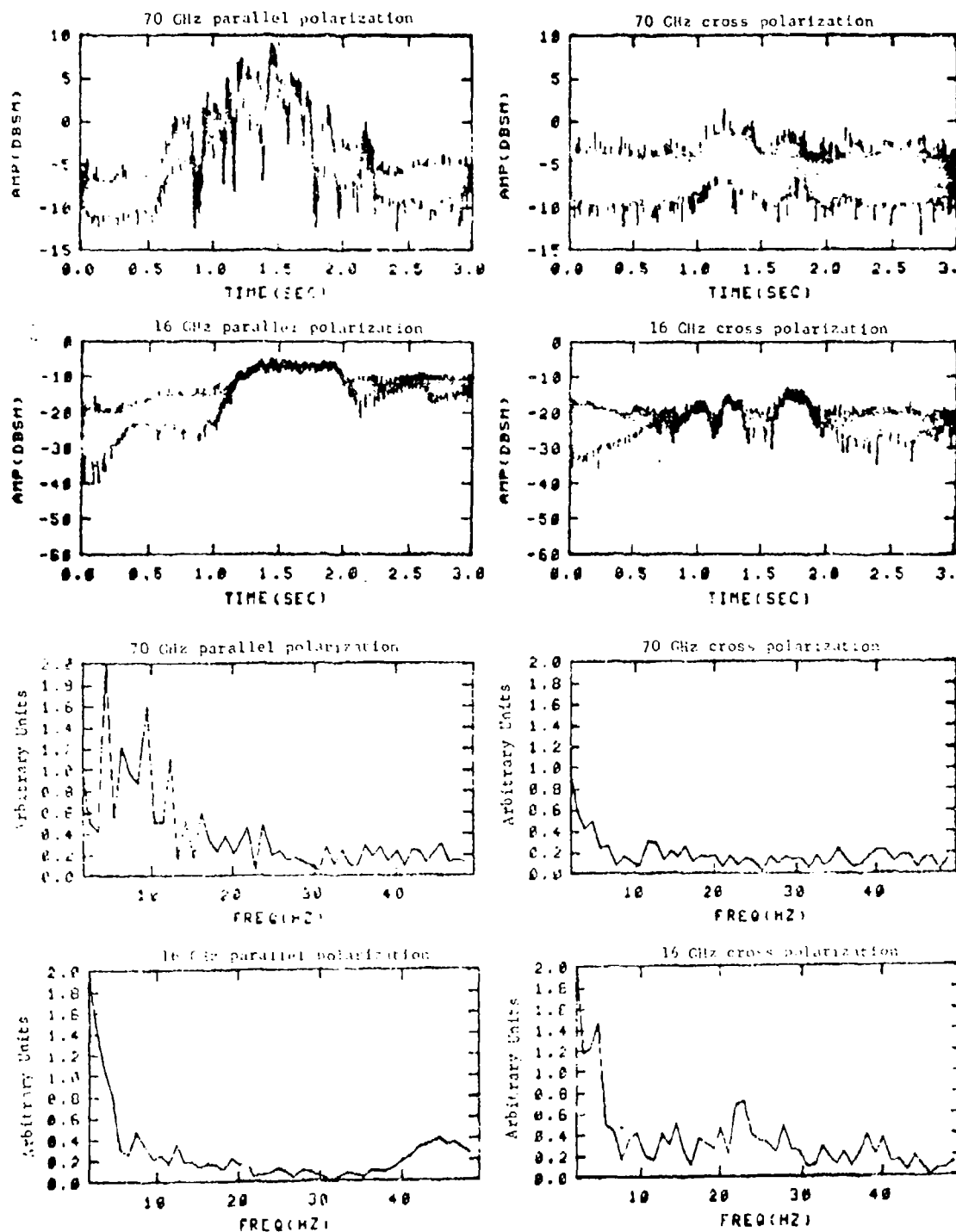
Figure 8.   Radar cross section vs. time and power density
spectrum of automobile.

fixed target is seen in both the time and spectral plots shown in Figure 8. The difference between the parallel and cross polarized components of the reflected signal is seen to be approximately 10 dB at the peak of the radar return for both frequencies.

Concluding Remarks

There is a limited quantity of data available at millimeter wave frequencys. Therefore, the radar systems engineer may not be able to intelligently select or reject these high frequencies as a possible candidate for a specific radar application.

It would be very desirable to accumulate a large data base on both clutter characteristics under varying environmental conditions and on specific targets of military or industrial interest.

References:

1. H. A. Ecker, J. L. Eaves, et al., "Study of Polarization Techniques for Target Enhancement," Technical Report AFAL-TR-67-102, Contract AF 33(615)-2593, Georgia Institute of Technology, Atlanta, Georgia, August 1967.

2. "Investigation of Polarization Agility as a Radar Parameter," Proceedings of the Seventeenth Annual Tri-Service Radar Symposium, May 1971, coauthor.

"EXPERIMENTAL HIGH POWER AMPLIFIER SYSTEM
FOR MM WAVE SATELLITE COMMUNICATIONS"
by

A. Castro - J. Healy
Raytheon Company
Wayland, Mass. 01778

ABSTRACT

This paper describes the development program of a high power ampli-
fier system for mm Wave signals to be used in Satellite Communication
mobile terminals and capable of a gain of 50 dB at 800W output power, over
more than 4 percent instantaneous bandwidth at Ka band frequencies. A
Traveling Wave Tube, Solid State Driver, passive waveguide components and
a high package density power conditioner were developed during this program,
which resulted in the practical realizations of new concepts in microwave
tube and Gunn Diode technologies and advances in the state of the art of
other components.

INTRODUCTION

The objective of this program has been the development of an experi-
mental High Power Amplifier (HPA) system for Satellite Communication
applications at upper Ka band frequencies. The operational requirement is
for a wideband amplifier system suitable for the mobile tactical environ-
ment of terminals to be used with the Lincoln Experimental Satellites 8
and 9 (LES 8 and 9). In this application a minimum 4 percent instantaneous
bandwidth would be desirable to permit the operation with the frequency
plan of both satellites without requiring retuning or redundant equipment.

DESIGN OBJECTIVES

Traveling Wave Tubes and Klystrons at the kW level have been
developed at low Ka Band and higher frequencies, however, they required a
bulky solenoid focussing system and exhibited relative narrow instantaneous
bandwidth.   The development of a permanent magnet focussed wideband
Traveling Wave Tube was, therefore, recognized as basic to accomplish the
objectives of this program. It was felt that 1 kW output power over a
4 percent instantaneous bandwidth was realizable, but just at the limit

of the capabilities of presently available permanent magnet materials. It was also apparent that heat transfer considerations in the slow wave structure and collector will necessitate liquid cooling of this tube.

At this output power level, many of the HPA high power passive waveguide components had to be developed, such as the high power circulator, couplers, switches, pressurization window, etc. The losses associated with these components were estimated to be 1 dB, resulting in rated power of 800 W at the output of the HPA.

The overall gain of the HPA was chosen to be compatible with the output levels obtainable from state of the art wideband multipliers or narrow band parametric upconverters. A nominal HPA drive level of 10 mW (+10 dBm) was adopted, requiring a gain in excess of 50 dB for the rated output. To expect the TWT to provide this gain over a relatively wide instantaneous bandwidth was considered impractical and a solid state driver was proposed. Both avalanche (IMPATT) and TED (Gunn) diode amplifiers may be possible candidates for implementing this driver. Although avalanche devices delivering hundreds of mW of output power were available, noise figure considerations favor TED devices. The noise figure of the HPA, which is mainly determined by the driver, is of special relevance in achieving low noise duplexing capability in the Satcom terminals. Since low noise Gunn Diode Wideband Amplifiers of output power capable of driving the TWT and input circuitry were not previously realized, the development project for this device was necessary.

The considerations above and the preliminary implementation concept resulted in the design objectives summarized in Table 1.

TABLE 1

HPA SYSTEM PERFORMANCE CHARACTERISTICS

FREQUENCY	36.7 to 38.2 GHz
	36 to 38.6 GHz DESIGN GOAL
±1.5 dB (±0.5 DESIGN GOAL)	
INSTANTANEOUS BANDWIDTH	200 MHz MIN
POWER OUTPUT (AT TWT FLANGE)	CONTINUOUSLY ADJUSTABLE UP TO 1 KW

TABLE 1 (continued)

OUTPUT WAVEGUIDE ASSY. LOSSES	1dB MAX.
LOAD VSWR	2 TO 1 OPERATIONAL
	NO DAMAGE UNDER ANY VSWR
MAXIMUM DRIVE POWER	10 MW
PHASE LINEARITY OVER 200 MHz	$\pm 2^{\circ}$ DESIGN OBJECTIVE
RESIDUAL PHASE NOISE	SIDEBANDS AT LEAST 37 dB BELOW
	CARRIER MEASURED IN 1 Hz BW
INPUT VSWR	1.3 TO 1 MAX.
DUMMY LOAD	INTERNAL
PRIME POWER	200/115 V 3P 4W
	PER MIL-STD-1399 TYPE 1
	60 THRU 400 Hz
DIMENSIONS	PER MIL-E-16400 PAR. 3.11.13.3
	NO DIMENSION TO EXCEED 32 IN.
COOLING	LIQUID COOLING
PRESSURIZATION	DRY AIR OR N_2

EQUIPMENT DESCRIPTION

A simplified block diagram of HPA system is shown in Figure 1. The design approach is to provide maximum flexibility for evaluation of the individual components and subsystems, in line with the experimental nature of this program.

The input signal is applied through a monitoring coupler to the input of the solid state driver. A remotely controlled attenuator at the output of the driver permits a continuous change of the HPA output power by changing the RF drive to the TWT. A latching ferrite switch is used for high speed cut - off of the TWT drive upon detection of RF faults or a waveguide TWT output window arc by the Arc Sensor. A differential phase shift high power circulator assures proper output matching to the tube in the presence of HPA output high VSWR. The output waveguide switch selects an internal dummy load or the HPA output as the HPA termination. Provision to incorporate one duplexing filter is shown by dotted lines. The output pressurization window is separately provided, permitting the pressurization of the output waveguide run from the HPA. A thermistor bridge is integral

HPA BLOCK DIAGRAM

FIGURE 1

E4-4
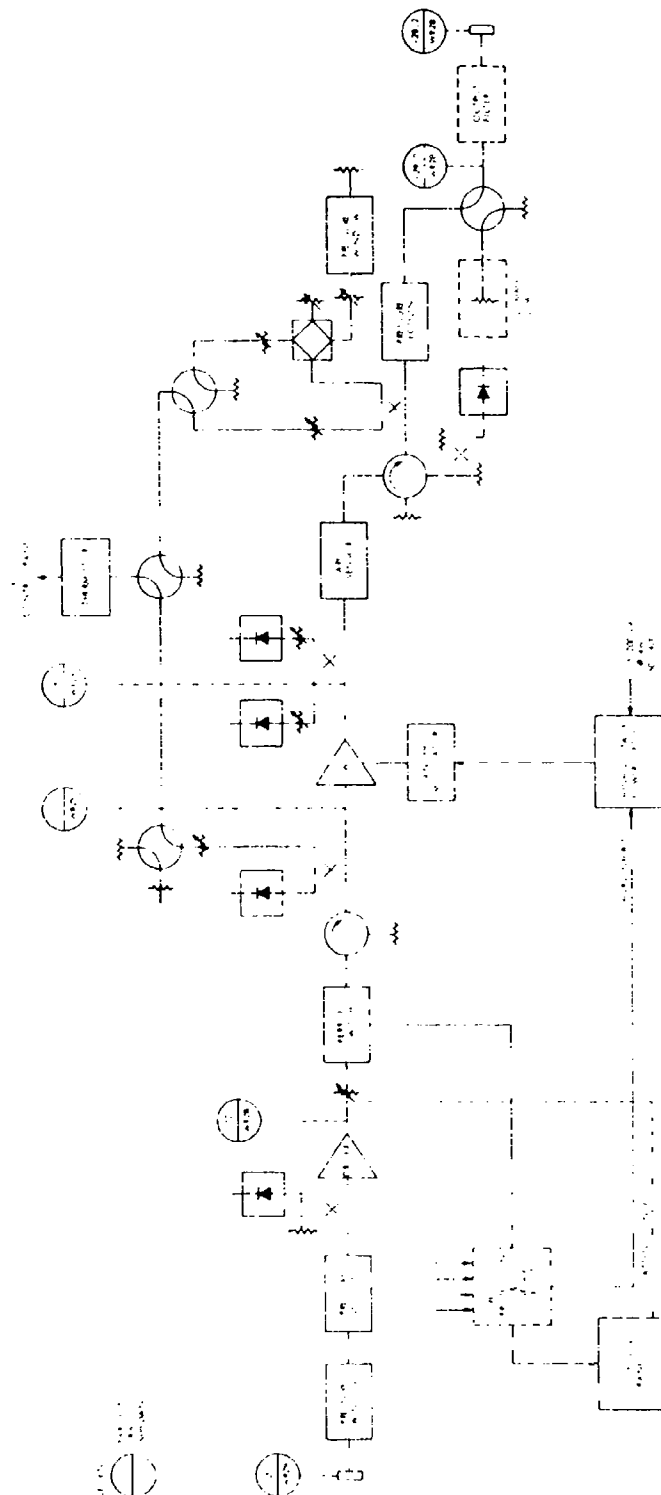
to the equipment and allows precise measurement of the HPA output forward
and reflected power and the TWT input power.

For meeting the intended installation constraints the equipment was
configured in two units having a 17.5 x 17.5 x 32 maximum envelope dimen-
sion, as shown in Figure 2. A Control Panel allows for remote operation
of the equipment and for experimental purposes, individual simultaneous
monitoring of critical parameters was provided.

DEVELOPMENT PROGRAMS

TRAVELING WAVE TUBE

The specifications for the 1 kW permanent magnet focussed TWT
development follow from the above design objectives and are given in
Table II.

TABLE II

TWT SPECIFICATIONS

FREQUENCY	36.7 TO 38.2 GHz
	36 TO 38.6 GHz (DESIGN OBJECTIVE)
POWER OUTPUT	1 KW MIN. INTO 1.2:1 VSWR
GAIN	43 dB AT 1 KW OUTPUT
$\pm$1dB INSTANTANEOUS BANDWIDTH	200 MHz MIN.
INPUT VSWR	1.85 TO 1 MAX.
NOISE FIGURE	35 dB SMALL SIGNAL
	38 dB AT 1 KW OUTPUT
AM/PM CONVERSION	6°/dB
PHASE LINEARITY OVER 1 BW	$\pm 6^{o}$
	$\pm 2^{o}$ DESIGN OBJECTIVE
HARMONICS	20 dB BELOW FUNDAMENTAL
FOCUSING	PPM

The design highlights and the most important techniques introduced
in this development program are given below.

Focusing System

A reasonably good beam coupling at mm waves will result in extremely
high beam density, and stringent mechanical tolerances. Good focusing
must be achieved in order to maintain low intercept current otherwise poor
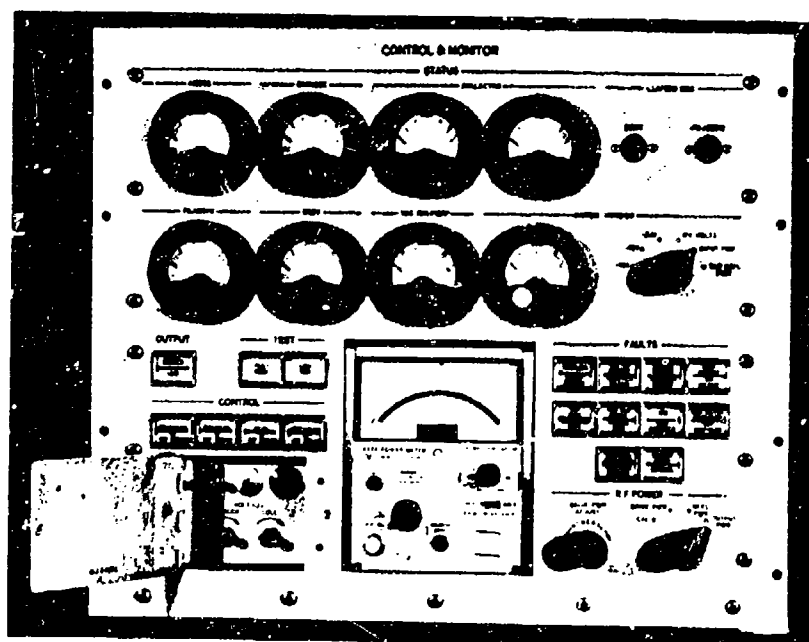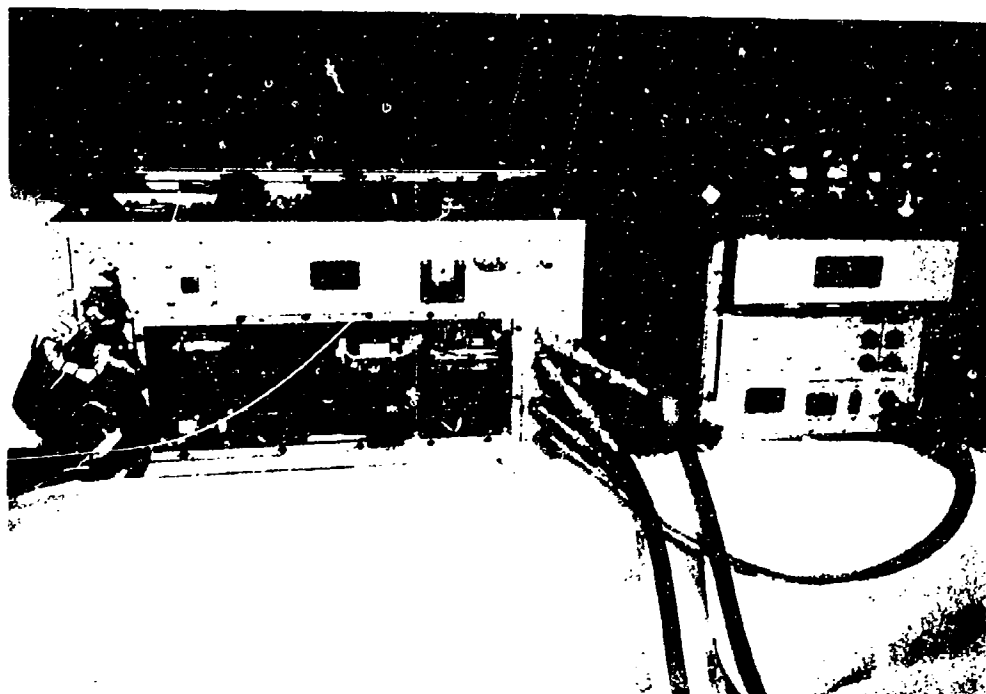
FIGURE 2

beam transmission will limit the maximum allowable beam current, and therefore, the output power obtainable without outgassing or melting the structure. This problem is compounded by the heat transfer difficulties due to the small physical size of the structure at these high frequencies.

It is apparent that focusing of the tube is of critical importance, even more considering the limitations of permanent magnets. Conventional coupled cavity permanent magent focused tubes use a Periodic Permanent Magnet (PPM) system integral to the slow wave structure. A new PPM focusing concept was introduced by Siemens, making the system, including pole pieces, external to the slow wave structure. As a result, the periods of the PPM system and slow wave structure are now independent and additionally, improved heat transfer characteristic is obtained in the all copper slow wave structure. This technique will, however, result in lower axial magnetic field than integral pole pieces, therefore, requiring magnetic material of very high energy product. A suitable magnetic field intensity for focusing the required beam power is obtained with Samarium Cobalt ($SmCo_5$) rings.

Slow Wave Structure

The slow wave structure consists of a three section coupled cavity structure separated by internal attenuators. The cavity design is similar to the Bell structure, and operates in the first space harmonic.

A velocity taper is introduced in the latter cavities of the last section in order to maintain the electronic efficiency over the instantaneous bandwidth.

Realization

The resulting operating parameters of the tube are given in Table III and a photograph is shown in Figure 3.

A modulating anode has been included in the gun design to facilitate turn on and off the tube. The static switch-on behavior of the tube exhibits good stability as shown in Figure 4. This characteristic is of particular concern since PPM focusing systems may exhibit regions of instability.

Figure 5 shows the TWT gain at 1 kW output power level vs frequency as tested in the HPA with the first prototype tube. Improvements were
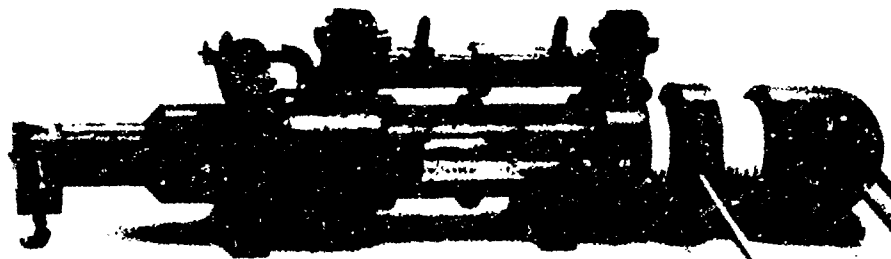
FIGURE 3

V 684
BEAM TESTER RESULTS
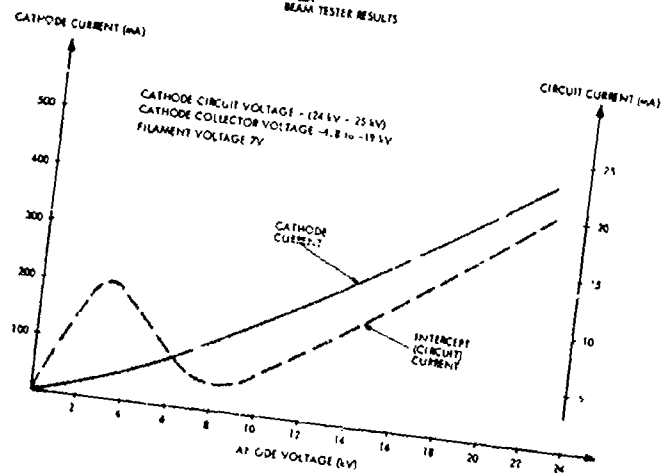
FIGURE 4

TWT GAIN CHARACTERISTIC
PILOT PROTOTYPE

FIGURE 5

E4-8
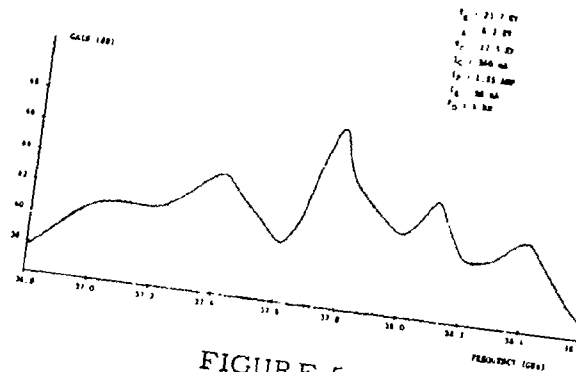
made in the internal matches of the tube and are reflected in the prelim-
inary measurements taken in the second prototype, shown in Figure 6.

TABLE III
OPERATING TWT VOLTAGES AND CURRENTS

	MINIMUM	NOMINAL	MAXIMUM
HEATER VOLTAGE	5.7V	6.3V	7.0V
HEATER CURRENT -- NORMAL OPERATING	--	--	1.5A
CATHODE -- BODY VOLTAGE	-23K	--	-26kV
BODY CURRENT	--	--	45 mA
COLLECTOR -- CATHODE VOLTAGE	+12 kV	--	+14 kV
CATHODE CURRENT	300	--	500 mA
MOD. ANODE VOLTAGE	-4kV	--	-10 kV

Figure 7 shows overall DC to RF efficiency measured in the first
prototype and for different collector depression levels at 1 kW power out-
out. Small increase in circuit current was experienced for collector
depression up to 66%.

Solid State Driver

During the design phase of the HPA program two amplifier designs were
evaluated. One was a two stage Avalanche Diode Amplifier (ADA) that
produced 200 mw with a gain of 15 dB and the other, a newly developed
single stage Gunn Diode Amplifier having the power, gain and bandwidth
equivalent to the output stage of the ADA. Table IV shows the trade-off
data for both amplifiers.

TABLE IV
DRIVER TRADE-OFF DATA

AMPLIFIER TYPE	AVALANCHE DIODE AMP 36.7 TO 38.2 GHz	GUNN DIODE AMP WITH DESIGN GOAL 36.0 TO 38.6 GHz
NUMBER OF STAGES	2	2
NOISE FIGURE	35 dB	18 TO 25 dB
OUTPUT POWER	100 MW	100 MW
GAIN	12 ±0.5 dB	12 ±0.5 dB

TABLE IV (continued)

GAIN VARIATION

OVER FREQ. RANGE	-	0.5 dB
OVER FREQ. RANGE AND 55 $\pm5^{\circ}$C	2.5 dB	1.0 dB
OVER 200 MHz SEGMENT AND 55 $\pm5^{\circ}$C	±0.5 dB	0.5 dB
PHASE LINEARITY (OVER 200 MHz)	1 USEC GROUP DELAY	±1 DEGREE
DC POWER	24.0V @ 0.5 AMP	9V @ 2 AMP.

Because of its favorable noise characteristics, the Gunn device was selected as the driver to the TWT. A description of this development is being presented elsewhere in this Conference.

Figure 8 shows the available drive power over frequency, at the input flange to the TWT, including the driver and all microwave components shown in Figure 1.

WAVEGUIDE COMPONENTS

Several standard Ka band catalog components are currently available, however, appreciable redesign was required for high power components. Of particular importance is the output ferrite circulator, since it defines the tube load and provides fault protection. Figure 9 shows the output waveguide assembly, including the circulator.

High Power Circulator Development

The ferrite circulator design used for the HPA was a 4 port differential phase shift type. The most critical parameter for the circulator was insertion loss since it controlled the electrical performance of the HPA and the thermal design of the circulator. The proper choice of ferrite material, ferrite bonding techniques and distribution of the water cooling to the elements of the circulator allowed insertion losses below 0.5 dB with isolation in excess of 20 dB.

HIGH VOLTAGE POWER SUPPLY

As discussed previously the TWT operates in a depressed collector configuration within the limits of voltages and currents given in Table III. For the intended tactical use of the equipment, techniques which will minimize the volume and weight of the equipment, in particular the power

TWT GAIN CHARACTERISTIC
(SECOND PROTOTYPE)
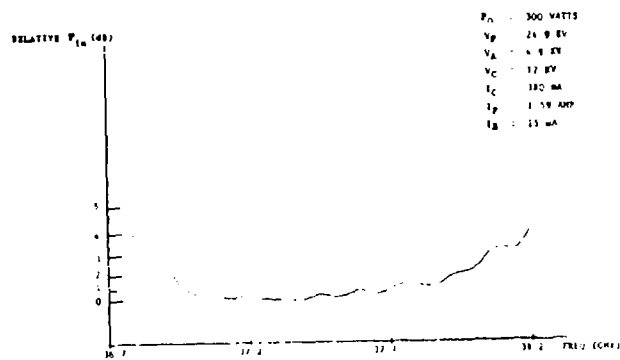
FIGURE 6

TWT EFFICIENCY CHARACTERISTICS
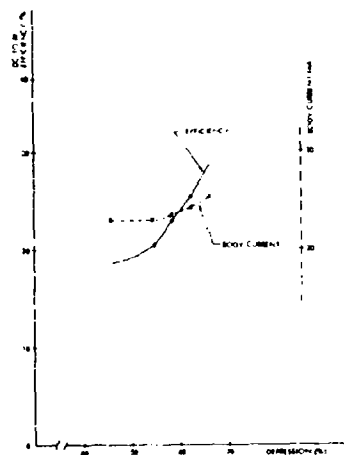
FIGURE 7

TWT INPUT POWER CHARACTERISTIC
FOR +10 dBm RF UNIT DRIVE LEVEL
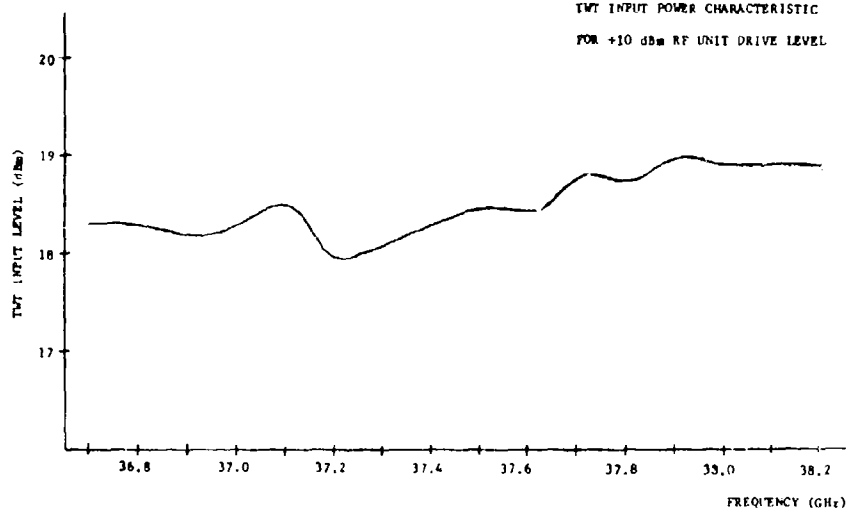
FIGURE 8

E4-11

supply, must be used. To accomplish this objective the following steps have been taken:

- An inverter type of power supply was proposed.
- Liquid cooling of subassemblies and components is used to the maximum extent possible.
- Oil immersed assemblies of all high voltage components maximizes the packaging density.

The simplified block diagram of the power supply is shown in Figure 10. The primary power line is rectified, filtered and inverted into a high frequency synthetic line, chosen to minimize the size of the High Voltage step up transformers and filters. A 10 KHz frequency and ferrite magnetic components were used in this design. The dual inverters allow voltage adjustment for initial set up and to provide the necessary voltage regulation, controlling the phase of one inverter with respect to the other.

The use of a high frequency synthetic line followed by rectification and filtering presents a number of important advantages in addition to size and weight. In the first place, the component values to achieve a given filtering characteristic are very small, resulting in small stored energy, therefore, minimizing the risk of destruction in the presence of arcs internal or external to the tube. The stored energy in this design is less than 4.5 joules in both the collector and cathode supplies. Also, the power supply may be turned off from the primary side by inhibiting the inverter trigger, which occurs every half cycle or within 50 microseconds, allowing extremely fast turn-off in the presence of a fault. No crowbar is required for adequate protection of the tube, thus avoiding the well known problems associated with these types of devices.

CONCLUSIONS AND ACKNOWLEDGEMENTS

The feasibility of achieving high power amplification at Ka band frequencies over a relative large instantaneous bandwidth, in a physical configuration suitable for being integrated into tactical satellite communication terminals was proven. As a result of fulfilling the design objectives, several advances in the state of the art of mm Wave active and passive components were accomplished.

FIGURE 9

HV POWER SUPPLY
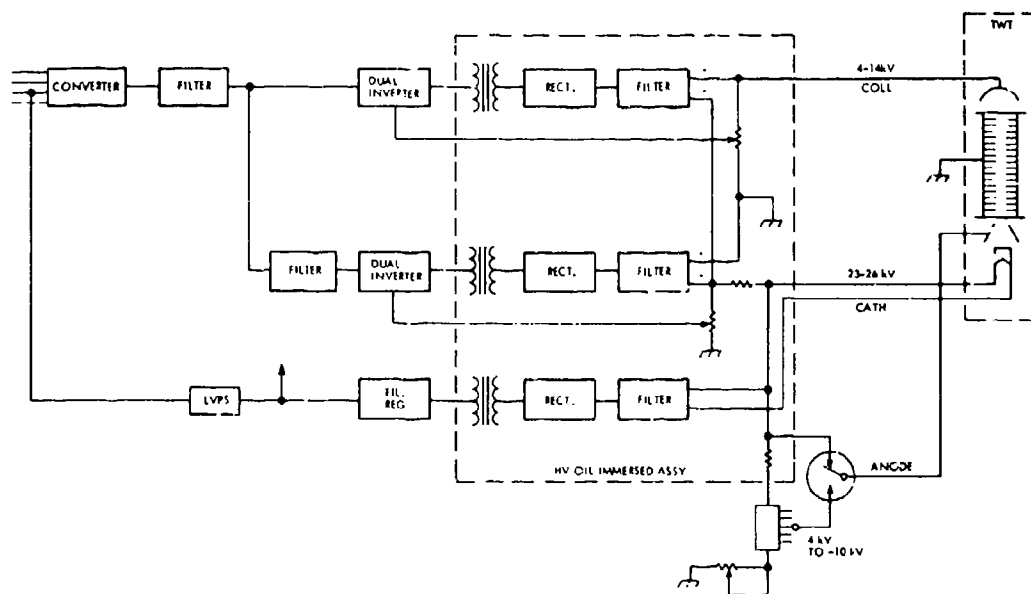
FIGURE 10

E4-13

ANALYSIS OF AN ANISOTROPIC DIELECTRIC RADOME*

by

Donald G. Bodnar and Harold L. Bassett
Systems and Techniques Department
Engineering Experiment Station
Georgia Institute of Technology
Atlanta, Georgia 30332

ABSTRACT

A grooved-dielectric radome panel is analyzed in terms of an arbitrary direction of incidence on N planar slabs each of which is dielectrically anisotropic, homogeneous and lossless. Using this model for the grooved panel, transmission coefficients of 90 percent or greater over a 10:1 frequency band and over $0°$ to $60°$ incidence angle are predicted and demonstrated experimentally. Measurements are presented on two panels from 3 to 35 GHz.

I. INTRODUCTION

Reflections from radomes can be eliminated by smoothly changing the dielectric constant of the radome from a value of one at the inner and outer surfaces to an arbitrary value in the interior [1]. The possibility of physically realizing such radome performance is analyzed in this paper for a particular class of grooved dielectric panels shown in Figure 1. This panel is made by machining triangular grooves into both sides of a flat, solid piece of dielectric. It has been experimentally demonstrated [2] that the panel shown in Figure 1 can indeed have broadband performance. The purpose of this paper is to establish a theoretical basis for this performance, present some new experimental data, and to provide some new design data on this type of panel.

The radome technique described permits very broadband radomes to be realized that also operate over a wide range of incidence angles thus eliminating the need to "tune" for a particular frequency and/or incidence angle.

Figure 1. Grooved broadband panel design.

Figure 2. Geometry of homogeneous, anisotropic slabs.
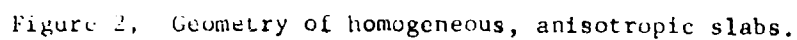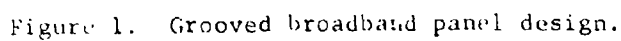
II. MATHEMATICAL MODEL OF PANEL

The panel shown in Figure 1 is both dielectrically inhomogeneous and anisotropic since the dielectric properties vary both with position and with direction at a particular position. This panel was modeled as a series of slabs each perpendicular to the z axis as shown in Figure 2. Each slab is homogeneous but anisotropic in general, and each is intended to represent the medium parameters at the corresponding z location in Figure 1. Let there be a total of N slabs including the semi-infinite isotropic-dielectric regions on either side of the central slabs. The m-th slab starts at $z = d_{m-1}$ and ends at $z = d_m$. In the m-th slab the permeability is a scalar constant μ and the rectangular components of the permittivity tensor are given by

$$\overline{\overline{\epsilon}}_m = \epsilon_o \begin{bmatrix} \kappa_{x_m} & 0 & 0 \\ 0 & \kappa_{y_m} & 0 \\ 0 & 0 & \kappa_{z_m} \end{bmatrix} \tag{1}$$

where ϵ_o is the free space permittivity and κ_{x_m}, κ_{y_m} and κ_{z_m} are the dielectric constants in the various coordinate directions.

A series of ordinary and extraordinary waves [3, 4, 5] will typically be generated in each of the layers of the panel when a single plane wave is incident from the 1-st layer. A superscript o and e will be used to distinguish between ordinary and extraordinary components, respectively As shown in Figure 2, the total electric field in the m-th layer will be composed of an incident field $\overline{E}_{i_m}$ traveling to the right and a reflected field $\overline{E}_{r_m}$ traveling to the left. Both of these electric fields will, in general, contain both ordinary and extraordinary components that travel in different directions with different velocities. Several ordinary and several extraordinary waves will be present in each $\overline{E}_{i_m}$ and each $\overline{E}_{r_m}$ if the optical axes

in each layer are arbitrarily oriented [5]. It can be shown that if (a) each slab is uniaxial (or isotropic), (b) the optical axis of each layer lies in the x-y plane, and (c) each optical axis is either parallel or perpendicular to all other optical axes ther (1) only one ordinary and one extraordinary component exists for each $\overline{E}_{i_m}$ (similarly for $\overline{E}_{r_m}$) and (2) the incident and reflected waves in a medium have the same ordinary and extraordinary propagation constants, namely β_m^o and β_m^e, respectively. Assumptions (a), (b), and (c) are valid for the panel in Figure 1 and will be made in all that follows.

According to Born and Wolf [3], and to Jones [4], the electric flux density $\overline{D}$ of the ordinary wave in a uniaxial crystal (assumption (a) above) is perpendicular to the principal plane while $\overline{D}$ of the extraordinary wave lies in the principal plane. The principal plane is defined to be the plane containing the optic axis and the direction of propagation. Thus in each region there are four principal planes, one for the ordinary and the extraordinary components of both the incident and the reflected waves.

A rectangular coordinate system will now be established for each of these four components in terms of the principal planes. For brevity, let $\overline{n}_m$ represent any of the four directions of propagation vectors. Let $\overline{u}_{o_m}$ be a unit vector in the direction of the optical axis in the m-th region. Notice that $\overline{u}_{o_m}$ is independent of which of the four direction of propagation vectors is selected for $\overline{n}_m$. Let $\overline{u}_{\perp_m}$ be a unit vector perpendicular to both the optical axis and the direction of propagation $\overline{n}_m$ such that

$$\overline{u}_{\perp_m} = \frac{\overline{n}_m \times \overline{u}_{o_m}}{\left| \overline{n}_m \times \overline{u}_{o_m} \right|} \tag{2}$$

Notice that $\overline{u}_{\perp_m}$ depends on which direction of propagation is selected for $\overline{n}_m$. Finally, an orthogonal coordinate system will be completed by defining a unit vector $\overline{u}_{\parallel_m}$ in the principal plane such that

$$\bar{u}_{\|_m} = \frac{\bar{u}_{o_m} \times \bar{u}_{\perp_m}}{\left| \bar{u}_{o_m} \times \bar{u}_{\perp_m} \right|} \tag{3}$$

The unit vectors $\bar{u}_{o_m}$, $\bar{u}_{\perp_m}$, and $\bar{u}_{\|_m}$ form a right-handed rectangular co-ordinate system which is termed an optic axes coordinate system. The ordinary component of $\bar{D}$ is colinear with $\bar{u}_{\perp_m}$ and the extraordinary component of $\bar{D}$ lies in the principal plane. Since each layer is uniaxial, the dielectric constant is independent of direction in any plane transverse to the optic axis. Thus, by choosing $\bar{u}_{o_m}$, $\bar{u}_{\perp_m}$, and $\bar{u}_{\|_m}$ as the axes, the permittivity tensor can be reduced to diagonal form with the $\bar{u}_{\perp_m}$ and $\bar{u}_{\|_m}$ components of the tensor being identical. Thus, the components of $\bar{E}$ along the $\bar{u}_{o_m}$ and $\bar{u}_{\|_m}$ transfer into the extraordinary component of $\bar{D}$ and the component of $\bar{E}$ along $\bar{u}_{\perp_m}$ transfers into the ordinary component of $\bar{D}$.

The field components in each layer are represented in terms of the optic axes coordinate system. By matching the tangential electric and magnetic fields at each interface $z = z_m$ one obtains the following relationship between optical-axes coordinate-system components on each side of the interface

$$\bar{\bar{A}}_{m+1}(d_m) \cdot \bar{E}_{m+1} = \bar{\bar{A}}_m(d_m) \cdot \bar{E}_m \tag{4}$$

The $\bar{\bar{A}}$ tensor is a 4 x 4 tensor whose components are given in appendix A while $\bar{E}_m$ and $\bar{E}_{m+1}$ are column vectors and

$$\bar{E}_m = \begin{bmatrix} E^i_{o_m} \\ E^i_{\perp_m} \\ E^r_{o_m} \\ E^r_{\perp_m} \end{bmatrix} \tag{5}$$

E5-5

and $\bar{E}_{m+1}$ has the same form as $\bar{E}_m$ with m replaced by m+1. The subscripts o and $\perp$ represent components along $\bar{u}_{o_m}$ and $\bar{u}_{\perp_m}$, respectively, for the appropriate incident or reflected wave. By inverting (4) and by repeated multiplication, the electric fields inside the panel may be eliminated and one obtains

$$\bar{E}_N = \bar{\bar{C}} \cdot \bar{E}_1 \tag{6}$$

where

$$\bar{\bar{C}} = \bar{\bar{B}}_{N-1} \cdot \bar{\bar{B}}_{N-2} \cdot \bar{\bar{B}}_{N-3} \cdots \bar{\bar{B}}_2 \cdot \bar{\bar{B}}_1 \tag{7}$$

and

$$\bar{\bar{B}}_m = \bar{\bar{A}}_{m+1}^{-1}(d_m) \cdot \bar{\bar{A}}_m(d_m) \tag{8}$$

Usually the incident field is known and the transmitted and reflected fields must be found. This can be done by partitioning (6) and solving the resulting equations. One then obtains

$$\bar{E}_r = - \bar{\bar{F}}_4^{-1} \cdot \bar{\bar{F}}_3 \cdot \bar{E}_i \tag{9}$$

$$\bar{E}_t = (\bar{\bar{F}}_1 - \bar{\bar{F}}_2 \cdot \bar{\bar{F}}_4^{-1} \cdot \bar{\bar{F}}_3) \cdot \bar{E}_i \tag{10}$$

where

$$\bar{\bar{F}}_1 = \begin{bmatrix} C_{11} & C_{12} \\ C_{21} & C_{22} \end{bmatrix} \qquad \bar{\bar{F}}_2 = \begin{bmatrix} C_{13} & C_{14} \\ C_{23} & C_{24} \end{bmatrix}$$

$$\bar{\bar{F}}_3 = \begin{bmatrix} C_{31} & C_{32} \\ C_{41} & C_{42} \end{bmatrix} \qquad \bar{\bar{F}}_4 = \begin{bmatrix} C_{33} & C_{34} \\ C_{43} & C_{44} \end{bmatrix} \tag{11}$$

and the C's in (11) are the elements of $\overline{\overline{C}}$, and

$$\overline{t}_i = \begin{bmatrix} E^i_{o_1} \\ \\ E^i_{\perp_1} \end{bmatrix} \qquad \overline{t}_t = \begin{bmatrix} E^i_{o_N} \\ \\ E^i_{\perp_N} \end{bmatrix} \qquad \overline{E}_r = \begin{bmatrix} E^r_{o_1} \\ \\ E^r_{\perp_1} \end{bmatrix} \qquad (12)$$

The incident, $\overline{t}_i$ reflected $\overline{t}_r$ and transmitted $\overline{E}_t$ fields in (12) are specified in terms of optic axis coordinate systems. For more convenient usage they need to be expressed in terms of rectangular coordinate components. If the incident field in rectangular components in medium 1 is given by

$$\overline{E}_i = (E_x, E_y, E_z) \qquad (13)$$

then

$$E^i_{o_1} = E_x \cos \theta_1 + E_y \sin \theta_1 \qquad (14)$$

$$E^i_{\perp_1} = E_x \, u^i_{x_{\perp_1}} + E_y \, u^i_{y_{\perp_1}} + E_z \, u^i_{z_{\perp_1}} \qquad (15)$$

The angle θ_1 is the orientation of the optic axis in medium 1 with respect to the x axis. Since medium 1 is isotropic θ_1 may be arbitrarily set parallel or perpendicular to the other optic axes. A similiar   can be made to convert $\overline{t}_t$ and $\overline{t}_r$ to rectangular components.

The dielectric properties of the panel in Figure 1 were modeled by use of a semi-infinite strip-array analysis [2, 6]. The dielectric constant for perpendicular polarization (see Figure 1) which represents κ_y and κ_z for region d_1 of Figure 1 is given by the zero of the following function:

$$f_\perp(\kappa_\perp) = -\frac{\pi}{2} + A \sqrt{\kappa_2 - \kappa_\perp} + \tan^{-1}\left[\sqrt{\frac{\kappa_2 - \kappa_\perp}{\kappa_\perp - \kappa_1}} \coth\left(B \sqrt{\kappa_2 - \kappa_1}\right)\right] \qquad (16)$$

where

$$A = 2\pi \frac{w}{\ell_1} \frac{\ell_1}{\lambda_o} \tag{17}$$

$$B = 2\pi \left(1 - \frac{w}{\ell_1}\right) \frac{\ell_1}{\lambda_o} \tag{18}$$

and w is the width of the strip at the z location of interest. The dielectric constant for parallel polarization which represents κ_y for region d_1 of Figure 1 is given by the zero of the following function:

$$f_{\parallel}(\kappa_{\parallel}) = A\sqrt{\kappa_2 - \kappa_{\parallel}} - \tan^{-1}\left[\frac{\kappa_2 \sqrt{\kappa_{\parallel} - \kappa_1}}{\kappa_1 \sqrt{\kappa_2 - \kappa_{\parallel}}} \tanh\left(B\sqrt{\kappa_{\parallel} - \kappa_1}\right)\right] \tag{19}$$

and A and B are defined as above. Equations 16 and 19 can be solved using Muller's method, Newton-Raphson or other techniques. By using an appropriate change in terms, (16) and (19) can be used to determine the κ's of region d_3 of Figure 1.

The propagation constant of the ordinary wave in the m-th medium is given by

$$\varsigma_m^o = k_o \sqrt{\kappa_{z_m}} \tag{20}$$

while that for the extraordinary wave is the solution of 7

$$(\beta_{m+1}^2 - \kappa_{y_{m+1}} k_o^2)(\beta_{m+1}^2 - \kappa_{z_{m+1}} k_o^2) n_{x_m}^2 \kappa_{x_{m+1}}$$

$$+ (\beta_{m+1}^2 - \kappa_{z_{m+1}} k_o^2)(\beta_{m+1}^2 - \kappa_{z_{m+1}} k_o^2) n_{y_m}^2 \kappa_{y_{m+1}}$$

$$+ (\beta_{m+1}^2 - \kappa_{x_{m+1}} k_o^2)(\varepsilon_{m+1}^2 - \kappa_{y_{m+1}} k_o^2)$$

$$\cdot \left(\frac{\beta_{m+1}^2}{\beta_m^2} - n_{x_m}^2 - n_{y_m}^2\right)\kappa_{z_{m+1}} = 0 \tag{21}$$

Since all quantities of interest in (21) are known in the first region they may be determined for all media to the right of it. The direction of propagation in each region can be determined from that in the first region by

$$n_{x_{m+1}} = \frac{\beta_m}{\beta_{m+1}} n_{x_m}$$

$$n_{y_{m+1}} = \frac{\beta_m}{\beta_{m+1}} n_{y_m}$$

$$n_{z_{m+1}} = + \sqrt{1 - n_{x_{m+1}}^2 - n_{y_{m+1}}^2} \qquad (22)$$

III. COMPARISON OF MEASURED AND PREDICTED PERFORMANCE

The initial performance predictions were based on the conditions for which the Richmond WKB solution is valid [1] for plane wave transmission through inhomogeneous layers. For a lossless panel, for any angle of incidence, total transmission of power is obtained; the insertion phase delays of the parallel and perpendicular components are equal, and the phase of the transmitted wave depends only on the average value of $\sqrt{\kappa(z) - \sin^2\theta}$ in the panel of thickness d.

The main problem with applying these results was that of realizing a practical structure that has the required variation, $\kappa(z)$, of dielectric constant. That is

(1) $\kappa(0) = 1.0$ (incident point),

(2) $\kappa(d) = 1.0$ (exit point), and

(3) $\left| \frac{d\kappa(z)}{dz} \right| \ll 2k \left[\kappa(z) - \sin^2\theta \right]^{3/2}$

as required by Richmond's WKB solution.

In utilizing these results for the panel in Figure 1, additional design

data were required. As previously reported [2], the spacing restriction
is:

$$2\ell/\lambda_o = \frac{1}{\sqrt{\kappa_2} + \sqrt{\kappa_1} \; |\sin\theta|} \; , \qquad (23)$$

where

θ_1 = angle of incidence,

κ_1 = 1 (dielectric constant of free space)

κ_2 = dielectric constant of panel material, and

2ℓ = center-to-center spacing of the strips.

There was also a restriction on the rate of change of the dielectric con-
stant with distance. The restriction for which the WKB solution is valid
is given by

$$\left| \frac{d\kappa}{dz} \right| << \frac{4\pi}{\lambda_o} \; [\kappa(z) - \sin^2\theta]^{3/2} \; , \qquad (24)$$

where

$\kappa(z)$ = real part of complex permittivity function, and

λ_o = operating free-space wavelength.

By utilizing Equations 23 and 24, design parameters were calculated for a
broadband panel and these data are tabulated in Table I. For a center-to-
center spacing of the grooves of 0.26-inch the upper frequency limit would
be 18 GHz (essentially the upper frequency limit is controlled by the groove
spacing.) The lower frequency limit is controlled by the depth of the
grooves, d_1, and for 2 GHz to 18 GHz operation, this value would be 5.8
inches. This thickness was impractical and it was decided to use a panel
thickness of 1.5 inches with 0.625-inch groove depths on each side of the
panel. The panel did have an upper frequency cut-off near 18.0 GHz while
the lower frequency cut-off was near 4.0 GHz. This panel is referred to
as Panel No. 1 in the section on measured results. Another Panel, No. 2,
was fabricated with a groove spacing of 0.125-inch and data are also
presented on this panel. Both panels were made of Rexolite.

TABLE I

Calculated Parameters for Broadband Panel

f_{max}, f_{min} (GHz)	ℓ (Inches)*	$d_1 min$ (Inches)
2	1.20042	5.78973
4	.60021	2.89487
6	.40014	1.92991
8	.30011	1.44743
10	.24008	1.15795
12	.20007	.96496
14	.17149	.82710
16	—	—
18	.13338	.64330
20	—	— —
22	—	—
24	.10004	.48248
26	—	—
28	—	—
30	.0800 3	.38598
32	—	—
34	—	—
36	.06669	.32165

*Note that ℓ is the half-spacing of the strips; the center-to-center spacing is 2ℓ.

A. Measurement Technique

A microwave phase shift bridge free-space technique was employed to determine the broadband panel insertion phase shift and insertion loss as functions of frequency, incidence angle and polarization. A Scientific-Atlanta phase/amplitude receiver was used in the measurements to obtain the panel transmission data.

A reference flat panel was inserted between the two horns in the sample arm of the phase shift bridge and the system was adjusted and calibrated so that the reference test panel transmission properties approached those of calculated data for a theoretical flat panel. Once the reference flat panel measurements were completed, the broadband panel was inserted into the test fixture and the transmission properties were recorded. These data were taken at 1.0 GHz intervals from 2.0 GHz to 24 GHz on Panel No. 1 and from 2.0 GHz to 40 GHz on Panel No. 2.

B. Measured Results

The panel transmission data are presented for the 0° and 60° incidence angle cases only. The data for the angles between 0° and 60° were measured, and since these data fall within the cases plotted, it was felt unnecessary to present each data point. Thus, only the extreme cases are presented here. It also reduces considerably the number of plots required to define each panel.

The transmission data for Panel No. 1 are presented in Table II. Both the measured and predicted values are shown. Note that the transmission properties of Panel No. 1 are excellent to about 20 GHz. For vertical polarization (the perpendicular polarization case), the insertion loss changes drastically near 20 GHz. On the low end of the frequencies tested, the panel did not transmit satisfactorily below 4.0 GHz. Panel No. 1 operated satisfactorily from 4 GHz to 18 GHz.

The transmission data for Panel No. 2 are presented in Table III. Again, only the 0° and 60° incidence angle cases are shown. The panel had good transmission properties from 4 GHz to 36 GHz. Transmission properties of the vertical polarization case, which is the worst case, are tabulated from 3 GHz to 35 GHz. Spot checks of horizontal polarization were made which indicated that the panel transmission properties are better for

TABLE II

COMPARISON OF MEASURED AND PREDICTED TRANSMISSION LOSS AND INSERTION PHASE DELAY FOR PANEL NUMBER 1

Freq. (GHz)	0° Incidence				60° Incidence			
	$\|T_{\|\|}\|$ (dB)	$\angle T_{\|\|}$ (degrees)	$\|T_\perp\|$ (dB)	$\angle T_\perp$ (degrees)	$\|T_{\|\|}\|$ (dB)	$\angle T_{\|\|}$ (degrees)	$\|T_\perp\|$ (dB)	$\angle T_\perp$ (degrees)
3	0.50* / 0.44	41 / 42	0.40 / 0.44	44 / 42	0.20 / 0.02	70 / 71	3.10 / 2.89	62 / 59
4	-0.15 / 0.06	55 / 57	0.10 / 0.06	55 / 57	-0.40 / 0.07	94 / 95	1.60 / 1.54	75 / 75
9	-0.22 / 0.02	135 / 135	-0.22 / 0.02	142 / 135	-0.25 / 0.10	-145 / -147	-0.14 / 0.10	-157 / -163
15	-0.15 / 0.00	-128 / -130	0.00 / 0.00	-134 / -130	-0.03 / 0.06	-7 / 0	0.30 / 0.4ϵ	-18 / -19
20	-0.10 / 0.00	-45 / -46	-0.15 / 0.00	-45 / -46	-0.30 / 0.00	125 / 128	-0.05 / 0.14	120 / 104
25	0.00 / 0.00	46 / 42	-0.05 / 0.00	41 / 42	0.40 / 0.09	-110 / -97	-12.9 / 0.03	-50 / -125
30	- / 0.00	- / 137	- / 0.00	- / 137	- / 0.04	- / 45	- / 0.14	- / 14
35	- / 0.00	- / -122	- / 0.00	- / -122	- / 0.04	- / -164	- / 0.03	- / 161

Upper figures are measured values, lower figures are predicted values.

E5-13

TABLE III

COMPARISON OF MEASURED AND PREDICTED TRANSMISSION LOSS AND INSERTION PHASE DELAY FOR PANEL NUMBER 2

Freq. (GHz)	0° Incidence				50° Incidence			
	$\lvert T_{\parallel} \rvert$ (dB)	$\angle T_{\parallel}$ (degrees)	$\lvert T_{\perp} \rvert$ (dB)	$\angle T_{\perp}$ (degrees)	$\lvert T_{\parallel} \rvert$ (dB)	$\angle T_{\parallel}$ (degrees)	$\lvert T_{\perp} \rvert$ (dB)	$\angle T_{\perp}$ (degrees)
3	0.50 / 0.44	45 / 42	0.35 / 0.44	43 / 42	0.00 / 0.02	74 / 71	2.85 / 2.89	63 / 59
4	-0.20 / 0.06	58 / 57	0.08 / 0.06	59 / 57	-0.25 / 0.07	102 / 95	1.30 / 1.55	79 / 74
9	-0.10 / 0.01	137 / 134	-0.20 / 0.01	137 / 134	0.10 / 0.09	-136 / -148	0.00 / 0.11	-152 / -165
15	0.05 / 0.00	-128 / -134	0.05 / 0.00	-125 / -134	0.05 / 0.06	-11 / -6	0.25 / 0.43	-13 / -25
20	0.05 / 0.00	-48 / -57	-0.10 / 0.00	-49 / -57	0.20 / 0.01	130 / 114	0.00 / 0.16	110 / 89
25	0.10 / 0.00	32 / 21	0.10 / 0.00	31 / 21	0.60 / 0.04	-93 / -124	0.60 / 0.01	-125 / -153
30	- / 0.00	- / 101	0.10 / 0.00	116 / 101	- / 0.07	- / 0	0.35 / 0.05	-7 / -34
35	- / 0.00	- / -177	0.10 / 0.00	-140 / -177	- / 0.06	- / 127	0.10 / 0.10	171 / 88

*Upper figures are measured values, lower figures are predicted values.

horizontal polarization than for vertical polarization. The agreement of
phase angles was worse for Panel No. 2 than for Panel No. 1 since the tops
of the wedges of Panel No. 2 were blunted instead of sharp as in the
mathematical model.

The computer analysis program, which is being presented in this paper,
was formulated during the panel measurement program. The analysis verifies
the measured data as indicated in Table II and III. By having this program,
one can analyze the transmission properties of any anisotropic dielectric
panel.

Appendix A

AMPLITUDE COEFFICIENT TENSOR

The tensors $\bar{\bar{A}}_m$ and $\bar{\bar{A}}_{m+1}$ have the same form only the subscript are different. The argument d_m of these tensor functions, however, is the same for both. For an argument d, the form of these tensors is as follows:

$$\bar{\bar{A}}_m(d) = \begin{bmatrix} A_{11} & A_{12} & A_{13} & A_{14} \\ A_{21} & A_{22} & A_{23} & A_{24} \\ A_{31} & A_{32} & A_{33} & A_{34} \\ A_{41} & A_{42} & A_{43} & A_{44} \end{bmatrix}$$

where

$$A_{11} = \left(\cos \theta_m + C_{\parallel i_m} u^i_{x_{d_m}} \right) e^e_m(d)$$

$$A_{12} = u^i_{x_{L_m}} e^o_m(d)$$

$$A_{13} = \left(\cos \theta_m + C_{\parallel r_m} u^r_{x_m} \right) e^{e*}_m(d)$$

$$A_{14} = u^r_{x\perp_m} e^{o*}_m (d)$$

$$A_{21} = \left(\sin \theta_m + C_{\|i_m} u^i_{y\|_m} \right) e^e_m (d)$$

$$A_{22} = u^i_{y\perp_m} e^o_m (d)$$

$$A_{23} = \left(\sin \theta_m + C_{\|r_m} u^r_{y\|_m} \right) e^{e*}_m (d)$$

$$A_{24} = u^r_{y\perp_m} e^{o*}_m (d)$$

$$A_{31} = \beta^e_m \left[-n^e_{zi_m} \sin \theta_m + C_{\|i_m} \left(n^e_{yi_m} u^i_{z\|_m} - n^e_{zi_m} u^i_{y\|_m} \right) \right] e^e_m (d)$$

$$A_{32} = \beta^o_m \left(n^o_{yi_m} u^i_{z\perp_m} - n^o_{zi_m} u^i_{y\perp_m} \right) e^o_m (d)$$

$$A_{33} = \beta^e_m \left[-n^e_{zr_m} \sin \theta_m + C_{\|r_m} \left(n^e_{yr_m} u^r_{z\|_m} - n^e_{zr_m} u^r_{y\|_m} \right) \right] e^{e*}_m (d)$$

$$A_{34} = \beta^o_m \left(n^o_{yr_m} u^r_{z\perp_m} - n^o_{zr_m} u^r_{y\perp_m} \right) e^{o*}_m (d)$$

$$A_{41} = \beta^e_m \left[n^e_{zi_m} \cos \theta_m + C_{\|i_m} \left(n^e_{zi_m} u^i_{x\|_m} - n^e_{xi_m} u^i_{z\|_m} \right) \right] e^e_m (d)$$

$$A_{42} = \beta^o_m \left(n^o_{zi_m} u^i_{x\perp_m} - n^o_{xi_m} u^i_{z\perp_m} \right) e^o_m (d)$$

$$A_{43} = \beta_m^e \left[n_{zr_m}^e \cos \theta_m + \upsilon_{\|r_m} \left(n_{zr_m}^e u_{x\|_m}^r - n_{xr_m}^e u_{z\|_m}^r \right) \right] e_m^{e^*}(d)$$

$$A_{44} = \beta_m^o \left(n_{zr_m}^o u_{x\perp_m}^r - n_{xr_m}^o u_{z\perp_m}^r \right) e_m^{o^*}(d)$$

To simplify manipulations, the following terms were defined. Let

$$e_m^o(d) = e^{-j\beta_m^o n_{zi_m}^o d}$$

$$e_m^e(d) = e^{-j\beta_m^e n_{zi_m}^e d}$$

on

$$e_{m+1}^o(d_m) = e^{-j\beta_{m+1}^o n_{zi_{m+1}}^o d_m}$$

$$e_{m+1}^e(d_m) = e^{-j\beta_{m+1}^e n_{zi_{m+1}}^e d_m}$$

and

$$e_m^o(d_m) = e^{-j\beta_m^o n_{zi_m}^o d_m}$$

$$e_m^e(d_m) = e^{-j\beta_m^e n_{zi_m}^e d_m}$$

The parallel components of the field were eliminated by using $\bar{n} \cdot \bar{D} = 0$ thus obtaining

$$E_{\parallel_m}^i = C_{\parallel i_m} E_{o_m}^i$$

where

$$C_{\parallel i_m} = -\frac{n_{xi_m}^e K_{x_m} \cos\theta_m + n_{yi_m}^e K_{y_m} \sin\theta_m}{n_{xi_m}^e K_{x_m} u_{x\parallel_m}^i + n_{yi_m}^e K_{y_m} u_{y\parallel_m}^i + n_{zi_m}^e K_{z_m} u_{z\parallel_m}^i}$$

and

$$E_{\parallel_m}^r = C_{\parallel r_m} E_{o_m}^r$$

where

$$C_{\parallel r_m} = -\frac{n_{xr_m}^e K_{x_m} \cos\theta_m + n_{yr_m}^e K_{y_m} \sin\theta_m}{n_{xr_m}^e K_{x_m} u_{x\parallel_m}^r + n_{yr_m}^e K_{y_m} u_{y\parallel_m}^r + n_{zr_m}^e K_{z_m} u_{z\parallel_m}^r}$$

The angle θ_m is used to specify the orientation of the optic axis with respect to the x axis in the m-th layer as

$$\bar{u}_{o_m} = \cos\theta_m \, \bar{a}_x + \sin\theta_m \, \bar{a}_y + 0 \, \bar{a}_z$$

REFERENCES

1. J. H. Richmond, "The WKB Solution for Transmission Through Inhomogeneous Plane Layers," IRE Trans. on Antennas and Propagation, Vol. AP-10, pp. 472-473, July 1962.

2. H. L. Bassett and G. K. Huddleston, "Broadband Radome Techniques," Interim Report Number 1, Georgia Tech Project A-1333, Atlanta, Georgia, February 1973.

3. M. Born and E. Wolf, Principles of Optics, New York: Pergamon Press, 1964, pp. 665-681.

4. D. S. Jones, The Theory of Electromagnetism, New York: Pergamon Press, 1964, pp. 329-332.

5. J. Strong, Concepts of Classical Optics, San Francisco: W. H. Freeman, 1958, pp. 128-133.

6. T. Morita and S. B. Cohn, "Microwave Lens Matching by Simulated Quarter-Wave Transformers," IRE Trans. on Antennas and Propagation, Vol. AP-4, pp. 33-39, January 1956.

7. R. E. Collin, Field Theory of Guided Waves, New York: McGraw Hill, 1960, pp. 97-102.

EFFECTS OF SURFACE MOISTURE ON THICK RADOMES AT 8 mm

by
R. L. Mather, J. M. Devan, and H. Milligan
Naval Electronics Laboratory Center
San Diego, California 92152

WATER EFFECTS, GENERAL AND QUALITATIVE

The principal purpose of the radome in a submarine application is to exclude water from the submerged antenna structure. The antenna properties will be used only when the submarine is surfaced. However, the radome may be covered with a residual water layer that remains after surfacing, or it may be wetted by splash, spray, or rain. Although it does not appear possible to obtain for computation purposes a rigorous mathematical description of the typical water layers that may occur on the radome surface, experimental studies have been made of antenna properties while the radome has been wetted with water spray. The combination of simple calculations and experimental data yields a first-order understanding of the radome water effects.

Because severe fundamental problems exist, both in the calculation and the experimental measurement of water effects, a qualitative conjectural picture of such effects is first presented in order to fit the available calculations and measurements into a coherent context.

Water has an anomalously high dielectric constant and loss tangent for the 35–40-GHz region in comparison with the dielectric materials used for the radome. Water layers a few thousandths of an inch thick cause major attenuations of the fields. Water drops larger than 100 microns ($=0.1$ mm $=0.004$ inch) in diameter (roughly the dividing line between fog and rain) are essentially opaque. For layers and drops of these small dimensions, surface tension forces are very significant. In experiment and application, insufficiently known surface tension effects introduce uncertainties.

The clean surface of the BI A-4 radome used in these experiments is quite water repellant. At low spray rates of fresh water, the surface is dotted with clinging drops separated by dry surface. A large fraction of the surface is essentially dry, and antenna performance is almost unaffected by the water drops. As the density of drops increases, a coagulation threshold is reached, and transient rivulets carry off many of the accumulated drops. Under certain conditions, the scattered radiation from these transient rivulets can be observed in the sidelobe regions of the antenna pattern (trickle noise). As the spray rate increases, the rivulets form more frequently and finally merge to form a continuous film over the surface, with accompanying high attenuation. The temporal unevenness of this film will amplitude-modulate the main beam (pitter-patter noise). Once such a film has formed and the run-off flow pattern has been established, the film thickness increases relatively slowly with spray rate.

The water film is established more easily and maintained longer if the radome surface has been contaminated or if the water contains certain kinds of impurities. A BI A-4-type radome was immersed in the ocean for several months and observations were made of the biologic fouling that occurred. The experiment indicated that biologic fouling may be an important factor in radome and antenna performance after immersion periods of 60 days. Ocean water from near the shore of Point Loma (perhaps slightly contaminated by San Diego sewage fallout) appeared more prone, qualitatively, to film formation on the BLA-4 than did San Diego city water. However, most of the experimental results for the two types of water were indistinguishable.

THEORETICAL CALCULATIONS

Supplementing the experimental observations were theoretical calculations in which the water was modeled by a uniform layer of dielectric over the radome surface. The dielectric and loss constants for the water layer are very high relative to those for the radome material. There has been uncertainty in the proper value for the water constants at 8-mm wavelengths, and we have used Dr. Howard E. Bussey of the National Bureau of Standards, Boulder, Colorado, as our expert on these constants. His latest recommended values for Copenhagen water (a laboratory-standard seawater) are listed in table 1. The value for the dielectric constant is some 15 percent higher (based on his experiments at these frequencies) than older values based on lower frequency measurements. The theoretical expression used to fit the dielectric constant data predicts changes with frequency and salinity which are small compared to those for changes of temperature. The predicted increase of water-layer attenuation between 0 and 20°C is about 35 percent.

An interesting feature of the theoretical calculations is the interaction of the internal reflections of the radome and water layers. These interactions are such that the peaks of transmission which occur near even numbers of quarter-wave thicknesses for the dry radome shift to odd numbers of quarter-wave thicknesses for water layers thicker than 2 millinches.

The effect of the added water layer on the antenna pattern is calculated to be quite small.

TABLE 1. SEAWATER DIELECTRIC PROPERTIES
(Recommended values for Copenhagen water by H. E. Bussey, Feb 74).

Temperature, °C	37.4 GHz		38.4 GHz	
	ϵ'	Tan δ	ϵ'	Tan δ
0	10.20	1.96	9.95	1.96
5	12.05	1.88	11.72	1.89
10	14.21	1.77	13.79	1.79
15	16.57	1.65	16.07	1.67
20	19.03	1.53	18.46	1.55
25	21.56	1.41	20.92	1.43

EXPERIMENTAL MEASUREMENTS WITH UNIFORM WATER FILMS

A uniform water film could be established experimentally on the radome surface in three ways: (1) the water could be held in place with absorbent paper tissue; (2) a laminar flow of water could be established over the radome surface; or (3) a continuous film of water could be formed over the radome surface under very high spray rates. The measurements under these conditions showed excellent agreement with the comparable calculations. Examples of such data are shown in figure 1 for transmission vs water film thickness.

The antenna pattern measurements show somewhat more degradation of the pattern with the water film than was predicted by calculations; however, the effects may not be outside those resulting from the experimental errors in the uniformity of the film.

EXPERIMENTAL MEASUREMENTS WITH WATER SPRAY

Experimental measurements done with water sprayed on the radome are closer to real Navy conditions, although all such measurements suffer from time variations of various kinds. During experiments with water spray, the antenna range site was somewhat windy so that the spray was wind-blown in a manner that might be expected at sea. (A time recording of the range signal for several spray rates is shown in figure 2.) Spray rates in excess of 30 inches per hour were required to maintain a continuous film over the BLA-4 radome surface. The signal loss shown in figure 2 resulted almost entirely from water on the radome surface and very little from spray suspended in the air. The time required for the signal to recover to within 0.25 dB of the dry radome transmission was about 30 seconds.

The antenna pattern measurements were made as the antenna-radome combination was turned at a constant rate. The resulting plotted function is a combination of both angular variations and time variations. The variations that were too rapid to be angular variations are attributed to time variations.

Two antennas were used within the radome: (1) a low-gain, small-aperture, linearly polarized, gain-standard horn, and (2) a high-gain, large-aperture (16-in.), right circularly polarized, parabolic dish. Antenna gain is used as an indicator of effective aperture size, and figure 2 shows that water spray effects are larger with the low-gain (small-aperture) antenna (as would be expected). No differences in effects could be attributed to the difference in polarization between these antennas.

Trickles form over the radome surface even at low spray rates. This temporary (lasting seconds) scattering point is separated from the main antenna location, and a beat between the scattered radiation and the direct beam is observable as the assembly is turned. This is more prominent with the small aperture (fig. 3) than with the large (fig. 4). An amplitude relative to the main beam can be assigned and is plotted in figure 5 against antenna gain.

The splatter of individual drops is presumed to disturb briefly (fraction of a second) the continuous water film formed at high spray rates to produce "pitter-patter" noise. This noise is observable as scattering in the sidelobe region (fig. 6 and 7), and its amplitude is also plotted in figure 5 against antenna gain. The pitter-patter also amplitude-modulates the main beam at low audio frequencies (below about 25 Hz), and the percent modulation is indicated in figure 8. The larger aperture is dramatically less subject to pitter-patter noise.

The figures 3, 4, 6, and 7 cover low and high spray rates and small and large apertures to give a rough overview of the effects of spray on antenna patterns. In figure 7, the relative sidelobe level for the near sidelobes has been increased by the spray. In other data, the relative increase has been of the order of or less than the main beam attenuation.

CONCLUSIONS

The effects of surface moisture on a thick radome at 8 mm have been observed under a variety of conditions and analyzed into a uniform film component, a trickle component, and a pitter-patter component. The uniform film effects appear to be calculable, and improved water dielectric constant information for these frequencies has been produced. The trickle and pitter-patter components have been measured for large and small effective apertures, with the expectation that apertures of other sizes will fall on the same curves.
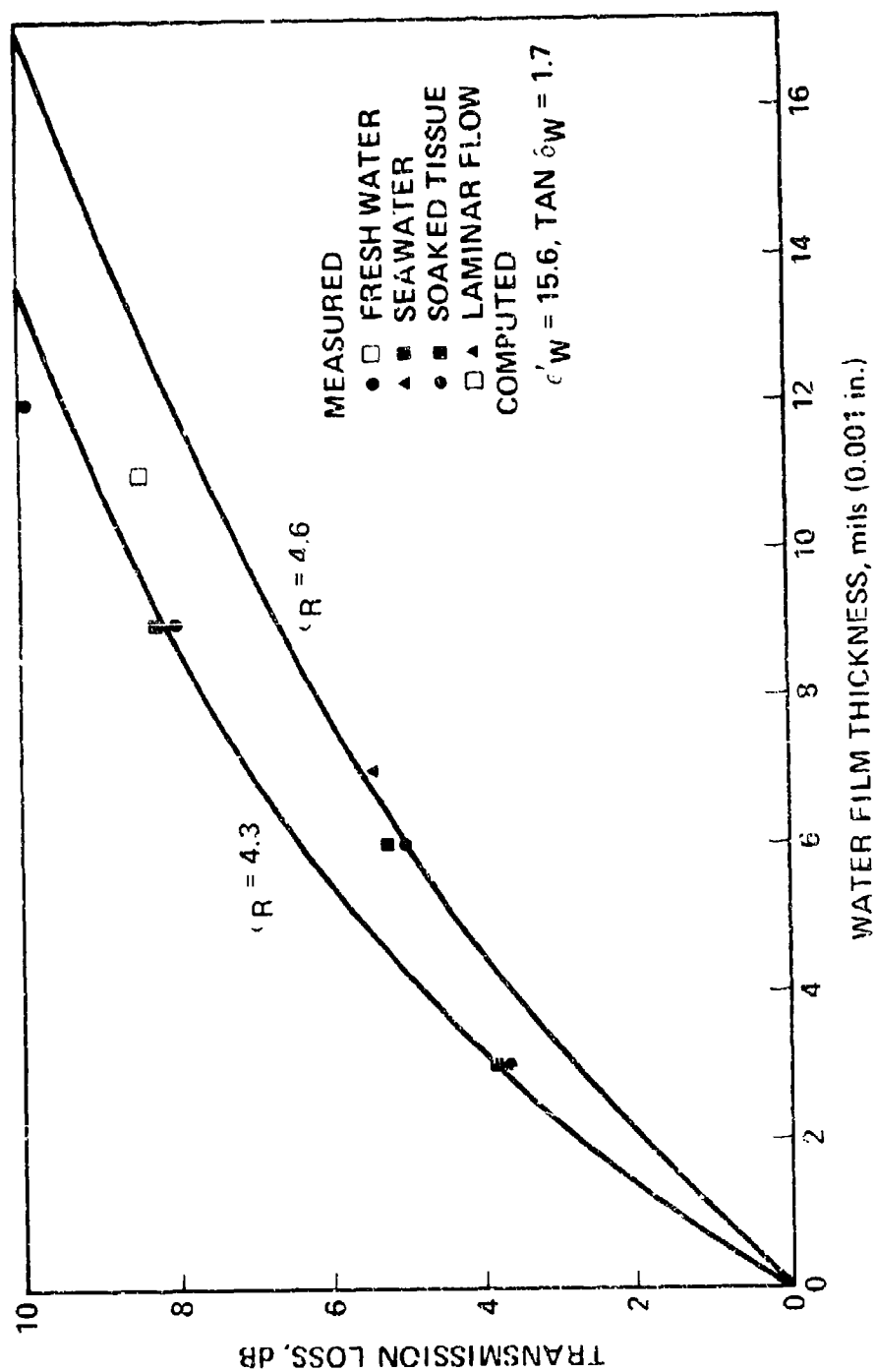
Figure 1. Normalized film transmission loss for simulated water films on BLA-4 radome with gain-standard horn antenna. $f = 37.5$ GHz.
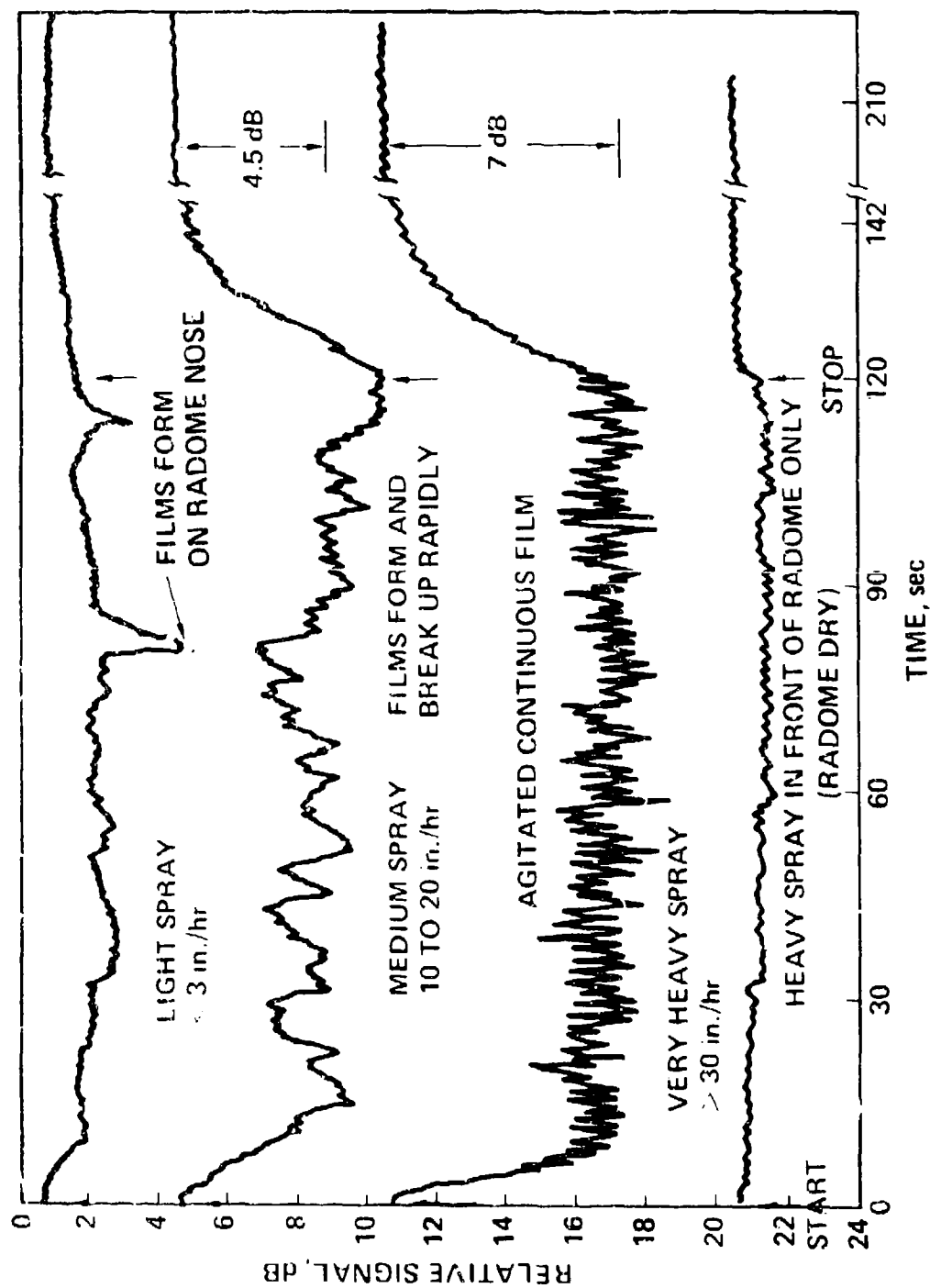
Figure 2. Gun-standard horn in BLA-4 radome — on-axis preliminary moisture effects test results with fresh water on an outdoor range.
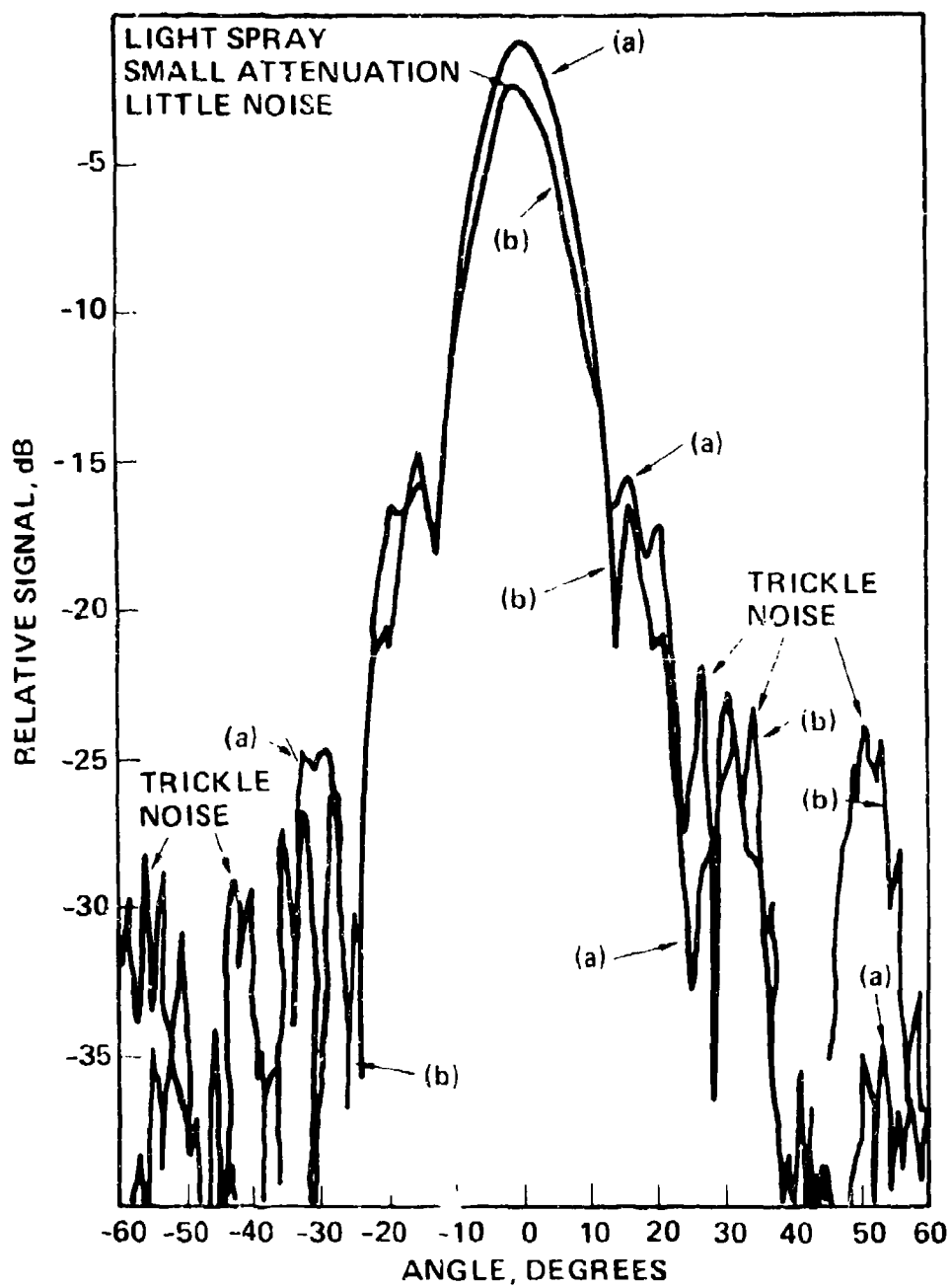
Figure 3. Trickle noise with gain-standard horn in BLA-4 radome at 3.5 GHz. (a) dry radome antenna pattern, (b) pattern with ocean water spray at 3 m. ht. Trickle noise −32 dB rel. Vertical linear polarization. 29 Nov 72.

Figure 4. Trickle noise with 16-inch diameter dish in Bl A-4 radome at 37.5 GHz: (a) dry radome antenna pattern, (b) pattern with ocean water spray at 3 in./hr. Trickle noise = -60 dB rel. Right circular polarization. 16 Jan 73.
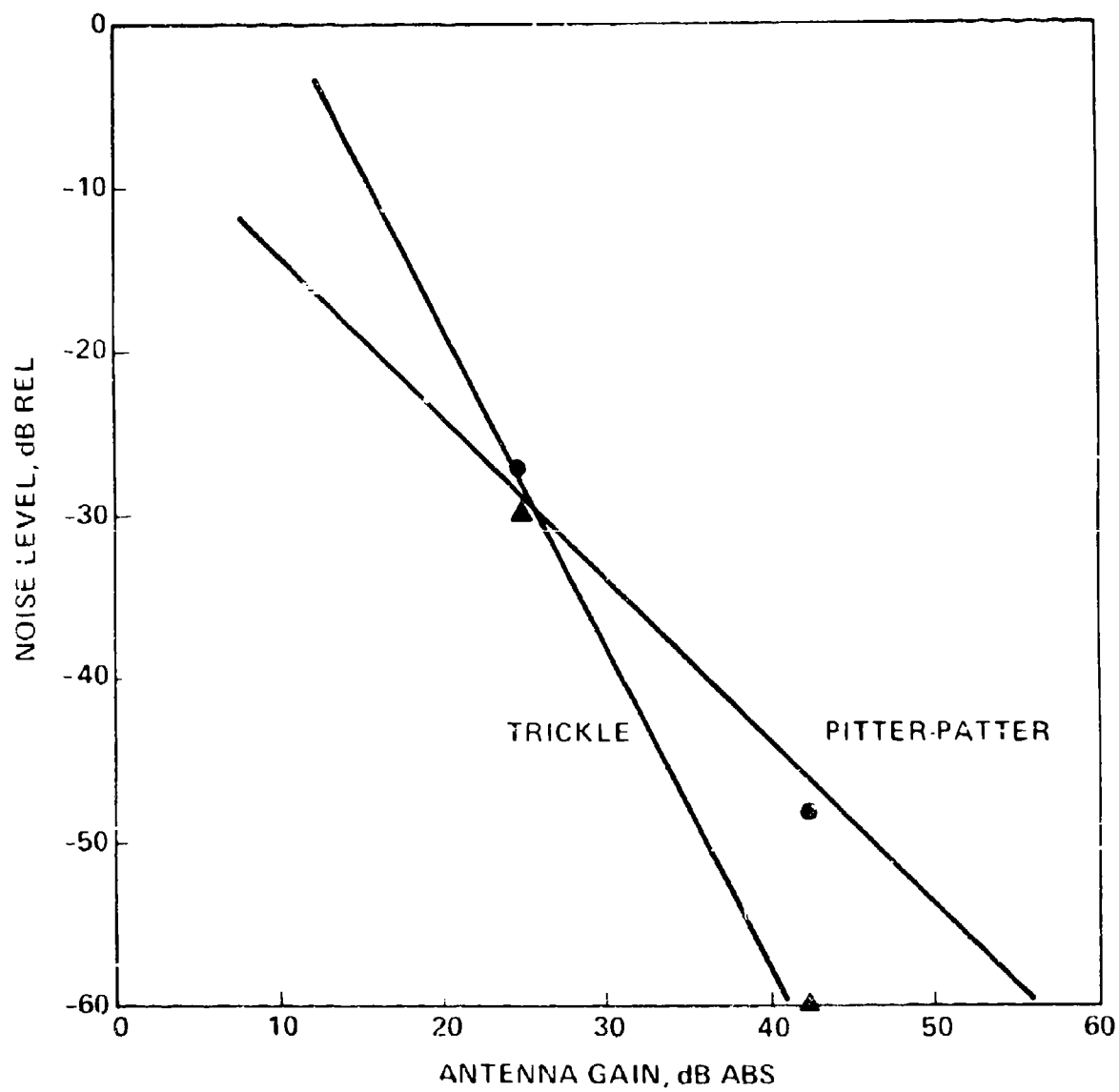
Figure 5. Transient water effects as a function of antenna gain. (▲) trickle noise, (●) pitter-patter noise.

Figure 6. Pitter-patter noise with gain-standard horn in BLA-4 radome at 37.5 GHz
(a) dry radome antenna pattern, (b) pattern with ocean water spray at 35 in. hr.
Pitter-patter noise in sidelobe region = -27 dB rel. Vertical linear polarization.
29 Nov 72.

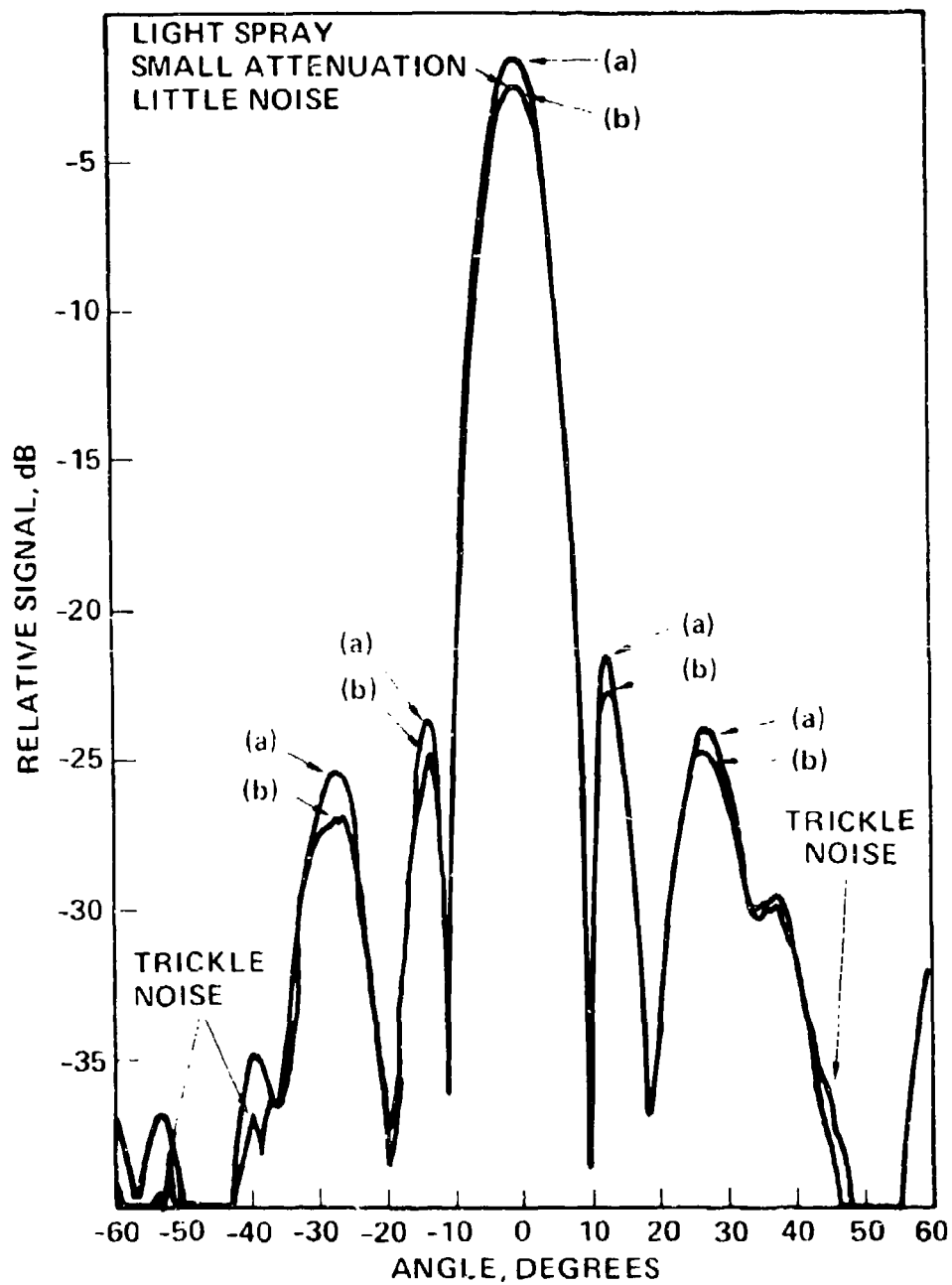Figure 7. Pitter-patter noise with 16-inch diameter dish in BLA-4 radome at 37.5 GHz. (a) dry radome antenna pattern. (b) pattern with ocean water spray at 35 in./hr. Pitter-patter noise in sidelobe region = −48 dB rel. Vertical linear polarization. 16 Jan 73.
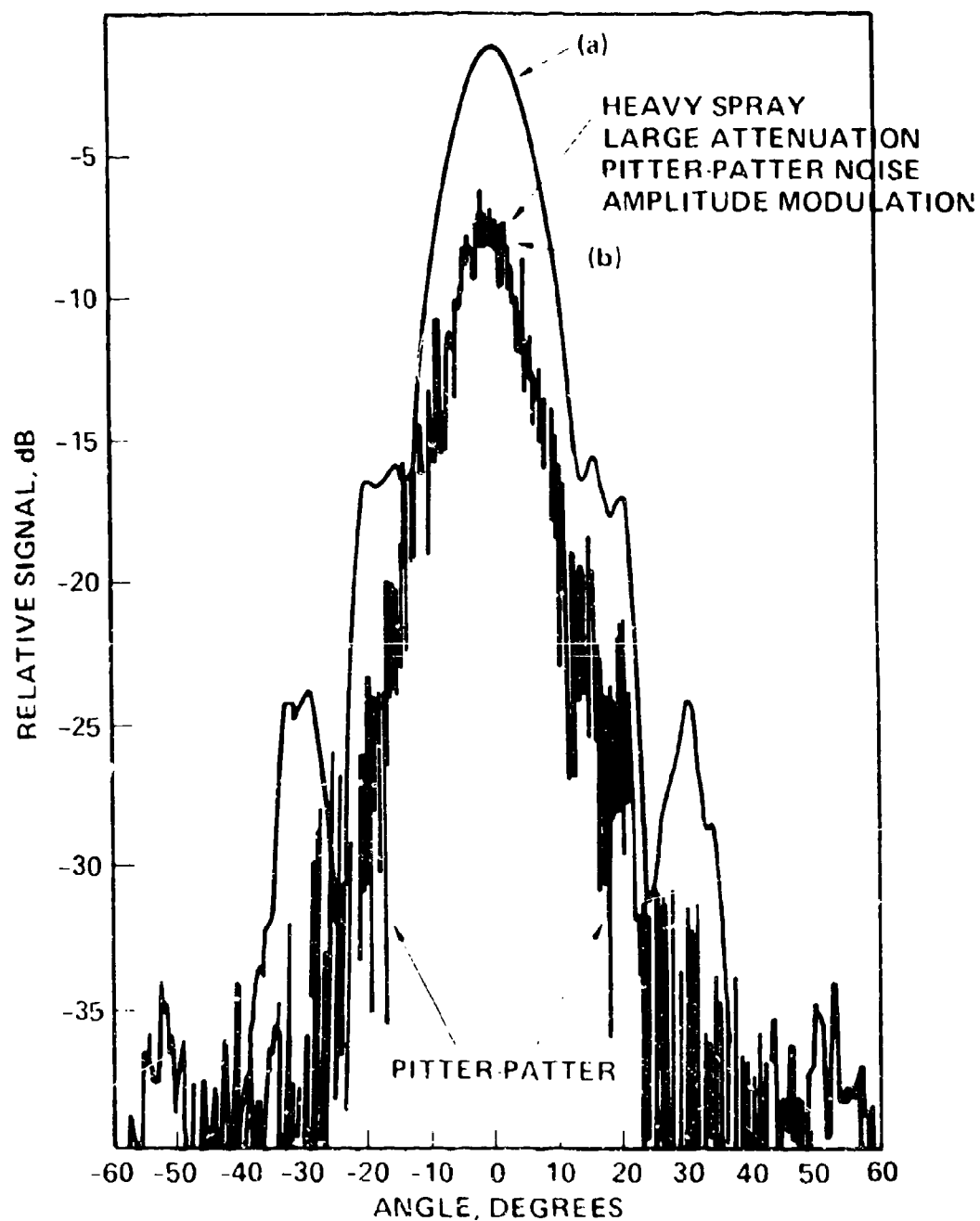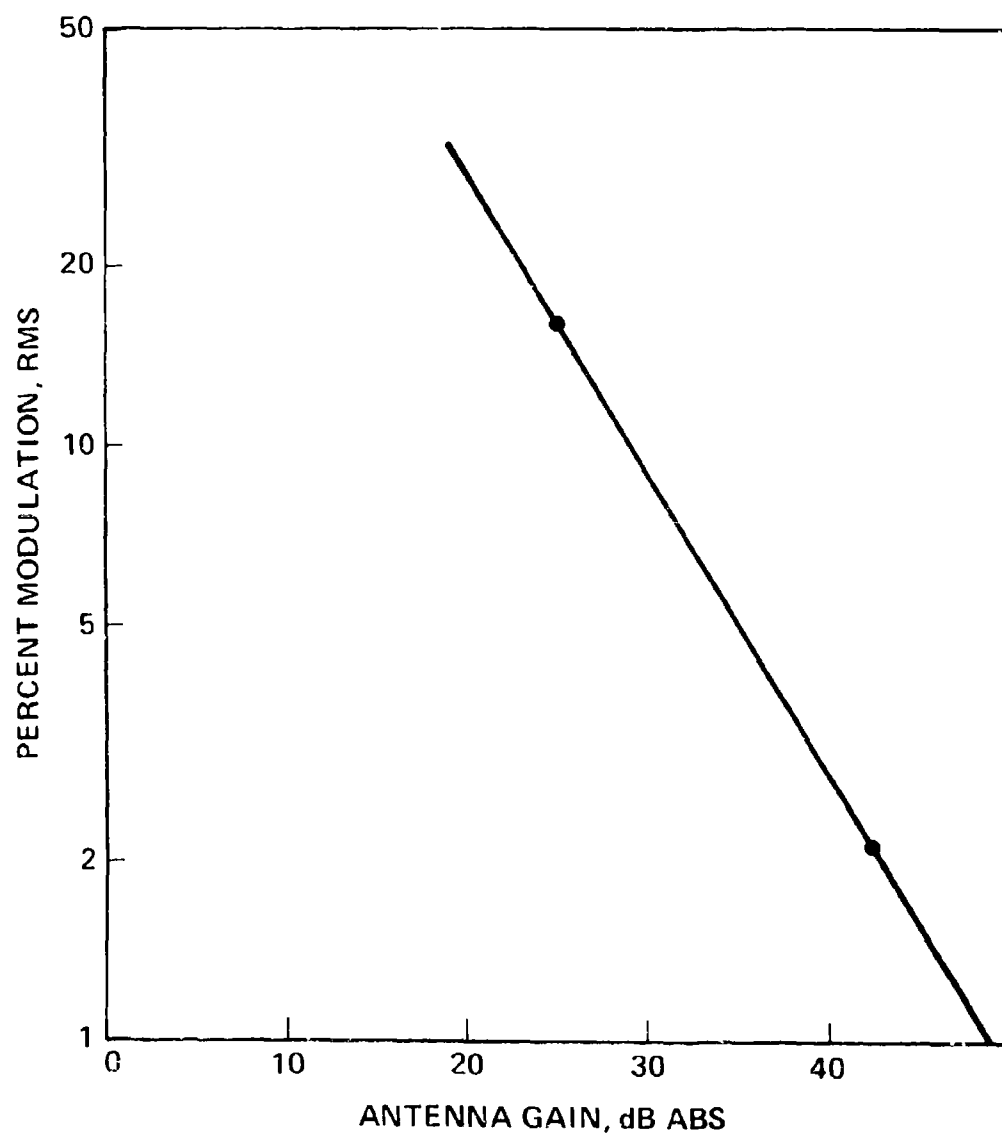
Figure 8. RMS pitter-patter noise modulation of main beam as a function of antenna gain.

SECOND AND HIGHER ORDER RADOMES
FOR MILLIMETER WAVES

by
R. A. Hayward and G. Tricoles
General Dynamics Electronics Division
San Diego, California 92138

1. INTRODUCTION

Millimeter wave radome techniques differ from those for centimeter waves even though both types can usually be analyzed with a single method and fabricated from identical materials. A major difference is in the thickness of the radome wall. For narrow band radomes*, which usually consist of a single homogeneous layer, the wall thickness t is either thin relative to the wavelength λ_d** or is approximately an integral multiple of $\lambda_d/2$. These thicknesses maximize the transmittance of a flat dielectric sheet for wave polarization parallel or perpendicular to the plane of incidence. The same thickness criteria apply to curved radomes because a radome can be locally approximated by flat sheets. Clearly, for the clases of radome designs such that t is much less than λ_d (thin wall design) or t approximately equal $\lambda_d/2$ (half wave design) a millimeter wave radome would be thinner than one for centimeter waves.

Although the thin wall and half-wave radomes are common for centimeter waves, at millimeter wavelengths the thickness may be too thin to withstand practical aerodynamic loads or pressures. In such cases, thickness values equal $2(\lambda_d/2)$ may be acceptable. If not, even higher order designs such as $3(\lambda_d/2)$, $4(\lambda_d/2)$ and so on may be necessary.

---

*A narrow band radome attenuates relatively little in a frequency band a few percent from the center frequency. Relatively little means usually that power transmittance exceeds -1 to -2 dB.

**The wavelength λ_d is the value in the dielectric; it is λ_0/n, where λ_0 is the wavelength in free space and n is the refractive index.

This paper gives predicted values of electromagnetic performance for higher order radome designs. The analytical method has been described earlier.[1] In addition, experimental data are presented to verify the accuracy of the method. This verification is new and significant because it evaluates the accuracy of the analytical method for thick radomes; in earlier work, only half wave and thin radomes had been utilized.

Although many variables affect radome design, the scope of this paper is restricted. The main variables treated are frequency the ratio of wall thickness to wavelength, the radome's shape and dielectric constant, the size and aperture distribution of the antenna enclosed by the radome and its orientation in the radome. We only illustrate general properties for wide ranges of parameters. For example, boresight error is presented for a streamlined radome for thickness ranging from small values to a full wavelength; this result shows some apprently little-known performance penalties in the boresight error of a full wave radome. In addition, the effects of defocussing a paraboloidal reflector are evaluated for a spherical radome, and it is shown that defocussing can increase transmittance by compensating phase aberrations.** In contrast, antenna defocussing seems inappropriate for streamlined radomes because incidence angles vary widely as the antenna beam is swept from the tip to the flatter parts of the radome. Multi-layer, broadband radomes are not included in this paper because some of their layers would be extremely thin.

Millimeter and centimeter wave radomes differ also because mechanical tolerances are more stringent for the smaller, millimeter waves. The wall thickness during manufacturing must be carefully controlled because transmittance minima occur when the thickness differs by $\lambda_d/4$ from the value for a maximum.

---

*References are collected at the end of the paper.
**Defocusing was suggested to us by Dr. R. Mather in private communications; see Reference 2.

The position of an antenna is a radome can also influence transmittance. Although such tolerances are important in practice, their detailed evaluation is outside the scope of this paper.

2. STREAMLINED RADOME

The boresight error and power transmittance were computed for a streamlined radome with length 24 free space wavelengths λ_o and diameter 11 λ_o. The radome's shape was ogival and its dielectric constant was 5.5. The enclosed antenna had uniform illumination, and provided symmetric and antisymmetric outputs for sum and difference patterns. Calculations were made with the theory of Reference 1 by computing antenna patterns. The aperture was subdivided into a $\lambda/2$ square grid, and a bundle of rays was traced through the radome for each pattern angle. The ray tracing was repeated for each gimbal angle. Figure 1 shows values of transmittance and boresight error for gimbal angles 8° and 16°, the region of maximum error.

The results show three maxima of transmittance at zero thickness, and when the ratio of thickness to wavelength corresponds to half-wave and full-wave thicknesses. The aperture diameter was 10 λ_o. For the half-wave thickness ($t/\lambda_o \approx 0.24$, or $t/\lambda_d \approx 0.5$) transmittance is high, and the boresight error ranges from 2 to 5 milliradians for the two gimbal angles. These errors are typical for uniformly thick radomes. For the full wave thickness, transmittance is also high, but the boresight error ranges from 6 to 9 milliradians.

These calculations for a streamlined radome shape show that a second order radome gives high transmittance but with boresight error approximately twice that of a half wave radome. This result is understandable because the phase delays of a full-wave radome are approximately twice those of a half-wave radome.

The accuracy of the analytical method was verified by comparing computed results with measured data. For example, Figure 2 compares measured and

computed H-plane patterns for the gimbal angle 0° (radome and antenna axes aligned). Figure 3 shows boresight error for the antenna axis gimballed in the H-plane. The radome for Figures 2 and 3 had small thickness variations to reduce boresight errors below those of Figure 1.

3.   HEMISPHERICAL RADOME

This section describes measurements and calculations for a blunt radome in a hemisphere on a circular cylinder.[2] Measured and computed farfield patterns and boresight error are presented for two distinct antennas. In addition, computed values of the wavefront propagated through the radome are given. These wavefronts are aberration functions. They are significant because they reduce transmittance. This mechanism, which is distinct from attenuation by absorption and reflection, can be reduced for spherical radomes by defocusing the aperture distribution.[2] Such defocusing is practical for reflector type antennas, and it is useful for spherical radomes; however, it seems less useful for streamlined radomes because incidence angles vary greatly as the beam traverses the tip region and illuminates the flatter portions of the radome.

3.1   Horn Antenna

The antenna was a pyramidal horn with aperture 2.2 in. by 2.7 in. The radome had 18.3 in. outside diameter, 0.625 in. thickness, dielectric constant approximately 4.3, and loss tangent 0.03. Measurement were made at 37.5 GHz so the radome was 4.11 wavelengths thick, in terms of wavelength in the dielectric. The thickness is larger than necessary for most applications, but this radome was available and was utilized to test the computed results. A four-wavelength thick radome would be practical for higher frequencies, approximately 100 GHz.

Figure 4 shows computed E-plane patterns with and without radome. The gimbal angle relative to the radome was 0°; the antenna and radome axes were aligned. The calculations were made by assuming that the aperture field was that

of the dominant waveguide mode and the aperture was subdivided by a mesh half the wavelength on a side. The main feature of these patterns is the 5 dB loss at the peak of the beam. For comparison, Figure 5 shows measured patterns, but at 37.5 GHz. The frequency difference occurred because the dielectric constant was underestimated. The frequency 38 GHz maximizes the measured transmittance. The measured loss is also 5 dB. Although measured and computed side-lobe levels differ for the radome case these discrepancies are attributable to reflections between the radome and antenna; The reflections are dropped from the calculations. The existence of reflections were verified by longitudinal displacements of the antenna. Pattern effects are shown in Figure 6.

3.2 Paraboloidal Reflector

The antenna was a paraboloidal reflector with 16 in. diameter. Its patterns were computed for the radome described in Section 3.1.

Reference 2 showed that transmittance was very low for the reflector antenna. Transmittance was -9.6 dB. This value is much lower than the -5 dB value predicted for a flat sheet and observed for the small antenna of Section 3.1. The flat sheet calculations include absorption and reflection. The explanation, given in Reference 2, is that the phase aberration of the radome defocuses the reflector.[3] The measured value of transmittance was increased to approximately -5 dB by refocusing the antenna in the radome to compensate its phase errors: see Reference 2.

Computed patterns and measured patterns for the refocused antenna in the 0.625 in. radome are given in Figure 9. The antenna axis is aligned with the radome axis. Figure 10a shows the measured patterns, for the antenna focused in free space, with and without radome. In Figure 10b are computed patterns where the antenna aperture distribution was refocused to compensate the radome aberrations.

Figure 11 shows patterns for the antenna rotated 90° so its aperture spans both the hemispherical and cylindrical parts of the radome.

Figure 12 summarizes beam shift. The values in Figure 12 are smaller than those in Figure 8 (for the smaller, horn antenna) because the larger aperture averages wavefront tilts.

The computed phase distribution of the wave propagated through the radome is shown in Figure 13 for a range of thicknesses. These graphs are the phase aberrations that defocus the reflector antenna.

ACKNOWLEDGMENTS

REFERENCES

1. G. Tricoles and E. L. Rope, Jour. Opt. Soc. Am. 54 (1964); see also Ch. 2 Radome Design Handbook (ed. by J. D. Walton), Marcel-Dekker.

2. R. L. Mather, J. M. Devan, and H. Milligan, U.S. Naval Electronics Laboratory Technical Note 2555, 27 Nov. 1973. This note contains tentative and unpublished information, but its measured data are utilized for comparison with calculations.

3. The observed transmittance loss follows from a relation between transmittance and mean square wavefront deformation. See M. Born and E. Wolf Principles of Optics. p. 462, Pergamon Press (1959).
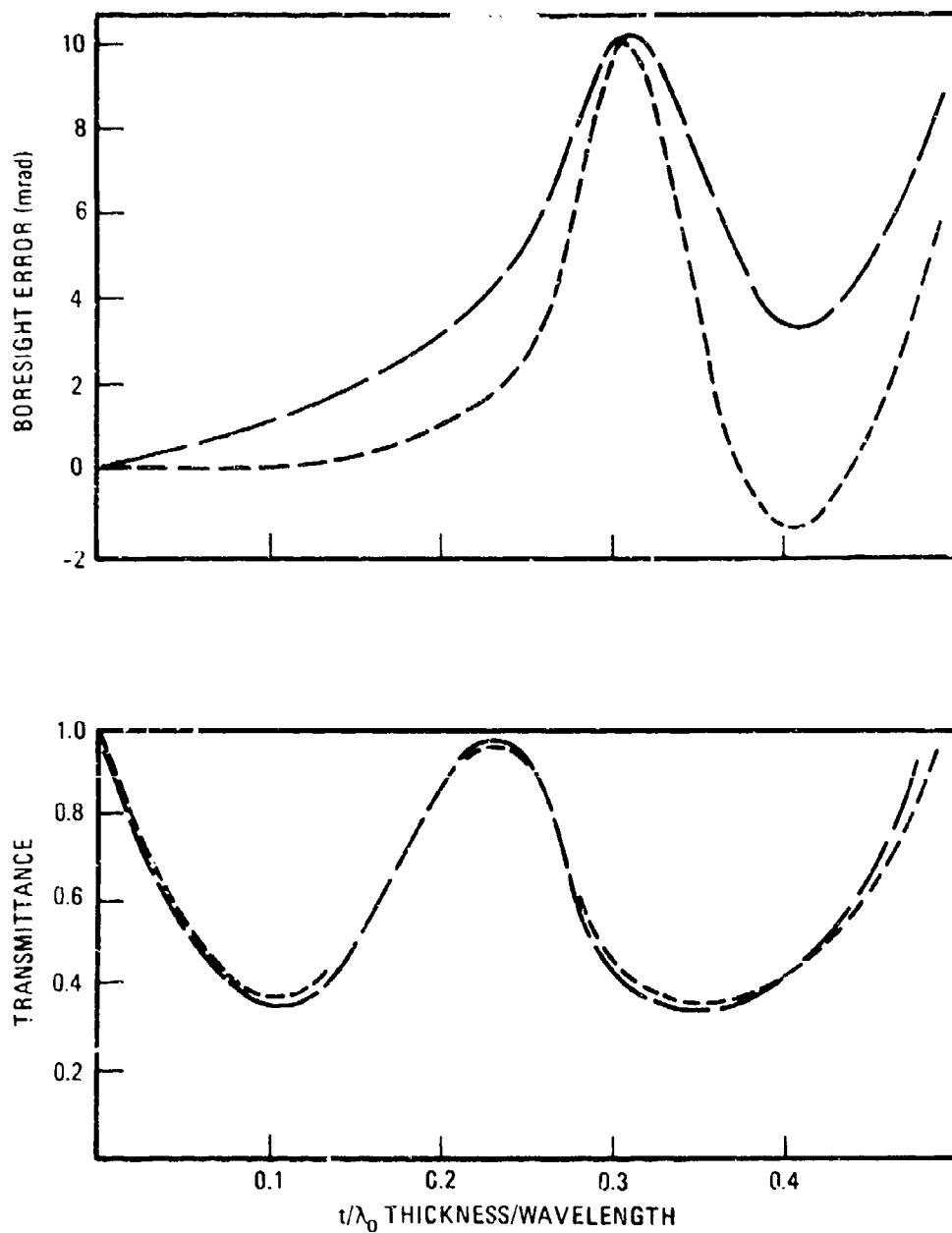
Figure 1. Computed boresight error and transmittance for an ogival radome.
length 24 λ_0, base diameter 11.2 λ_0, dielectric constant 5.5, loss
tangent 0.0003. The antenna had diameter 9.6 λ_0 and uniform
distribution; (----) 8° gimbal angle; (--) 16° gimbal angle. λ_0 is
the free space wavelength. The electric field was vertical, and
the antenna axis was displaced in the horizontal plane.
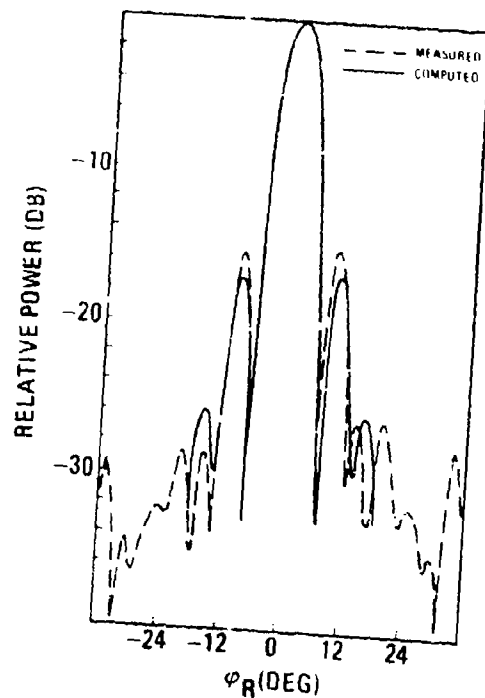
Figure 2. H-plane patterns for 0° gimbal angle
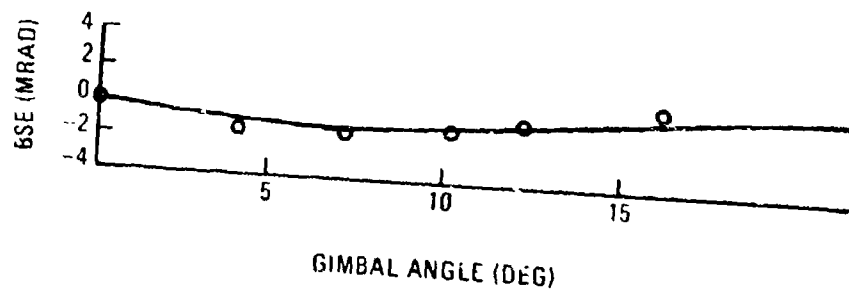
Figure 3. Boresight error for H-plane scan. Measured —; Computed 0.

E7-8
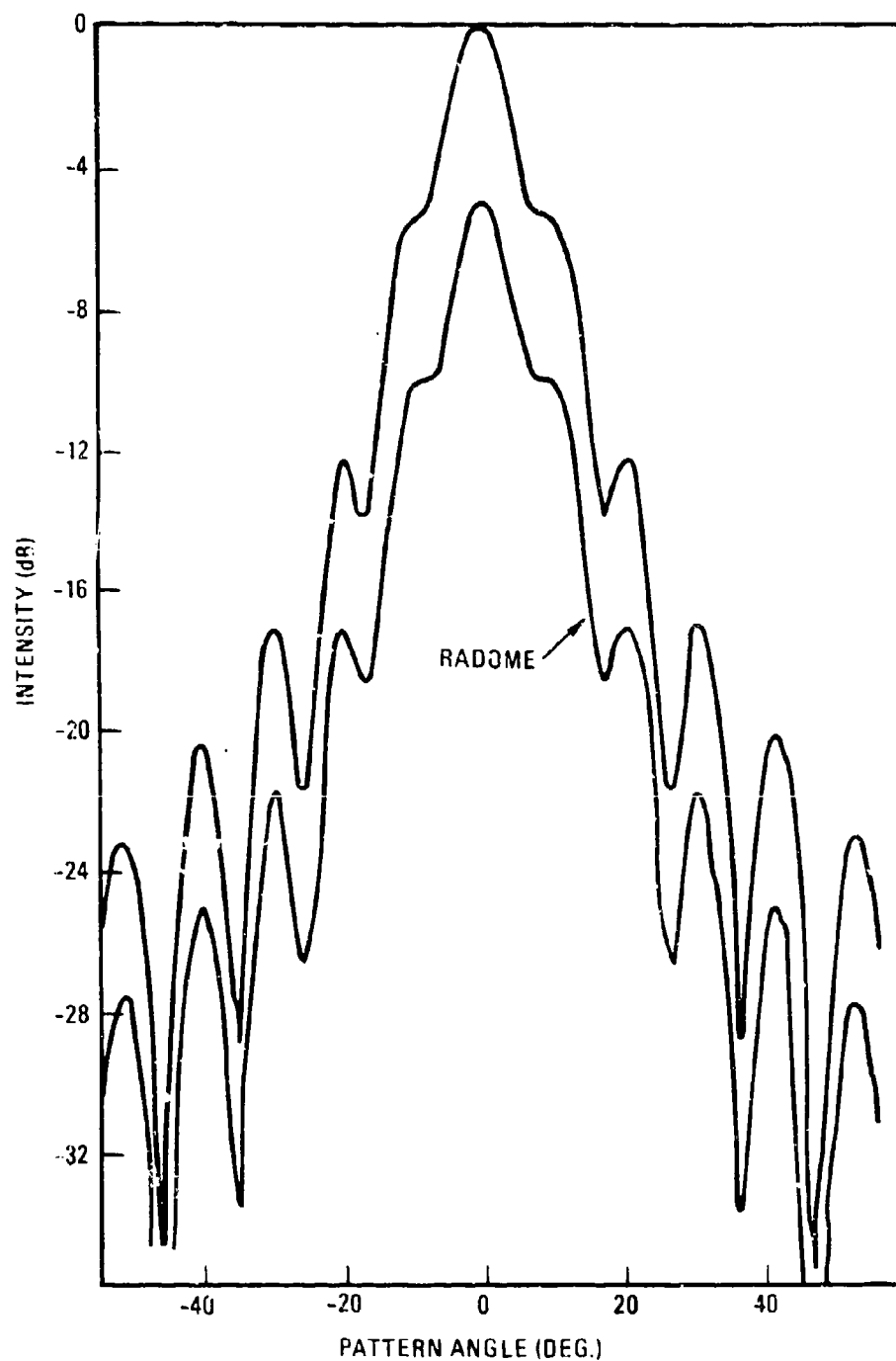
Figure 4. Computed E-plane pattern of horn antenna with and without hemispherical radome 18.3 in. outside diameter, 0.63 in. thick. Horn aperture 2.2 in. × 2.7 in. Frequency 38 GHz. Dielectric constant 4.3; loss tangent 0.03.
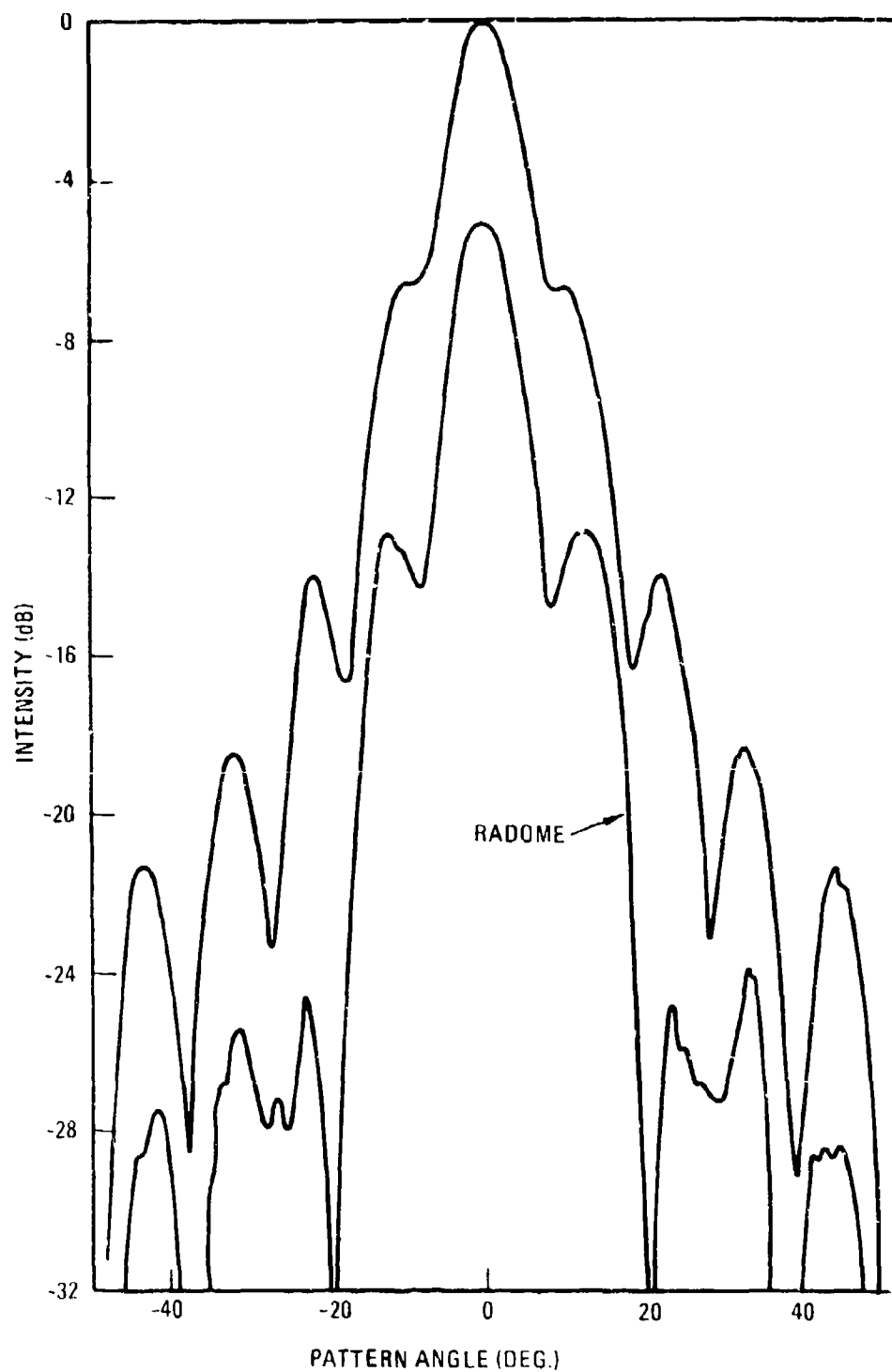
Figure 5. Measured E-plane patterns of horn antenna at 37.5 GHz. Parameters as in Figure 4.
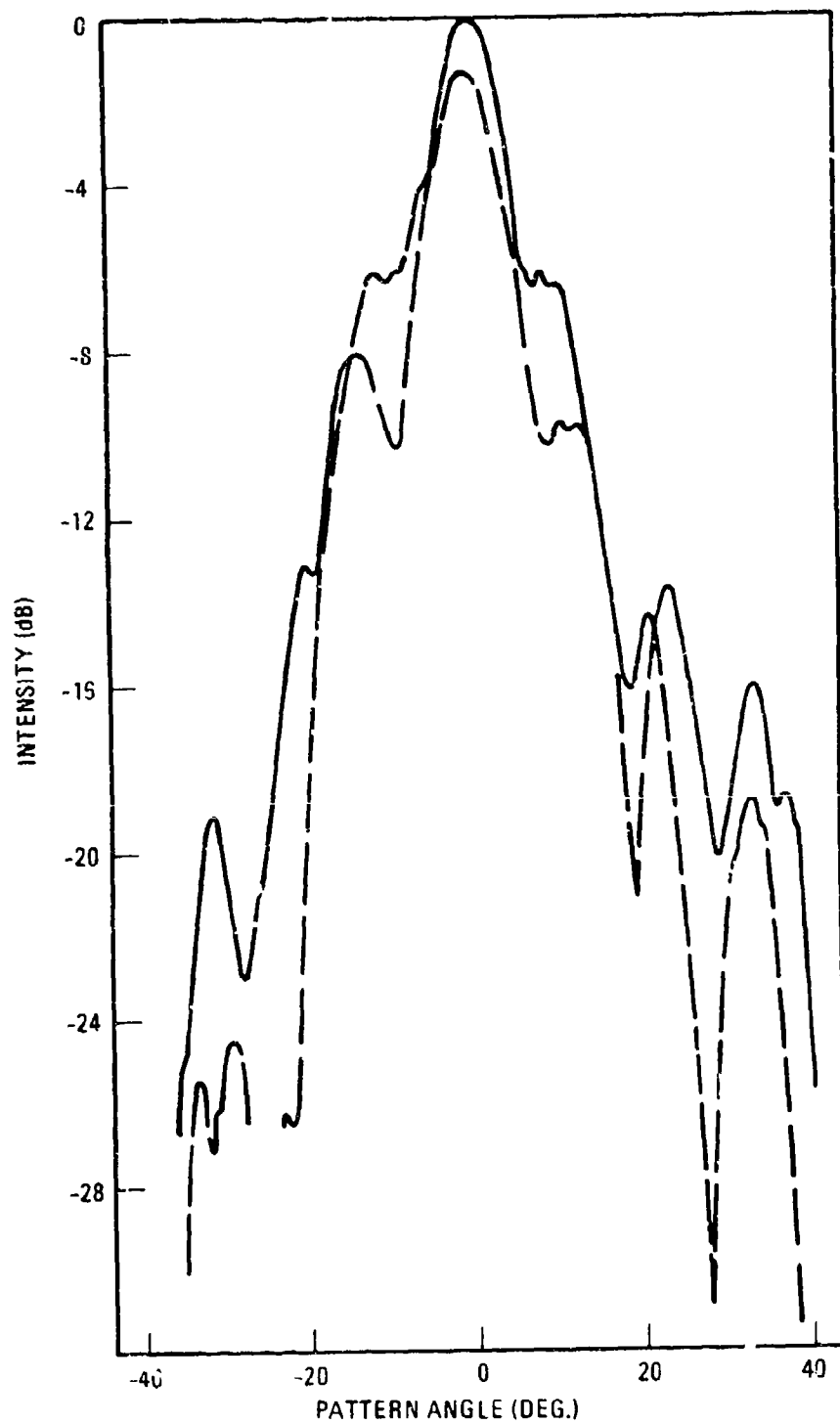
Figure 6. Measured E-plane patterns for two positions of the
antenna in the radome. Aperture at center of
radome — —; Aperture 3.6 in. forward — .
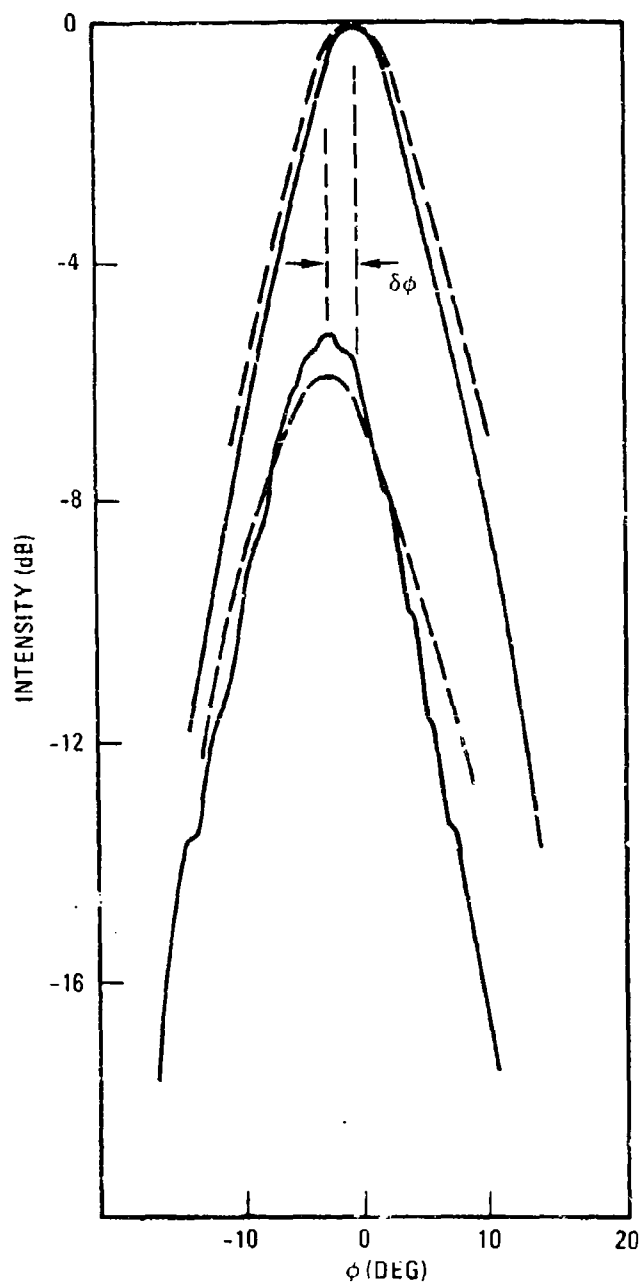
Figure 7. H-plane patterns corresponding to Figures 4 and 5, except that aperture displaced 6 in. in the H-plane. Upper pair of curves without radome. Lower curves with radome. Measured ——— ; computed — —. The boresight error $\delta\phi$.
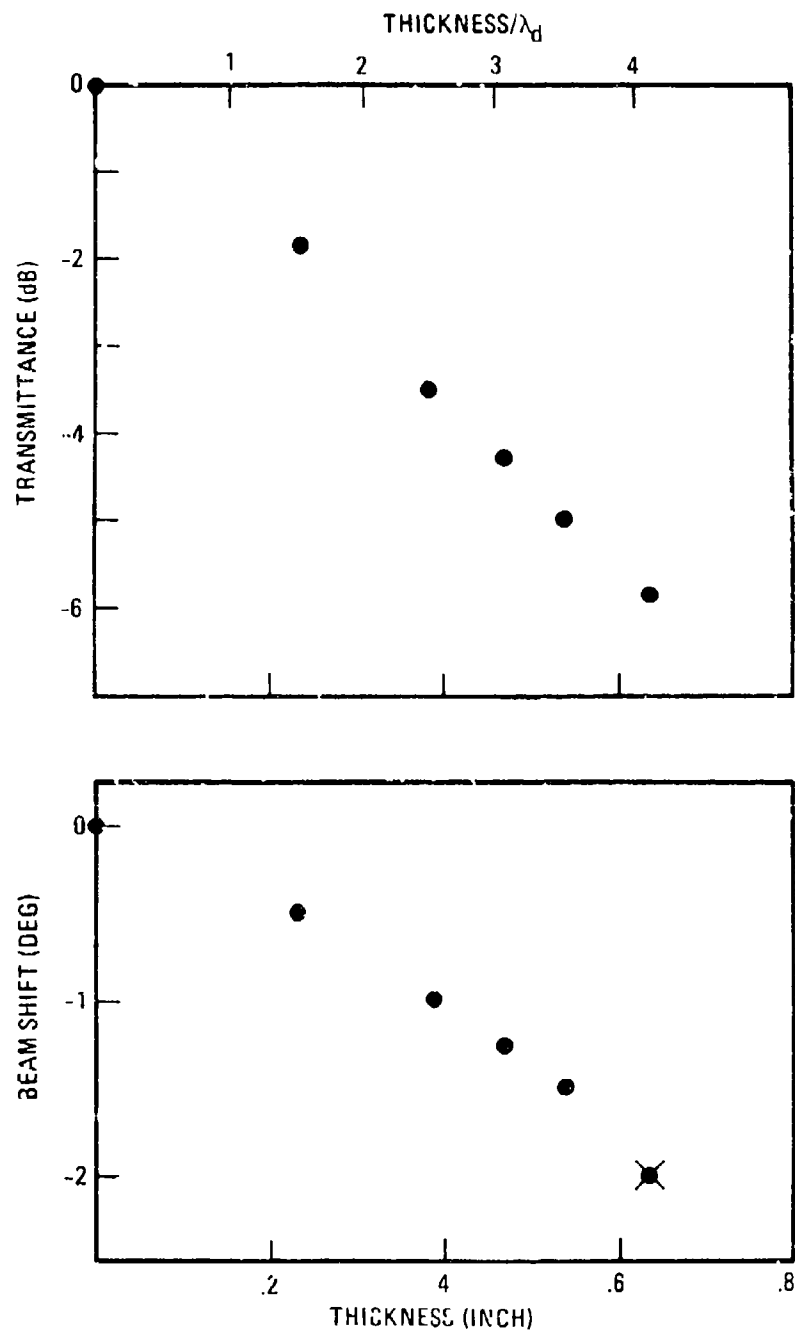
Figure 8. Beam shift and power transmittance in the H-plane for horn
antenna offset 6 in. in H-plane. Computed at 38 GHz (•), with
dielectric constant 4.3, loss tangent 0.03. Measured (x) at
37.5 GHz. λ_d is for 38 GHz.
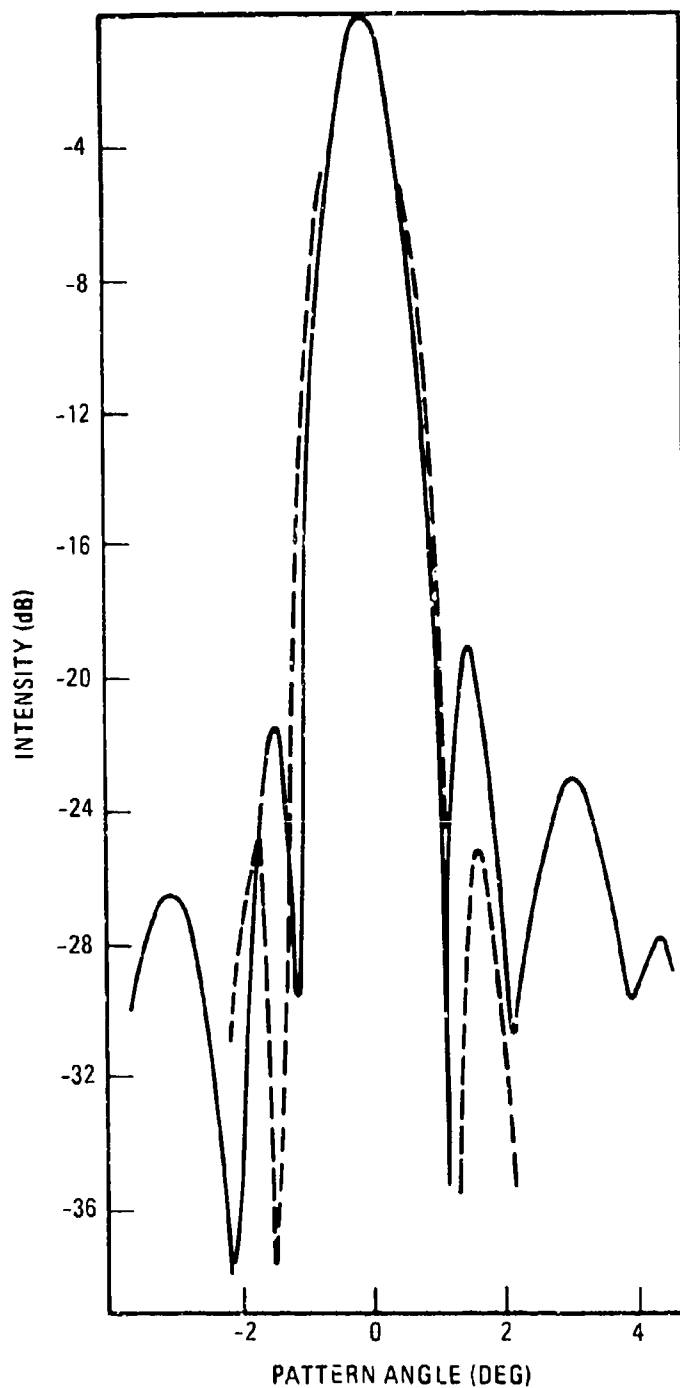
Figure 9. H patterns of 16 in. antenna in hemispherical radome. Gimbal
angle 0°. Measured (—) at 37.5 GHz. Computed at 38 GHz,
(— — —). The antenna has been refocused to compensate
aberrations.

E7-14
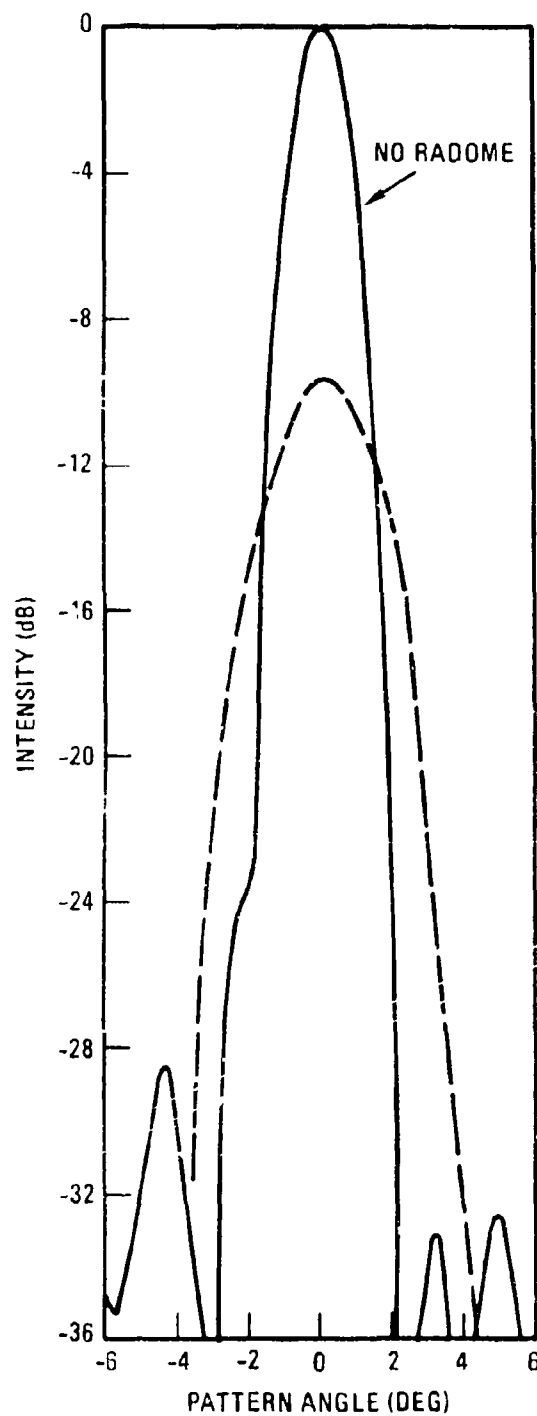
Figure 10a. Measured H-plane patterns of 16 in. antenna, not refocused – 37.8 GHz
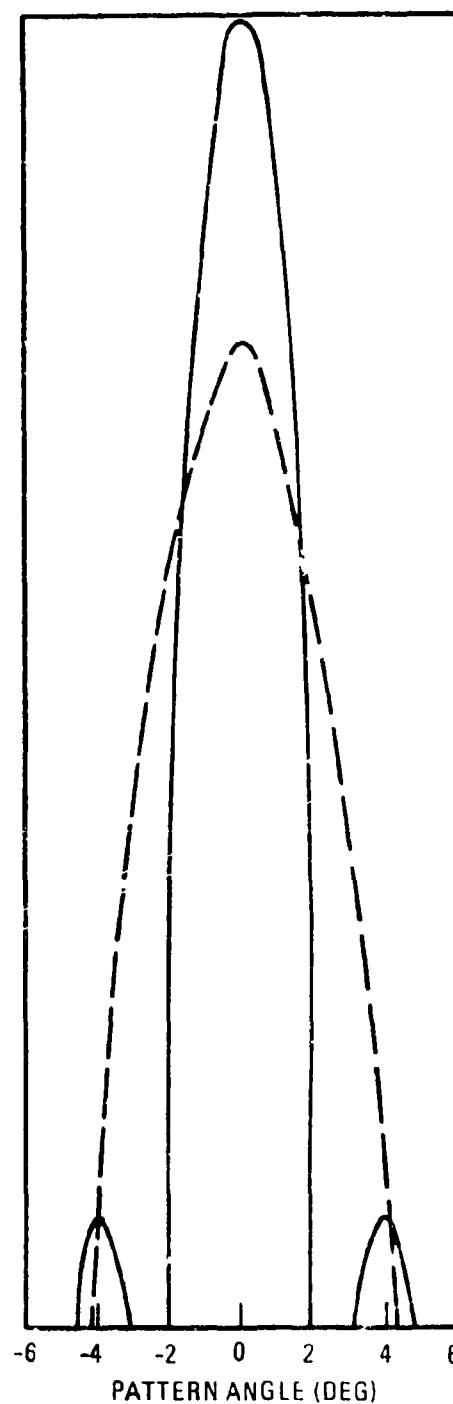
Figure 10b. Computed H-plane patterns of 16 in. antenna. Aperture distribution refocused to simulate radome aberrations – 37.8 GHz
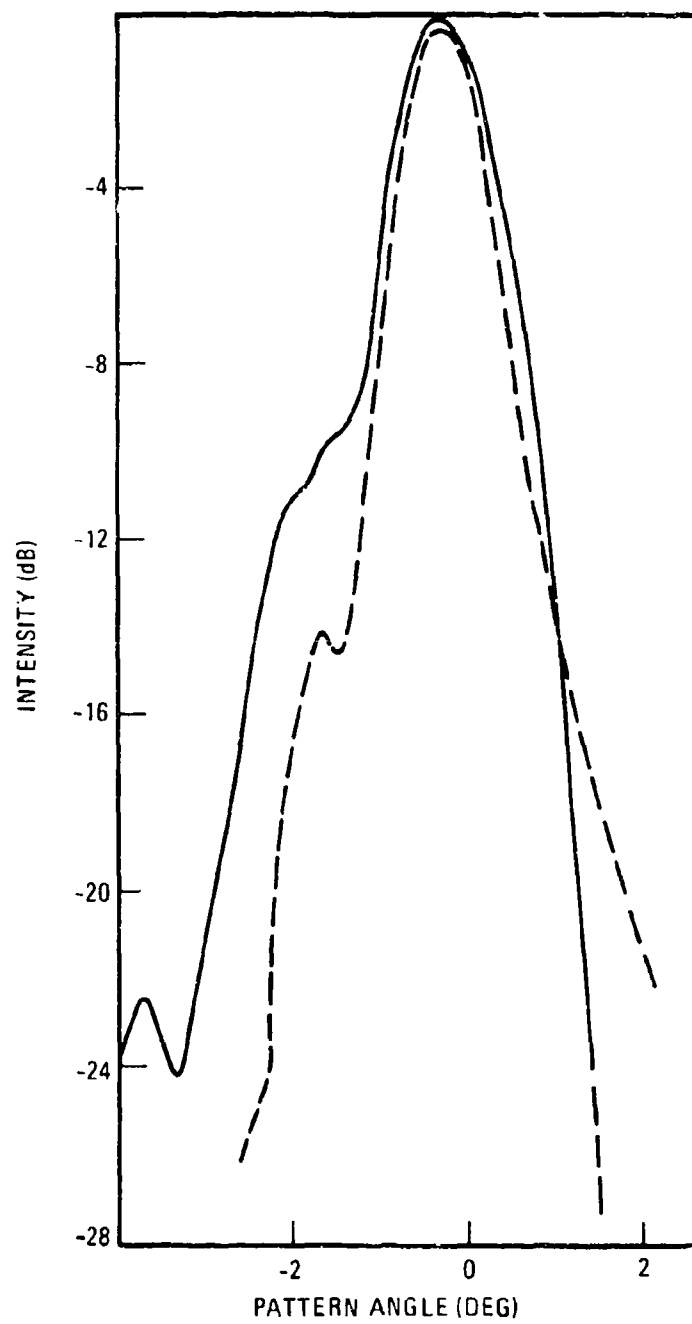
Figure 11. As in Figure 9 but for 90° gimbal angle
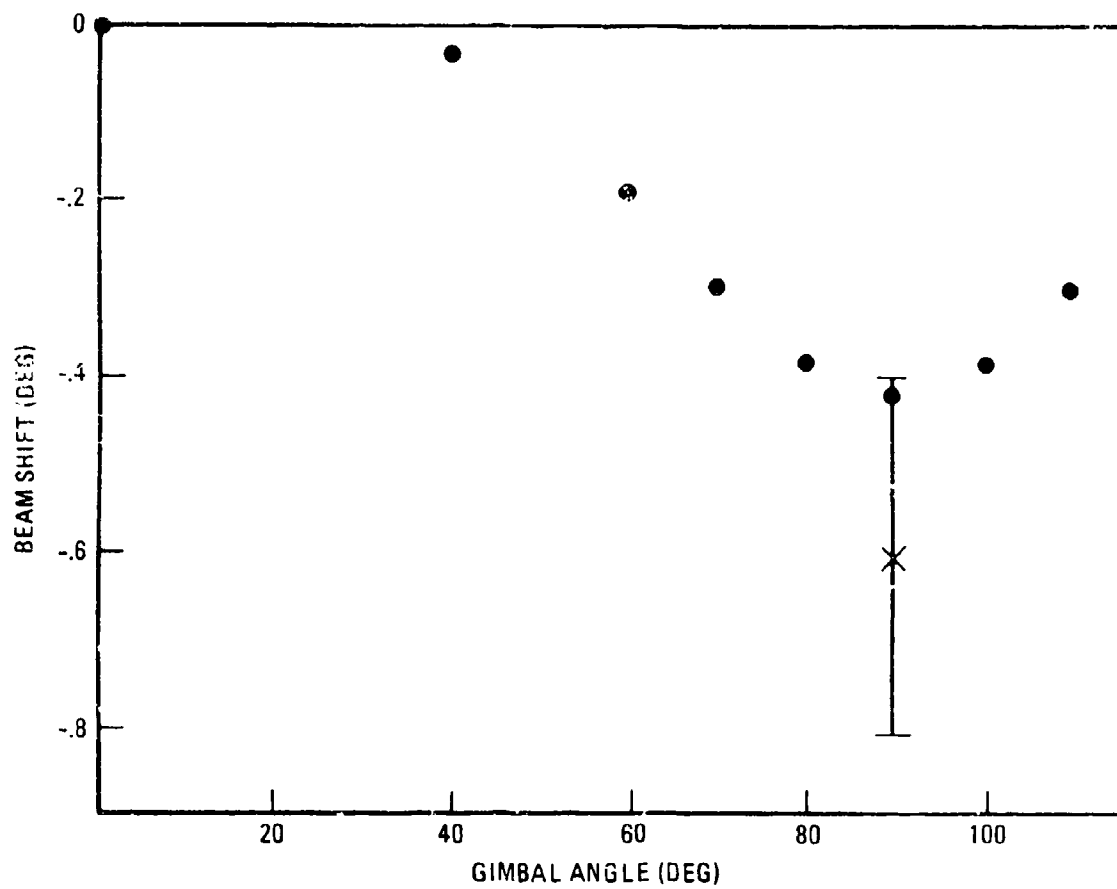
Figure 12. Beam shift for 16 in. antenna is 18.3 in. radome; Thickness
0.625 in.; Computed ( ) at 38 GHz; Measured at 37.5 GHz.

E7-17
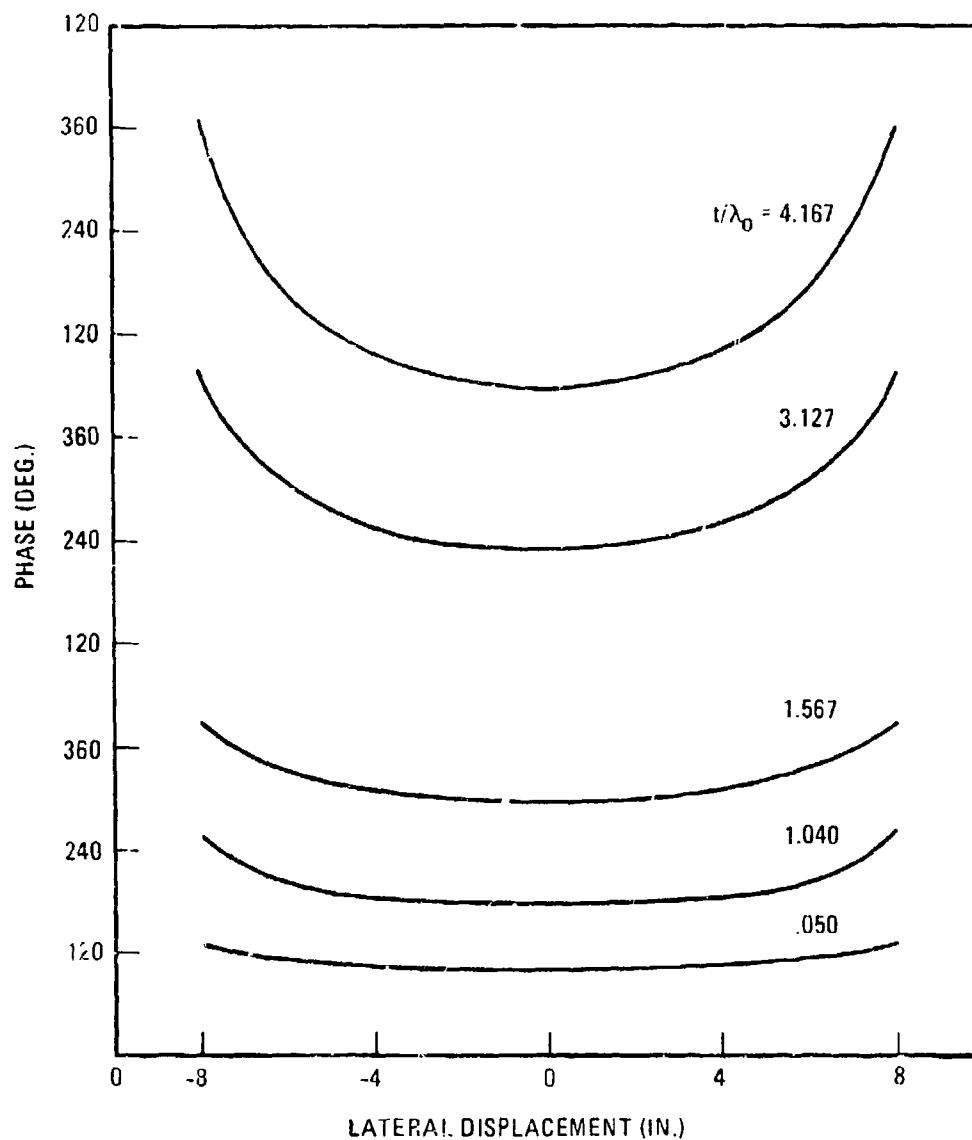
Figure 13. Computed phase distributions for a wave propagating
through the 18.3 in. radome with various thicknesses.
Frequency 38 GHz.

E7-18

SESSION F
EHF Systems

F1
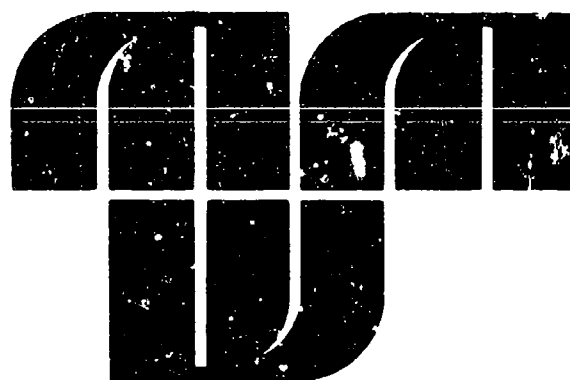
DEVELOPMENT AND TEST OF A 95 GHz TERRAIN IMAGING RADAR

by

Fred P. Wilcox
Goodyear Aerospace Corporation
Litchfield Park, Arizona 85340

INTRODUCTION

This paper describes Goodyear Aerospace Corporation's millimeter-wave radar system and preliminary test results. The transmitted wavelength of the radar is approximately 3.15 millimeters, which corresponds to a carrier frequency of 95 GHz. The radar system consists of a pencil beam antenna, narrow pulse transmitter, crystal mixer superheterodyne receiver, and a plan-position indicator (PPI) display.

The millimeter-wave radar offers significant advantages over longer wavelength systems because relatively high resolution can be obtained with physically small and comparatively low-cost equipment. High resolution at X-band with present-day radar technology is obtained by using physically large antennas, pulse compression, and/or synthetic aperture techniques which lead to large, heavy, complex systems that are expensive to manufacture. At short ranges of the order of five miles, a real aperture millimeter-wave radar transmitting a narrow pulse provides a high-resolution, real-time display. Unlike an optical sensor, a high-resolution airborne, millimeter-wave radar theoretically offers an excellent MTI capability with the ability to operate at night and will contine to perform with reduced range in inclement weather.

The carrier frequency for a millimeter-wave radar should be chosen after considering component availability, atmospheric attenuation, and rainfall

backscatter effects. Foul weather radar performance is directly related to atmospheric attenuation and rain backscatter. Backscatter or rain clutter increases the minimum noise level, and attenuation reduces the signal level returned from a target. Thus, the overall signal-to-noise ratio is reduced and results in reduced detection capability. After all these facts were considered, 95 GHz was selected because

1. Atmospheric attenuation becomes more severe with increasing frequency, but windows, or low attenuation regions, occur in the frequency spectrum. One window is centered at about 95 GHz.

2. Hardware at 95 GHz is becoming readily available.

3. Although attenuation caused by rain is more severe at 95 GHz than at 70 GHz, this effect is compensated for because the backscatter from the rain is lower at 95 GHz than at 70 GHz. The lower backscatter at the higher frequency can be attributed to the following:

    a. The volume of rain from which the signals can reflect is proportional to λ^2 for a fixed-aperture-size pencil beam antenna, and λ for an equivalent elevation shaped beam antenna

    b. The index of refraction of water varies directly with λ. Thus, there is less mismatch at the raindrop surface at 95 GHz than at 70 GHz and therefore less scatter.

The analysis used to predict the foul weather performance of millimeter-wave radar has been summarized in a Goodyear Aerospace paper entitled "Millimeter-Wave Weather Performance Projections," presented at the 1974 Millimeter-Wave Conference.

SYSTEM DESCRIPTION

The millimeter-wave radar system can be broken down into three basic blocks: antenna, transmitter-receiver, and display. Figure 1 is a simplified block diagram of the millimeter radar system. The antenna is hard mounted to the transmitter-receiver. Scanning is accomplished by rotating the antenna, transmitter-receiver package. Figures 2 and 3 are photographs of the antenna, transmitter-receiver package showing how the radar is mounted on the pedestal and the microwave hardware assembly. Figure 4 is a photograph of the transmitter tube and the high-voltage pulse modulator.

System parameters are summarized as follows:

Operational frequency	95 GHz
Display type	PPI
Range resolution	10 ft (τ = 20 ns)
Azimuth resolution	40 ft/NMI (-6 dB)
Range (maximum displayed)	8 NMI
Azimuth scan angle	360 deg
Primary power requirement	115 VAC, 3 phase, 400 Hz, 700 watts total.

The antenna is a two-foot parabolic reflector with a Cassegrain feed. A switchable polarizer on the antenna feed provides the capability of transmitting either left-hand circular, right-hand circular, or linear polarization. Both azimuth and elevation antenna position signals are supplied to the display. The gain of the antenna is 52 dB, and the 3-dB beamwidth is 0.38 degree.

F1-3
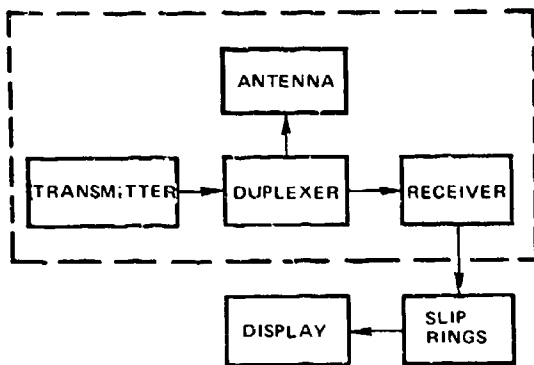
Figure 1 - Millimeter-Wave Radar
Simplified System Diagram
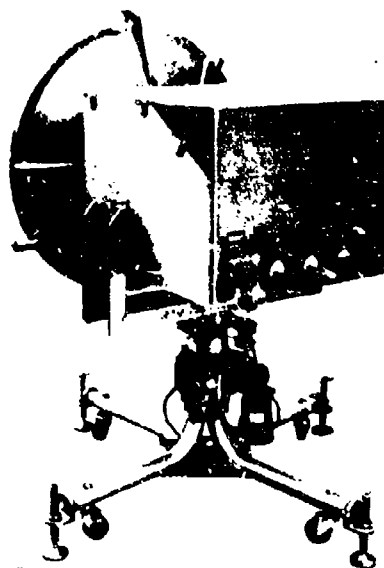
4703-2

Figure 2 - Antenna and Transmitter-
Receiver Mounted on
Pedestal
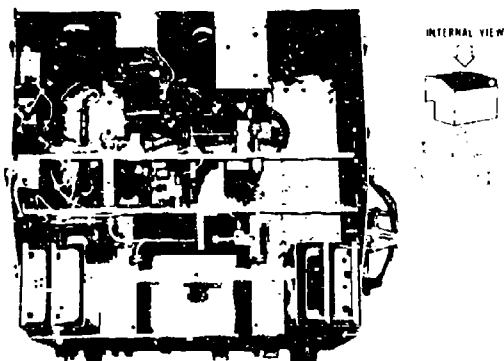
4703-3

Figure 3 - Transmitter-Receiver In-
ternal View
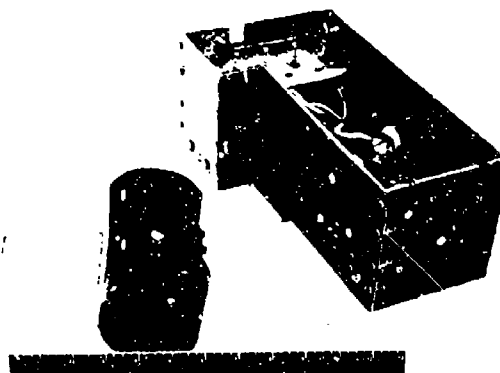
4703-4

Figure 4 - Magnetron and Modulator

The transmitter includes the high-power RF tube, high-power waveguide components, modulator, and the necessary timing and protective circuitry. Low-voltage power supplies are common to the transmitter-receiver. An Amperex DX423 magnetron, capable of generating 8 kW of RF power, is used as the high-power tube. The modulator circuit is a thyratron line type with a Darlington pulse forming network (PFN) driving the magnetron. The high voltage required to charge the PFN is developed by a solid-state magnetic modulator rather than a high-voltage DC supply. This magnetic modulator reduces the requirements of the DC power supply from approximately 2 kV down to about 250 volts. The RF pulse width is 20 nanoseconds.

The receiver contains an RF local oscillator, mixer, IF amplifiers, and detector. A single-ended crystal mixer is used as the receiver front end. The local oscillator is a low-power klystron.

The preamplifier-IF amplifier section has a center frequency of 335 MHz and a passband of 80 MHz with an overall gain of greater than 100 dB. The IF amplifiers have built-in gain controls. The gain can be electronically controlled and provides a 60-dB range. After amplification at IF, the received signal is detected, amplified, and fed to the display unit.

The display unit is a PPI utilizing a five-inch cathode-ray tube (CRT). The image on the display is built up by scanning the antenna in both elevation and azimuth. A camera is used to photograph the display as the antenna scans, thus producing a photograph of the radar image.

Three display ranges are provided 1.5, 5, and 8 miles. Range marks can be superimposed on the display in 0.1-mile steps throughout the entire range. Also,

a single range mark to a 0. 1-mile accuracy may be positioned on the display at the desired range.

TEST RESULTS

All tests were performed at Goodyear Aerospace, Arizona Division. During the test phase of the program, the radar was placed atop the radar tower on Building 13 (see Figure 5). Note that radar transmission from the roof of the radar tower on Building 13 is blocked by Buildings 6 and 26. The palm trees, signs, water tower, and telephone poles surrounding the test site all cast long radar shadows, as is apparent on the imagery.

The radar platform is only 54 feet above the ground, presenting a problem in that the incidence angles are very shallow. Figure 6 is photographs taken from the roof of the radar tower. These photographs have been superimposed on a plan view of the plant area. Note the radar shadows cast by the various buildings surrounding the radar tower. Figure 6 accents the shadow problem and shows some of the areas with very small radar cross-section that are clearly visible in the radar imagery. From an elevation of 54 feet, the incidence angle or grazing angle of the radar beam is approximately 6 deg at 500 feet range and decreases to 0.5 deg at 1 mile.

Figure 7 is an aerial view, or plan position photograph, and a sample of radar imagery made from the roof. The aerial view has the same geometrical terrain relationships as the radar imagery, while Figure 6 illustrates the limited field of view of an optical sensor located at the radar site.

Figures 8 through 11 are examples of the radar imagery made with the milli-meter-wave radar. Imagery of the same area made at different times was
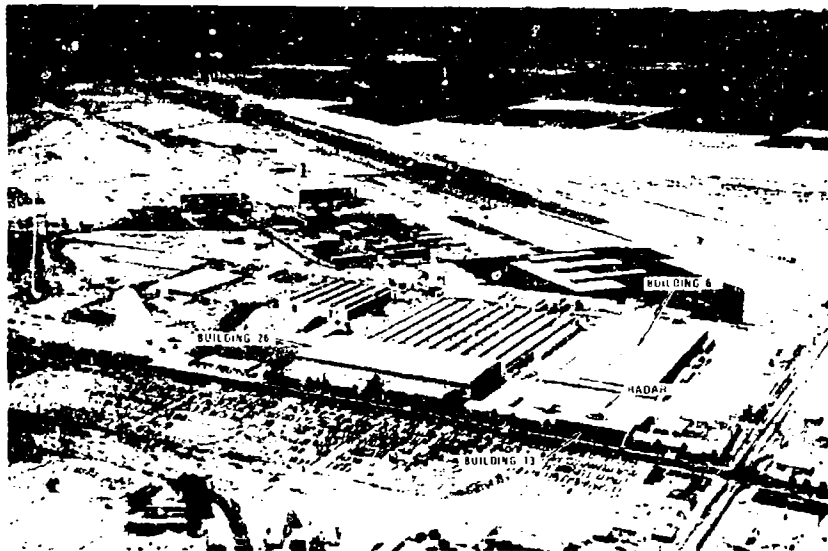
4703-5

Figure 5 – Aerial View of Goodyear Aerospace, Arizona Division
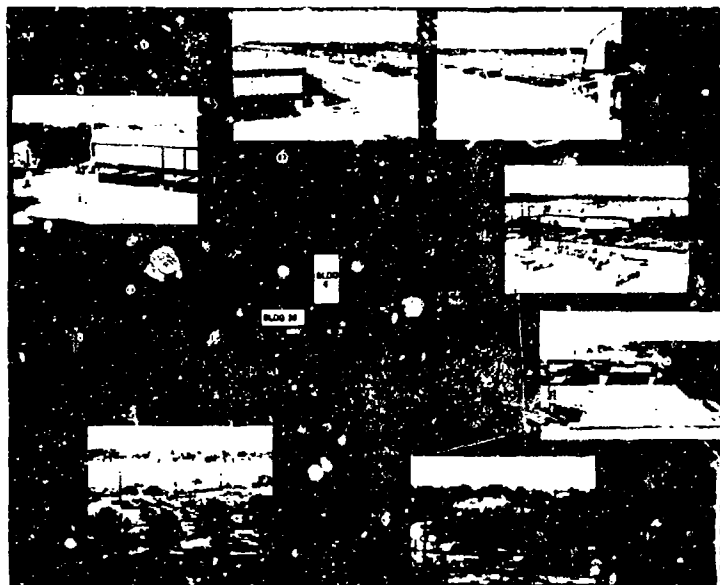
4703-6

Figure 6 – Site Layout and Shadow Effects
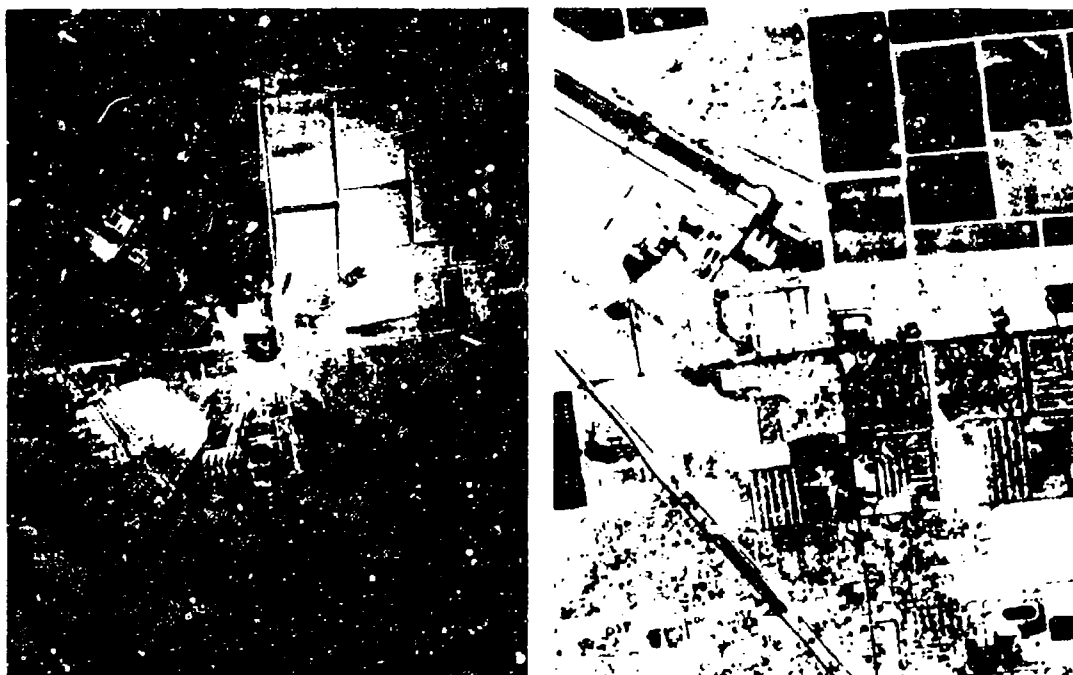
4703-7

Figure 7 – Radar Imagery versus Aerial Photography
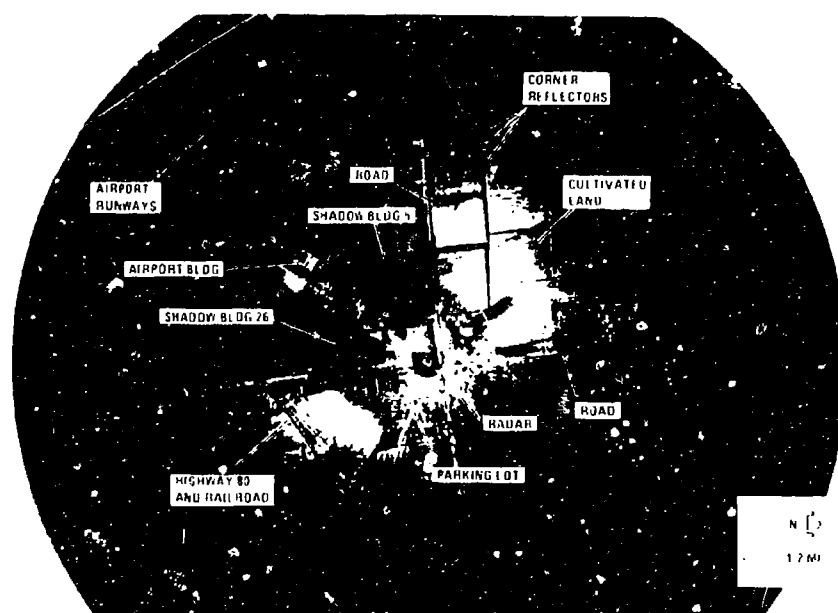
4703-8

Fig re 8 – Goodyear Aerospace Plant and Vicinity 20 November 1973 (PM)

F1-8

20 NOV 73 – PM

20 NOV 73 – AM

4703-9

Figure 9 – Change Detection – Parking Lot

F1-9
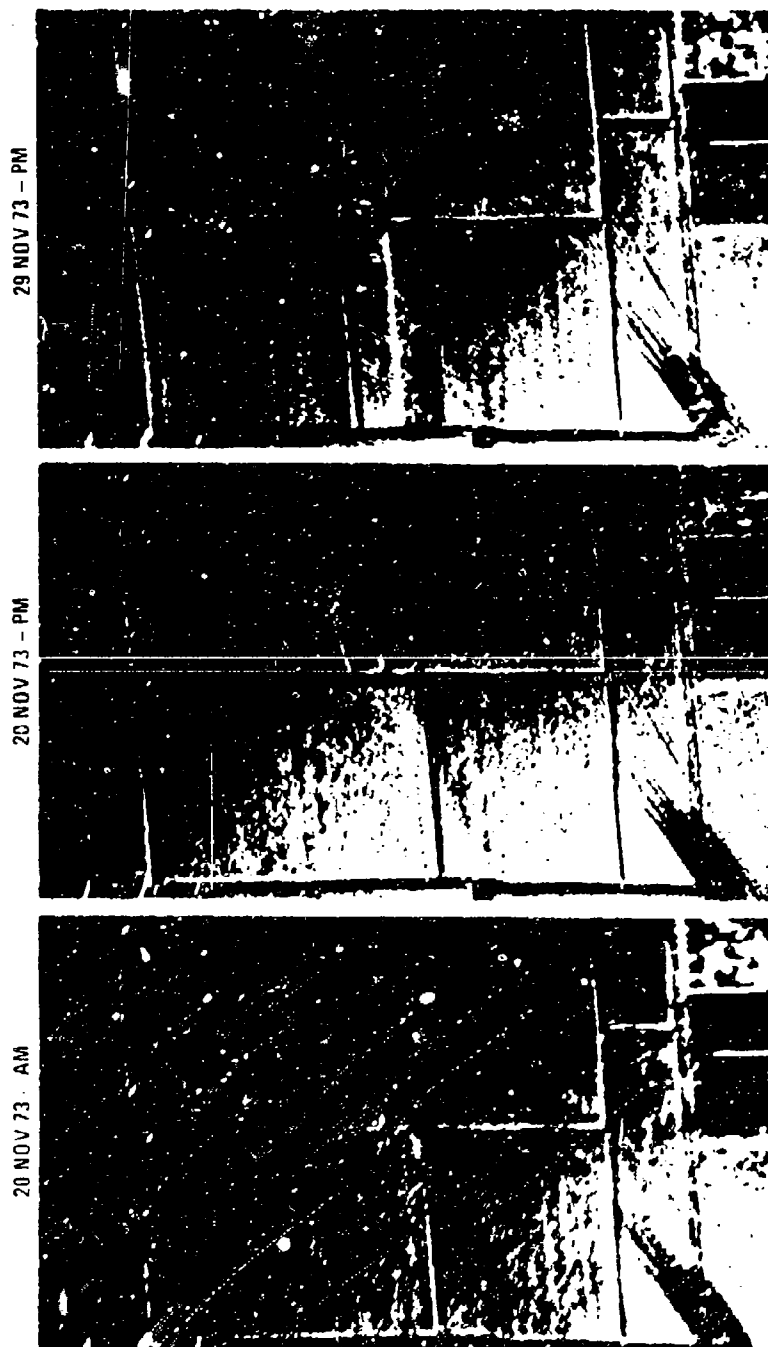
Figure 10 – Change Detection – Cultivated Areas
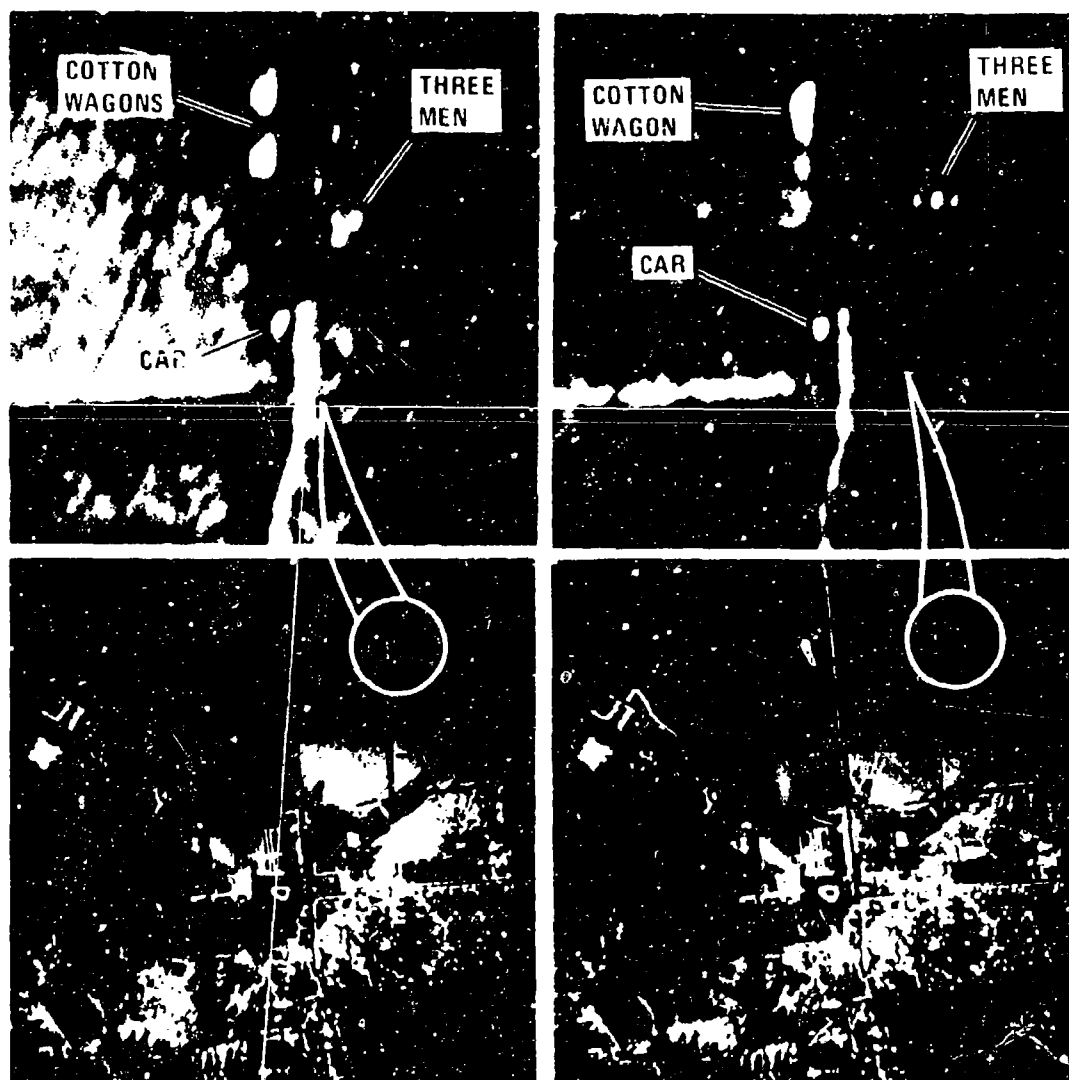
4703-11

Figure 11 - Change Detection - Men

compared to that of Figure 8. Some very interesting change detection can be done with three radar images. For example, close scrutinization of the Goodyear Aerospace parking lot reveals that there are significant differences. In Figure 8 the eastern boundary of the parking lot is lined by 55-gallon drums, but in another sample of imagery, it was noted that the drums were missing. Figure 9 is an enlargement of the parking lot areas of the images and clearly reveals the difference. Inspection of the farmland in the northwest corner of Figure 8 and two other samples of imagery also discloses detail differences. Figure 10 is an enlargement of the farmland area in the northwest corner imaged at three different times. In the earliest image on the left-hand side, it can be seen that a farmer is just starting to disk under the cotton vines in preparation for plowing, but imagery made approximately four hours later (center) shows that about three-fourths of the cotton plants in one field have been disked under. The right-hand side, made nine days later, shows that the field in the northwest corner has been plowed, leveled, and the dirt has been mounded in rows in preparation for raising hay. Note that the rows of cotton were running north and south and the rows in the newly planted hay field are running east and west.

Figure 11 is two pieces of imagery made about an hour apart. The enlarged sections of the imagery reveal images of three men standing in the field. In one image, the men were standing in a triangular pattern, and in the other, they were standing side-by-side in a straight line. Note that in one image, two cotton wagons are parked in the field, and in the other image, only one cotton wagon is present. The car is a 1970 Ford Comet convertible with the top down. Range from the radar to the men was approximately 3100 feet.

Imagery demonstrating the long range capability of the radar has been made. With the display range set at eight nautical miles, point targets are visible out to the edge. Power poles are visible out to a range of six miles. The near-range

detail in the imagery made on the eight-mile scale is comparable to that of Figure 8.

CONCLUSIONS

Millimeter-wave radar can satisfy the requirement for a relatively all-weather, lightweight, compact, inexpensive sensor for various operational applications. Some hardware obstacles do exist, e.g., high-gain, shaped vertical beam antennas; inexpensive, long-life RF power sources, and less expensive RF mixers are not yet available. Increased interest in millimeter waves for solving tactical problems will stimulate component development. Reduced complexity is the key to producing an inexpensive system. Millimeter waves provide a tool for obtaining high performance with simplified equipment.

It has been demonstrated that a real aperture, short pulse millimeter-wave radar has an excellent terrain and cultural target imaging capability even at very low depression angles. Although no direct quantification of the radar parameters has been made, the imagery results demonstrate that an obvious adequacy of the parameter combination exists. In particular, cultural targets such as building dihedral and trihedral corners, that normally cause receiver saturation problems at X-band, are effectively suppressed in the millimeter-wave radar imagery. Because of the very limited first Fresnel zone dimensions at millimeter wavelengths, multipath interference also appears to be virtually nonexistent at 95 GHz.

Assuming that the altitude of the radar was 1000 feet rather than 54 feet, the present system would map out to 3 nautical miles. If the altitude were increased to 2000 feet, the range would be extended to 3.5 nautical miles. Using techniques described in "Millimeter-Wave Weather Performance Projections," the range as

a function of rainfall rate has been projected. Figure 12 is a curve showing the relationship of the radar range to rainfall rate. It is interesting to note that greater than one-mile range is predicted for rainfall rates lower than 15 milli-meters per hour.

A major impediment to operating in a forward area appears to be the lack of confidence which both the pilots and engineers have exhibited in the performance of a self-contained airborne system for instrument landing. Contributing to this reluctance is the inability of a pilot to detect potential hazards such as aircraft, vehicles, personnel, debris, or other obstructions on a runway during a low-visibility landing. The test results made with a millimeter-wave radar operating on a stationary platform supply the necessary detail, but experiments must be perf᠎ med to determine if the necessary detail can be obtained from a moving pla   ᠎.
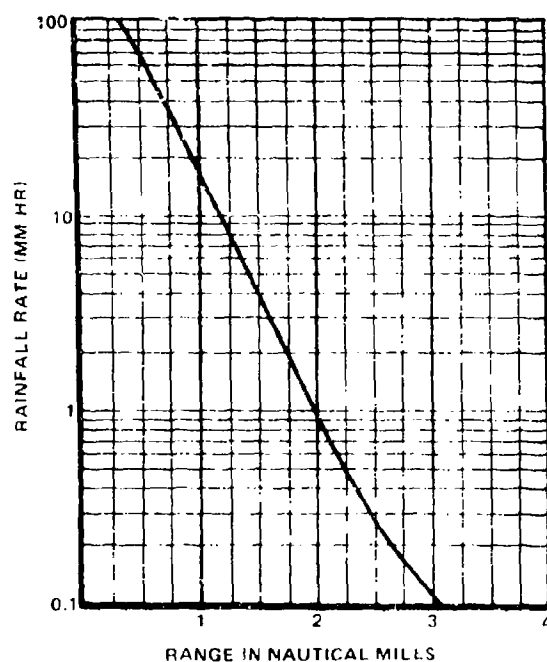
4703-12

Figure 12 - Radar Range versus Rainfall Rate (1000-Ft Altitude)

F1-14

MILLIMETER MONOPULSE RADAR FOR LOW ANGLE TRACKING

by

Frank A. Kittredge, Edward Ornstein, and Michael C. Licitra
Naval Research Laboratory
Washington, DC 20375

Introduction

It is common experience that the tracking accuracy of tracking radars deteriorates at low elevation angle. At elevation angles of less than two beamwidths, multipath errors become large, resulting in increasing errors and eventual loss of track[1]. A study was made to determine what improvement might be expected if a millimeter tracking radar were added to a conventional tracking radar[2]. The study led to the design and construction of a 35-GHz monopulse radar system to be mounted on the same precision tracking pedestal as a 9.3-GHz monopulse tracking radar. This system is now in operation and is capable of tracking cooperative targets to lower elevation angles than previously possible. The results are consistent with the theoretical predictions.

The rationale behind the design of the millimeter monopulse system is based on a simple relation to pattern shapes; however, other factors such as the difference in reflection coefficients at microwave and at millimeter waves which can be significant and helpful. Given that monopulse radars are subject to increasing errors as the elevation angle becomes less than two beamwidths, it follows that if the beam is made very narrow the elevation angle for accurate tracking could be reduced a proportional amount. There are at least two obvious ways to narrow the beamwidth of a radar: increase the aperture, or raise the radiated

---

1. D. K. Barton, "Radar System Analysis," Prentice-Hall, 1964, pp 327-331.

2. F. H. Thompson and F. A. Kittredge, "A Study of the Feasibility of Using 356 Hz and/or 94 GHz as a Means of Improving Low Angle Tracking Capability," NRL Memo Report 2249 (AD-725108), May 1971.

frequency. A simple calculation will show that to achieve a 0.2° beam-
width at C band requires an aperture in excess of 50 feet, for X band an
aperture approaching 40 feet, and for K_a band an aperture of 10 feet.
We, therefore, chose to raise the frequency and maintain a reasonable
aperture. The 35-GHz frequency was chosen because of the availability
of commercially-available components and because the atmospheric losses
at this frequency are much less than at any other portion of the milli-
meter band. A study of the literature indicated that we should expect
attenuation of .15 dB/Km for fair weather and an attenuation of 0.62
dB/Km for a ht rain of 4 mm/hr. Higher rain rates, particularly
local thunderstorms, would cause much higher losses.

System

The experimental high-angular resolution monopulse system consists
of a conventional X-band monopulse tracker combined with a narrow-beam
K_a-band tracker on a single FPS-16 type precision tracking pedestal
(Fig. 1). In an operational configuration it is anticipated that the
two trackers would use a combined feed with a common antenna. The X-band
monopulse tracking radar has a 7-foot dish with a beamwidth of 1°, and
the K_a-band monopulse tracking radar has a 10-foot dish with a beamwidth
of 0.2° mounted on an FPQ-4 precision tracking pedestal (Fig. 1). The
X-band antenna is mounted above the K_a-band antenna as seen in Fig. 1.
A boresite TV camera with a 6-inch f/8 lens is mounted on the elevation
axis for observing closed-loop tracking performance. The receiver "front
ends" are mounted at the output of the monopulse feed circuitry at the
back of their respective antennas and consist of local oscillators,
balanced mixers, and preamplifiers. The K_a-band magnetron and modulator
are also located on the antenna pedestal to reduce transmission losses.
The millimeter waveguide is pressurized with 15 psig of Freon 12 to pre-
vent voltage breakdown at the operating peak power of 130 kW. The
remainder of each system with the operating console is located in a
room directly below the pedestal.

The operating console (Fig. 2) contains the range trackers and
indicators for both systems, a digital angular readout in both elevation

and azimuth, and a boresite TV presentation that can be recorded with a
synchronized 16-mm camera. The console also contains a provision to
initiate tracking in either system independently or a system hybrid in
which one radar controls one axis and the other radar controls the other
axis. It is also possible to track one axis only by either radar with
the remaining axis on manual control. The range gates for each radar
are independent with a digital readout in X band only. Typically, the
X-band system is the primary tracker, and the closed-loop tracking function
is switched over to the K_a-band system in the heavy clutter and multipath
regions or in multi-target situations. Other situations could require
different modes of operation.

Figure 3 gives the basic parameters of each system.

	X-band	K_a-band
Frequency	9.3 GHz	35 GHz
Peak Power	50 kW	130 kW
Beamwidth	1.0°	0.2°
Noise Figure	13 dB	10 dB
Pulse Length	0.25 μsec	0.25 μsec
PRF	1 KHz	1 KHz

Figure 3

A basic block diagram of the system (Fig. 4) shows the major components
and method of switching between systems.

Results

The data presented here are initial results. The data are insuf-
ficient for quantitative comparison but readily demonstrate the tracking
improvement qualitatively.

A graphic presentation of what we expect to accomplish with the
narrow millimeter beam is shown in Fig. 5, in which the radar is now able
to track a low-altitude target without excessive clutter. The same narrow
beam also reduces multipath reflection, as shown in Fig. 6.

The tracking runs from which the data for this paper were derived were done with an S-2D as the cooperative target. The runs were radial except for the drift caused by cross winds. The flights were kept over water to minimize changes in reflectivity and for ease in altitude control. The elevation error signals from each radar were taken from amplified monopulse angle error detector outputs which are used as inputs to the pedestal servo system. These signals were recorded on a 2-channel recorder, one elevation error signal on each channel. However, the 2-channel recording on the next two figures is a composite of identical runs in which each radar is closed-loop tracking independently so that the recorded error signal is for that particular system in a closed-loop tracking condition. Figure 7 shows the error output from the elevation channels when either the X- or the K_a-band radar is tracking at an aircraft altitude of 1,000 feet. This is used as a reference run above the multipath region. This figure covers a range segment of approximately 2,000 yards at a total range of about 10,000 yards. As expected, there appear to be no multipath components in these tracks. A small $2\frac{1}{2}$-cycle oscillatory component evident in all these recordings was traced to a low frequency resonance in the elevation axis. However, a corrective filter network has since helped reduce this effect. From simple geometry and antenna pattern information, a strong multipath condition would be expected at X band, but negligible multipath at K_a band when the aircraft is at about 200 feet altitude. The traces in Figure 8 show this effect on a 200-foot altitude target. The upper trace is for the X-band radar operating closed-loop, and the lower trace is for the K_a-band radar operating closed-loop. The ranges are again 8,000 to 10,000 yards. The X-band multipath is producing very large error signals as large as ± 1.8 milliradians. A very small multipath component is occasionally visible superimposed on the K_a-band signal.

A much clearer demonstration of the reduction in multipath by K_a-radar is contained in a short section of boresite film. This film was made during the same day that Figures 7 and 8 were derived, but not the same run. For these runs, the aircraft flew at 150 feet altitude for the X-band track segment and at an even lower altitude of 100 feet for

the K_a-band track segment. For the X-band segment, first section of film, the multipath error builds up as the range increases, until the radar loses track. On the second section, the X-band radar starts track with increasing multipath errors to a range of 13,000 yards; at this range the system is switched to the K_a-band radar with a strong reduction in tracking error and continues tracking to 30,000 yards.

I should like to emphasize that these are preliminary results with this system. We expect to be able to improve overall pedestal noise and radar noise figure values. As another point of interest, our observations to date lead us to believe that the radar cross section for this particular aircraft is substantially greater at K_a band than at X band and the reflection coefficient significantly low at K_a band for the somewhat choppy sea conditions. We hope to determine this after improving the system.
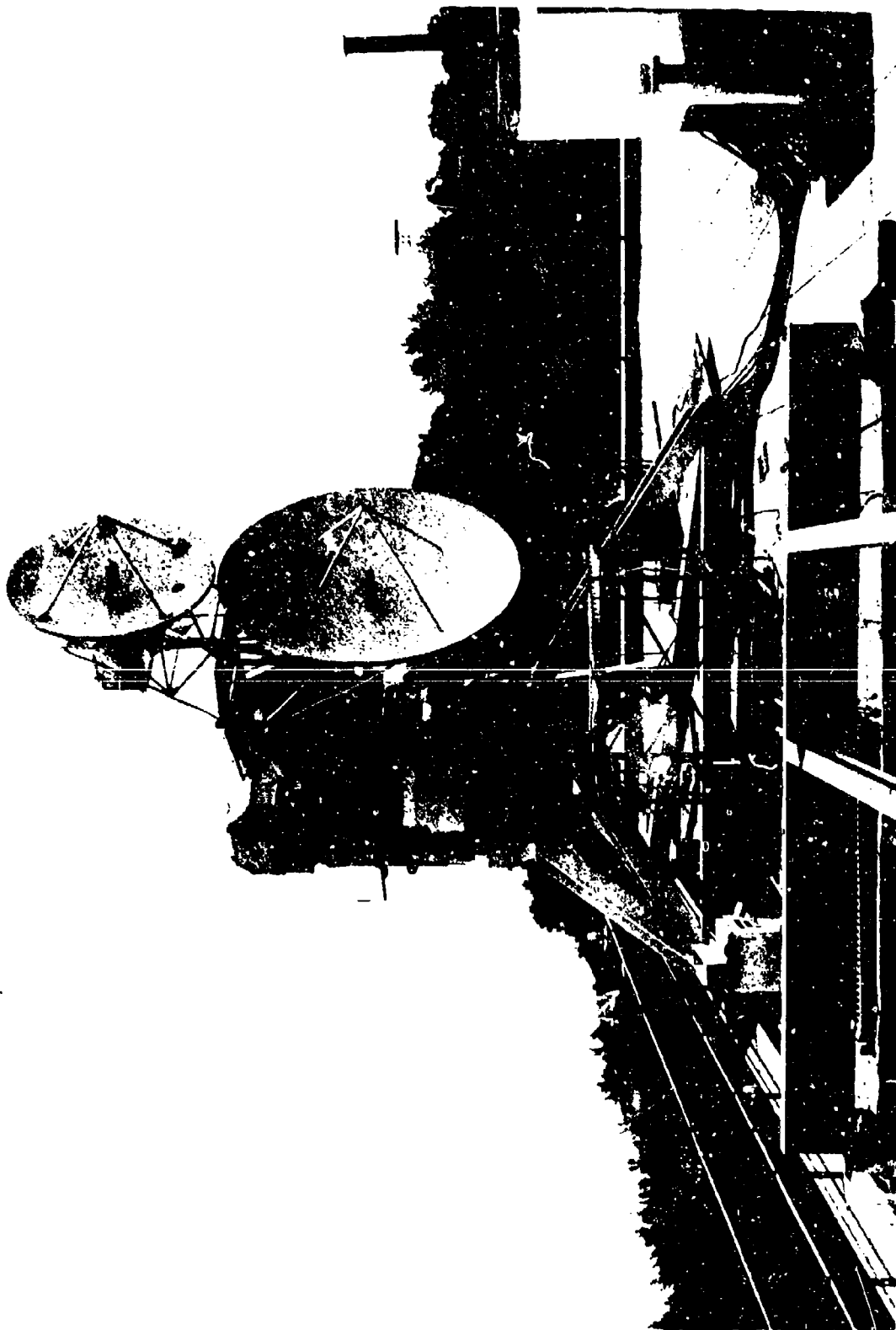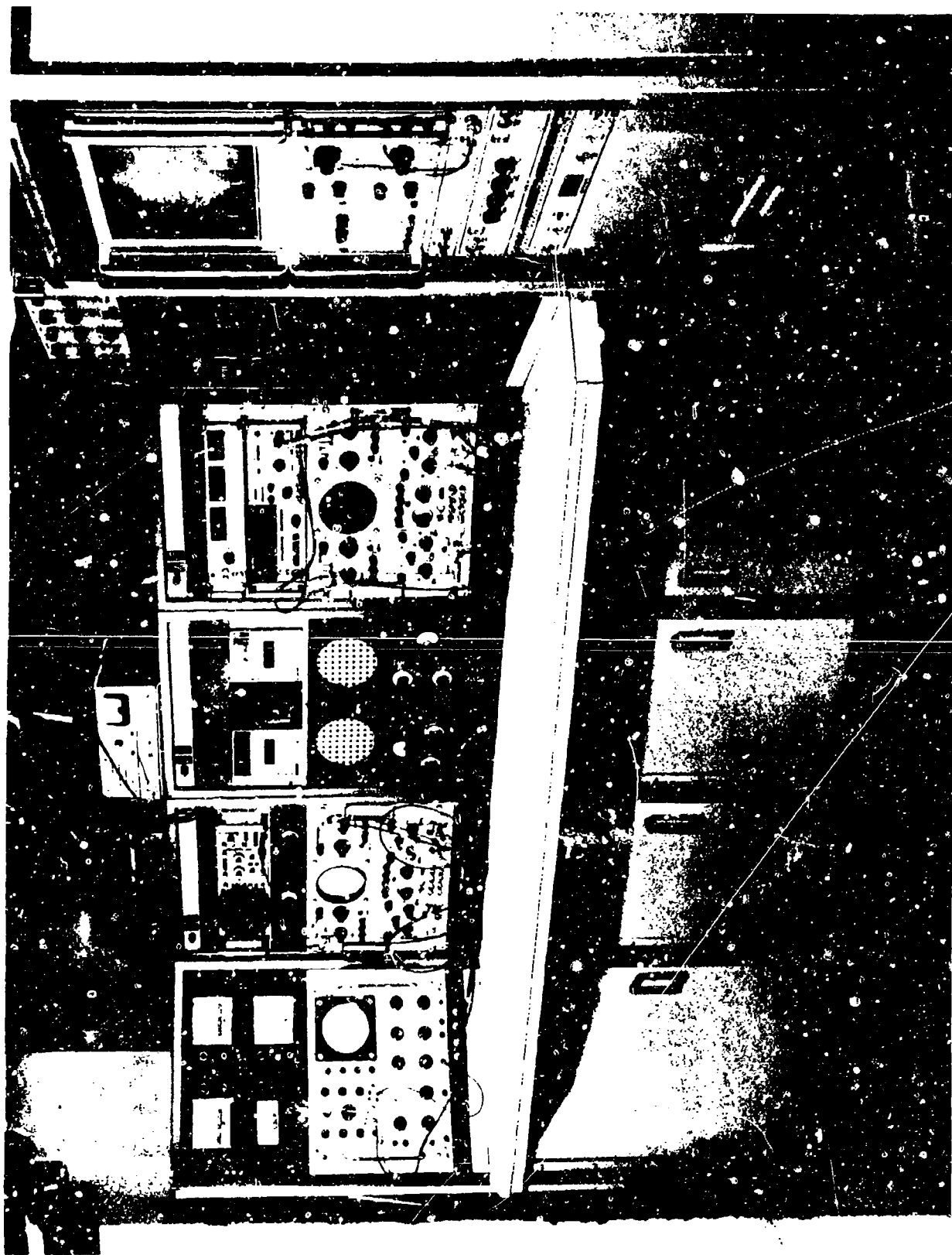
FIGURE 1

FIGURE 2

SYSTEM COMPARISONS

	X BAND	Ka BAND
FREQUENCY	9.3 GHz	35 GHz
PEAK POWER	50 Kw	130 Kw
BEAMWIDTH	1.0°	0.2°
NOISE FIGURE	13 dB	10 dB
PULSE LENGTH	0.25 jμ sec.	0.25 jμ sec.
P. R. F.	1.0 KHz	1.0 KHz

FIG 3

SIMPLIFIED SYSTEM BLOCK DIAGRAM
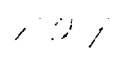
FIG 4

COMPARISON OF Ka BAND vs X BAND TARGET
TO CLUTTER FOR LOW ANGLE TRACKING
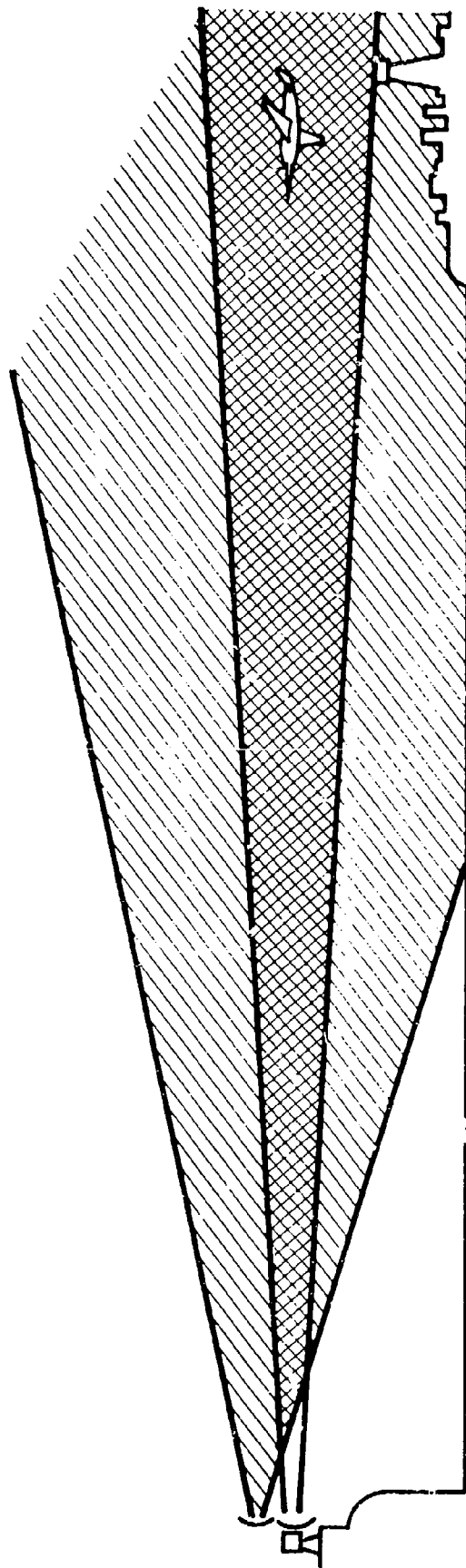
B.W. $_{Ka}$ = 0.2°

B.W. $_X$ = 1.0°

FIG 5

COMPARISON OF Ka BAND vs X BAND MULTIPATH REDUCTION FOR LOW ANGLE TRACKING

X BAND   B.W. = .02°

Ka BAND   B.W. = 1.0°
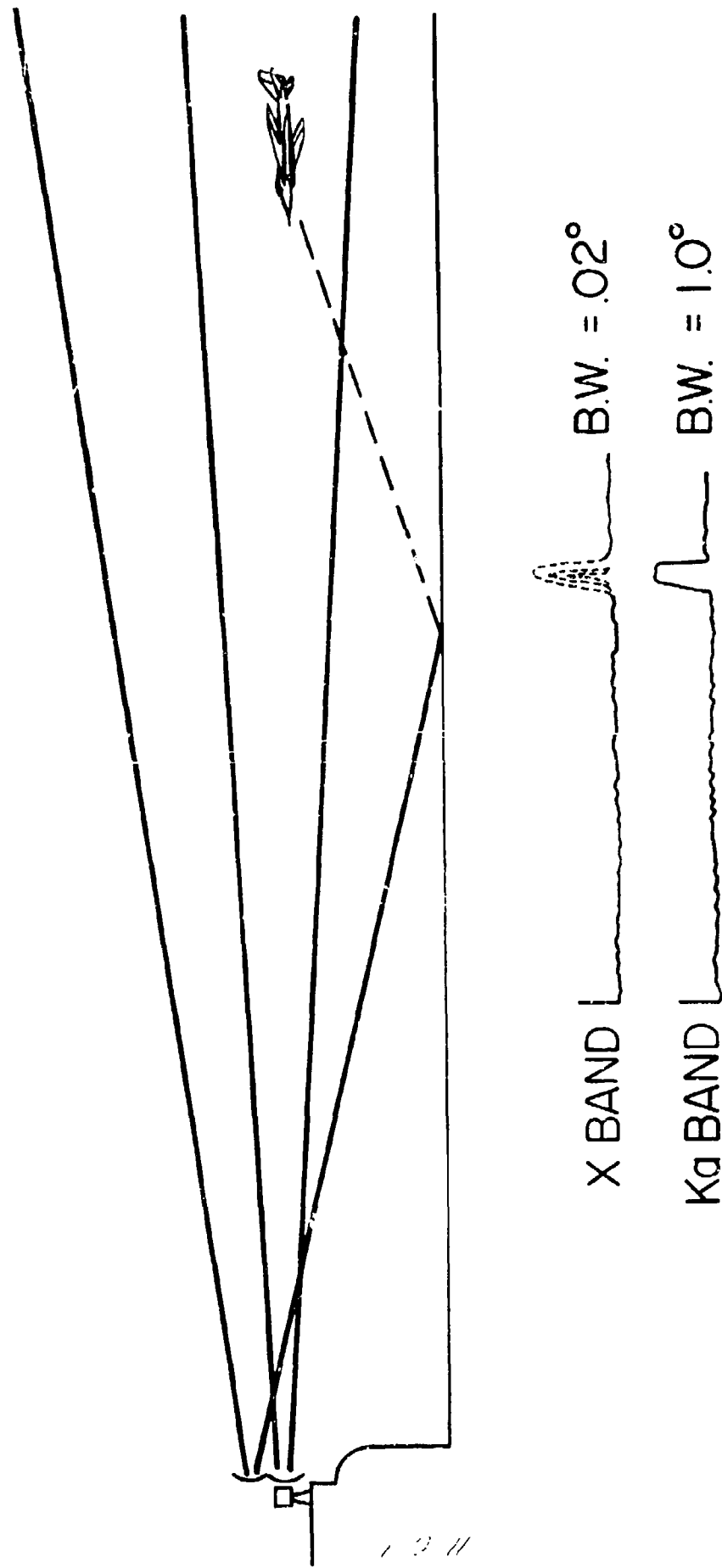
FIG 6
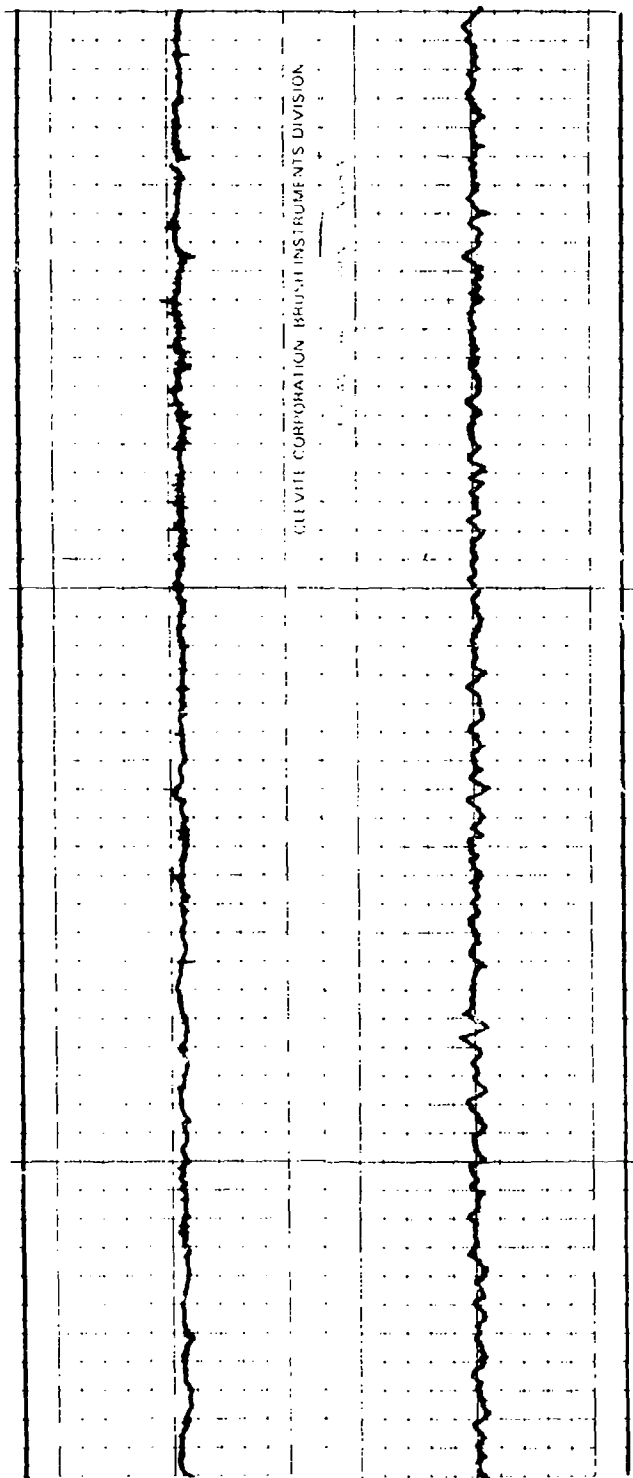
FIGURE 7

ELEVATION ERROR OUTPUT
TRACKING S2-D at 1000 ft.
UPPER TRACE X BAND .35mr/div
LOWER TRACE Ka BAND .26mr/div
RANGE 8-10,000 yds.
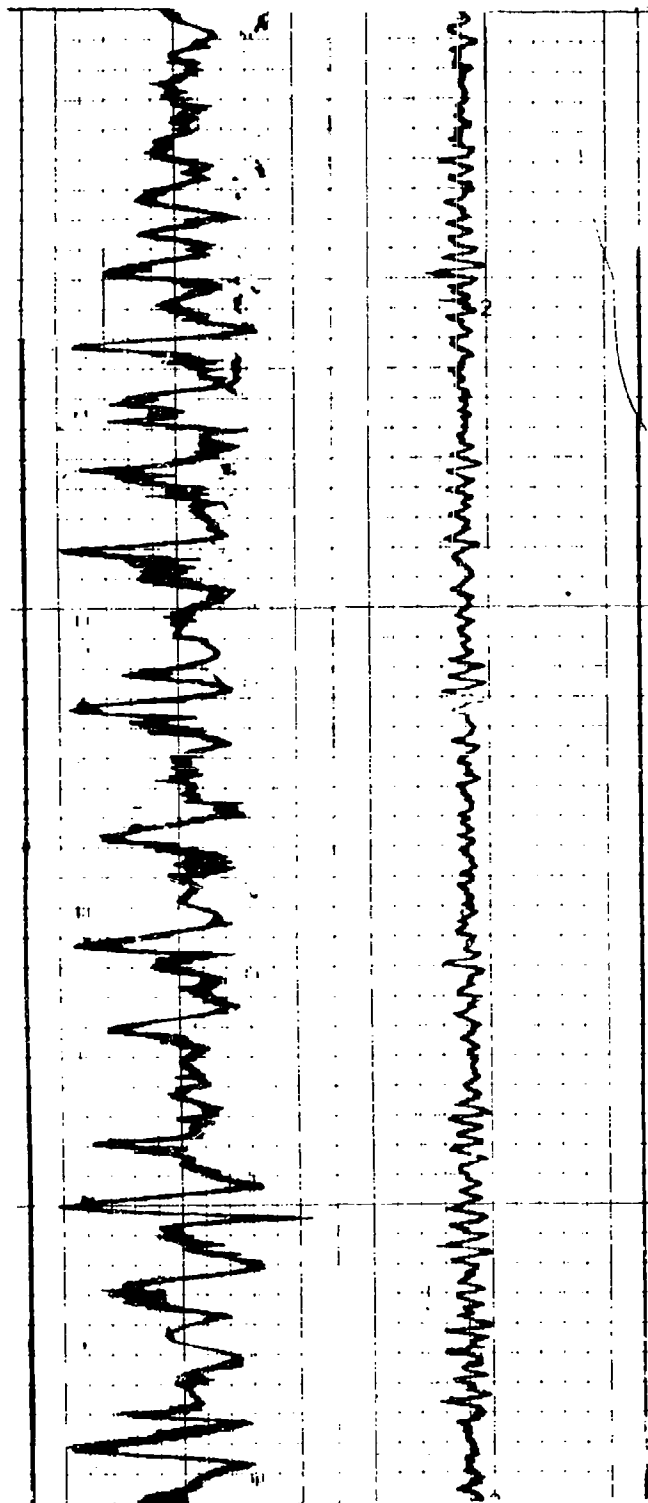
FIGURE 8
ELEVATION ERROR OUTPUT
TRACKING S2-D at 200 ft.
UPPER TRACE X BAND .35mr/div
LOWER TRACE Ka BAND .26mr/div
RANGE 8-10,000 yds.

AN EXPERIMENTAL MILLIMETER MONOPULSE
TRACK RADAR

K. L. Koester, Dr. L. H. Kosowsky, & J. F. Sparacio

Norden Division
United Aircraft Corporation
Norwalk, Connecticut 06856

INTRODUCTION

The need to satisfy high accuracy sensing requirements
for obstacle avoidance, low angle track, and multitarget
resolution has led to consideration of radar operation in
the millimeter wavelength region of the RF spectrum. Of
particular interest to the radar designer are the inherent
advantages that millimeter wave radar systems offer in the
area of high accuracy target tracking in a clutter environment.
Among the advantages of a millimeter radar system are improvements
in target resolution, velocity sensitivity, and accuracy.

The tracking of complex targets at millimeter wavelengths
requires a detailed knowledge of the glint characteristics
of the object as well as the clutter environment in which
it may be immersed. The glint signature of an object is
a function of its shape, aspect angle, scattering centers,
and material composition. Each of these factors is wavelength
dependent and contributes to the magnitude and statistical
variation of angular glint. Extrapolation of available
data at lower frequencies has not proved reliable in the
case of ampl ude istics and has necessitated the development
of measuring equipment to obtain experimental data.

Norden has been engaged in the research and development
of millimeter radar systems for more than eight years. As
part of this work, the propagation characteristics of millimeter
wave energy have been determined, target and clutter signatures
have been measured at 70 GHz, and the effect of weather and
clutter on system performance have been examined in detail.

During the last year, Norden has developed a microwave
system for a four-lobe amplitude monopulse track radar operating
at 70 GHz. The antenna/receiver subsystem was designed for
a static tracking accuracy of better than 1.0 milliradian
and achieved an accuracy of better than 0.7 milliradian.
The experimental system is described in detail and results
of system tests including the measured error curve are presented
Performance of the system in clear air and adverse weather
is analyzed.

THE TRACK PROBLEM

Approach

Many military situations require accurate tracking
of a relatively small target in close proximity to a large,
competitive clutter area. Solutions have proceeded along
a number of different paths:

    a. Clutter suppression by statistical data processing
       (e.g. MTI)

    b. Coherent techniques (e.g. pulse compression and
       synthetic aperture)

    c. Narrow beam, high resolution antennas

Of the techniques listed, the direct generation of
narrow beams by multiwavelength apertures provides the simplest
approach to resolving small targets in the presence of clutter.
In order to utilize reasonable size antennas, the designer
is forced to high frequencies of operation. The following
sections examine the nature of tracking in the millimeter
wavelength region of the RF spectrum. Propagation limits
that exist in the millimeter band are discussed. Lastly,
an experimental monopulse radar operating at 70 GHz is described
together with pertinent data describing its parameters and
operating characteristics.

Monopulse Concepts

As defined by Rhodes[1], "Monopulse is a concept of precision direction finding of a pulsed source of radiation. The direction of the pulsed source...is determined by comparing the signals received on two or more antenna patterns simultaneously." This paper deals with an amplitude comparison monopulse system, in which the microwave signals received from two squinted antenna patterns are combined to obtain simultaneously, both the sum and difference signals. Figure 1 shows the feed/comparator for a single plane monopulse antenna. (The Norden system which will be described is a four-lobe monopulse which provides difference signals in both azimuth and elevation.

In a single channel configuration, the sum pattern is used for transmission, while both the sum and difference patterns are used for reception. The magnitude of the difference signal provides information on the magnitude of the
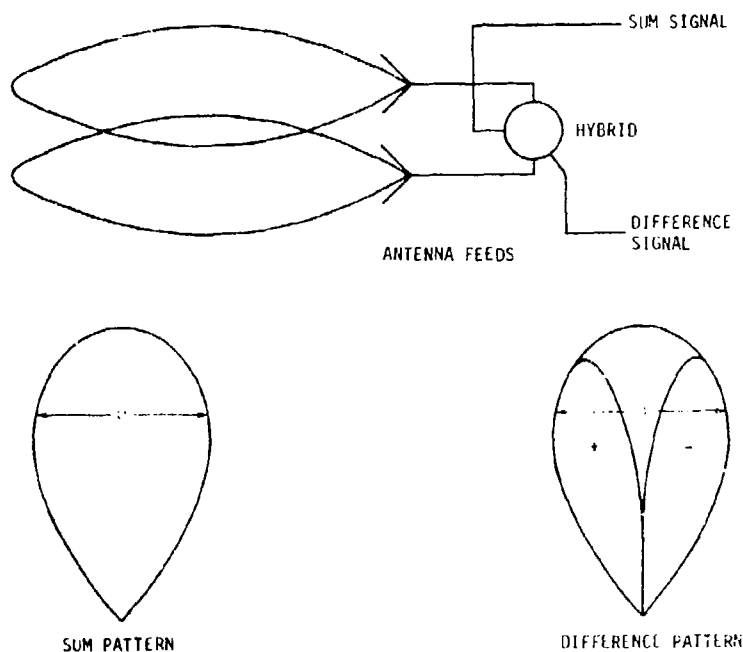
Figure 1. Functional Block Diagram of Amplitude Comparison Monopulse Antenna

angle-off-boresight. The sum signal provides range information and is used as the reference to determine the sense of the angle-off-boresight. The sum and difference signals are amplified separately and combined in a phase sensitive detector to produce the sensor error signal.

Of primary concern to the designer of a monopulse radar is the ability of the radar to track a target with a high degree of sensitivity and to discriminate against scatterers in the vicinity of the target. Both of these conditions are optimized with narrow, highly directional antenna beams. The generation of narrow beams with confined apertures requires operation at high frequencies consistent with component availability, noise considerations, and propagation restraints.

Angular Glint

The instantaneous radar signature of complex targets is influenced by such factors as contour shape, aspect angle, and number of scattering centers. All of these characteristics are wavelength dependent and result in angle noise or target glint. In addition, the motion of these scattering centers causes interference patterns that impart a time variation to the radar signature, which is also directly related to the incident frequency. Thus, as frequency is increased, the glint can be expected to both change its probability density function and broaden its power spectral density.

To minimize the effect of angular glint, most lower frequency systems utilize frequency agility to achieve rapid decorrelation. Although this technique is very effective, it increases the cost and complexity of the radar system. As noted previously, because of the naturally occurring interferences due to target relative motion or change in aspect angle, rapid decorrelation can be realized by employing milli- meter wavelengths at constant frequency. A detailed discussion of glint as a function of operating frequency is beyond the scope of this paper.

DESIGN CONSIDERATIONS

Frequency Considerations

The primary considerations in the selection of frequency relate to antenna size, transmission properties of the atmosphere, and the state of component technology. Since radar systems must be designed to operate under adverse weather conditions, such as rain, fog, and cloud cover, close examination must be made of attenuation and backscatter in these media, as a function of radar wavelength.

From an installation point of view, selection of a high frequency would be advantageous in reducing antenna swept volume, with a corresponding reduction in radome size and the attendant structural, cost, and weight problems. Since swept volume varies approximately as the cube of the antenna size, any reduction in antenna size would prove quite beneficial. An increase in frequency to achieve this benefit, however, must be weighed against possible deleterious effects of propagation in adverse weather.

Propagation

Most military applications require track radars to operate under adverse weather conditions such as rain, fog, and cloud cover. The attenuation and backscatter coefficients of the millimeter frequencies (35, 70, and 94 GHz) are summarized in the following paragraphs.

Clear Air

The attenuation of millimeter energy in clear air has been analyzed in the literature[3]. Further investigations have been conducted by Norden[4]. Clear air attenuation coefficients for millimeter frequencies of interest are shown in Table 1.

Table 1. Clear Air Attenuation Coefficient

Frequency GHz	New Band Designation	Old Band Designation	Attenuation Coefficient dB/km
35	K	K_A	0.18
70	M	V	0.41
94	M	W	0.24

Rain

The performance of a radar operating in rain is degraded
by the absorption and scattering of the energy by the raindrops.
For analysis purposes, the attenuation coefficient for light
and heavy rain is given in Table 2 for the three millimeter
frequencies of interest.[4,5,6]

Table 2. Rain Attenuation and Backscatter Coefficient

Frequency GHz	Light Rain (1 mm/hr)		Heavy Rain (16 mm/hr)	
	Attenuation (dB/km)	Backscatter (cm^2/m^3)	Attenuation (dB/km)	Backscatter (cm^2/m^3)
35	0.24	0.21	4.0	4.9
70	0.73	0.72	6.9	4.1
94	0.95	0.89	7.4	3.9

In addition to the attenuation, the energy reflected
back to the radar is of interest since it contributes additional
noise to the system. The backscatter coefficients are also
presented in Table 2 [4,5,6]. Forward scattering is substantial
in the 70 and 94 GHz region but its effect on system performance
is not well known.[4]

As can be seen, the backscatter cross section per
unit volume of heavy rain is comparable for 70 GHz and 94
GHz radars and is actually less than for 35 GHz systems.
Thus, a 70 or 94 GHz radar operating in heavy rain would

have less rain clutter than a 35 GHz system with the same
aperture. A 94 GHz system would have slightly less rain
backscatter than a 70 GHz system at the heaviest rain rates,
but the attenuation at 94 GHz is greater than at 70 GHz.

Fog and Clouds

The attenuation coefficient for millimeter propagation
in fog and clouds has been investigated in detail [6,7,8]. It has
been shown that the attenuation is linearly dependent on the
liquid water content of the fog. In addition, there is a signifi-
cant temperature dependence. The attenuation coefficient
is given in Table 3 for a liquid water content of 0.1 g/m^3,
corresponding to an optical visibility of 120 meters for
a radiation fog and 300 meters in advection fog.

Table 3. Attenuation Coefficient of Fog

Liquid Water Content - 0.1 g/m^3

Frequency GHz	Attenuation Coefficient dB/km	
	0°C	40°C
35	0.11	0.034
70	0.36	0.133
94	0.47	0.22

The backscatter coefficient of fog in the millimeter
radar band is more than two orders of magnitude smaller than
that of rain[4] and, therefore, has a negligible effect on
radar system performance.

Frequency Selection

The theoretical analysis and experimental work performed
by Norden has demonstrated that millimeter radar systems
will provide adequate adverse weather performance.

During the course of Norden's internally funded programs,
a careful comparison was made of cost and availability of
components at both 70 and 94 GHz. Greater availability and
lower cost of components led to the choice of 70 GHz as a
representative frequency for experimental work in the millimeter
band. The work ac 70 GHz is compatible with 94 GHz requirements
permitting design anywhere within the band.

MONOPULSE RADAR SYSTEM DESCRIPTION

Norden has developed an antenna/receiver package for
a four-lobe amplitude monopulse radar operating at 70 GHz.
A similified data processing unit has also been developed.
Figure 2 is a block diagram of the system.
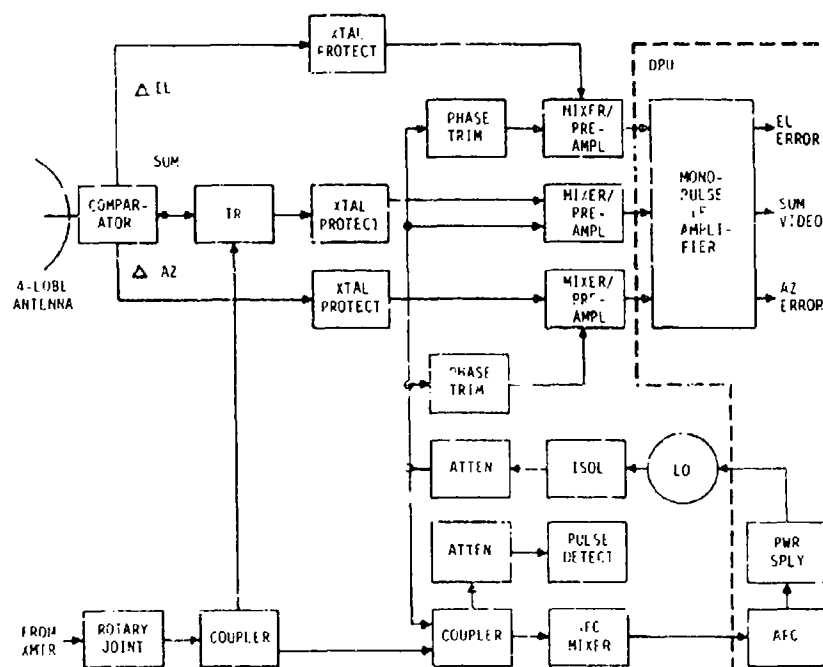
Figure 2. Monopulse Antenna/Receiver Block Diagram

Antenna

The antenna is an 18-inch parabola with an f/D ratio of 0.67. The flatness of the parabolic antenna offers immunity to coupling caused by cross polarized energy[9]. Cross talk between the sum and difference channels is on the order of -30 dB. The microwave comparator and four-horn feed are constructed as an integral unit to minimize precomparator phase shift. A manual polarization selection capability allows the choice of either vertical or horizontal polarization depending on antenna orientation.

Sum channel gain at the comparator is 47.2 dB. The radiation pattern is a pencil beam with a 3-dB beamwidth of 0.66 degree and first sidelobe levels of about -20 dB with respect to the sum peak. Figure 3a shows the H-plane sum pattern, and Figure 3b shows the H-plane difference pattern. The null depth of the difference pattern is -32 dB. The four lobe antenna was designed for use between 69 and 71 GHz and meets its performance specifications over this region. Figure 4 shows the monopulse antenna and support structure.

Microwave

The microwave package incorporates specially designed waveguide assemblies to minimize insertion loss. Losses for the difference channels are on the order of 1.55 dB each while the sum channel loss is about 2.5 dB. Duplexing is provided by a dual TR duplexer having 0.02 erg spike leakage and 1.5 µs recovery time. Translation to IF is accomplished by mixer/preamplifier assemblies using Schottky Barrier diodes in a balanced mixer configuration. The units provide 25 dB minimum gain (RF to IF) with a noise figure of 10 dB and a 20 MHz bandwidth centered at 60 MHz, resulting in a receiver sensitivity of about -87 dBm. The sensitive Schottky crystals are protected by a switchable ferrite attenuator inserted before the mixer in each channel.
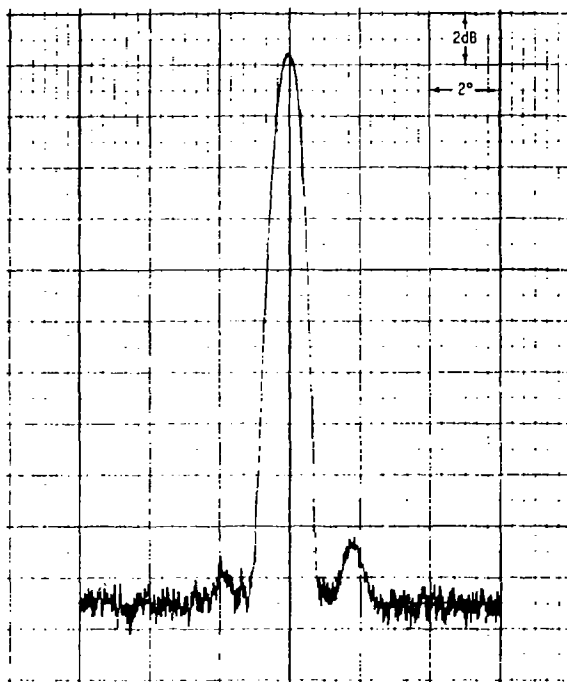
Figure 3a.　H-Plane Sum
　　　　　　　Pattern
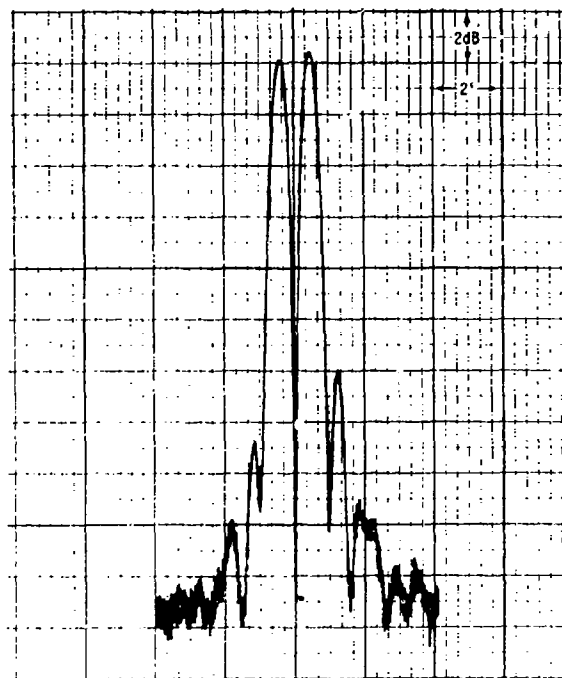
Figure 3b.　H-Plane
　　　　　　　Difference
　　　　　　　Pattern
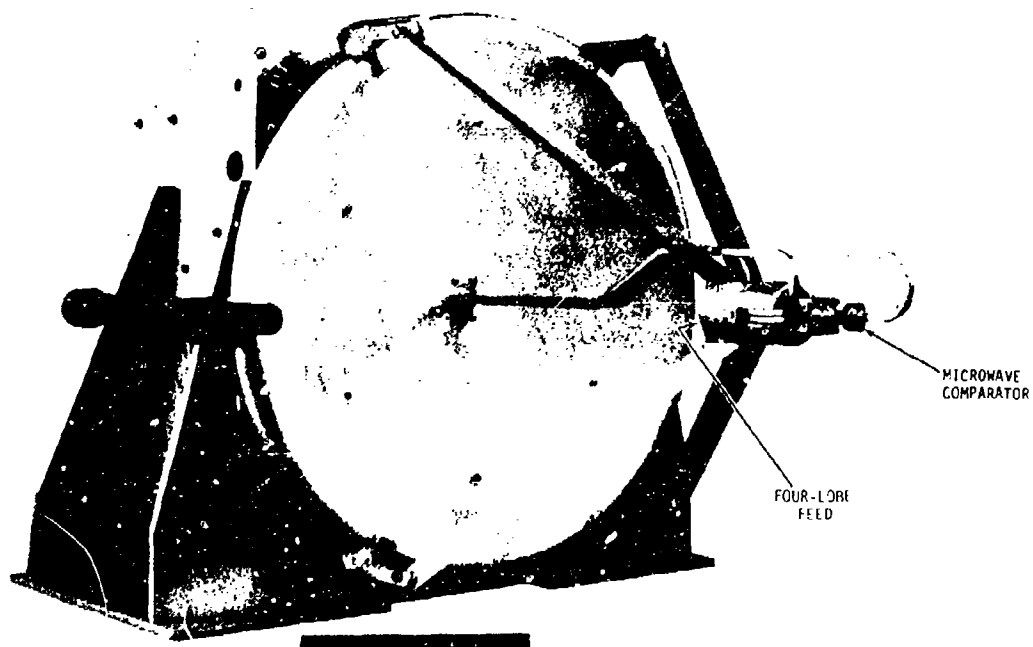
Figure 4.　Norden Millimeter Monopulse Antenna

An IMPATT diode oscillator is used as the system local oscillator. A voltage-controlled current source drives the IMPATT which, used in conjunction with an AFC module, maintains the IF within 1 MHz of the center frequency. Sum and difference microwave channels are shown in Figures 5 and 6 respectively.

Receiver

Amplitude monopulse information contained in the IF signals is converted to phase information by the Monopulse IF (MIF) Processor and phase detected to determine the angle-off-boresight in each difference channel. The sum channel signal is split with one output acting as a reference for the phase detector and the other output processed through a log amplifier for information and display purposes. The overall receiver dynamic range is 68 dB.

The angle-error output voltages of the MIF Processor are a function of the phase difference between the sum and difference channel signals and range from zero volts for the on-boresight condition to a maximum value of about 100 mV. The polarity or sense of the error signal depends on the location of the target with respect to the antenna boresight axis. For targets below or to the left of the axis, the sense is positive. For targets above or to the right of the axis, the sense is negative.

Of particular interest is the slope of the angle-error curve, especially in the linear region around boresight, since it is this signal that will ultimately provide the control signals for the servo system. For the millimeter track radar, the slope (or scale factor) at the output of the MIF Processor is 30 mV/mR in the linear region.
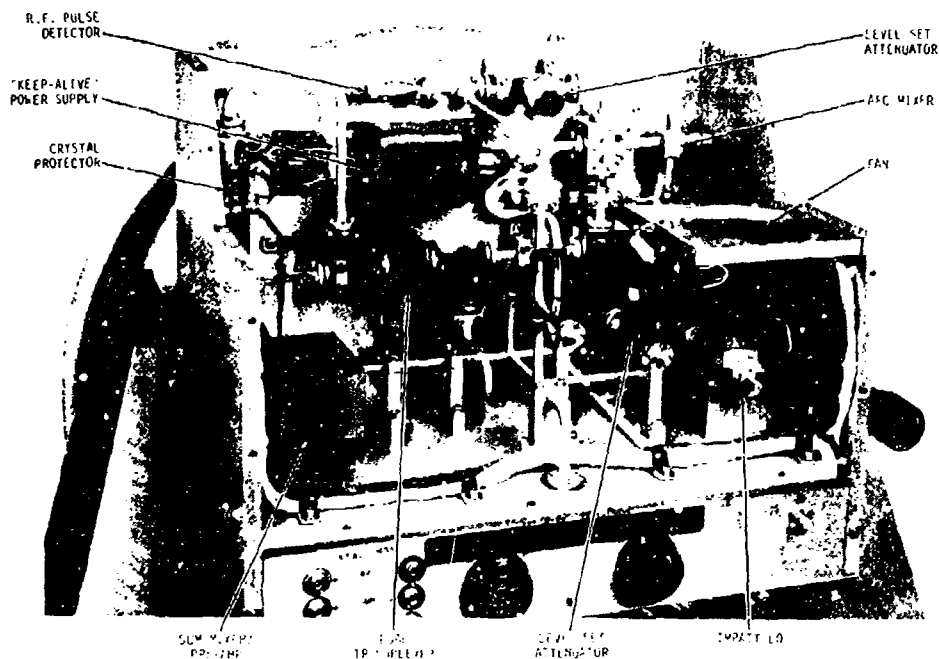
Figure 5. Sum Channel Microwave
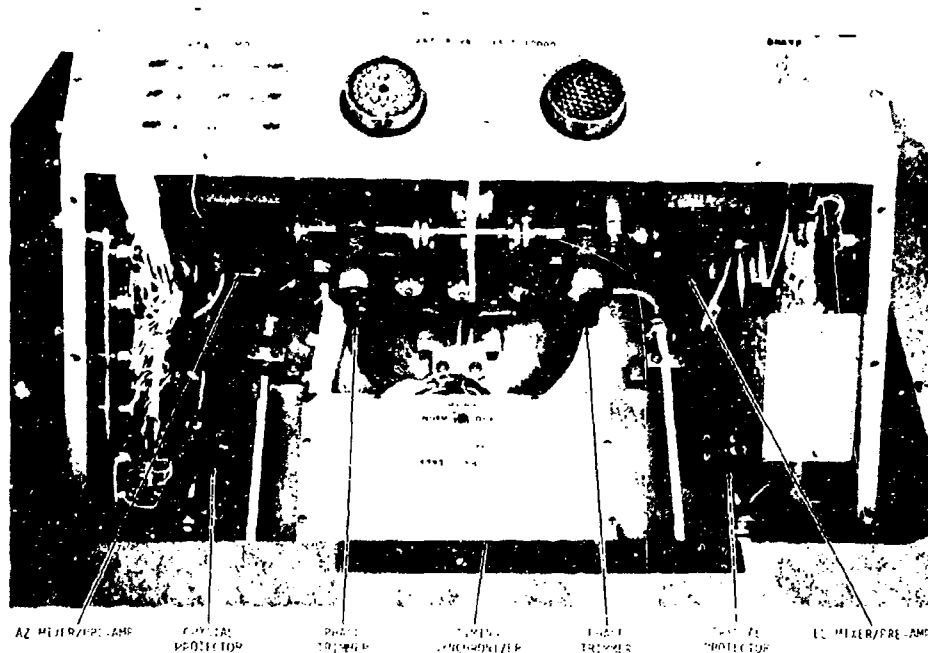
Figure 6. Difference Channel Microwave

ERROR SIGNAL (mV)
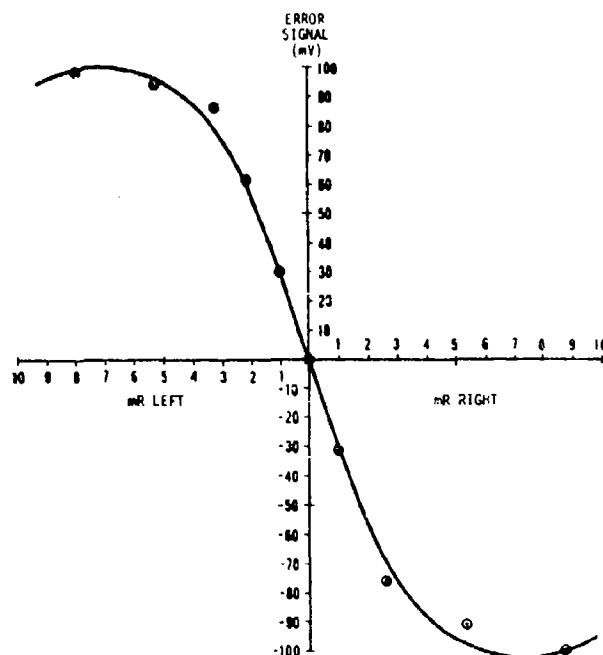
Figure 7. MIF Processor Azimuth Error Output

Figure 7 is a plot of the angle error curve as measured
at the output of the MIF Processor for the azimuth channel.
The error curve for the elevation channel is essentially
the same.

Data Processing Unit

A Data Processing Unit (DPU) provides the essential
circuitry needed to process the A/R signals. Circuits contained
in the DPU include the timing and range gate generators,
angle-error boxcars, the range tracking module, and the MIF
and AFC modules.

Transmitter Modulator

The Transmitter/Modulator uses a conventional line
type thyratron modulator and current pulse regulator to produce

a stable 100 nanosecond pulse. The magnetron provides 10 kW peak power at a 0.0004 duty cycle. A ferrite isolator prevents magnetron pulling due to load VSWR. A pressurization unit provides 31 psia of dry air pressure to prevent arcing in the waveguide and pulse transformer housing.

Static Tracking Accuracy

Static accuracy of the system is the amount of error measured at the output of the MIF Processor. It was found to be 0.56 mR in azimuth and 0.64 mR in elevation.

This error is broken down into its contributing portions (RF, IF, and Video) as follows:

	RF	IF	Video
Azimuth	0.29 mR	0.11 mR	0.16 mR
Elevation	0.34 mR	0.17 mR	0.13 mR

Box error for the Antenna/Receiver alone is the error measured at the input to the MIF. This error is 0.4 mR in azimuth and 0.51 mR in elevation.

System Performance Calculations

The Norden Millimeter Track Radar will undergo a series of evaluation tests at the Norden facility in the near future. One means of comparing its performance with that of other systems is to predict its performance against a standard target. Using the system parameters, range calculations were performed for a 1 square meter target in clear air and adverse weather conditions. The following assumptions were made:

Probability of Detection = 90%

Probability of False Alarm = 10^{-12}

Integration Improvement = 10 dB

Table 4 summarizes the results of the calculations. The range varies from 9.6 kilometers in clear air to 4.1 kilometers in moderate rain conditions.

Table 4. Millimeter Track Radar Performance
Against a One Square Meter Target

WEATHER CONDITION	ATTENUATION COEFFICIENT (dB/Km)	MAX. DETECTION RANGE (Km)
Clear Air	0.41	9.6
Drizzle (0.25 mm/hr)	0.63*	8.2
Light Fog (120 m visibility)	0.69*	8.0
Moderate Rain (4 mm/hr)	2.71*	4.1

*Includes 0.41 dB/Km clear air attenuation

CONCLUSIONS

Design considerations for a millimeter monopulse radar have been analyzed and indicate that high accuracy, adverse weather performance can be achieved in the millimeter band. An experimental 70 GHz monopulse system was described and experimental data presented. It was shown that the system is capable of static tracking accuracy better than the 1.0 milliradian objective.

ACKNOWLEDGEMENT

REFERENCES

[1] Rhodes, Donald R., *Introduction to Monopulse*, McGraw-Hill, New York, 1959.

[2] Kosowsky, L., et. al, *The Reduction of Angle of Arrival Scintillation by a Frequency Shifting Technique*, presented at the National Electronics Conference, 1963.

[3] Rosenblum, E. S., *Atmospheric Absorption of 10 to 400 KMCPS Radiation*, Microwave Journal, pp 91-96, March 1961.

[4] Koester, K. L., *Millimeter Wave Propagation*, Norden Technical Report 4392 R 0005, 12 September 1973.

[5] Kosowsky, L. H., and Koester, K. L., *Millimeter Radar for Landing Applications*, presented at the 26th Annual National Forum of the American Helicopter Society, 1970.

[6] Koester, K. L. and Kosowsky, L. H., *Design Considerations for a Millimeter Radar ILM*, presented at Federal Aviation Administration Planning Review Conference, 1971.

[7] Koester, K. L. and Kosowsky, L. H., *Attenuation of Millimeter Waves in Fog*, presented at the Fourteenth Radar Meteorology Conference, 1970.

[8] Koester, K. L. and Kosowsky, L. H., *Millimeter Wave Propagation in Fog*, presented at IEEE Antennas and Propagation Symposium, 1971.

[9] Jones, E. M. T., *Paraboloid Reflector and Hyperboloid Lens Antennas*, IEEE Transactions, Vol. AP-2, July 1954.

UNCLASSIFIED

"100 GHz DIAGNOSTIC IMAGING TECHNIQUES"

by

Maynard H. Dawson and Floyd F. Rechlin

DARE Technology, Inc.

San Diego, California 92120

FOREWORD

This presentation covers the development and application of a 100 Ghz
RCS measurement and diagnostic imaging facility under U.S. Army Contract No.
DAAK02-70-C-0240 and, at present, Contract No. DAAK02-72-C-0441. The sponsor-
ing organization for this project was the U.S. Army Mobility Equipment Re-
search and Development Center (USAMERDC), Fort Belvoir, Virginia 22060.

DISCUSSION

The configuration of any functional, man-made target is invariably made
up of a large number of protuberances, dihedrals, and corner reflectors that,
when illuminated by radar, collectively create its detectable total return,
commonly referred to as its radar cross-section (RCS). These same individual
centers also create a distinguishable pattern or microwave image that can be
recognized by advanced, high resolution radar. As a result, it is imperative
for military applications that these critical reflective elements be identi-
fied, measured, and corrective actions initiated to alter or mask such a
characteristic radar signatures.

Such data has usually been obtained to this point by measuring the gross
return from full scale vehicles; this inherently involved the problems of
positioning awkwardly large vehicles on turntables or pylons, obtaining only

F4-1

rudimentary data for only a restricted number of possible surveillance angles, and trying to tolerate the uncontrollable downtimes and variations in measurements that are always typified in outdoor tests. Such inherent disadvantages in full scale testing influenced the U.S. Army to develop the subject indoor microwave modeling facility, wherein complete control can be maintained over all test conditions and full advantage taken of the flexibility of handling and treatment with lightweight models. In this effort, 100 GHz was selected as sufficiently high enough a frequency to permit the study of easily handleable models scaled up to K_u- band.

Basic to this development was the requirement for a capability to first record and quantitatively measure a weapon system's total reflectivity or RCS pattern at all azimuth settings and any practical surveillance angle, so that its attitudes of critical return could be identified. The facility configuration designed to accomplish this task can be seen in the first viewgraph accompanying this paper; this configuration is referred to as the monostatic mode.

In this mode, the microwave illumination from the depicted transmitter horn is directed toward a "half-silvered" (in reality, a half-reflective) mirror. Part of this radiation passes directly through this element and is absorbed by the RAM located directly opposite the transmitter; the remainder is reflected at 90 degrees toward the study object, then reradiated back from the target area to the receiver, where it can be processed and recorded on an X-Y plotter as a function of total RCS return versus azimuth setting.

Mention should be made of the design consideration behind the right-angle configuration, with separate transmitter and receiver horns and a half-silvered mirror, which was selected for this facility. This, at first, might appear complicated when compared to the more conventional monostatic range arrangement which uses the same horn for direct transmission and reception along the same axis without a mirror. In practice, however, the right-angle arrangement actually results in a much more efficient and easily adjustable system and, most important, the very delicate and easily
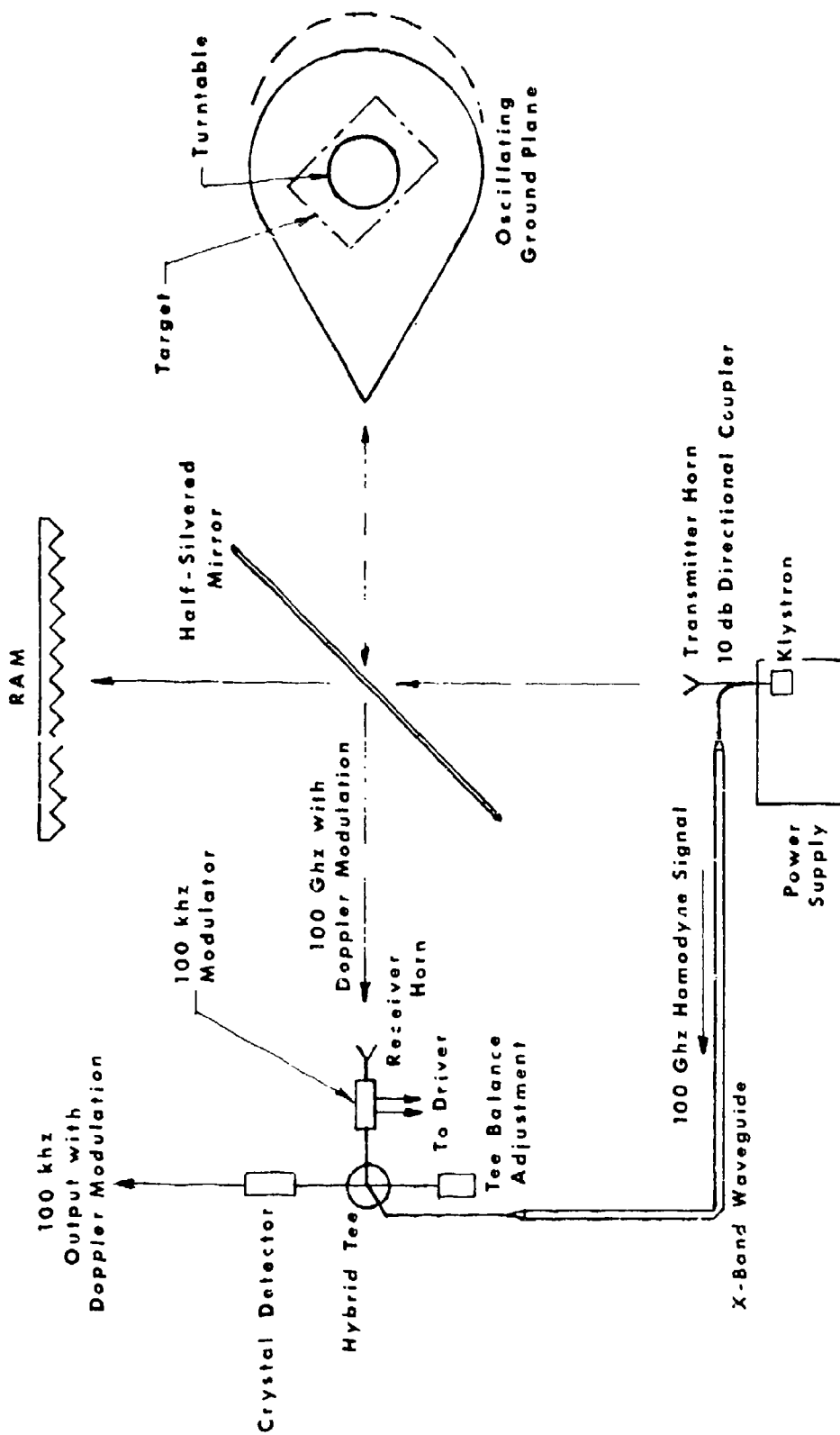
MONOSTATIC MODE

DARE Technology

disturbed adjustments normally required to isolate exact return levels are eliminated by the spacial separation of the receiver from the high field strengths produced around the transmitter.

The necessary differentiation between target return and the indoor background is accomplished by mechanically oscillating the test object and its mount in the direction of the incident radiation at a frequency that is continuously variable from zero to two-thirds cycles per second. The return from the target is then mixed with another signal of fixed path length; these beat with each other, as in a Doppler radar system, with the amplitude of the beats measuring the amplitude of the reflection.

The synthetic ground plane on which the target is mounted is completely metallic. In its center is a turntable which allows the target to be rotated through 360°; the resulting continuous azimuthal readout drives the X-axis of a conventional X-Y recorder, with the Y-axis being the RCS return. Further, for full hemispherical analyses, the supporting mount of the ground plane and target can be easily reconfigured to provide data for any preselected elevation angle of interest.

To repeat, the above monostatic mode for this facility has been designed to provide quantitative data on the RCS of target models at all azimuth settings and at preselected angles of surveillance. Once such data has been obtained, this facility is configured into the diagnostic imaging mode shown in the second accompanying viewgraph. Here, it can be seen that the same major components are still employed, with two additions to provide the required imaging capability, i.e., a focusing microwave lens and the mechanisms which can precisely displace the target and mount in both the longitudinal and lateral directions.

As noted by the arrows in this sketch, the energy from the transmitter is still reflected from the half-silvered mirror to the study object; in the imaging mode, however, the return from the target then passes through the focusing lens to the receiver system. This lens provides a resolution of

DIAGNOSTIC IMAGING MODE
(MACROSCOPE)

Longitudinal Movement

Lateral Movement

Imaging Zone

Vertically Movable Lens

TV Camera

Veiwing Aperture

Output

GARE Technology

F4-5
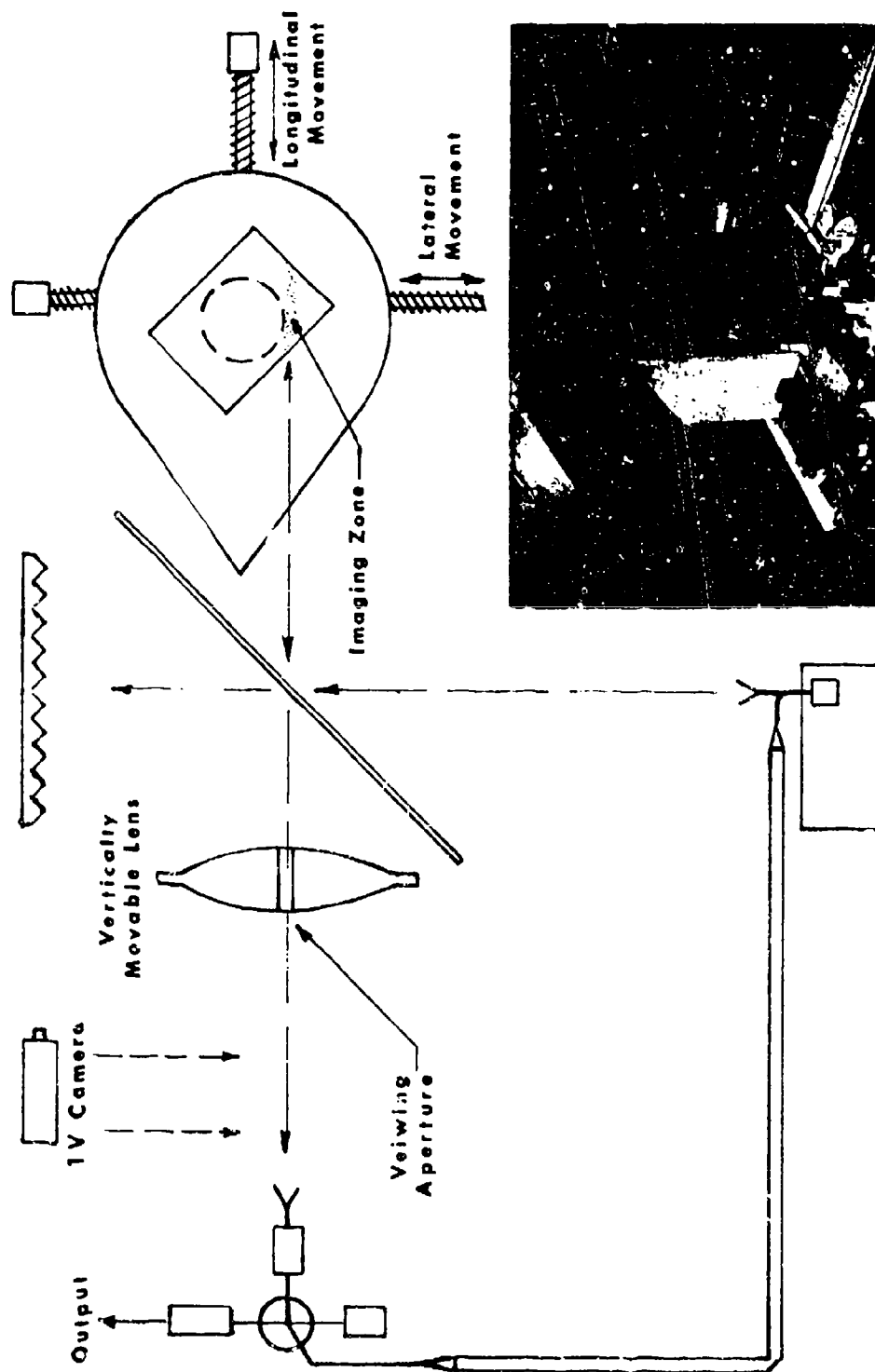
1/2", which, for a 10th scale subject model, would be equivalent to a 5" full scale resolution at X-band. In operation, the target is initially focused through the lens by being remotely displaced via the depicted longitudinal movement mechanish. The resulting image field in focus at the receiver can then be directionally scanned, either manually or automatically, by programming the lens to move up and down the height of the field and then incrementally displacing the target laterally at the end of each such vertical traverse. In this manner, the total field can be progressively scanned to provide a two-dimensional probe of all critical imagery.

As indicated in the third viewgraph, three effective readout systems have been installed to aid in the diagnosis of the resulting imagery. First, a graphical method is generally employed in the monostatic mode where the processed Doppler signal forms the Y-input to an X-Y recorder; this, along with the associated azimuthal information from the turntable to the X-input of the recorder, results in a complete RCS plot of the target's total reflectivity over 360° of rotation. This same Y-input of the processed Doppler signal to the recorder can also be used in the diagnostic imaging mode to provide quantitative data on that portion of the target which is in the exact focus of the lens.

The second (audio) readout system, provides an excellent means for immediately identifying critical "flare spots" encountered during the progressive scanning of the focused field. Here, any such individual points of high reflectivity are automatically manifested by a noticeable gain in the volume of a continuous background signal of approximately 3 khz.

As stated earlier, the location, pattern, and levels of all such individual contributors to return constitute a specific "signature" of a weapon system which can be identified by a sophisticated threat radar. Because of the criticality of such composite imagery, therefore, a third readout system has also been installed which provides a visual raster display of the scanned imagery on the depicted TV monitor. With this optical readout system, each resolved point of large return encountered during a sequential field probe

READOUT SYSTEMS

BARE Technology. Inc.

Signal Processing Section

100 khz Doppler + Noise
(From Receiver Section)

20-100 hz Doppler

Oscilloscope

Signal Conversion Section

3.1 khz Doppler

Loudspeaker
(AUDIO)

From Turntable Transducer

X-Y Plotter
(GRAPHICAL)

X

Y

(X-Input)
Target Lateral Position

(Y-Input)
Lens Vertical Position

Input Interface

Scan Conversion Memory

TV Camera

Keying Circuit

TV Monitor
(VIDEO)

F4-7
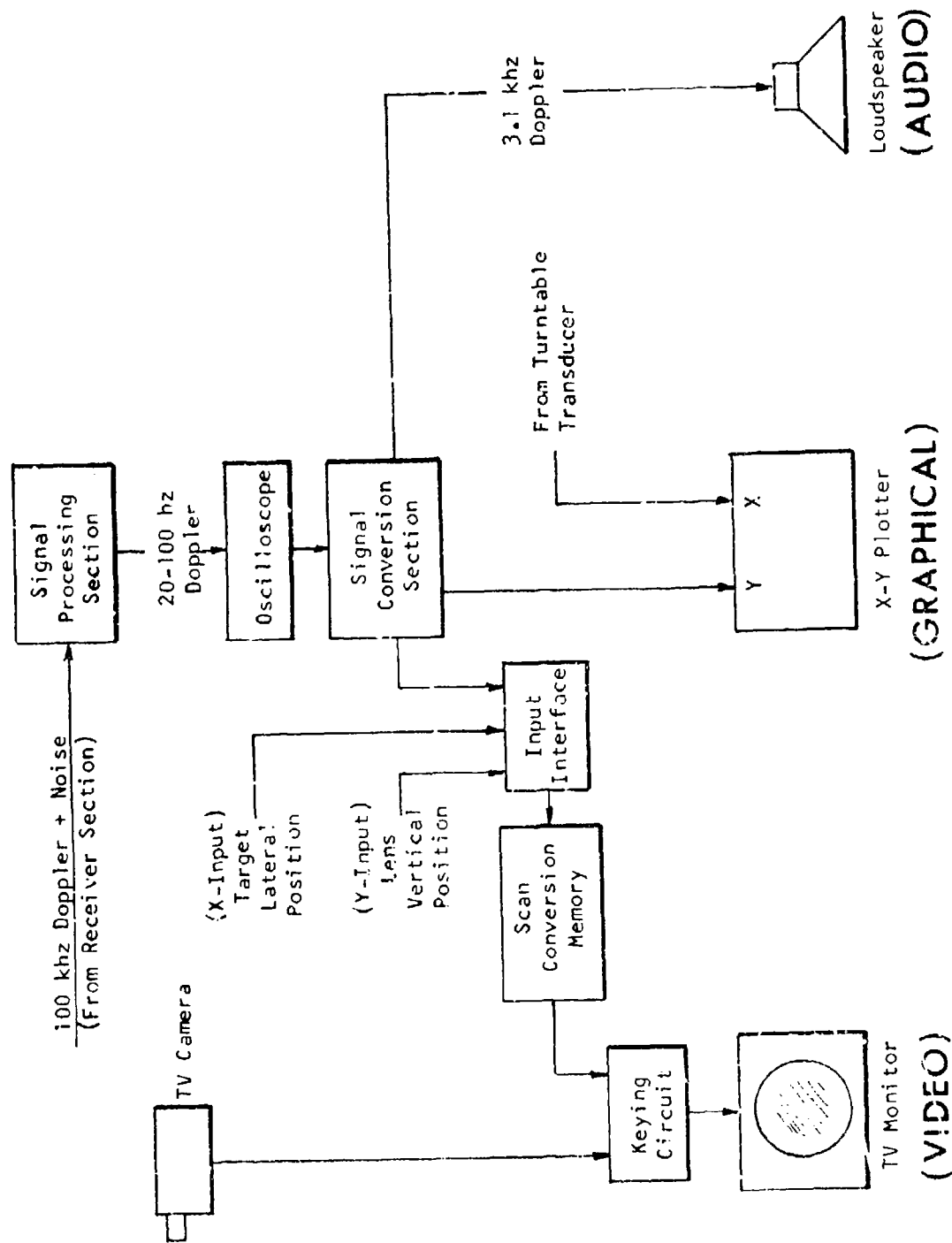
is stored on the tube of a special Scan Conversion Memory (SCM) unit, from which they can be read on a real-time or as-required basis on the TV monitor. Further, the optical picture of the target from the indicated closed circuit TV camera can be superimposed on the video presentation of the radar imagery, so that each critical element can be immediately identified in its physical relationship to the target.

An overall view of this facility is provided in the fourth viewgraph. Here, it can be seen that all of the electronics and controls are located on three work tables arranged in the form of a loose "Z", with the video readout apparatus located at the far left, the major operational and receiver equipment at the center, and the transmission system at the right. Other features in this photograph are the ground plane in the right background, upon which an operator is adjusting a study model, and the half-silvered mirror and frame. At the time this photograph was being taken, a video picture of the target was about to be recorded; thus, the microwave lens has been manually lifted above the field of view and the closed circuit TV camera centered in the picture moved into place along the viewing axis from the receiver horn to the target.

One unclassified example of the diagnostic imagery obtainable with this 100 GHz facility for a 10th scale model of the Army's M-113 APC is presented in the fifth viewgraph; using this linear scaling technique, the depicted return pattern corresponds to that from the full scale vehicle illuminated by an operational X-band radar. It should also be pointed out that all three of these photographs are closeups of the TV picture, which tends to reduce the optical clarity. In this viewgraph, the recorded microwave pattern of the model can be seen in the upper right hand corner, the optical view from the closed circuit TV camera is on the opposite side, and the superimposed combination of these two views is in the lower left hand corner; through the use of the latter composite presentation, the physical location of all critical elements is apparent.

Particular attention is invited to the "splash" shown in the ground plane directly in front of this model. This type of physical interaction, which is

F4-9
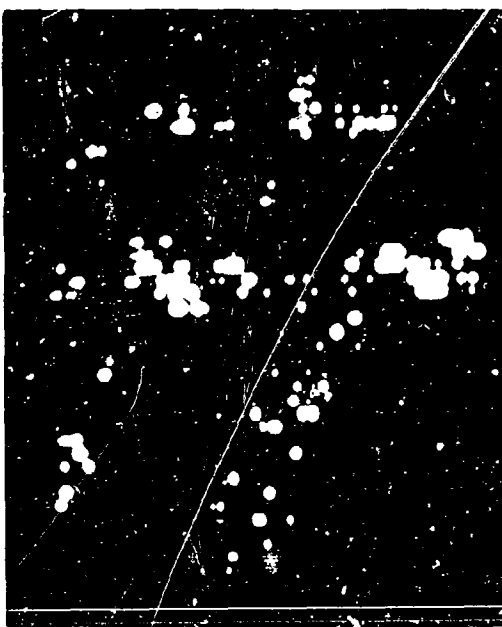
IMAGERY STUDY

- 45° From Rear-On
- 18° Elevation Angle
- Vertical Polarization
- Metallic Skirts
- No Machine Gun
- Metallic Ground Plane

DARE Technology

F4-10

seldom identifiable on a full scale range, can be the subject of detailed analysis due to the 1/2" resolution of this 100 GHz system. The criticality of such microwave behavior can be noted in the photographs of the sixth viewgraph. Here, the same model was imaged both on the metallic ground plane and after the latter was covered with radar-absorbing material. An electronic processing system is currently being installed which will allow the imagery from these extremes in return to be factored by the measured reflectivity coefficient of any natural terrain, thus permitting valid real-life interaction studies.

It is obvious that the resulting combined capabilities of detail resolution, frequency scaling, and natural reflectivity duplication causes this 100 GHz facility to be an excellent laboratory tool for realistically diagnosing microwave interactions, in detail, of any irradiated configuration, either man-made or natural. To illustrate, the return levels and precise distribution from various simulations of terrains and sea states can be systematically and quantitatively investigated; recently completed studies of such natural phenomena demonstrated that the results obtainable at this 100 GHz frequency are directly comparable with those for the full scale situation.

GROUND PLANE EFFECTS
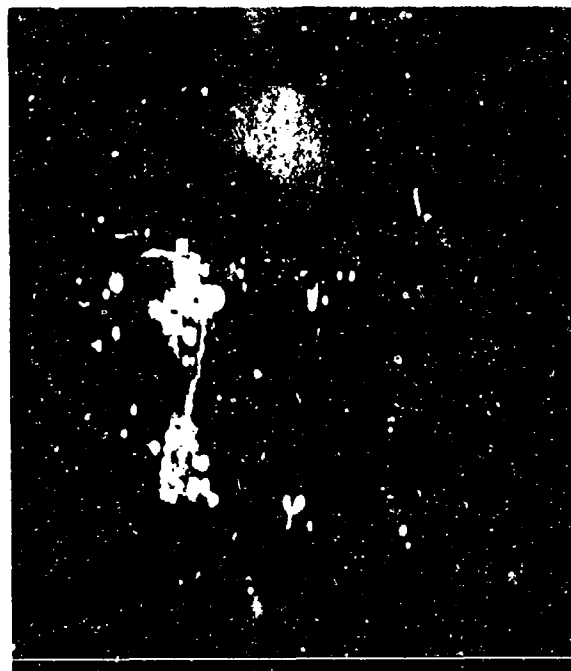
- 10° From Head-On
- No Machine Gun
- Vertical Polarization
- 18° Elevation Angle
- Metallic Skirts

DARt Technology

MILLIMETER WAVE PASSIVE SENSING FROM SATELLITES

by
Herbert G. Pascalar
Aerojet ElectroSystems Company
1100 W. Hollyvale Street
Azusa, California 91702

INTRODUCTION

The potential for applications to meteorology and geophysics of satellite-based millimeter wave radiometric (i. e., passive) sensing of thermal radiation emitted by the atmosphere and from the earth's surface was recognized in the early 1960's[1]. Millimeter wave technology advances since that time have led to the development of satellite-borne imaging systems. An example of a global radiometer map produced by a 19.35-GHz electronically scanned radiometer on the Nimbus E meteorological satellite is shown in Figure 1. The intense, essentially black body, radiation from land surfaces is seen to be essentially unobscured by cloud cover. As a result of the low radiation from water surfaces, regions of high atmospheric water content and cloud precipitation are clearly observed over the oceans.

This paper summarizes the applications and technology for satellite-based radiometric sensors.

Background

A brief chronology of events in the last decade serves to illustrate the development of millimeter wave sensor technology for meteorological satellite applications. One of the first was oriented to a requirement for synoptic mapping of cloud precipitation over oceans[2]. As a consequence of their intense millimeter wave emission, cloud precipitation cells were expected to offer strong contrasts relative to the cool radiation background of water surfaces. These contrasts offered the possibility of mapping the rain cloud distribution with an imaging type millimeter wave sensor. Operational requirements for imaging and considerations of spacecraft attitude stabilization indicated the need for an inertialess electronically

RADIO BRIGHTNESS OF THE WORLD

NIMBUS-5 ELECTRICALLY SCANNED MICROWAVE RADIOMETER

(λ = 1.55 cm)
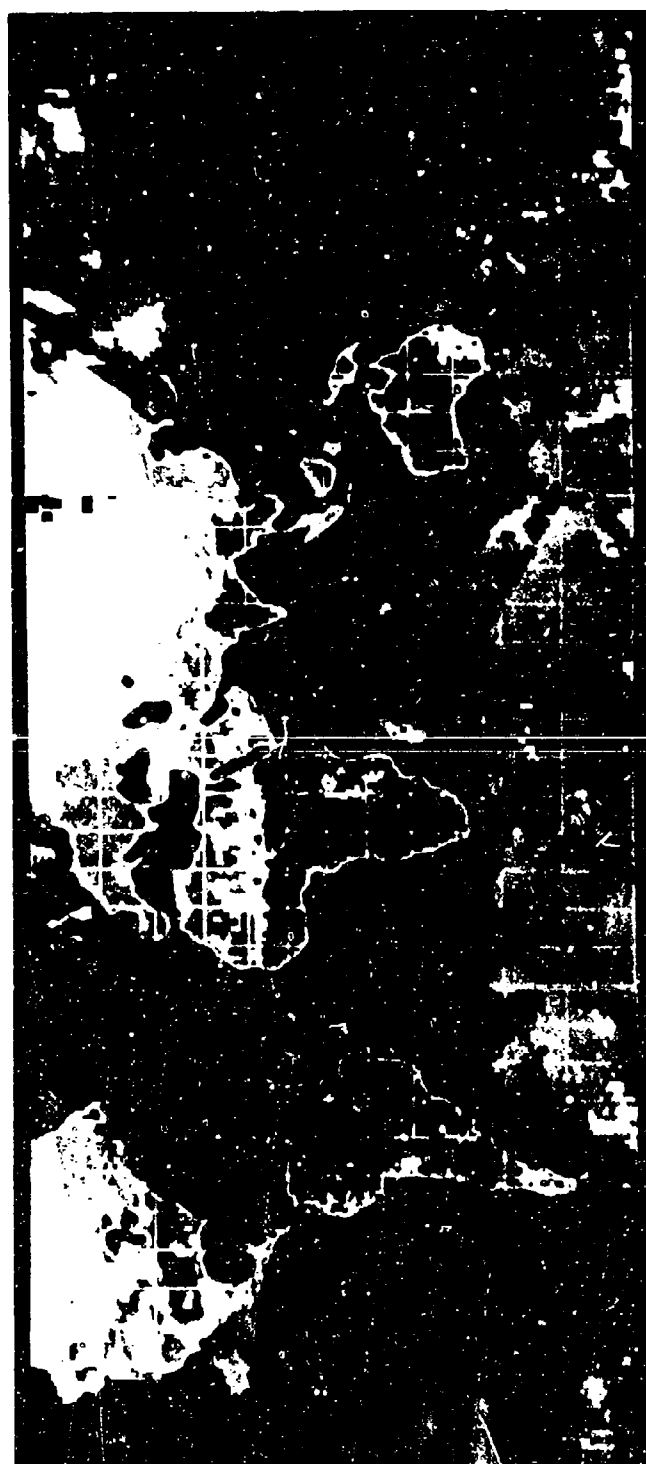
12 – 16 January 1973

Figure 1. Radiometric Brightness of the World Produced by the Nimbus E Electrically Scanning Microwave Radiometer

scanned antenna. Although operation at frequencies in the 30 to 40 GHz region offered improved spatial resolution, millimeter wave technology limitations in 1965 restricted the choice of sensor frequency to 20 GHz or less. The availability of a clear radio-astronomy channel resulted in the final choice of a 19.35 GHz operating frequency. Advances in millimeter wave materials and semiconductor devices, occurring in the mid-1960's, made possible the development of a completely solid-state electronically scanned radiometric imager[3]. Tests of an airborne prototype imager conducted by NASA in 1967 demonstrated its successful application to mapping of rain cells in cloud cover and also identified potential capabilities for sea state and sea ice applications[4]. An evaluation of the test results established the final design specifications for the 19.35 GHz radiometric imager to be flown on the Nimbus E satellite.

Subsequently, NASA conducted extensive airborne investigations of the frequency dependent emission characteristics of sea state and sea ice phenomena. The results of these investigations led to the selection of sea ice mapping as a principal application for an advanced model of a radiometric imager to be flown on the Nimbus F satellite. This imager, developed in the time period 1971 to 1973, operates at 37 GHz and simultaneously measures both the horizontally and vertically polarized components of surface radiation. It is currently installed on the Nimbus F spacecraft which is scheduled for launch in the latter half of 1974.

The second category of millimeter wave sensors implemented on the Nimbus E and F satellites are oriented to quantitative measurement of atmospheric parameters. These parameters include: the temperature of discrete layers of pressure altitude and the integrated path contents of both liquid water and water vapor. On the Nimbus E satellite, this information is supplied by a five-channel millimeter wave spectrometer. Three channels centered at 53.65, 54.9 and 58.8 GHz in the oxygen absorption spectrum respond to radiation originating predominantly from 10-km-thick layers of the atmosphere centered respectively at altitudes of approximately 4, 11 and 18 km. Two channels centered at 22.235 and 31.4 GHz responding to water vapor and liquid water respectively, provide information

regarding atmospheric moisture content. A high degree of accuracy is required of these radiation measurements in order to provide meteorologically useful information. Limitations in receiver sensitivity particularly for the 50-60 GHz channels which existed at the start of the spectrometer development in 1969, precluded spatial scanning. The successful design within spacecraft payload constraints was made possible by developments in millimeter wave latching ferrite switches and Gunn oscillators. A factor of four improvement over the originally specified sensitivity was achieved in the flight model spectrometer due to recent advances in the technology of Gallium Arsenide Schottky barrier diodes. The results achieved by the interpretation of the data from the Nimbus E millimeter wave spectrometer have demonstrated the ability to provide useful estimates of atmospheric temperature profiles in the presence of most cloud cover conditions where profiling by infrared sensors is impossible. The ability to provide quantitative indications of atmospheric water vapor and liquid water has also been shown[5].

The following sections summarize (a) the impact on sensor design of the radiation emission characteristics used in the specific applications, and (b) the design features of current spaceborne millimeter wave sensors and projected future requirements.

SURFACE AND ATMOSPHERIC EMISSION

Millimeter wave thermal radiation levels are conveniently characterized by a brightness temperature value, T_B, equal to the temperature of an equivalently radiating black body. As indicated in Figure 2, both surface and atmospheric radiation contributions are included in satellite observations. The observed brightness temperature, T_B, is described by $T_B = t(\epsilon T + \rho T_s) + T_a$. Where t and T_a are, respectively, the transmission factor and radiative emission associated with the atmospheric path between the surface and the sensor. The quantities ϵ and ρ correspond, respectively, to the emissivity and reflection factors of the surface. The thermometric temperature of the surface is given by T, while the brightness temperature, T_s, characterizes the atmospheric radiation incident

Figure 2. Microwave Radiometric Sensing of Surface and Atmospheric Radiation

$$T_R = t(\epsilon T + \rho T_S) + T_a$$

OBSERVED RADIATION

T_a (FROM ATMOSPHERE)

$t(\epsilon T)$

$t(\rho T_S)$

ATMOSPHERE

EMITTED

REFLECTED

INCIDENT

ϵ, T_p

ρT_S

(FROM ATMOSPHERE): T_S

OCEAN SURFACE

on the surface which is in turn reflected toward the sensor with a magnitude T_s. For surface sensing applications, operating frequencies are chosen in the atmospheric transmission bands with the objective of making the surface emission, ϵT, the predominantly observed radiation, i. e. , $T_B \cong \epsilon T$. In like fashion for an atmospheric sensing applications, the appropriate atmospheric absorption band is selected to minimize the contaminating effects of surface emission.

Surface emission characteristics must be considered in the selection of a sensor design for a particular application. The selection process can be understood by examining the requirements in sea ice surveillance. There it is desired to detect the boundaries of open water leads, and also to observe those contrast features associated with ice bodies of varying composition and structure. The detection of open water bodies can be optimized by selection of sensor polarization and look angle to maximize the contrast observed between water and ice. The contrasts permitting the detection of changes in ice quality are maximized by selection of sensor operating frequency.

Millimeter wave radiation from calm water surfaces is much lower than that from ice surfaces. As a result of the higher level radiation emitted from ice surfaces, water bodies are distinguished by their "cold" contrasts with respect to ice backgrounds. Recent investigations show the radiation from ice surfaces to be relatively insensitive to sensor polarization and look angle[6, 7, 8]. Consequently these sensor parameters are selected to maximize the contrast of water bodies. The dependence of radiation from water surfaces on sensor view angle and polarization is shown in Figures 3a and 3b. From that data it is seen that horizontally polarized sensors employed at a view angle of 40° to 60° with respect to nadir provide maximum values of "cold" contrast for water bodies. The remaining sensor parameter, i. e. the operating frequency, is selected to maximize the contrasts associated with different types of ice.

Differences in the millimeter wave radiation emitted from ice bodies are believed to result from variations in brine distribution characteristic of the ice age. Ice is conveniently described as "new" or "old. "
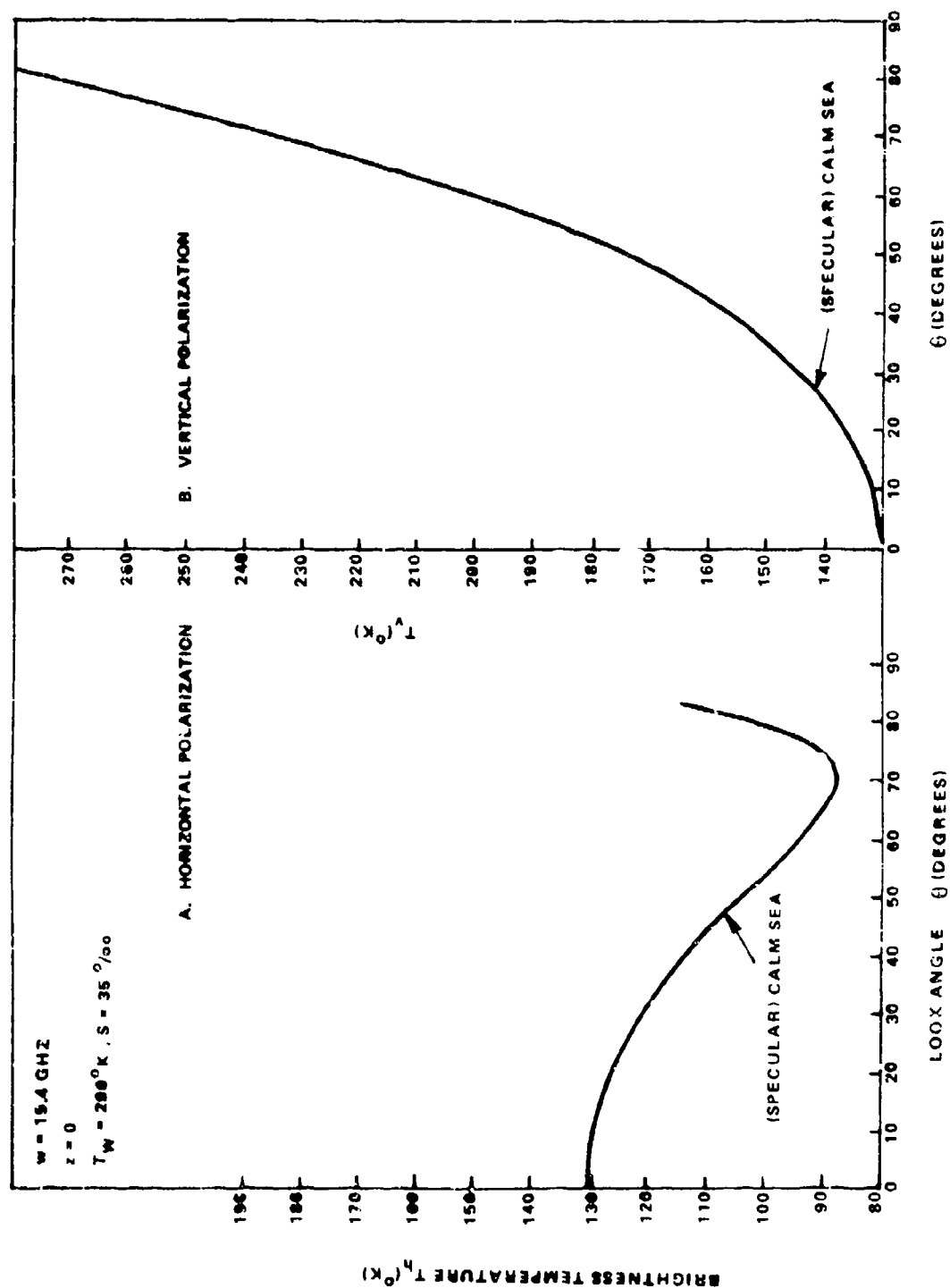
Figure 3. Horizontally and Vertically Polarized Radiation from Calm Sea Surface

New ice is considered to have been recently formed and not to have experienced the recurrent thawing and refreezing which characterizes the thermal history of old ice. In newly formed ice the surface concentration of brine is sufficient to cause absorption and emission characteristics similar to those of a black body. The gradual downward migration of brine with age and/or acceleration of this trend during thawing conditions leaves a surface residue of low brine ice partially filled with pockets evacuated by the brine. The lowered direct emission of the resulting surface ice as well as the scattering of internal radiation by the air pockets causes radiation from old ice to be significantly lower. Theoretical predictions based on this model appear to be in agreement with direct experimental observations [9, 10, 11, 12].

The frequency dependence of the radiation emitted from old ice, new ice and calm water surfaces is presented in Figure 4. It is seen from this data that in the vicinity of 37 GHz, contrasts indicative of ice age are equivalent in magnitude to those observed for water bodies. Thus an operating frequency of 37 GHz appears best suited for sensing both the age-dependent features of sea ice as well as the presence of water surfaces.

Consideration of the various surface emission characteristics has shown that the most useful contrasts for sea ice surveillance are provided by a sensor responding to horizontally polarized 37-GHz radiation observed at view angles in the vicinity of 50°. Larger view angles are excluded by consideration of sensor spatial resolution.

Quantitative measurements of surface radiation are frequently necessary in scientific investigations of surface phenomena. These measurements require that the contaminating effects of the intervening atmosphere be evaluated. The known radiation characteristics of water surfaces permit them to be used as known reference sources of surface radiation. From Figures 5a and 5b, respectively, it is seen that the horizontally and vertically polarized components of radiation from calm seas are essentially independent of water temperature. A large difference between the two
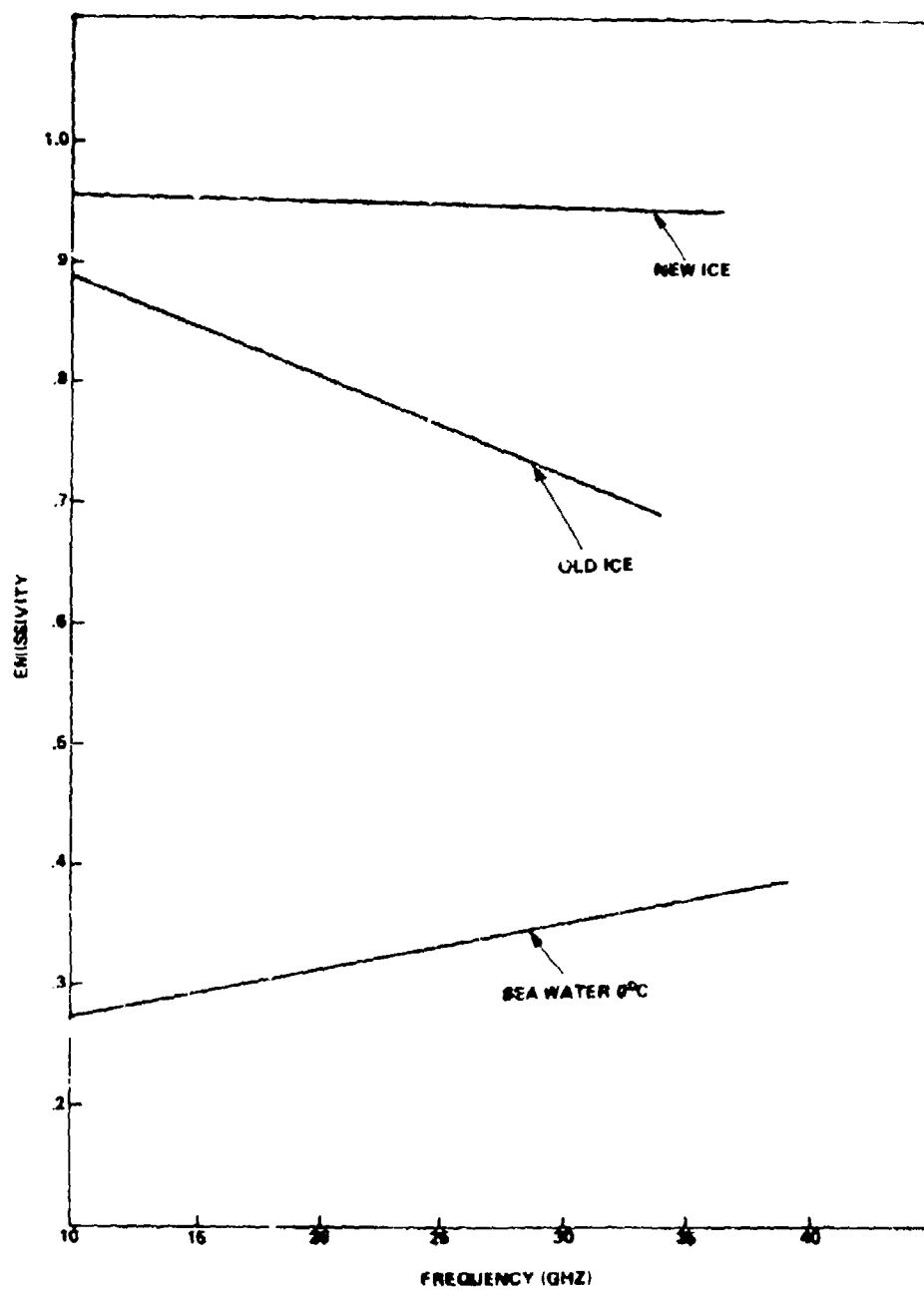
Figure 4. Sea Ice and Water Emissivity Dependence on Frequency
Polarization: Horizontal; Look Angle 50°

polarization components is also noted. It is thus apparent that sea surface
radiation can serve as a constant source of radiation for the purpose of
evaluating the transmission and radiation properties of the atmosphere.
The remotely observed values of horizontally and vertically polarized
surface radiation are equally affected by the atmospheric path to the sensor.
Consequently, from the difference of the remotely sensed values of horizon-
tally and vertically polarized radiation, it is possible to infer the atmos-
pheric path transmission factor, t . This quantity, together with the abso-
lute radiation values measured for the individual polarizations, identify
the atmospheric radiation, T_A . These values of t and T_A derived from
water surface observations may then be employed to correct for atmos-
pheric effects in measurements of adjacent ice surfaces having the same
atmospheric environment.

RADIOMETRIC IMAGERS FOR METEOROLOGICAL SATELLITES

Imaging radiometers developed for the Nimbus meteorological
satellites employ electronically scanned phased array antennas in order
to map the earth's surface. The 19. 35 GHz imager on the Nimbus E satel-
lite linearly scans a horizontally polarized antenna beam over a $\pm 50^{\circ}$ range
of nadir angles in a plane perpendicular to the flight direction. The 37-GHz
imager on the Nimbus F satellite conically scans a dual-polarized antenna
beam at a constant nadir angle of approximately 45° as shown in Figure 6.

Basic Configuration

The essential system elements common to both imagers are
shown in Figure 7. The beam steering network is synchronized by the
timing and control unit to actuate a step-wise angular scan in which dis-
crete surface elements are individually measured for equal time intervals.
Overlapping of adjacent surface samples insures uniform mapping.

A radiation brightness, T_b , from a surface element within the
main beam of the antenna results in an antenna radiation temperature out-
put signal, $T_A = E_b T_b$. Where E_b is termed the main beam antenna
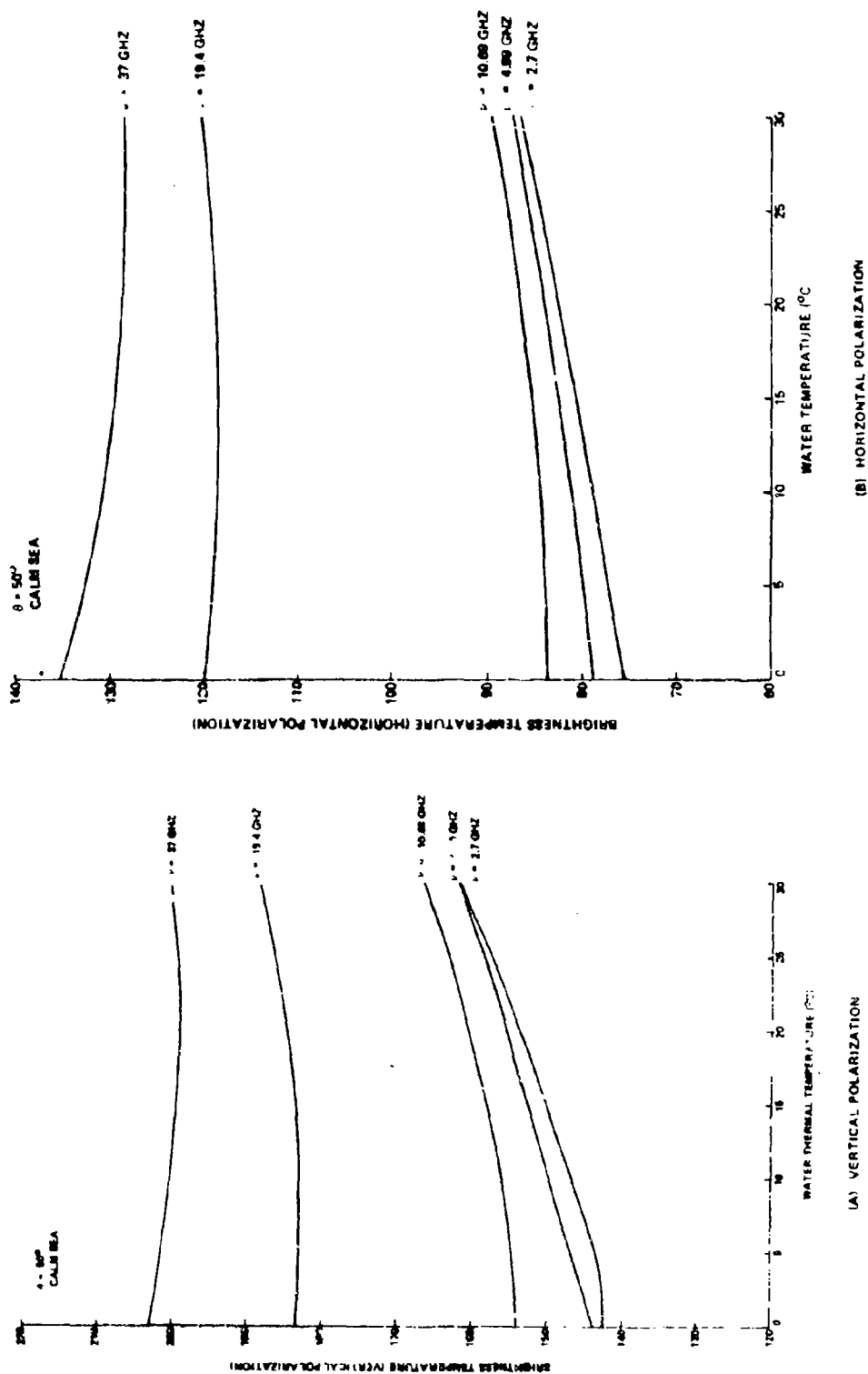efficiency of the antenna. A performance requirement of $E_b \geq 0.9$ was

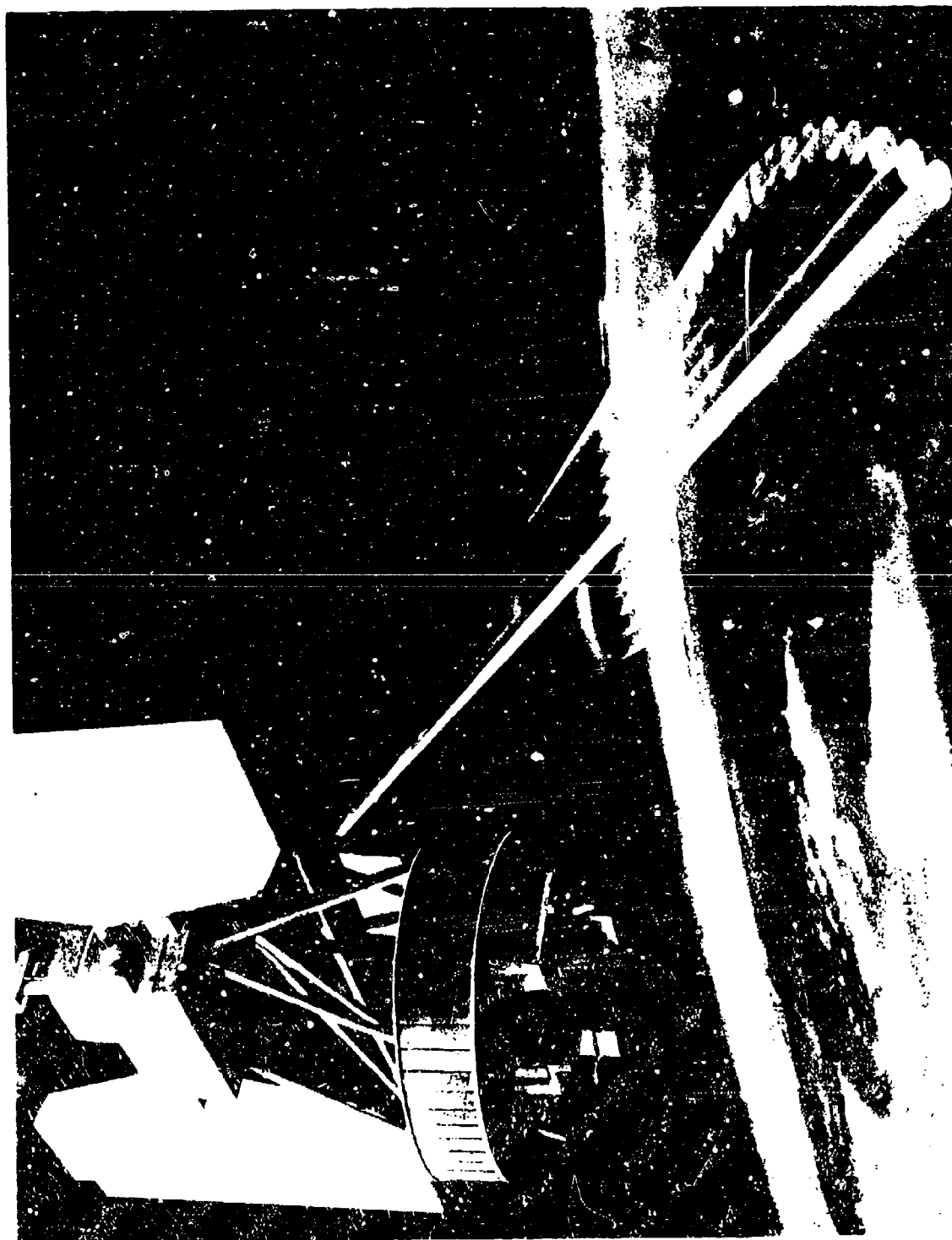Figure 5. Microwave Signatures for Calm Water Surfaces

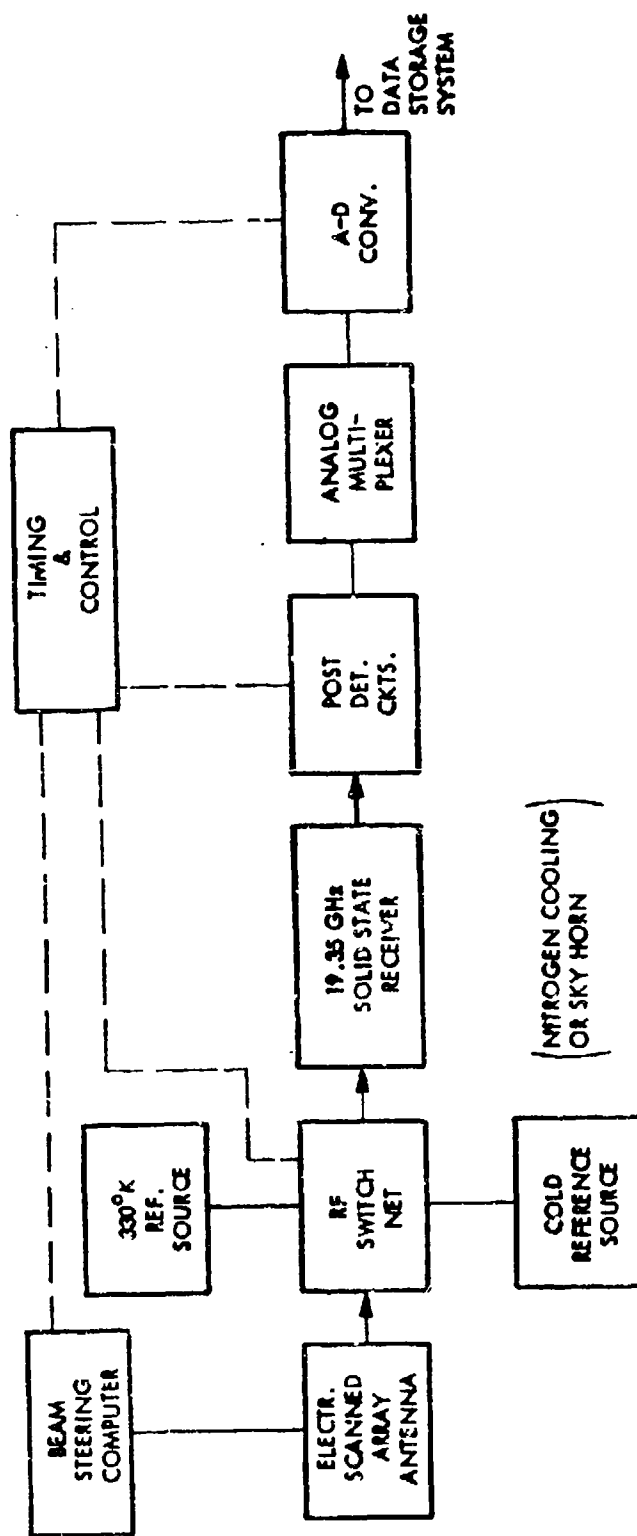Figure 6.   Surface Scanning of 37-GHz Dual Polarized Radiometric Imager

Figure 7. Meteorological Satellite Radiometer General Block Diagram

a principal design objective for the phased array antennas. A transmission loss, L , within the antenna and its connecting line to the receiver further reduces the signal at the receiver input to a level, $T_A = (E_b L^{-1}) T_b$.

The radiometric receiver consists of a low-noise millimeter wave receiver which is preceded at its input by a ferrite switching network. This network is activated by control unit timing signals to switch the receiver input, at a 600-Hz rate, between the antenna and a hot body reference at known temperature, $T_{R1} = 300^0 K$. The resulting input to the receiver thus alternates periodically between levels T_A and T_{R1} . Double sideband type superheterodyne receivers are employed to provide a predetection gain described by a bandwidth B and a noise temperature T_e . Upon square law detection, the periodic waveform is amplified and synchronously demodulated to produce an output voltage, $e_o = G_r(T_{R1} - T_A)$, where G_r is the system radiometric gain.

The reference temperature, T_{R1} , is controlled and monitored with an error of $\pm 0.1^0 K$. Consequently, it is then possible to accurately infer the value of T_A to the extent that G_r is accurately known. Updated values of G_r are accurately derived from a calibration following each scan. During calibration, the input network substitutes a cold reference source at a known temperature, T_{R2} , in place of the scanning antenna.

In the spacecraft imagers, this reference is supplied by a wide beamwidth scalar feed horn antenna directed toward the cold sky. The recorded receiver calibration voltage, $e_{cal} = G_r(T_{R1} \cdot T_{R2})$, permits the antenna temperature, T_A, to be determined by $T_A = T_{R1} - (T_{R1} - T_{R2})(e_o / e_{cal})$. This relationship is used in subsequent ground-based data processing to determine the brightness values of individual surface elements. Because of potential errors introduced by various thermal radiation sources, their temperatures are monitored and periodically recorded for data correction purposes.

The errors introduced by system thermal noise are represented by ΔT_A , an rms value of fluctuations in antenna temperature given by:

$$\Delta T_A = 2(T_e + T_A)(B\tau)^{-1/2}$$

where τ is the time that individual surface elements dwell in the scanning antenna beam. Taking into account the transmission loss associated with the antenna as well as its beam efficiency, the rms error in the measurement of T_b, i. e. $NE\Delta T$, is then given by $NE\Delta T = E^{-1} L(\Delta T_A)$.

The receiver outputs corresponding to the individual surface measurements as well as calibration voltages and "housekeeping" data are individually digitized and interfaced through a parallel-to-serial converter to the spacecraft data recording system.

Nimbus E Radiometric Imager

At an orbital altitude of 592 nautical miles, the 19.35-GHz radiometric imager on Nimbus E has a subsatellite surface resolution of 14.5 nautical miles. A cross track scan of ±50° covers a path width of approximately 1700 miles on the earth's surface. The system performance parameters of the imager together with the specifications of the antenna and receiver subsystems are presented in Table 1.

The basic operating mode discussed above and the block diagram of Figure 7 serve to describe the operation of this instrument. The antenna beam is stepped through 78 steps in a scan period of approximately 4 to 5 seconds. An observation time of 50 milliseconds at each beam position results in a value of $NE\Delta T \approx 1°K$. Absolute temperature calibration errors are less than $2°K$.

The imager employs an electronically scanned traveling wave type planar array shown in Figure 8a. The planar array consists of 103 linear array elements consisting of edge-slotted waveguides which are connected through Reggia Spencer type ferrite phase shifters to the individual slot apertures of a similarly slotted waveguide section. Radiation collected by that section constitutes the antenna output to the radiometric receiver. The number of slots and their tapered coupling to the linear arrays determines the intrack beam characteristics of the antenna. Similarly, the number of linear arrays and their tapered coupling to the collecting section establishes the cross track beam shape.

Inertialess electronic scanning is accomplished by current control of the individual phase shifters located in series with the linear

Table 1

DATA SUMMARY FOR ELECTRONICALLY SCANNED RADIOMETRIC IMAGER ON NIMBUS E SATELLITE LAUNCHED DECEMBER 11, 1972

Imaging Parameters

Orbital Altitude	600 nautical miles
Subsatellite Surface Resolution	14. 5 nautical miles
Surface Swathwidth	1700 nautical miles
NEΔT	1. 5°K

System Parameters

Center Frequency	19. 35 GHz
Dynamic Range	50°K - 330°K
Cross Track Angular Scan	$\pm 50^{\circ}$
Beam Positions	78
Absolute Accuracy	1. 5°K

Antenna Parameters

3-dB Beamwidth	1. 4° x 1. 4° (broadside)
Polarization	Horizontal
Beam Efficiency	>90% (within $\pm 35^{\circ}$ scan angle)

Receiver

Type	Superheterodyne
Center Frequency	19. 35 GHz
IF Frequency	100 MHz
Bandwidth	300 MHz
Double Channel Noise Figure	6 dB

Physical Configuration

Dimensions	37" x 37" x 4"
Weight	68 lb
Deployment	37" x 37" face — nadir pointing
Power Consumption	42 watts at 24. 5 Vdc

a. Front View - Phased Array
   Antenna Surface

b. Rear View - Beam Steering Control
   Network and Electronics Enclosure

Figure 9. Nimbus E 19.35 GHz Radiometric Imager

arrays, which are oriented in the flight direction. A linear distribution of these relative phase shifts focuses the beam in the cross direction at a nadir angle determined by the phase slope. Sets of phase shifter currents are selected to provide phase slopes corresponding to different pointing angles. These are then selected in a programmed sequence to step-scan the sensor in the cross track direction. Errors introduced by these phase shifters are sufficiently low to maintain sidelobe suppression of greater than 23 dB and beam efficiency in excess of 92% for most beam pointing angles. A total transmission loss of less than 2.2 dB results from the waveguide and phase shifter elements of the antenna.

A five-port ferrite switching network used for modulation switching and calibration introduces insertion loss of less than 0.8 dB.

The superheterodyne receiver input consists of a balanced mixer with silicon Schottky barrier diodes driven by a Gunn-type local oscillator. This is followed by a low-noise IF amplifier with a 100-MHz bandwidth centered at 100 MHz.

These radiometric receiver components together with the post-detection, beam steering, and timing electronic circuitry are mounted on the back surface of the phased array antenna as shown in Figure 8b. The result is a very compact package configuration with a thickness of 4 inches.

Nimbus F

The 37-GHz radiometric imager installed on the Nimbus F satellite is oriented to sea ice applications. Its basic design principles are similar to those of the imager operating on the Nimbus E satellite. The fundamental differences in comparison to the imager on the Nimbus E satellite are illustrated by the block diagram of Figure 9 and by the system performance and subsystem specifications listed in Table 2.

In addition to an improved angular resolution as a result of shorter wavelength, significant differences from the Nimbus E imager include: (a) sensing of both polarization components of the observed radiation and (b) conical scanning of the beam pointing angle.
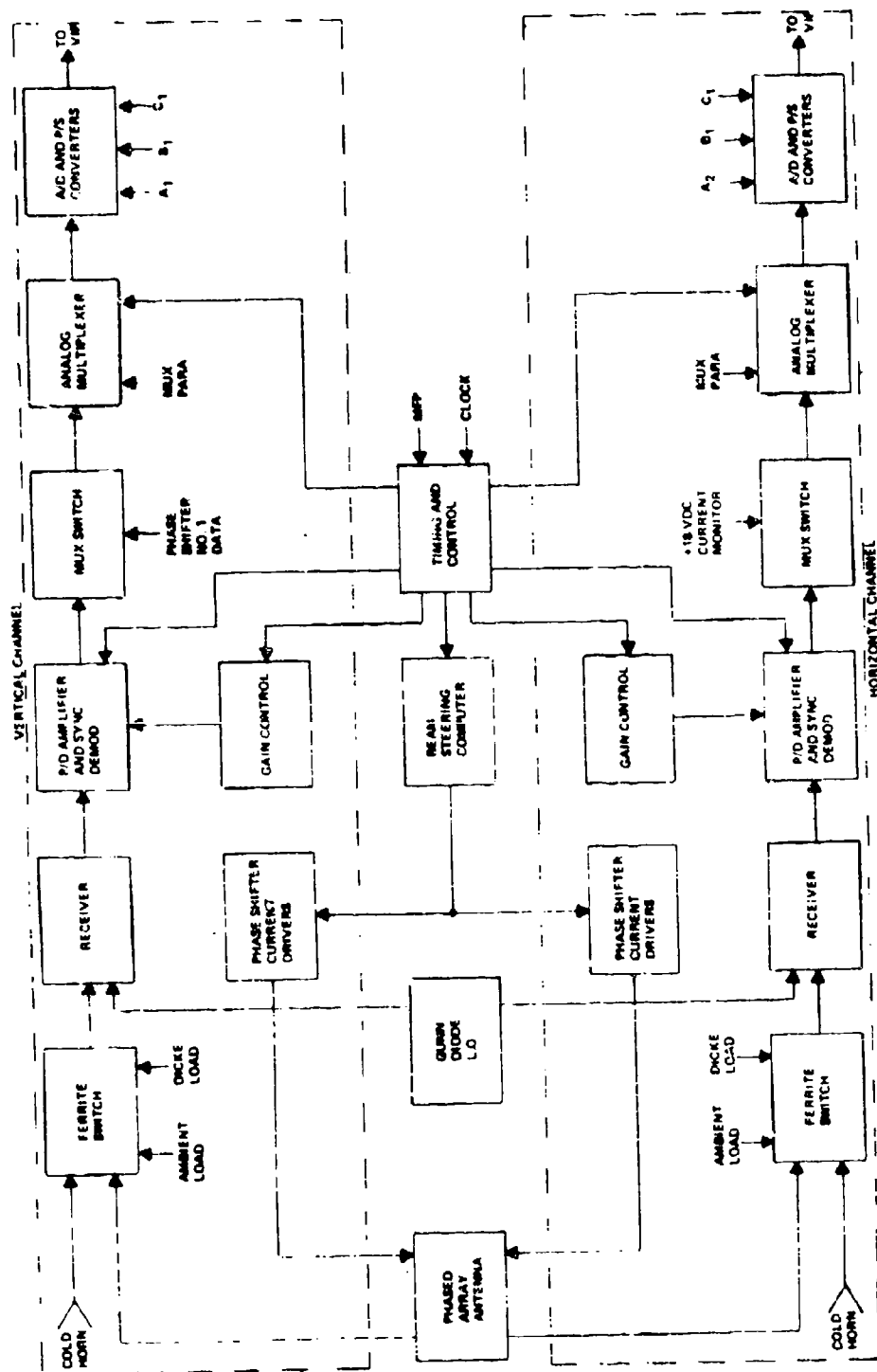
Figure 9. Nimbus F ESMR Block Diagram

Table 2

SPECIFICATIONS FOR 37-GHZ DUAL POLARIZED
IMAGER ON NIMBUS F SATELLITE

System Parameters

Center Frequency	37 GHz
Dynamic Range	50° to 330°K
Conical Scan Arc	$\pm 35^{\circ}$
Beam Positions	71
Absolute Accuracy	2°K

Antenna Parameters

Beamwidth	$1.17^{\circ} \times 0.73^{\circ}$
Beam Efficiency	>90%

Receiver Parameters

IF Band	10 - 110 MHz
Double Channel Noise Figure	6 dB

Physical Configuration

Dimensions	39" x 39" x 4"
Weight	99 lb
Deployment	39" x 39" faces forward
Power Consumption	55 watts at 24.5 volts

Design principles similar to those of the 19.35-GHz imager were employed for the 37-GHz dual polarized array. In addition to higher frequency operation, the primary challenge was the requirement for 0.1° angular coincidence of the orthogonally polarized beams.

Instead of edge-slotted rectangular waveguides, the individual linear arrays employ square waveguides with planar crossed perpendicular slot radiating apertures. The perpendicular slots of the individual apertures are coupled to the two orthogonal transmission modes in the square waveguide. Beam pointing coincidence of the cross polarized beams is

achieved by equalization of the effective interelement phase shifts in the two orthogonal transmission line modes. At the outputs of the 109 individual linear array elements, orthomode transducers separate the two polarization components of the received radiation into two individual rectangular waveguide outputs. These two polarization components are then individually beam-steered by two groups of current controlled phase shifters. The phase shifter outputs of both groups are collected by a separate edge-slotted waveguide array to form the two orthogonal polarization ports of the antenna.

These antenna ports feed two separate 37-GHz radiometric receivers which are designed on the same principles employed in the 19.35 GHz imager. The configuration of the assembled instrument is seen in the photographs of Figures 10a and 10b which respectively show the planar antenna surface and the electronics equipment mounted on the back surface of the antenna. The flight model has been successfully tested and installed on the Nimbus F spacecraft.

FUTURE APPLICATIONS AND TECHNOLOGY

Current applications of millimeter wave radiometric sensors on meteorological satellites have demonstrated the ability to close information gaps resulting from the inherent limitations of sensors at visual and infrared wavelengths.

Future applications of millimeter wave passive sensing from satellites appear oriented toward significantly improved spatial resolution and toward achieving an improved interpretation of surface phenomena by simultaneous sensing at several widely separated frequencies. Large platforms, e.g. Shuttle, accommodating antenna dimensions of several meters, would permit 30 to 40 GHz sensors to achieve surface resolutions of less than one nautical mile. However, in addition to spatial resolution, useful applications of imaging also imply some minimum requirements for scanned field of view and system sensitivity. Consideration of these requirements identifies the need for higher rates of antenna scanning and receiver noise reduction that are associated with progressively improved
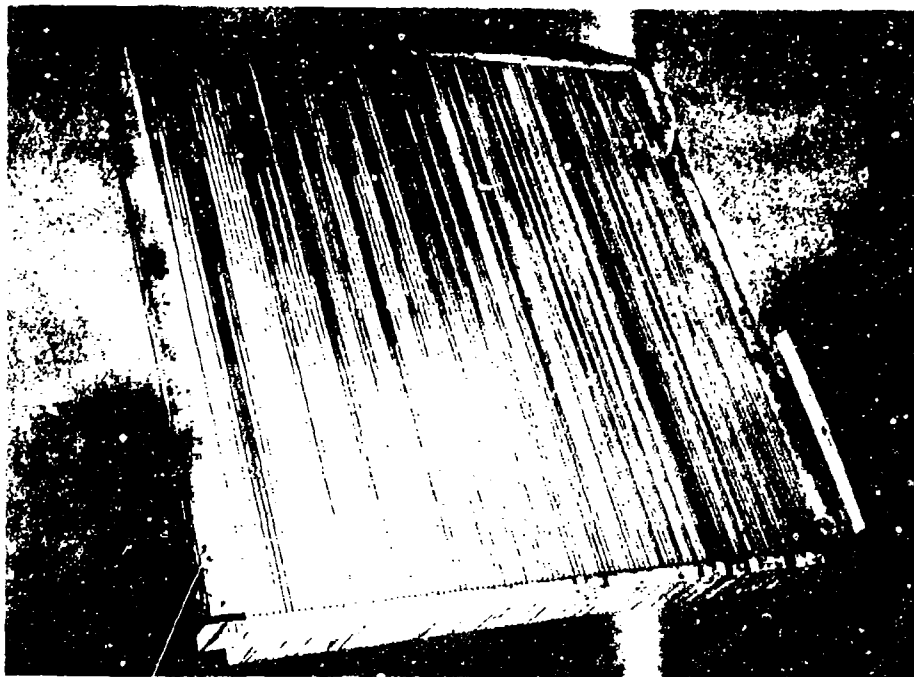
a. Front View of Antenna Array
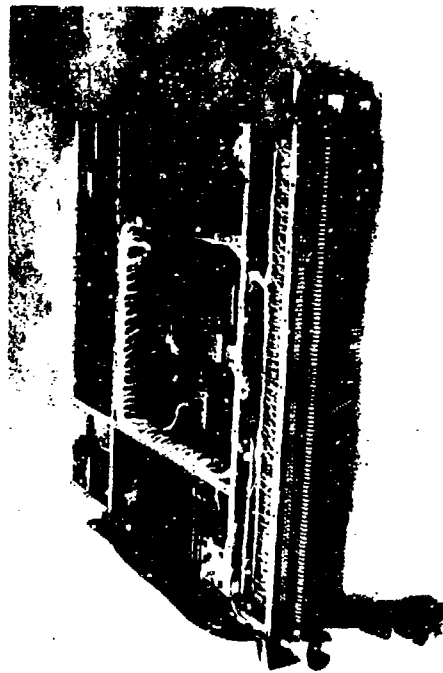
b. Rear View: Radiometer and Beam Steering Electronics

Figure 10. 37 GHz Dual Polarized Radiometric Imager

spatial resolution. Current system noise levels are within a factor of four from the minimum noise background established by earth surface radiation. Consequently, present single beam/receiver scanning type sensors are limited in principle to a factor of four improvement in spatial resolution. For greater values of resolution improvement, these sensors will experience a directly equivalent reduction in measurement sensitivity.

More immediate restrictions on high resolution imaging are imposed by antenna scanning technology. For any significant field of view, mechanical scanning of high resolution sensors does not appear compatible with spacecraft attitude stabilization requirements. For present electronically scanned antennas, switching time limitations in the ferrite phase shifters must be reduced to permit significantly greater scan rates. This however will most likely be achieved at the cost of higher power consumption which is bounded by spacecraft power allotted to individual sensors.

Analysis of phased array antennas used in current spaceborne millimeter wave imagers indicates that mechanical tolerances and loss considerations limit their achievable resolution improvement to a factor of four.

Thus, for those applications requiring large improvements in spatial resolution without sacrifice of system sensitivity, it will be necessary to develop new systems concepts. Such concepts will most probably resort to multiple beam antennas and multiple receivers to simultaneously sense numerous surface resolution elements.

A variety of ground-based multibeam passive sensor concepts have been implemented by radio astronomers for celestial mapping. Some of these concepts employ IF beam-forming techniques and may prove adaptable to satellite-based sensing. However, practical implementation will require dedicated developments in the areas of array antenna, integrated circuit low-noise receivers, and IF beam-forming techniques. In this respect, millimeter wave passive sensing may follow the same path experienced in the evolution of thermal infrared sensors from single detector scanners to sophisticated multidetector arrays.

ACKNOWLEDGMENT

REFERENCES

1. "The Applications of Passive Microwave Technology to Satellite Meteorology," Symposium, August 1962, Rand Corporation Memorandum RM-30401-NASA.

2. Beuttner, J. K., "Rain Mapping from Weather Satellites with the Help of Centimeter Waves," Naturwissenshaftan, 50, pp 591-592, 1963.

3. Falco, C. U. and G. Oister, "Microwave Radiometer Design and Development," Aerojet-General Corporation Final Report on Contract NAS5-59680, November 1967.

4. Nordberg, W., et al, "Preliminary Results from Aircraft Flight Tests of an Electronically Scanning Microwave Radiometer," NASA Goddard Space Flight Center Report X-622-57-352, 1967.

5. Staelin, E., et al, "Microwave Spectrometer on the Nimbus 5 Satellite: Meteorological and Geophysical Data," Science, 28 December 1973, pp 1339-1341.

6. Nordberg, W., J. Conaway, D. Ross and T. Wilheit, Journal of Atmospheric Science 28, 429-435, 1971.

7. Wilheit, T. and W. Nordberg, et al, "Aircraft Measurements of Microwave Emission from Arctic Sea Ice," Remote Sensing of the Environment 2, 129-139, 1972.

8. Gloersen, P., W. Nordberg, T. Schmugge and T. Wilheit, "Microwave Signatures of First Year and Multi-Year Ice," Journal of Geophysical Research, Vol. 78, No. 18, 3554-3572, 1973.

9. Poe, G., A. Stogryn, A. Edgerton, "A Study of the Microwave Emission Characteristics of Sea Ice," Final Technical Report No. 1749R-2 (DOC Contract No. 2-35340), September 1972.

10. Meeks, D., G. Poe, R. Ramseier, "A Study of Microwave Emission Properties of Sea Ice," AIDJEX 1972, First Interim Report, Report 1786R-1, August 1973.

11. Meeks, D., G. Poe, R. Ramseier, "A Study of Microwave Emission Properties of Sea Ice," AIDJEX 1972, Second Interim Report, Report 1786R-2, December 1973.

12. Stogryn, A. and G. Poe, "A Study of Microwave Emission Properties of Sea Ice," Final Report (in preparation), DOC Contract No. 2-35340, February 1974.
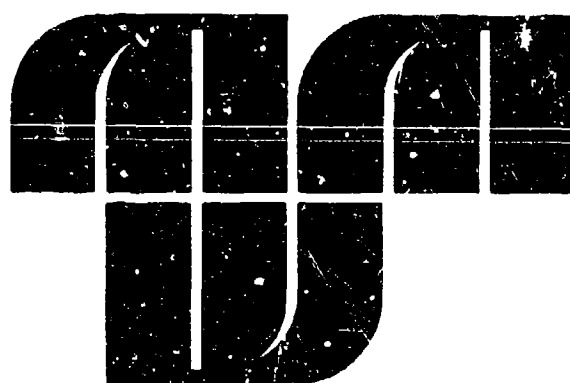
Supplementary
Papers

ACTIVE MILLIMETER-WAVE INTEGRATED CIRCUITS*

H.J. Kuno and Y. Chang

Hughes Aircraft Company
Torrance, California 90509

H. Jacobs and M.M. Chrepta

U.S. Army Electronics Command
Fort Monmouth, New Jersey 07703

ABSTRACT

This paper describes a new class of active millimeter-wave
integrated circuits of high resistivity silicon image line
dielectric waveguide configuration. Integrated FM oscillators,
PIN diode modulators, detectors, and an oscillator-modulator-
detector module have been developed.

ACTIVE MILLIMETER-WAVE INTEGRATED CIRCUITS*

H.J. Kuno and Y. Chang

Hughes Aircraft Company
Torrance, California 90509

H. Jacobs and M.M. Chrepta

U.S. Army Electronics Command
Fort Monmouth, New Jersey 07703

SUMMARY

Solid state millimeter-wave devices have developed rapidly into components for practical systems in recent years. However the cost of waveguide circuit components is relatively high. This is partly due to the close tolerances required at millimeter-wave lengths. The low cost microwave integrated circuit (MIC) utilizing stripline or microstripline configurations at lower microwave frequencies is not directly applicable at millimeter-wa e range because of practical limitations such as excessive losses and geometric limitations at high frequencies. It has been shown that rectangular dielectric waveguide can be used for effective low loss millimter-wave transmission.[1-4] Chrepta and Jacobs[5-7] have recently demonstrated that, by using high resistivity semiconductors

such as silicon as dielectric waveguides, active devices
may be integrated into the dielectric guide. In this
paper, we report the successful integration of millimeter-
wave devices into silicon dielectric guide circuits at
V-band (50-75 GHz) which demonstrates the feasibility of
a new class of low loss and low cost active millimeter-
wave integrated circuits capable of performance comparable
to those of the conventional waveguide circuits.

Shown in Figure 1 is a cross-sectional view of a
dielectric waveguide integrated FM oscillator. The wave-
guide was made of high resistivity (7900 ohm-cm) silicon
of 0.100" in width and 0.022" in height placed on a gold
plated metal image plane. The image plane was also
used as the oscillator heat sink, electrical ground, and
mechanical support. The above guide dimensions were
chosen to allow low loss propagation of the dominant
E_{11}^{Y} mode in the V-band (50-75 GHz) range. A packaged
IMPATT diode with extremely low parasitics (package capa-
citance $\approx$ 0.1 pF and inductance $\approx$ 0.04 nh) was placed in
a hole in the silicon dielectric guide and mounted on
the image plane as shown in Figure 1. The diode was
located about 2.5 wavelength from one end of the dielectric
guide. The other end of the dielectric was tapered to

an angle of about 30° and inserted into a regular WR-15
metal waveguide. The angle was chosen to ensure smooth
dielectric to metal guide transition. Maximum CW output
power of 50 mW was obtained at 58.3 GHz when the diode
was biased at 180 mA. The oscillator frequency was
continuously tunable by varying the bias current over a
bandwidth of 6 GHz. Shown in Figure 2 is the tuning
characteristics of the integrated oscillator. The output
power variation was less than 1 dB from 55.7-58.7 GHz.

Figure 3 shows an integrated PIN diode amplitude
modulator. The circuit configuration was similar to that
of the integrated oscillator. Maximum on-off ratio of
10 dB was measured between 6 mA forward bias and 5 volts
reverse bias.

Figure 4 shows an integrated detector. An Au-Ni
whisker was used to contact the detector diode (junction
diameter ~ 5 µm). The detector sensitivity was about
30 mV/mW.

We have also constructed an oscillator-modulator-
detector module and have demonstrated the feasibility of
multi-functional millimeter-wave integrated circuits.

ACKNOWLEDGEMENT

REFERENCES

1. R.M. Knox and P.P. Toulios, "Integrated Circuits
    for the Millimeter-through Optical Frequency Range,"
    Proceedings of the Symposium on Submillimeter-waves,
    Polytechnic Press of the Polytechnic Institute.

2. S.E. Miller, "Integrated Optics,An Introduction,"
    Bell System Technical Journal, Vol 48, pp. 2-59-2069,
    Sept. 1969.

3. E.A.J. Maratili, "Dielectric Rectangular Waveguide
    and Directional Coupler for Integrated Optics"

4. S.P. Schlesinger and D.D. King "Dielectric Image Lines,"
    IRE Trans on Microwave Theory and Techniques, Vol.
    MTT-6, pp. 291-299, July 1958.

5. M.M. Chrepta and J. Jacobs, "Bulk Semiconductor Quasi-Op
    Optical Concept for Guided Waves for Advanced Milli-
    meter-wave Devices," USALCOM Tr No. 3482, Sept. 1971

6. M.M. Chrepta and H. Jacobs, "A Bulk Semiconductor
    Millimeter wave Phase Shifter," USAECOM Tr No. 3513,
    November 1971.

7. H. Jacobs and M.M. Chrepta, "Semiconductor Dielectric
    Waveguides for Millimeter-wave Functional Circuits,"
    1973 IEEE G-MTT International Microwave Symposium,
    pp. 28-29, University of Colorado 4-6 June 1973.

BIAS FILTER
DISC RESONATOR
TO POWER SUPPLY
WR-15 GUIDE
TIP ANGLE 30°
SILICON DIELECTRIC WAVE GUIDE
DISC RESONATOR
HEAT SINK & IMAGE PLANE
PACKAGED IMPATT DIODE
HEAT SINK

DETAILED VIEW OF DIODE MOUNTING
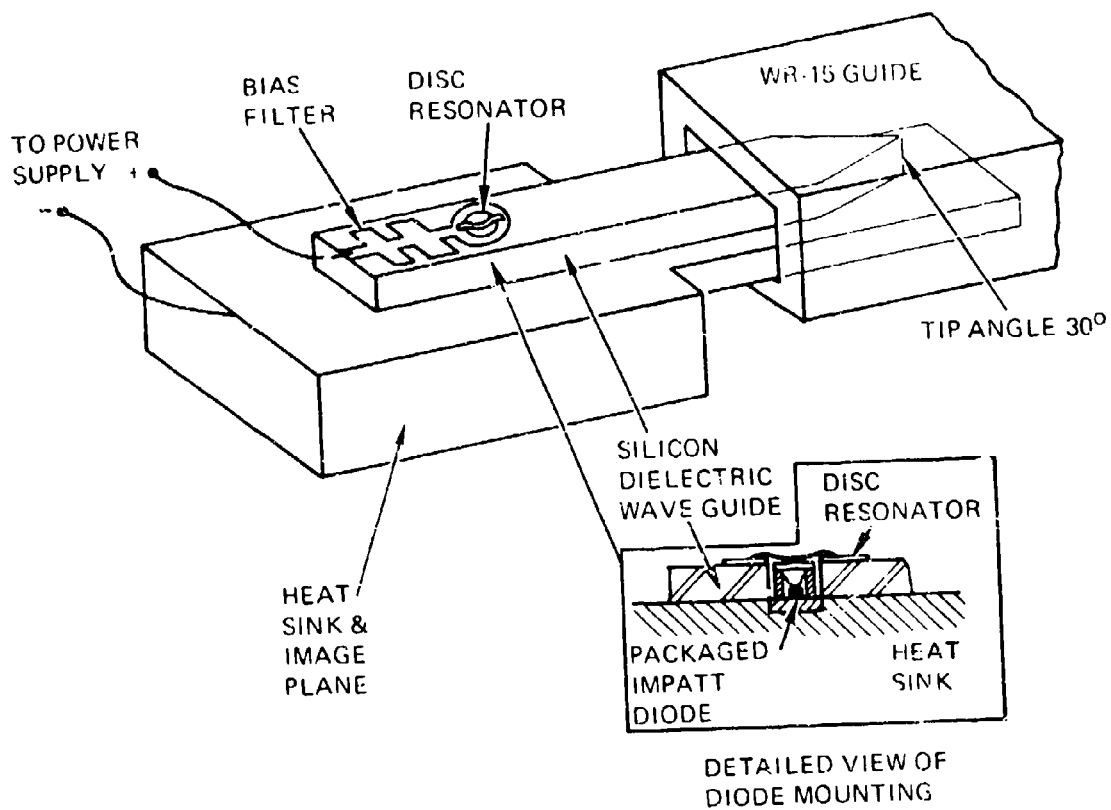
Fig. 1   Integrated millimeter-wave IMPATT oscillator.
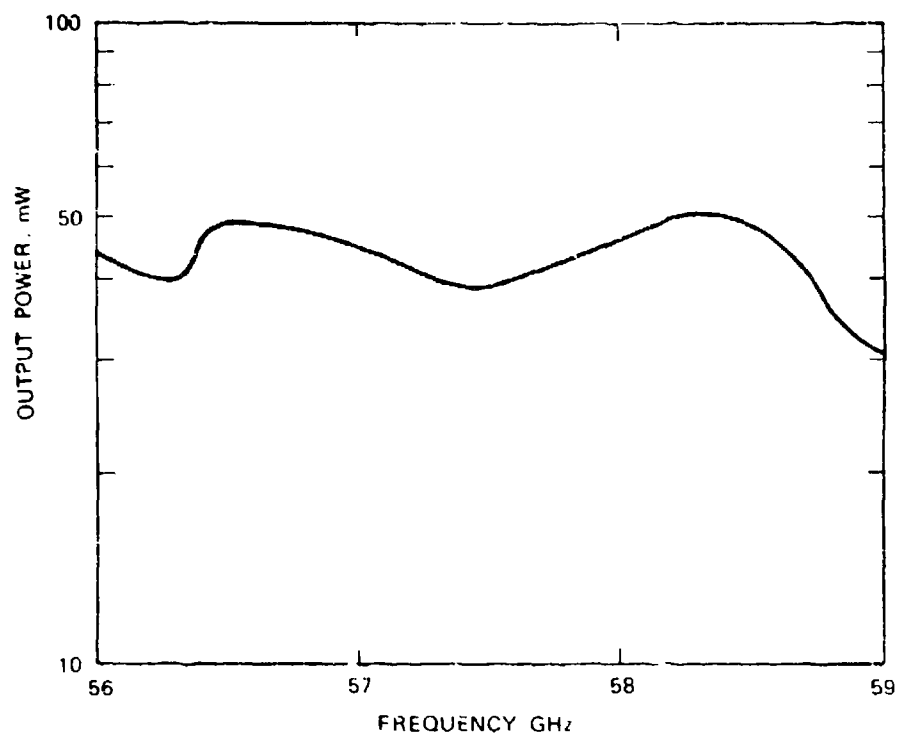
Fig. 2   Frequency tuning characteristics
         of a dielectric waveguide IMPATT
         oscillator.

SILICON
DIELECTRIC
WAVE GUIDE

TO DIODE
BIAS

METALLIZED
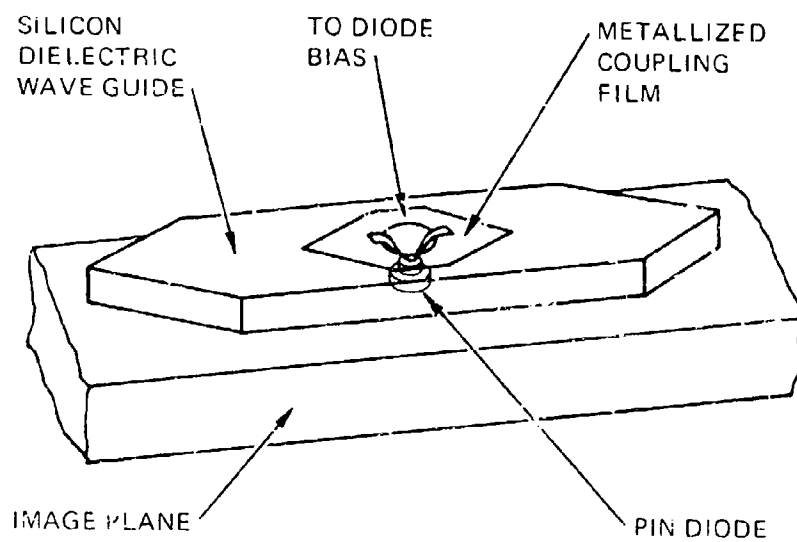COUPLING
FILM

IMAGE PLANE

PIN DIODE

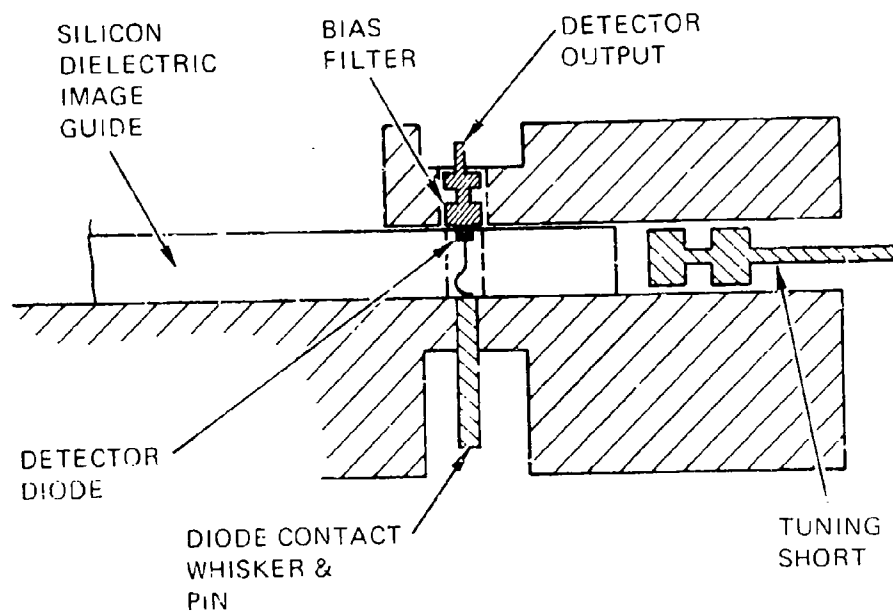Fig. 3   Integrated millimeter-wave
         PIN diode AM modulator.

Fig. 4   Integrated millimeter-
wave detector.

MINIATURE PEDESTAL
AND MILLIMETER WAVE ANTENNA

by Douglas G. Worth
Radiation, A Division of Harris-Intertype Corporation

ABSTRACT

This paper will discuss the mechanical design of a miniature antenna pedestal designed and built by Radiation in 1973 for the Department of the Navy. This unit is designed for use atop a Navy submarine periscope, hence it is imperative that it be of minimum size and weight. These and other design parameters will be discussed in this paper and the design effected as a result will be explained in a technical manner. The design of the pedestal is dictated primarily by the limited space available. Unlike most antenna structures which are designed from the "ground-up," this limited space dictated that the pedestal be designed from the "outside-in." Another complexity of the design is the requirement to have several pieces of electronics mounted directly to, and moving with, the horn in order to reduce RF losses. Photographs of the pedestal are shown in Figures 1 and 2.

FIGURE 1. PHOTO OF PEDESTAL,
FRONT QUARTER VIEW

FIGURE 2. PHOTO OF PEDESTAL,
REAR QUARTER VIEW

DESIGN PARAMETERS

For the particular application atop a submarine periscope, several design parameters were imposed upon the antenna.

1. The antenna pedestal assembly must fit and operate inside a radome specially designed to adapt to the periscope head and to withstand water pressures and temperature changes at great depths. Figure 3 shows the details of this radome.

2. The antenna pedestal must be of the two-axes type to obtain necessary sky coverage. The submarine periscope shall serve as a quasi-third axis which can be positioned in the general direction of the satellite.

3. The sky coverage must be such that the antenna will point to any point in space which lies between the true local elevation angles of 0° to 90° inclusive and shall maintain this coverage under all combinations of submarine motions within the accuracy stated in design parameter 4. The ship's roll is $\pm20^{o}$ maximum and pitch is $\pm10^{o}$ maximum. The azimuth axis travel should be no less than $\pm70^{o}$.

4. The pedestal shall have a pointing error of no greater than 0.5^{o}. Of this the static pointing accuracy must be no greater than 0.3^{o}, leaving 0.2^{o} for dynamic error.

5. The horn used with the pedestal must be a minimum of four inches in diameter.

RADOME

The size of the radome for this unit was based on studies conducted at the Naval Underwater Sound Lab. Two criteria establish the size of the radome. It must have a small radar cross section, and it must fit behind a cowling of limited height when the ship is underway.

Its shape is determined by strength requirements, and the bullet shape is the strongest shape practical for use where large uniform pressures exist over the entire exterior surface. This radome (shown in Figure 3) is made of a high-strength, low RF loss, fiberglass laminate.

CONFIGURATION OF PEDESTAL

Having a two-axes pedestal in mind, the most obvious possibility to explore is the elevation over azimuth configuration. The elevation over azimuth pedestal has a sometimes serious disadvantage of requiring high azimuth tracking rates near zenith attitudes. This disadvantage can be effectively eliminated by canting the azimuth axis at an angle from vertical. The periscope may then be positioned in azimuth, such that the area of antenna coverage requiring maximum azimuth tracking rates is shifted out of the satellite's path.

If the pedestal were to be mounted on a stationary base, cant angle would be chosen based on the highest tracking rates possible, as well as the intended sky coverage. If the cant angle is too large, tracking rates are excessive when the target is near horizon. If the cant angle is too small, rates are excessive when the target is near zenith.

Since this pedestal is to be mounted on a submarine which rolls and pitches, the angle at which to cant the azimuth axis is based primarily on the ship's motions as specified in the design parameters. The azimuth cant angle should be large enough such that it will still be positive during even the worst-case combination of ship's roll and pitch. This worst-case combination of ship's motion is $\pm 22.4^O$, therefore, the cant angle was chosen at 25°. This means that the azimuth axis will always make at least a 2.6^O angle with vertical, and most of the time it will make very near a 25° angle. This configuration satisfies design parameters 2 and 3.

Pedestal-to-periscope adapter housing

This item has a cylindrical overall shape. It is machined on top to accommodate the radome and its seal, and on the bottom to fit the threaded connection on the periscope head. Inside are mounts for several pieces of electronics and a waveguide mode transition. It is important that the heat generated in the electronics on and near the pedestal be removed, and hence the adapter housing is made of forged bronze. Near the top are four mounting bosses machined for attaching the azimuth mounting plate. Figures 1 and 2 show this piece as the large bronze housing on which the pedestal is attached.

Azimuth mounting plate

This piece is bolted directly to the four bosses machined in the adapter housing. The main function of this plate is to form a base for mounting the azimuth yoke trunion bearings and the azimuth drive box. The azimuth mounting plate is placed at a 25° angle to horizontal, and the yoke turns about an axis which is perpendicular to this plate. Other equipment attached to the azimuth mounting plate is the azimuth synchro and the azimuth bumper stops. This plate is shown in the upper right-hand corner of Figure 4. The shape and size of this plate is determined by the space within the area it fits. Due to the 25° slant at which it is mounted, the azimuth mounting plate's lower end lies in the pedestal-to-periscope adapter housing and its upper end lies in the radome. All gears used in the pedestal are stainless steel. All drive gears are made of type 17-4 PH stainless because of the high strength of this alloy. To eliminate differential thermal expansion between the azimuth drive gear and the mating gear, as well as for the stiffness, the material used for this plate is type 303 stainless steel.

Azimuth drive box

The three-stage azimuth gearbox has an overall gear ratio of 112:1. Refer to Figure 5. The gearbox consists of a housing and cover enclosing the drive motor and the first-stage pinion/gear pair. Outside the gearbox is another pinion and gear stage. The gear of this stage is an idler which meshes with the azimuth drive gear. The drive motor is a dc torque type with a peak stall torque rated at 9-inch ounce. Its dimensions are 1.5 inches OD and 0.375 inch wide. It was first considered to use a dc torque motor directly coupled to the 1:1 axes in azimuth and elevation. However, the physical size of a motor producing full drive torque prohibited this

approach. Also, use of a gear reduction allows the motor to operate at higher speed. This results in a higher operating voltage level due to the larger back EMF. Operating with this higher back EMF is beneficial because at these higher values, it can better be utilized to close a velocity loop in the servo system.

The azimuth drive gears are made from type 17-4 PH stainless steel. All gears are within the AGMA quality number range of 12 to 14 with backlash designation D. Azimuth drive gears inside the gearbox have a diametral pitch of 96, while those outside are 80 pitch. Backlash at the 1:1 azimuth axis is approximately one-tenth degree. The azimuth synchro is run directly off the 1:1 azimuth drive gear via a type 303 stainless antibacklash gear. Since the gears are stainless, the gearbox is made of type 303 stainless steel. This compensates for thermal expansion, while at the same time providing additional stiffness.

All bearings in the azimuth gearbox are preloaded by the same method, use of wave spring washers on the outer race of one of the two bearings on a shaft. Ball bearings are used exclusively throughout the antenna. Due to the clean environment inherent with the use of a sealed radome, no contacting seals are used on any bearings. Since there are only two gear shafts in the pedestal which are nearly vertical, there are only two places in the pedestal where dirt could fall directly into a bearing. Two bearings in the cover of the azimuth gearbox are shielded for this reason (see Figure 5). The decision not to use contacting seals on any bearings throughout the pedestal was made for two reasons. The friction in the pedestal is a major contributor to the torque budgets in both axes, even without sealed bearings. Also, there are places in the gearboxes where the extra width of a sealed bearing makes the bearing too bulky for the space available.

Yoke

The shape and size of the radome interior is a large factor in determining yoke design. The fact that the yoke turns about an axis that does not coincide with the vertical center line of the radome fixes the envelope volume in which the yoke must fit. This envelope turns out to be ice cream cone-shaped. That is, the yoke must be cut from a piece of metal that has the geometry of a sphere resting in the large end of a cone. The angle of this cone is $50°$ (2 times $25°$) and it intersects the sphere tangentially. Refer to Figure 6 for the yoke configuration. Since the yoke houses part of the elevation gear train, it is made of type 303 stainless steel, thus eliminating differential thermal expansion while providing stiffness and strength.

At the lower end of the yoke is the azimuth trunion which fits into bearings in the azimuth mounting plate. A machined area inside this trunion accommodates the azimuth rotary joint. Immediately above the trunion, the azimuth drive gear is attached to the yoke. The yoke arms are formed just above the drive gear. The starboard yoke arm is devoted entirely to housing the elevation drive box, while the port yoke arm houses the elevation rotary joint, the port elevation trunion and bearing, elevation zero pinhole, and elevation bumper stops. A slot is machined along the center of the port yoke arm to accept the waveguide run between the azimuth and elevation rotary joints.

Elevation drive box

The volume available for the elevation drive train is considerably less than that available for azimuth. As a result, the elevation motor and gear train are an integral part of the yoke assembly, as can be seen in Figures 6 and 7. The elevation drive motor is the same as that described for the azimuth drive box. The motor and first pinion/gear pair are located in the type 303 stainless steel elevation gearbox cover. The elevation axis main drive gear and the starboard elevation trunion bearing are housed by the yoke itself. The overall gear ratio of the two-stage elevation drive train is 75.111:1.

The elevation synchro is driven by a segmented gear which is pressed into the starboard yoke arm. The synchro shaft is attached to a type 303 stainless antibacklash gear which meshes with the segmented gear. The gears are of the same material and AGMA quality as the azimuth drive gears. The diametral pitch is 96. Backlash in the elevation gearbox measured at the 1:1 axis is also approximately one-tenth degree. As in the azimuth gearbox, bearings are all radial ball-type with no seals, and in this case, no shields since there are no bearings exposed to an opening in the gearbox. The elevation drive unit is completely enclosed, encasing motor, all bearings and gears; and the starboard elevation trunion as shown in Figure 6. Preloading is obtained as in azimuth by the use of a wave spring washer arrangement on each shaft in the gearbox.

HORN

The horn has the shape of a right truncated cone. The lens has a parabolic curvature, the curved portion is on the inside, while the outside surface is flat with concentric grooves. The included angle of the core is 60^0 and the inside diameter of the large end is four inches. The horn is made from type 6061 T-6 aluminum, and the lens is a dielectric of low RF attenuation.

Several shaped mounting surfaces are machined into the exterior of the horn body. These mounts are designed to accommodate several pieces of electronic equipment. Three units are attached directly to the horn to reduce RF losses, the low noise amplifier, IF amplifier, and third-stage local oscillator. Other units attached to the horn exterior are the accelerometer and the elevation synchro mount. The accelerometer furnishes an input to the positioning electronics (servo system) to account for ship's motion, periscope rotation, etc.

POINTING AND TRACKING CHARACTERISTICS

Sky coverage

For the pedestal to be capable of pointing between 0^0 and 90^0 local elevation angles, the elevation axis travel must be greater than 90^0 by twice the angle of the worst-case combination of ship's roll and pitch. This worst-case combination angle is 22.4^0, hence the angle which the elevation axis must subtend is 134.8^0. With the periscope perfectly vertical, then the pedestal will point 22.4^0 below horizon and 22.4^0 beyond zenith. During even the most violent pitching and rolling of the submarine, the true local elevation look angle will be at least 0^0 to 90^0.

The azimuth axis travel is $\pm 70^O$. Due to the 25° azimuth cant angle, this results in a true local azimuth angle subtending $\pm 71..^O$

Adjustable alignment pin receptacles are supplied for zeroing both the azimuth and elevation axes. There are two receptacles in elevation: one for zeroing at 0° elevation and one for 25°. Only one alignment pin receptacle is provided in azimuth; this is for zeroing at 0°.

Pointing error

The pointing error of the pedestal is specified to be less than 0.5^O with less than 0.3^O of this as the static pointing error, and less than 0.2^O as the specified dynamic error. By using high-quality drive gears to achieve low transmission error and backlash, a high gear train accuracy is achieved. By using close tolerances on machining the yoke, the orthogonality and verticality errors are controlled within acceptable limits. Radial play in both the azimuth and elevation trunion bearings are removed by use of angular contact bearings and positive preloading. This is done in the azimuth trunion by use of a retainer ring which screws onto the lower end of the threaded trunion and bears upon the inner race of the lower bearing (see Figure 4). The elevation trunion bearing preload is attained by adjusting shim thicknesses which also adjust the length of the elevation axis. Unlike gear shafts inside the two gearboxes, these azimuth and elevation trunion bearings carry a large enough load that wave spring washers would not be effective in removing radial play, especially under dynamic conditions. All these mechanical features of the antenna pedestal contribute to a low pointing error. The servo system accuracy is also a great contributor to the pointing accuracy. For this reason, the azimuth and elevation synchros (size 8) are purchased with a specified accuracy of 0.05^O. These synchros, or angular position resolvers, furnish the servo system electronics with data signals indicating the antenna's pointing angles in azimuth and elevation. The synchro-to-digital converter transforms the output of these synchros into a 14-bit digital position word for use by the computer.

Tracking rates

The maximum tracking velocity in elevation is 30°/second and 40°/second in azimuth. Maximum tracking accelerations are 40°/second^2 in elevation and 60°/second^2 in azimuth. These rates are based on data obtained from computer-generated velocity and acceleration plots which were made for an elevation over azimuth positioner with the azimuth canted at 25° from vertical. However, the motors have ample power, and the pedestal inertia is low enough that much higher tracking rates could be achieved if necessary.
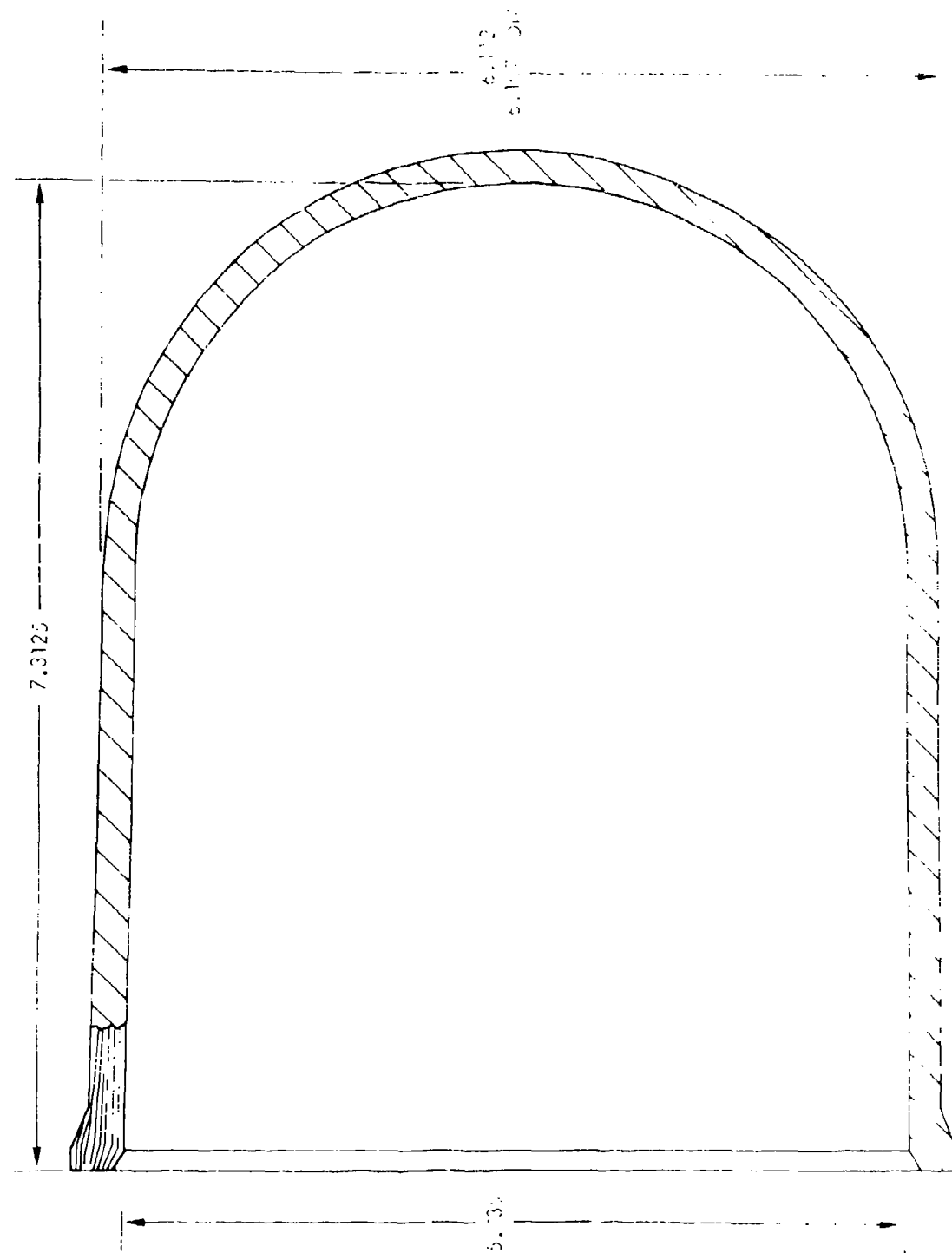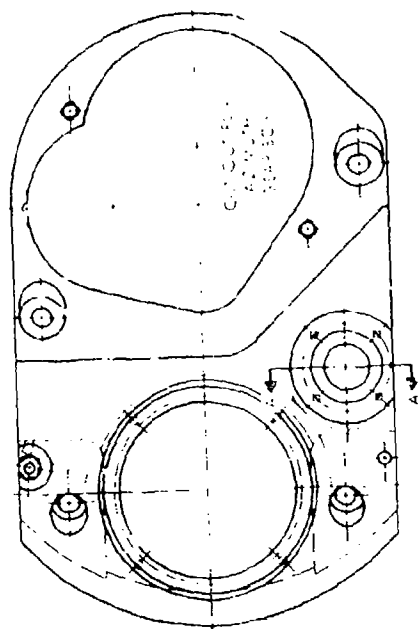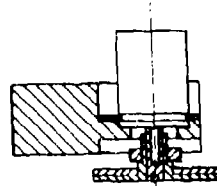
FIGURE 3. RADOME

SECTION A-A
SYNCHRO AZIMUTH
SYNCHRO AND GEAR

AZIMUTH MOUNTING PLATE

RADOME

YOKE

AZIMUTH
ALIGNMENT
PIN

RADOME HOLD
DOWN RING

PEDESTAL-TO-PERISCOPE
ADAPTER HOUSING

AZIMUTH
GEAR BOX

MOUNTING
BOSSES

AZIMUTH
MOUNTING
PLATE
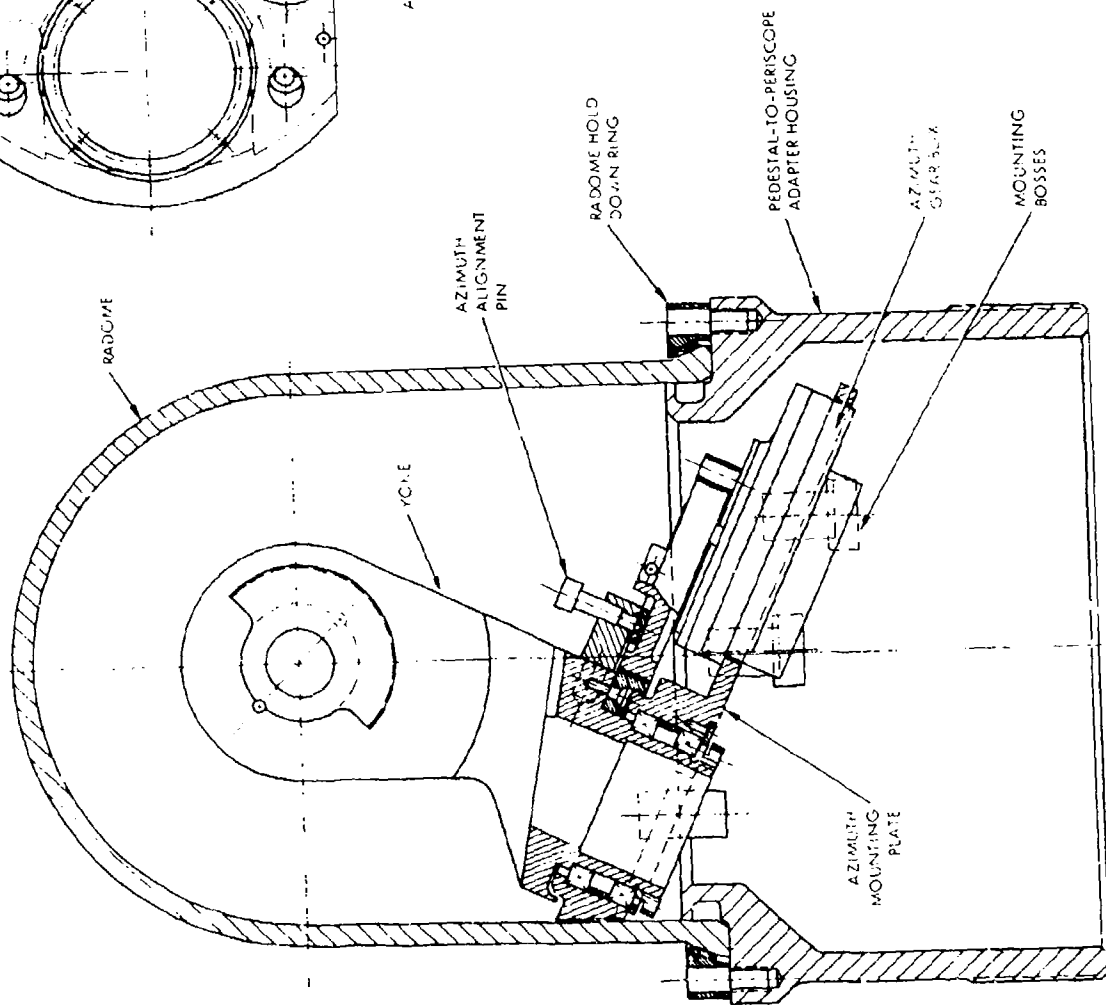
FIGURE 4. AZIMUTH CONFIGURATION

S2-8

WAVE SPRING WASHER

PRECISION WASHER

WAVE SPRING WASHER

WAVE SPRING WASHER

87902-3

SECTION A-A

SECTION B-B

PRECISION WASHER

MOTOR

PRECISION WASHER

RECESS FOR MOTOR

A

A

B

B

FIGURE 5. AZIMUTH GEARBOX CONFIGURATION

ELEVATION ROTARY JOINT

WAVEGUIDE

SIDE VIEW OF YOKE ONLY

87902-4

FULL SECTION THROUGH ANTENNA

YOKE

AZIMUTH ROTARY JOINT

AZIMUTH MOUNTING PLATE

FIGURE 6. YOKE CONFIGURATION

STARBOARD
ELEVATION
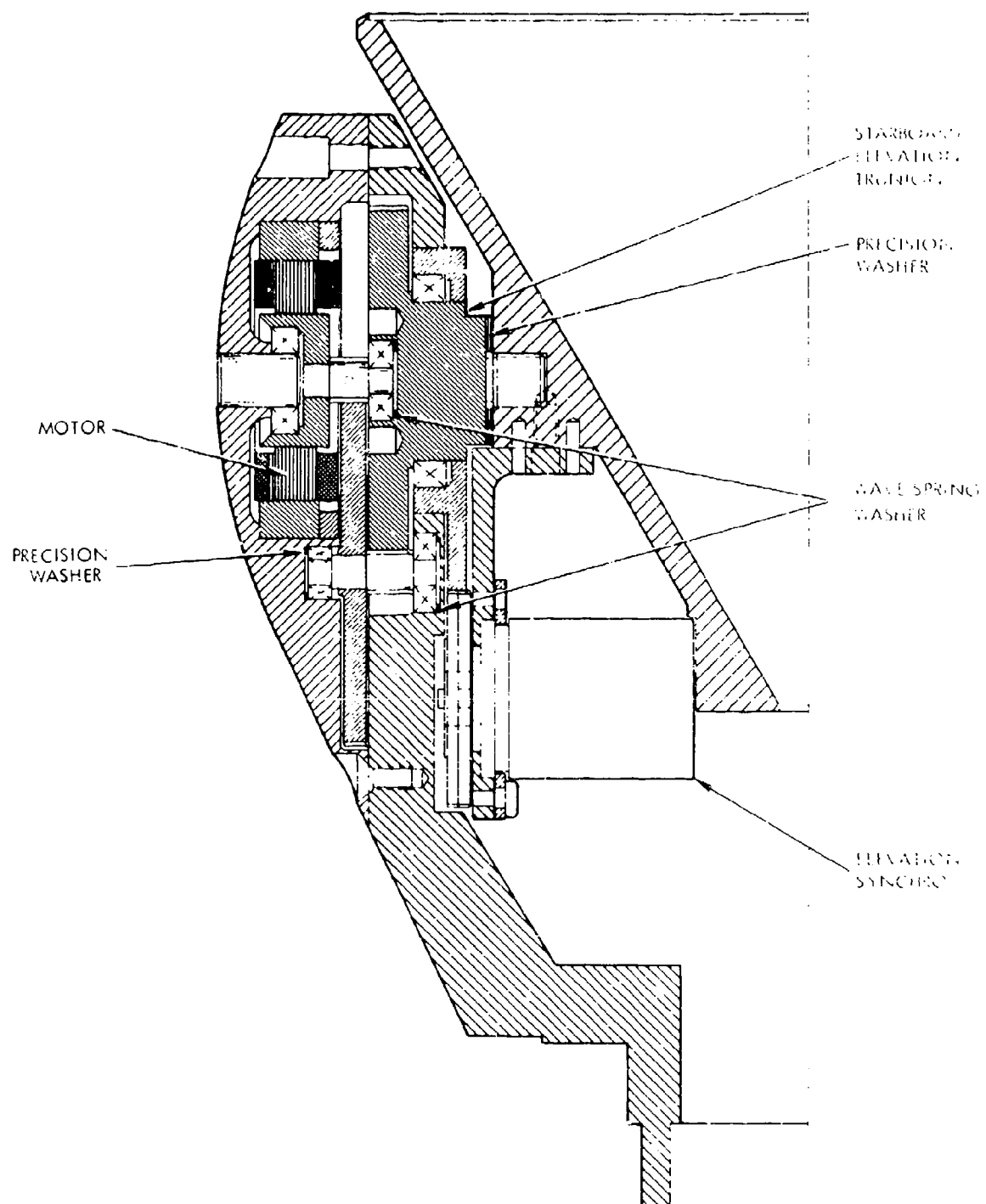TRUNNION

PRECISION
WASHER

MOTOR

PRECISION
WASHER

WAVE SPRING
WASHER
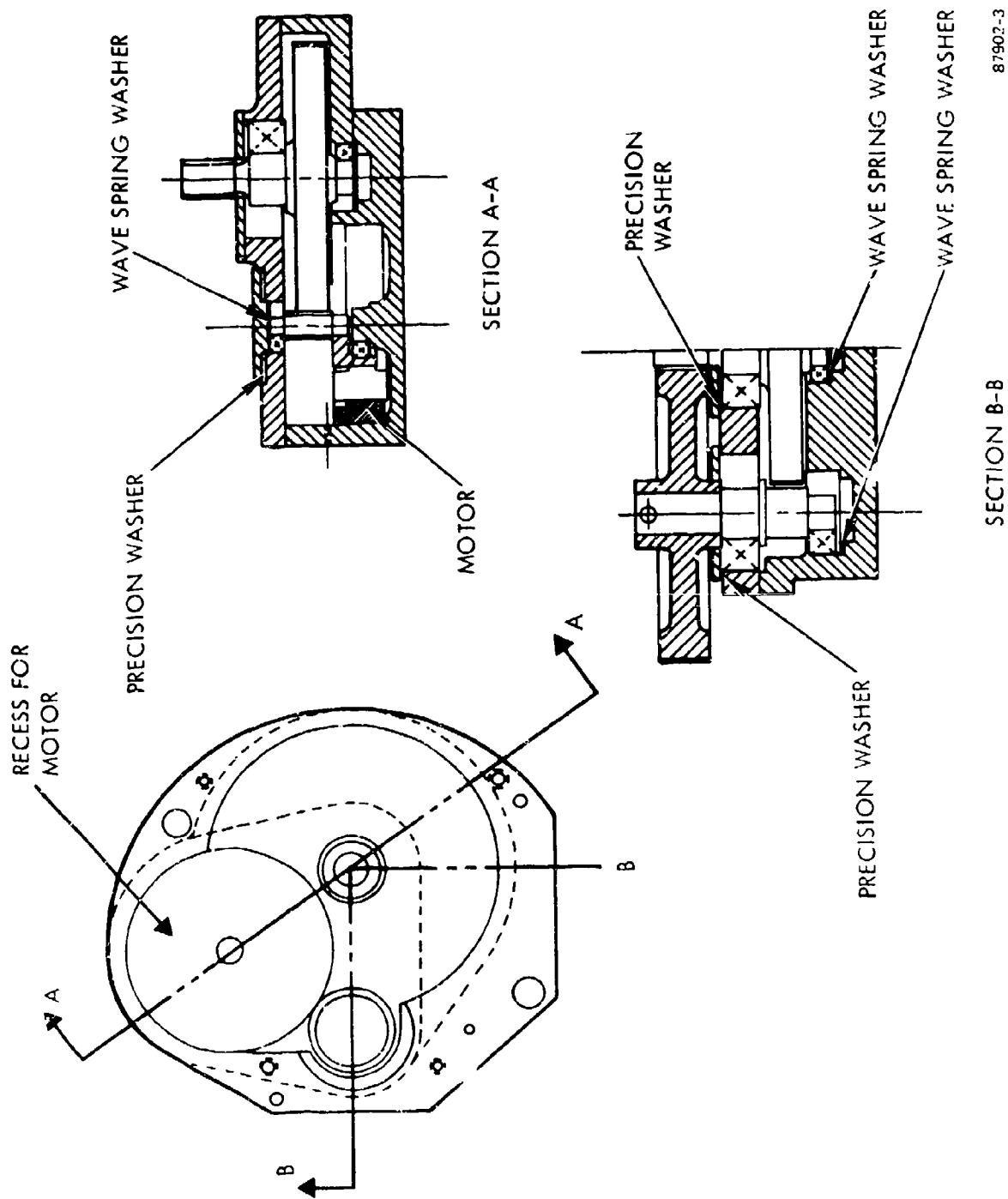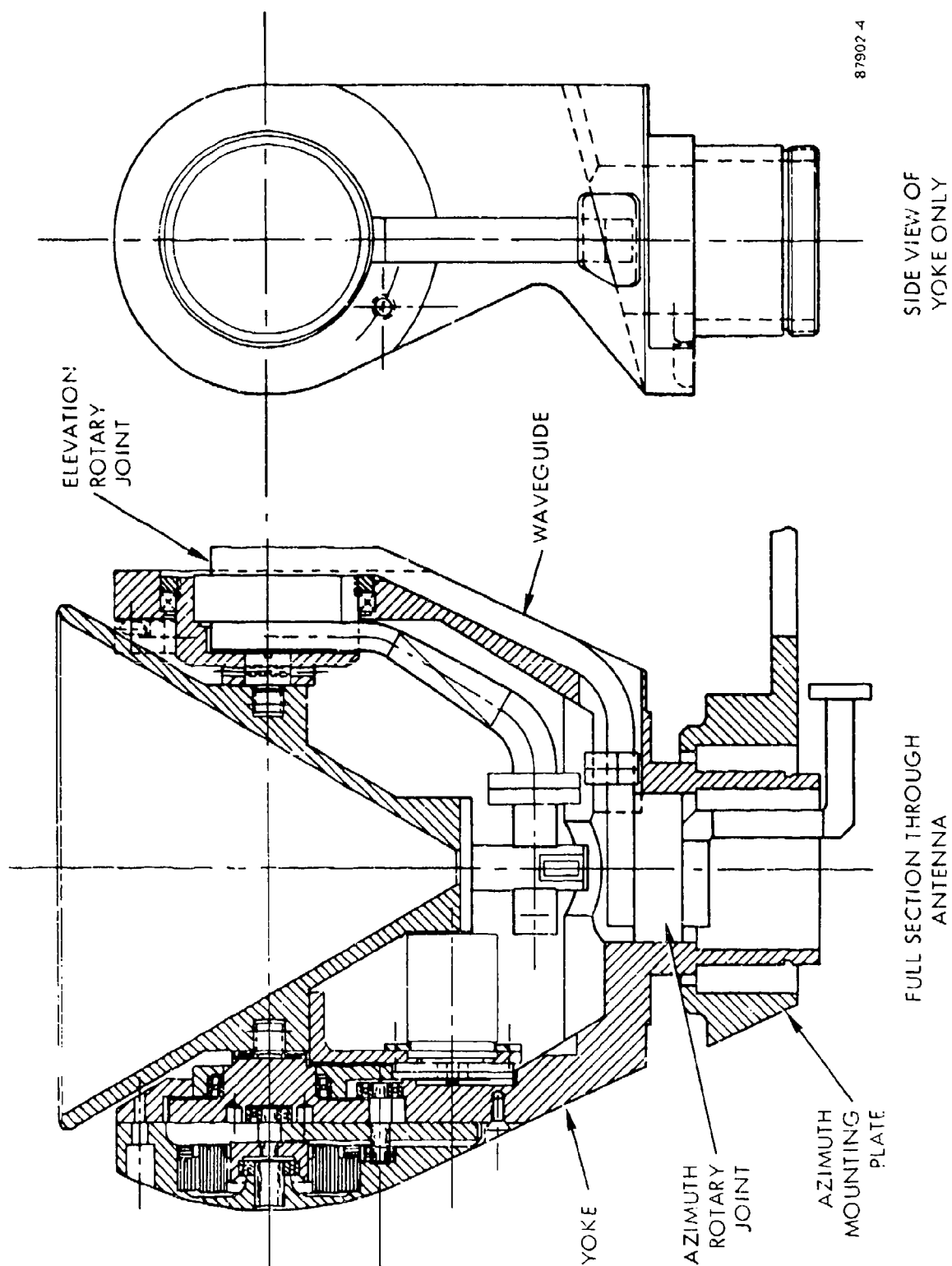
ELEVATION
SYNCHRO

FIGURE 7. ELEVATION GEARBOX LAYOUT